1991

Application of the boundary element method to elastic wave scattering problems in ultrasonic nondestructive evaluation

Paul Jay Schafbuch
Iowa State University

Order Number 9126246

Application of the boundary element method to elastic wave scattering problems in ultrasonic nondestructive evaluation

Schafbuch, Paul Jay, Ph.D.

Iowa State University, 1991

U·M·I
300 N. Zeeb Rd.
Ann Arbor, MI 48106

Application of the boundary element method to elastic wave scattering problems in ultrasonic nondestructive evaluation

by

Paul Jay Schafbuch

A Dissertation Submitted to the
Graduate Faculty in Partial Fulfillment of the
Requirements for the Degree of

DOCTOR OF PHILOSOPHY

Department: Aerospace Engineering and Engineering Mechanics
Major: Engineering Mechanics

Approved:

Signature was redacted for privacy.

In Charge of Major Work

Signature was redacted for privacy.

For the Major Department

Signature was redacted for privacy.

For the Graduate College

Members of the Committee:

Signature was redacted for privacy.

Iowa State University
Ames, Iowa
1991

TABLE OF CONTENTS

GENERAL INTRODUCTION

Nondestructive evaluation (NDE) is concerned with ensuring that material defects in components of engineered systems do not prevent those components from fulfilling their intended purpose. Defective materials can be classified in two ways. Overall material properties may not be as expected due to improper composition or processing. Secondly, localized imperfections may (and on some length scale always do)[1] occur as a result of component manufacturing processes or use. Given the reality of imperfect materials, engineering decisions must be made regarding the fitness-for-purpose of individual components. These decisions depend on the strength of evidence suggesting a significant flaw exists, the likelihood of failure under expected loads, the ramifications of failure, and the cost of replacing the part. Fitness-for-purpose may be inferred by testing a prototype, by testing sample component(s) or a specimen bar from randomly selected production runs, or by testing similar samples from every production run. These tests may be destructive (the part cannot be used again) or nondestructive. A destructive test may yield more information but the value of the part is lost. With destructive proof tests, the adequacy (or lack thereof) of the remaining parts is only inferred through association with the tested part. For critical components, sampling each production run may be sufficient for certifying overall material properties, but localized imperfections occur randomly and hence confound the notion of adequacy though association. In principle, maximum reliability can be ensured by testing all critical components, which by necessity must be a nondestructive test. Therefore, NDE plays a significant role in modern engineering practice[2].

Randomly occurring imperfections which may lead to localized failure can, under certain circumstances, be tolerated. Defining these circumstances is the goal of damage-tolerant design philosophy[3]. In other cases, complete failure is acceptable because the penalty is slight. However, if the structural integrity of nuclear power

reactor vessels or commercial aviation engines is compromised in a nonlocalized fashion, the results can be disastrous both in terms of human life and financial losses. There are countless other examples where a failure, if it occurred, may not be as sensational but nevertheless needs to be prevented if possible because human life and large investment in plant and equipment are at risk. In contrast to just intercepting impending failures, inspections can be used to justify extending the useful life of components that would be discarded under a probabilistic fracture mechanics philosophy[4]. Consequently, there is broad based support of NDE research into developing inspection techniques which can detect and characterize material flaws accurately.

Ultrasonic testing (UT) is one prominent technology utilized for NDE[5]. Typically, ultrasound of a frequency ranging from one to ten megahertz is passed into the material. The approach relies on the defect having different elastic properties than the surrounding material. This inhomogeneity will then disturb (scatter) the ultrasonic wave field. Information about the anomaly may be inferred from how these waves are scattered. Determining the best way to generate, collect, and interpret this information for various material/defect/component combinations is a primary research task. There are many important phenomena which must be understood in order to extract detailed quantitative information from UT, as illustrated by the schematic depiction in Figure 1. The conversion of an electrical signal to acoustic waves by piezoelectric or electromagnetic-acoustic transducers; the propagation of acoustic waves in a liquid bath or couplant; transmission through liquid-solid interfaces; propagation through an elastic solid which may be anisotropic; the interaction of the elastic wave field with the flaw or flaws (scattering); and the processing of received signals must all be understood quantitatively[6].

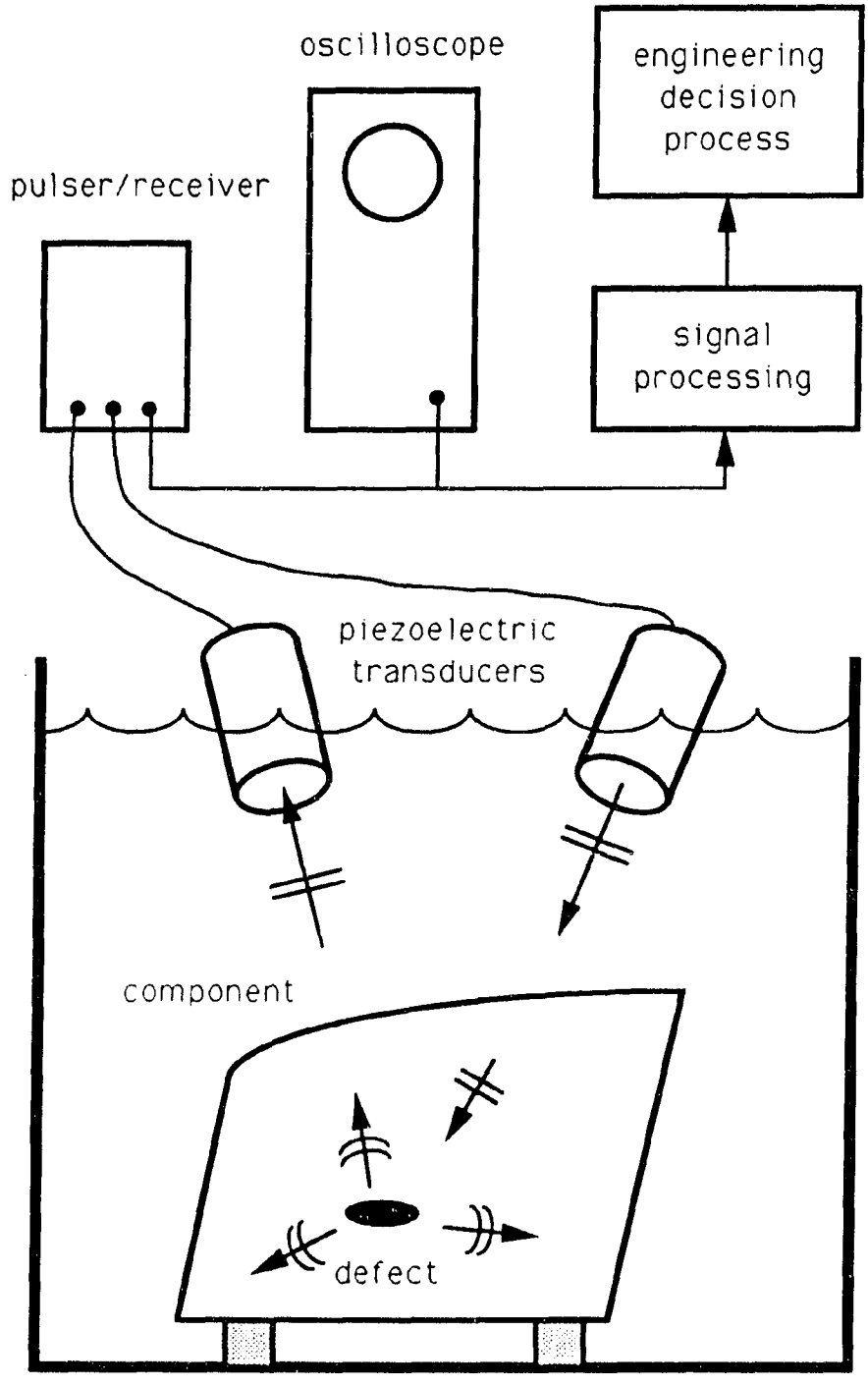

Figure 1 Conceptualization of a typical immersion ultrasonic test

The research presented in this dissertation focuses on the elastic wave scattering process itself. As with all the phenomena associated with UT, mathematical modeling and experimental work are necessary. This work deals with the mathematical modeling of arbitrarily shaped defects in a homogeneous, isotropic elastic medium. Although most metal alloys are not truly homogeneous, it still is fruitful to consider them as such, especially when the troublesome defects are much larger than the interspersed phases or grains. While many important materials, such as composites, are certainly not isotropic, the elastic wave scattering problem in anisotropic materials is so difficult that the assumption of isotropy has been employed in the majority of work to date[4].

Although the study of elastodynamic phenomena has a lengthy history, considerable progress has been made in the understanding of scattering over the last few decades[7]. However, even with the simplifying assumptions mentioned above, scattering problems are intractable without resorting to approximate and/or numerical approaches, except for a few very simple geometries. Much of the progress over the last fifteen years has been with approximate solution techniques for low frequency, high frequency, or small impedance mismatch (*cf.*, References 4 and 8). Often combined with these approximations are simplifications due to restricted defect geometries, such as planar cracks or axisymmetric voids[4]. While these special solutions deal with many important defect cases, they are not completely general. Results from numerical methods for elastic wave scattering from arbitrarily shaped defects at wavelengths on the order of the flaw size have only appeared recently. These methods are needed because naturally occurring defects have irregular shapes and because intermediate frequency inspections have certain advantages[9]. These methods include T-matrix, method of optimal truncation, finite element, and finite difference[4]. Additionally, one very promising numerical approach based on the boundary element method (BEM) had been identified for this purpose[10].

The scope of this work is to apply this previously developed, general BEM for elastic wave scattering to ultrasonic NDE problems. Since the scattering process is only a portion of a total UT model, the general code is first adapted to the complete ultrasonic modeling framework. Specifically, this effort includes developing several means to calculate standard measures of scattering and coupling to existing beam models. Secondly, this general approach requires nontrivial computational resources and user intervention, consequently a complete investigation of the methodology includes addressing issues of efficiency. Improvements in modeling productivity range from developing interfaces to commercial mesh generation software to code and algorithm improvements. Third, establishing the accuracy and reliability of predictions under a wide variety of conditions is prudent in assessing these procedures as a useful NDE research tool. The computer codes and defect models are verified through extensive comparisons with other analytical, numerical, and experimental results. Guidelines and methods for establishing accurate predictions are developed and certain difficulties are addressed. Finally, these procedures provide benchmarks for investigations of various approximate solution schemes.

In order appreciate the increment in knowledge and engineering capability that this dissertation represents, one must be cognizant of the prior work in elastic wave scattering and the boundary element method. The following two sections refer to fundamental background on which this work is based. They are not intended to be complete, but rather to place this work in the context of classical mechanics, applied mathematics, and related disciplines. More recent and directly relevant prior work is cited as appropriate throughout the body of this document.

Background on Elastic Wave Scattering

A full understanding of the elastic wave scattering phenomena requires an appreciation of linear elasticity[11] and wave mechanics[12]. The motions generated for an ultrasonic inspection are well within a material's elastic limit. The governing partial differential equation (PDE) for a linear, homogeneous, isotropic material dates back to Navier[7]. In vector form with no body forces, we have

$$\mu \nabla^2 \mathbf{u} + (\lambda + \mu) \nabla (\nabla \cdot \mathbf{u}) = \rho \ddot{\mathbf{u}} \tag{1}$$

where λ and μ are the Lamé constants, $\mathbf{u}$ represents the vector displacement field, and ρ is the density. The solution of this equation over a domain with suitable boundary conditions is the essence of elastodynamics problems. This equation governs vibration, radiation, propagation, diffraction, and scattering[8]. Scattering is a part of the study of waves which describes the diversion of incoming wave energy by an inhomogeneity in the propagating medium. The additional key concept which is needed for scattering problems is the Sommerfeld radiation condition. Mathematically, it is stated as[8]:

$$\lim_{r \to \infty} r \left[\frac{\partial \mathbf{u}}{\partial r} + \frac{1}{c} \frac{\partial \mathbf{u}}{\partial t} \right] = \mathbf{0}, \quad \lim_{r \to \infty} \mathbf{u} = \mathbf{0} \tag{2}$$

where c is the wave speed and r is the radius of a large sphere. Physically, it can be interpreted to mean that no wave propagates to the interior of a domain from infinity.

One strategy for approaching this problem is to assume time-harmonic motion[8], i.e., $\mathbf{u} = Re[\hat{\mathbf{u}} e^{-i\omega t}]$ with $\hat{\mathbf{u}}$ complex to account for differences in phase. A general transient solution can be generated by a Fourier transformation of frequency domain

solutions[7]. The advantage of the time-harmonic approach is a reduction of the PDE to only spatial dependence at a given frequency. In terms of the longitudinal (compressional) wave number, k_L, the governing relation is

$$\frac{\lambda+\mu}{\lambda+2\mu}\nabla(\nabla\cdot\mathbf{u})+\frac{\mu}{\lambda+2\mu}\nabla^2\mathbf{u}+k_L^2\mathbf{u}=\mathbf{0}. \tag{3}$$

Next we present the fundamental connection to acoustics.

If the wave bearing medium is an ideal fluid which does not support shear stresses, the value of μ is zero. Also $\mathrm{div}(\mathbf{u})$ is related to pressure, p, through the bulk modulus (Lamé constant), λ. The governing relationship in this time-harmonic form is the famous Helmholtz equation[8],

$$(\nabla^2+k_L^2)p=0. \tag{4}$$

Scattering governed by this equation is acoustic scattering and the waves are compressional in nature. (Alternately, an acoustic field is often expressed in terms of a potential function Φ and the fluid velocity vector is the gradient of this function.) The simple, scalar nature of this governing relation is one reason that problem solving developments in acoustic scattering precede those of the more general elastic case. The elastic case can also be expressed through the Stokes-Helmholtz decomposition as a set of three coupled Helmholtz equations[8]. Acoustics has many important applications which require scattering solutions. This topic has been studied intensely. Consequently, many of the concepts, conventions, and terminology from acoustic scattering have been

adopted by the elastic wave scattering community. Since texts dedicated to elastic wave phenomena have limited coverage of scattering[8,13-15] the interested reader is encouraged to also consult any acoustics text, e.g., References 16 or 17.

Many other branches of physics deal with wave phenomena, including hydrodynamics[18], optics[19], electromagnetism[20], and quantum mechanics[21]. These disciplines have been the source of other important ideas such as ray theory and wave polarization from optics and weak scattering approximations from quantum mechanics. Some terminology has been borrowed from the electromagnetic scattering, principally radar, community. Geophysics is another applied area which has motivated and utilized wave theory, in both earthquake and oil exploration studies. The similarity of scattering theory among all these disciplines is striking and insight can be gained by consulting the suggested or other references.

The fundamental complication of elastic wave scattering compared to acoustic scattering is due to the ability of an elastic solid to carry shear stresses. In addition to compressional waves, an elastic medium can support waves of distortion. The distortional waves, also known as equivoluminal, secondary, shear, or transverse waves, travel at a slower speed. These two types of waves exist within the bulk of an elastic medium and the total internal displacement field can be thought of as the sum of fields of each type. At the boundary of each homogeneous domain, these two fields are coupled through the boundary conditions. Elastic solids also have other wave types at boundaries and interfaces such as Rayleigh, Stoneley, Love, and head waves[7,8]. It is this plethora of modes that confounds analytical treatment. However, numerical methods based on the fundamental field quantities are oblivious to wave type interpretation - the physical solution is generated as a matter of course from the general field equation.

Background of the Boundary Element Method

The methods used to solve boundary value problems are so numerous that it is almost naive to attempt to create a complete classification scheme. Various attributes allow them to be categorized several ways. The methods may deal with the differential equation and boundary conditions directly or with an equivalent integral relationship and boundary conditions. Series solutions[22] and the finite difference method[23] deal with the PDE directly. The former is considered an analytical approach while the latter is numerical. The best known integral based methods are variational principles and the method of weighted residuals. Integral based approaches do little to aid analytical solutions but are a useful basis for numerical computation. The highly successful finite element method (FEM) is based on either variational or residual approaches. Another way to categorize is whether the method deals with the domain of the problem or the boundary of that domain. The Rayleigh-Ritz method is a domain based variational principle whereas the Trefftz method works with the boundary. Boundary methods are noted for dealing with infinite domains and field singularities[24].

One of the boundary methods is the so-called boundary integral equation method (BIEM)[10]. This acronym is sometimes used interchangeably with BEM, but a subtle distinction should be noted[25]. The BIEM is the analytical means by which the boundary integral equation (BIE) is formulated. The numerical methodology used to convert that expression to a computer assisted computation is the BEM. Therefore, BEM is a means for solving a BIE.

Boundary integral equations may be classified as direct or indirect[26]. In the direct method the field variables appear explicitly, whereas the indirect method is formulated

in terms of functions from which the true field variables can be determined. One approach to acoustic problems, known as the layer potential method, is an example of an indirect BIE[27]. The direct method is the basis of this work.

Direct boundary integral equations can be derived or interpreted a number of ways. From an integral calculus point of view, Green's identity relates the Laplacian operator over a domain, D, to normal derivatives at the boundary of that domain, B [22].

$$\int_D [u\nabla^2 U - U\nabla^2 u]dD = \int_B \left[u\frac{\partial U}{\partial n} - U\frac{\partial u}{\partial n} \right] dB \tag{5}$$

holds for sufficiently smooth scalar functions u and U. From a more general linear operator perspective, the relationship is

$$\int_D [uL(U) - UL^*(u)]dD = \int_B M_n(u,U)dB \tag{6}$$

where L is considered to be an elliptic operator with adjoint L^* and M_n is a related boundary gradient operator. This form includes the homogeneous linear operator corresponding to the elastodynamic PDE (1).

The second key concept in the BIEM is the use of the free-space Green's function as the function U in Equations (5) or (6). A Green's function is, in general, a solution to a PDE over a given domain with some particular boundary conditions. In this case, "free-space" connotes a full-space with radiation boundary conditions. In the terminology of Equation (6), a Green's function or "fundamental solution" has the property,

$$L[U(\mathbf{p},\mathbf{q})] = -\delta(\mathbf{p}-\mathbf{q}) \tag{7}$$

where δ is the Dirac delta function[22]. The fundamental solution has a physical interpretation in mechanics, namely, the field at $\mathbf{q}$ generated by a concentrated load at $\mathbf{p}$.

For the homogeneous operators which we are considering, manipulation of Equations (6) and (7) will result in a formula for the field at any point in the domain in terms of the field at the boundary. In a well posed problem, only half of the boundary values are given. The remaining boundary values can be determined by taking the point $\mathbf{p}$ to the boundary, B, and then solving the resulting BIE. For the case of the Laplacian operator in 3D, the BIE appears as

$$\frac{1}{2}u(\mathbf{p}) = \oint_B \left[\frac{1}{4\pi r}\frac{\partial u}{\partial n} - u\frac{\partial}{\partial n}\left(\frac{1}{4\pi r}\right)\right] dB(\mathbf{q}) \tag{8}$$

at any point where the boundary is smooth. In this simple example, the fundamental solution is $(-1/4\pi r)$ with $r = |\mathbf{p}-\mathbf{q}|$.

From a method of weighted residuals point of view, the finite element and boundary element methods stem from a common foundation. The finite element method may be interpreted as based on a "weak" form of the residual statement. This form is the result of integrating the residual statement by parts once. An "inverse" form is arrived at by integrating by parts again. If the fundamental solution is used as the weighting function, the inverse form constitutes a BIE as derived above. It should be noted that the Trefftz boundary method results when a different choice of weighting function is made[11,26].

Boundary integral equations are a particular type of integral equation in which the domain of integration is fixed. In this regard they are similar to the classic Fredholm integral equation type and the abundant theory for Fredholm equations can often be drawn upon[28]. For acoustic and elastodynamic phenomena, the BIEs have singular kernels which makes them more formidable to work with both analytically and numerically than the compact kernel Fredholm equations. Depending on the problem and the formulation, these equations may be weakly, strongly, or hypersingular and the integral values may need to interpreted in a Cauchy principal value (CPV) or finite-part sense[25]. Dealing with these singularities is the final step of the BIEM.

As previously mentioned, the boundary element method is a means of solving a BIE. The integral of the unknown field function is approximated by first dividing its domain into segments or "elements". Over each element the field quantities and the geometry are interpolated by local basis functions in terms of values at specific points called nodes. In this aspect the term "element" has identical connotation as it does in FEM. Distributed field quantities are thus expressed in terms of discrete parameters, resulting in an equivalent algebraic equation. In our BEM the BIE is collocated, or written for each node point. In essence, collocation forces the discretized BIE to be valid at each node. This approach is analogous to the collocation method of weighted residuals. Other approaches such as method of moments, least squares, etc. are possible[28].

A Note about the Dissertation Organization

The body of this dissertation is divided into four sections designated Part I though Part IV. Each section corresponds to a separate archival journal article written on this research. Each article conveys a particular portion of the inter-related subjects addressed. The sections are word for word identical with the published papers except

for some alterations to make this document uniform in style or as part of the yet to be completed peer review process. The equation, reference, and figure numbers are local to each part. Tying these parts together is the present general introduction and a general conclusions section at the end. This organizational structure is known as the alternate dissertation format.

Part I is a paper which will appear in the *Journal of Nondestructive Evaluation* entitled "Application of the boundary element method to elastic wave scattering by irregular shaped defects". The intended audience of this article is ultrasonic NDE researchers who are interested in a modeling tool which can solve specific classes of problems. The "solution" can be specific predicted values to compare with experimental results or parametric studies. The emphasis is on adapting BEM procedures to model ultrasonic scattering and making comparisons with other theories and experiments involving irregular shapes. The authors of this paper are Paul J. Schafbuch, R. Bruce Thompson, and Frank J. Rizzo.

Part II is a brief note which will appear in the *Transactions of the ASME - Journal of Applied Mechanics* called "Eigenfrequencies of an elastic sphere with fixed boundary conditions". This problem was encountered in research on the fictitious eigenfrequency difficulty which arises with our BIE formulation of exterior domain scattering problems. Previously, a solution to this fundamental elastodynamics problem had never been completely worked out. This work has application beyond elastodynamic BEM research. The authors of this note are P. J. Schafbuch, F. J. Rizzo, and R. B. Thompson.

Part III is a paper submitted to the *International Journal of Numerical Methods in Engineering* named "Boundary element method solutions for elastic wave scattering in 3D". This section emphasizes the numerical aspects of the capability for 3D elastic wave scattering at intermediate frequency. This work presents results for rigid and elastic

inclusions and cavities of an ellipsoidal shape. The modeling of cracks with thin voids is discussed. Finally, results from a numerical investigation of the fictitious eigenfrequency difficulty are presented and interpreted in light of recent theoretical findings. The authors of this paper are P. J. Schafbuch, F. J. Rizzo, and R. B. Thompson.

Part IV deals with the interaction of two scatterers. This paper entitled "Multiple elastic scatterer interaction via Born and farfield approximations" will be submitted to *The Journal of the Acoustical Society of America*. It describes and demonstrates the efficiency of a hybrid method for interaction effects. The realm of applicability of two simple, but robust, approximations is investigated for cases involving a pair of voids. The authors of this paper are P. J. Schafbuch, R. B. Thompson, and F. J. Rizzo.

Additionally, there is an Appendix A which contains significant research results which are not, at this point, being published in the aforementioned articles or in the *Review of Progress in Quantitative Nondestructive Evaluation* conference proceedings[29,30]. These results include selected scattering amplitudes from a family of elliptical cracks for $k_L a$ up to three.

Finally, Appendix B describes the software developed as part of this effort. The program organization and file structure is reviewed so that future researchers may use and further develop these programs. It also highlights the coupling of our scattering codes to commercial computer-aided-engineering (CAE) software.

PART I.

APPLICATION OF THE BOUNDARY ELEMENT METHOD TO ELASTIC WAVE SCATTERING BY IRREGULAR DEFECTS

Abstract

A time-harmonic boundary element formulation for elastic wave scattering in 3D is adapted to ultrasonic NDE. Defect classes addressed are volumetric voids and inclusions, and crack-like elliptical voids. For axisymmetric flaws, comparisons are made with method of optimal truncation (MOOT) and transition-matrix calculations. Comparison to experiment is made for more general shapes. For crack-like voids, comparisons are made with the Kirchhoff, geometric theory of diffraction (GTD), and quasistatic asymptotic approximations. The efficiency and usefulness of the boundary element method (BEM) in finding the bounds of applicability of these approximate theories are demonstrated. An example of a flaw characterization technique based on intermediate frequency scattering data simulated by BEM is given. The ability of BEM to handle nonplanar incident fields, as described by a transducer beam model, is shown. Other computational and modeling efficiencies of the BEM are noted.

Introduction

The need for quantitative ultrasonic NDE techniques has motivated much progress in the understanding of elastic wave scattering by imbedded inhomogeneities and in the ability to numerically model the scattering process for specific cases. In order to obtain solutions, a variety of simplifying assumptions has been utilized. There are low frequency approximate solutions for very small (relative to the inspection wavelength)

defects, both volumetric[1] and crack-like[2]. At high frequency, there are solutions based on the Kirchhoff approximation[3] or on the geometric theory of diffraction (GTD)[4] for crack-like flaws. The Kirchhoff approximation can also be applied to volumetric defects[5].

These approximations are valid for a number of special cases found in practice. However, they do not in general give accurate results when the wavelength is comparable to the flaw size. In that intermediate frequency range, the strategy has been to limit the possible geometries of the simulated defect. A separation of variables analytical solution exists for spheres[6]. For more general volumetric shapes, there are eigenfunction expansion based solutions such as MOOT[7], T-Matrix[8], and finite element[9]. These methods have in practice only been implemented for axisymmetric shapes. There has also been considerable success in finite difference and finite element solutions of 2D planar problems[10,11]. The analogous geometric restriction for crack-like defects is to assume the crack is circular and/or planar. All of these approaches, with the exception of the sphere's solution, are computationally intensive.

Similar geometric simplifications are also often made regarding the incident field. Beam models are often used which account for diffraction, refraction, and attenuation of the field emanating from the transducer. But normally the incident field is assumed to be locally planar over the whole defect[12] or at each "flash point" of cracks[13] to simplify the scattering calculation.

In this paper, a method is reported which fills the obvious gap - arbitrarily shaped 3D flaws in the intermediate frequency range with general incident fields. The scattering from single, isolated defects in an otherwise homogeneous, isotropic, elastic full-space is

treated. The defects may be either voids or homogeneous isotropic inclusions. We note that Temple[14] has a 3D finite difference code for inhomogeneous, anisotropic, bounded media but it is only feasible for near field scattering.

The uses of the scattering solutions offered guidance in the selection and development of our method. Current thinking gives three major uses for such a method. The first use is in probability of detection (POD) models which must consider a statistical range of parameters such as flaw size, orientation, and position relative to transducers and/or the component surface[15]. Another use is as a catalog of forward scattering solutions for the flaw characterization or "inverse scattering" process. Determining the limitations of simpler more efficient calculation procedures is the third use. For example, in this paper we use our method to find the error of a long wavelength scattering model for cracks as a function of frequency. Clearly, computational efficiency is important for a method employed in any of these three applications so that a reasonable number of cases over the expected range of parameters can be calculated.

Boundary Element Method

The time-harmonic formulation of the boundary element method (BEM) for elastodynamics has some features which make it particularly attractive for solving these kinds of scattering problems. These features include rigorous treatment of the Sommerfeld radiation condition for an unbounded medium, reduction in the dimensionality of the problem, reusable matrices, direct methods for calculating flaw induced signals, and other instances of computational savings. Especially important is the fact that domain boundaries do not have to be introduced artificially. The BEM is a method for solving a boundary integral equation (BIE).

Integral equation

The BIE is derived by applying Green's Reciprocal Identity to the elastic wave partial differential equation (PDE). This identity converts a volume (domain) integral to a surface (boundary) integral for an elliptic operator such as the time-harmonic wave equation. This reduction in dimension is a significant advantage over domain type methods like finite difference and finite element.

Solutions in the frequency domain are the most convenient form in many instances. Sometimes they are thought to be rather indirect, if the desired result is a time domain waveform, because the solution must be generated at numerous frequencies followed by a Fourier transform. Alternately, one could time step the hyperbolic form of the PDE. We find that much coarser meshes can be used with the time-harmonic approach.

The appropriate BIE for this elastodynamic scattering problem is given in Reference 16. The BIE is an expression relating the complex displacement vector, u, and traction vector, t, along with their fundamental solution (free-space Green's function) counterparts, U and T.

$$\mathbf{C}^T(\mathbf{p})\mathbf{u}(\mathbf{p}) = \int_S [\mathbf{t}(\mathbf{q})\mathbf{U}(\mathbf{p},\mathbf{q}) - \mathbf{u}(\mathbf{q})\mathbf{T}(\mathbf{p},\mathbf{q})]dS(\mathbf{q}) + \mathbf{u}^I(\mathbf{p}) \quad (1)$$

where q is a generic point of the flaw boundary S. The field point p has been taken to the boundary. The tensor C depends on the surface topology at point p, i.e., if p is on a side, edge, or corner[16]. U and T are complicated functions of frequency and the distance between points p and q. They are singular when p = q and oscillate throughout space.

Superscript I on $\mathbf{u}$ refers to the incident field, while no superscript implies the total field. Equation (1) is used to find the unknown total field quantities at the surface from specified boundary conditions and the incident field.

Algebraic equations

The BIE is converted to algebraic equations by discretizing the flaw surface into curvilinear quadratic and triangular sections or elements. Any shape can be fabricated. The actual surface geometry is then interpolated by quadratic polynomials over each element in terms of nodal coordinates. Each field variable is also represented by a quadratic interpolation of nodal quantities. The integrals are performed by Gauss quadrature. The number of Gauss points used varies according to the severity of fundamental solution fluctuation. Specifics of this procedure are given in Reference 17. Sample meshes are shown in Figures 1 through 4. The program has a feature which allows problems with a plane of symmetry to be defined by meshing only one-half the actual shape. This use of symmetry significantly reduces the required computation.

The BIE is written for the host medium for each node point $\mathbf{p}$. If the flaw is an inclusion, a degenerate form of Equation (1) with no incident field is also written for the flaw material at each of those same nodes. In addition to material property changes, the surface normal and (sometimes) values of $\mathbf{C}^T$ change for the complimentary domain. Interface displacements and tractions are matched-up as usual. This results in a set of simultaneous, linear algebraic equations. The equation set has the form of a matrix whose coefficients depend on flaw geometry, frequency, and material properties, and a right hand side vector which contains the components of the incident field at each node. The unknown vector consists of nodal values of displacement and/or traction which must be solved for after boundary conditions are imposed. This form is very convenient because the numerous possible incident fields and flaw orientations that must be

considered by a POD model are merely different right hand side vectors. The matrix is fully populated due to global influence of the fundamental solution, but it can be formed and decomposed once, saved, and then used repeatedly with various incident fields.

$$\begin{bmatrix} \text{coefficients depend on} \\ \text{geometry, frequency,} \\ \text{and material properties} \end{bmatrix} \begin{Bmatrix} \mathbf{u} \\ \mathbf{t} \end{Bmatrix} = \begin{Bmatrix} \mathbf{u}^I \\ \mathbf{0} \end{Bmatrix} \tag{2}$$

Adaptation of the BEM to Ultrasonic NDE

The solution to the set of simultaneous algebraic equations provides a complete description of the motion and stress state at the flaw surface for a given incident field. To convert this information into something useful for modeling NDE responses, additional formalisms are needed. Ultimately one wants to determine the signal due to the presence of a given flaw for a particular inspection arrangement. Several routes are possible.

Scattering amplitudes

Often the scattered field is characterized by a scattering amplitude, A, which defines the spherically spreading wave that is generated in the farfield by plane wave illumination of the flaw. For elastic waves

$$\frac{\mathbf{u}^S \cdot \hat{\mathbf{d}}^S}{|\mathbf{u}^I|} \rightarrow \frac{A(\theta^I, \phi^I, \hat{\mathbf{d}}^I, \theta^S, \phi^S, \hat{\mathbf{d}}^S)}{R} e^{ik_m R} \tag{3}$$

with R large. A is a function of incident and scattered direction (θ, ϕ) and polarization $(\hat{\mathbf{d}})$ as well as scattered mode wavenumber (k_m). A has units of length and we use the

typical convention, that the characteristic dimension of the scatterer has length of one unit, for our numerical results. R is the distance from the apparent source of the spherical wave and $|\mathbf{u}^I|$ denotes the amplitude of the incident plane wave. Here, and throughout this paper, an $e^{-i\omega t}$ time dependence is implied.

Scattering amplitudes can be computed from the surface displacement solution. This solution is for the total field at the host medium boundary. The scattered field at any point in the host domain can be determined from this surface solution. For these points, the integral equation is no longer singular and the C tensor is merely the identity matrix. Then employing the field decomposition rule for the scattered field

$$\mathbf{u}^S = \mathbf{u} - \mathbf{u}^I, \tag{4}$$

we get the so-called interior representation integral:

$$\mathbf{u}^S(\mathbf{p}_0,\omega) = \int_S [\mathbf{t}(\mathbf{q},\omega)\mathbf{U}(\mathbf{p}_0,\mathbf{q},\omega) - \mathbf{u}(\mathbf{q},\omega)\mathbf{T}(\mathbf{p}_0,\mathbf{q},\omega)]dS(\mathbf{q}) \tag{5}$$

To get farfield scattering amplitudes, we select a point $\mathbf{p}_0$ sufficiently far removed from the flaw and in the desired direction and then calculate the scattered displacement field there. For the case of L-wave illumination, there are two amplitudes on a plane of symmetry - scattered displacement in the direction of propagation (L-L) and a mode converted transverse component (L-T) with polarization $\hat{\mathbf{d}}^S$.

$$A_{L\text{-}L} = \mathbf{u}^S \cdot \mathbf{p}_0 e^{-ik_L|\mathbf{p}_0|}/|\mathbf{u}^I| \tag{6}$$

$$A_{L\text{-}T} = |\mathbf{p}_0|\sqrt{(\mathbf{u}^S \cdot \mathbf{u}^S) - (\mathbf{u}^S \cdot \hat{\mathbf{p}}_0)^2}\, e^{-ik_T|\mathbf{p}_0|}/|\mathbf{u}^I| \tag{7a}$$

$$\hat{\mathbf{d}}^S = \frac{\mathbf{u}^S - (\mathbf{u}^S \cdot \hat{\mathbf{p}}_0)\hat{\mathbf{p}}_0}{\sqrt{\mathbf{u}^S \cdot \mathbf{u}^S - (\mathbf{u}^S \cdot \hat{\mathbf{p}}_0)^2}} \tag{7b}$$

with

$$\hat{\mathbf{p}}_0 = \mathbf{p}_0 / |\mathbf{p}_0| \tag{7c}$$

Similar equations can be written for T-wave incident fields.

Farfield kernels

Since the scattering amplitude is defined in the farfield of the flaw, a more computationally efficient method than the standard interior representation integral approach is possible. Reference 16 gives the fundamental solution for 3D elastodynamics as:

$$U_{ij} = \frac{1}{4\pi\rho\omega^2 r^3}\left\{\delta_{ij}\left[(k_2 r)^2 e^{ik_2 r} + D\right] + C\frac{\partial r}{\partial x_i}\frac{\partial r}{\partial x_j}\right\} \tag{8a}$$

with

$$C = \sum_{m=1}^{2} (-1)^m e^{ik_m r}[3 - 3ik_m r - (k_m r)^2] \tag{8b}$$

$$D = \sum_{m=1}^{2} (-1)^m e^{ik_m r}[ik_m r - 1] \tag{8c}$$

where k_1 corresponds to k_L and k_2 corresponds to k_T. The expression for T is:

$$T_{ij} = \frac{1}{4\pi\rho\omega^2 r^4}\{\lambda e^{ik_1 r}(k_1 r)^2(ik_1 r - 1)\frac{\partial r}{\partial x_j}n_i + \mu e^{ik_2 r}(k_2 r)^2(ik_2 r - 1)\left(\delta_{ij}\frac{\partial r}{\partial n} + \frac{\partial r}{\partial x_i}n_j\right)$$
$$+ 2\mu\left[C\left(\delta_{ij}\frac{\partial r}{\partial n} + \frac{\partial r}{\partial x_j}n_i + \frac{\partial r}{\partial x_i}n_j\right) + F\frac{\partial r}{\partial x_i}\frac{\partial r}{\partial x_j}\frac{\partial r}{\partial n}\right]\} \qquad (9a)$$

with C from Equation (8b) and

$$F = \sum_{m=1}^{2} -(-1)^m e^{ik_m r}[15 - 15ik_m r - 6(k_m r)^2 + i(k_m r)^3] \qquad (9b)$$

In all of these equations ρ denotes density, ω denotes angular frequency, n_j are the components of the unit inward normal $\hat{\mathbf{n}}$, and the Lamé constants are λ and μ. Since p_0 is far away, the asymptotic limit of these kernels as $r = |\mathbf{p} - \mathbf{q}|$ goes to infinity can be used:

$$U_{ij}^{\infty} = \frac{1}{4\pi\rho\omega^2 r}\left\{\delta_{ij}k_T^2 e^{ik_T r} + \left[k_L^2 e^{ik_L r} - k_T^2 e^{ik_T r}\right]\frac{\partial r}{\partial x_i}\frac{\partial r}{\partial x_j}\right\} \qquad (10)$$

$$T_{ij}^{\infty} = \frac{ik_L^3}{4\pi\rho\omega^2 r}\{\lambda e^{ik_L r}\frac{\partial r}{\partial x_j}n_i + \mu\left(\frac{k_T}{k_L}\right)^3 e^{ik_T r}\frac{\partial r}{\partial n}\left[\delta_{ij} - 2\frac{\partial r}{\partial x_i}\frac{\partial r}{\partial x_j}\right]$$
$$+ \mu\left[\left(\frac{k_T}{k_L}\right)^3 e^{ik_T r}n_j + 2e^{ik_L r}\frac{\partial r}{\partial x_j}\frac{\partial r}{\partial n}\right]\frac{\partial r}{\partial x_i}\} \qquad (11)$$

In Equations (10) and (11) the partial derivatives of r are merely the direction cosines of the desired scattering direction. If these expressions are combined with the Equations

(5), (6), and (7), compact expressions for A result. See Appendix Equations (A4) and (A5). The use of the asymptotic form reduces the computation time of this step by one-half.

Electromechanical reciprocity integral

Auld's electromechanical reciprocity relationship[18] is a powerful tool for the prediction of an electrical signal produced by transducers due to the presence of a flaw in an elastic medium. $\delta\Gamma_F$ is defined as the flaw induced change in the received signal, and is found to be a function of particle velocity $\dot{u}$ and stress $\vec{\vec{\tau}}$ for state "a" - transmitting transducer illuminating the medium with the flaw present - and for state "b" - receiving transducer acting as a transmitter with the flaw absent. Specifically, one finds

$$\delta\Gamma_F = \frac{1}{4P}\int_S [\dot{u}_a \cdot \vec{\vec{\tau}}_b - \dot{u}_b \cdot \vec{\vec{\tau}}_a] \cdot \hat{n}\, dS \qquad (12)$$

where P is the incident electrical power and the integral can be taken over any closed surface S that contains the flaw. We take S to be the flaw surface itself where the BEM automatically provides displacement (hence velocity) and traction fields. For problems such as stress analysis, proponents of domain type methods argue that computational savings due to reduction in dimension with the BEM are lost by the need to calculate interior fields via repeated use of the interior representation integral. But, for flaw signal prediction problems, knowledge of the field throughout the domain is unnecessary. The BEM inherently provides just the information needed by the reciprocity integral. For a void, there is the additional simplification that $\vec{\vec{\tau}}_a$ is zero. $\vec{\vec{\tau}}_b$ is calculated by spatial differentiation of the displacement field provided by a beam model.

$$\tau_{ij} = \delta_{ij}\lambda\frac{\partial u_m}{\partial x_m} + \mu\left(\frac{\partial u_i}{\partial x_j} + \frac{\partial u_j}{\partial x_i}\right) \tag{13}$$

The correspondence between the farfield scattering amplitude, A, and the change in signal due to a flaw under the quasi-plane wave assumption, $\delta\Gamma_F$, was given by Thompson and Gray[12].

$$\delta\Gamma_F = \frac{\pi\rho\omega c_b^2 I_a I_b A}{iP} + E_1 + E_2 \tag{14}$$

where the subscripts have similar connotations as in Equation (12), the I's are displacement amplitudes, c_b is the speed of waves generated by the "b"-state transducer, and the E's are error terms. (In Reference 12, velocity amplitudes are used and so an "extra" $-\omega^2$ appears in our formula). The derivation of Equation (14) involved the integration of various field quantities on the surface of an imaginary sphere of radius R containing the flaw. The error term, E_1, involves nonplanarity of radiation patterns and deviations of scattered fields from their spherically spreading farfield form, both over the surface of the sphere. E_2 is an infinite series of terms of order $(k_b R)^{-n}$ formally arising as a result of multiple integrations by parts over the surface of the sphere. By choosing a particular value of R, large with respect to the flaw size, it was shown that a sufficient condition for the errors to be small was "that the illuminating fields are quasi-planar over the volume of the flaw and that the scattering amplitude is slowly varying over the set of angles subtended at the flaw by the transducer." As noted in Reference 12, the sum of the errors in Equation (14) must be independent of R since the exact and the approximate solutions do not depend on R. In the Appendix, we formally confirm that assertion[19] by showing that the choice of S equal to the surface of the flaw, rather than the surface of a "large" sphere, also leads to Equation (14).

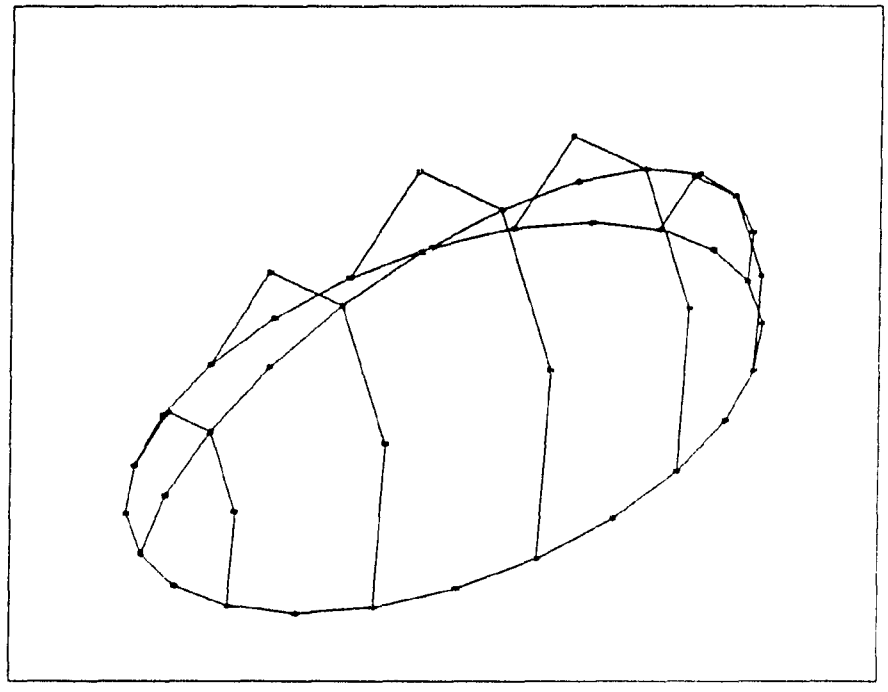

Figure 1 Oblate (2:2:1) spheroid model - 12 elements

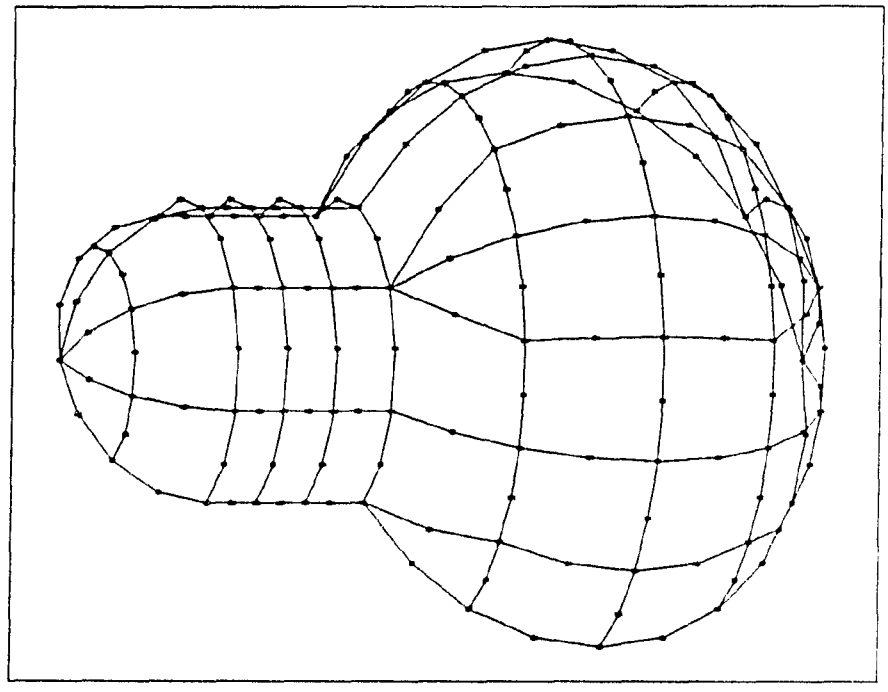

Figure 2 "Pinocchio" model - 56 elements

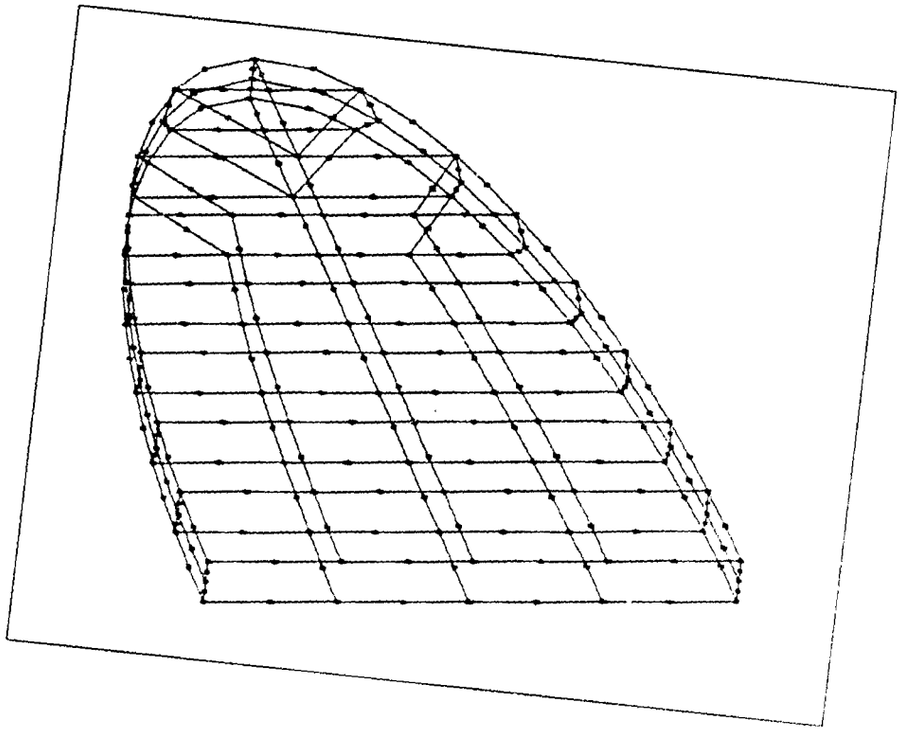

Figure 3 Elliptical (50:12:5) frustrum disc model - 92 elements

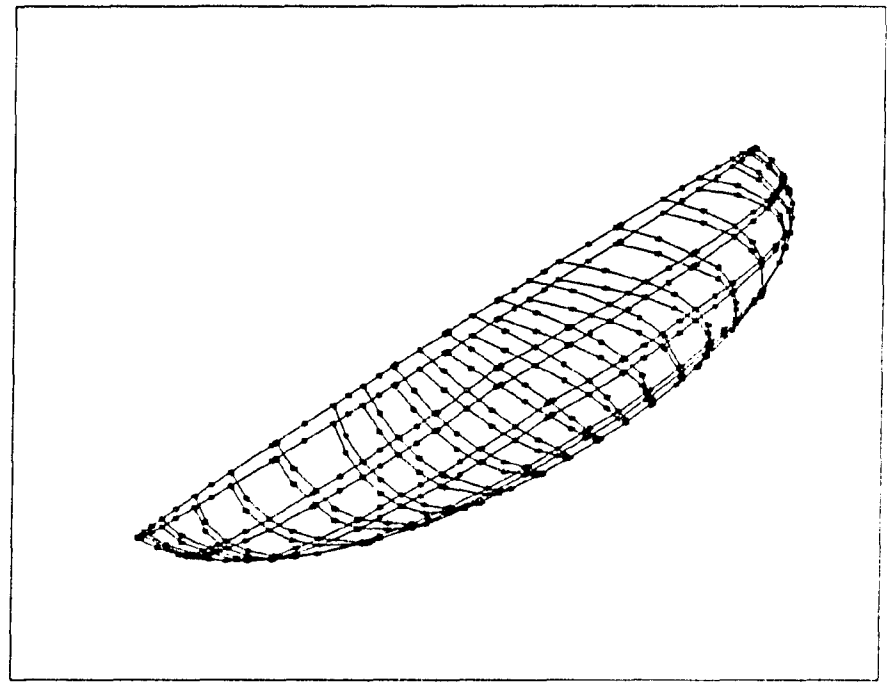

Figure 4 Elliptical (14:7:1) "crack" model - 140 elements

Incident fields

When flaws are small relative to the ultrasonic beam features, the quasi-plane wave assumption remains valid and the specification of the incident field at the BEM nodes is a straightforward process. For example, incident L-wave displacements with the implied harmonic time dependence are:

$$\mathbf{u}^{I}(\mathbf{p}) = I_a \frac{\mathbf{k}}{|\mathbf{k}|} e^{i\mathbf{k}\cdot\mathbf{p}} \qquad (15)$$

where $\mathbf{k}$ is the wave vector, and I_a is the local displacement amplitude of the incident field.

The BEM works just as well for incident fields which are not planar but which can be reasonably approximated by the quadratic interpolation functions of the flaw model's elements. In such cases, a more sophisticated approach such as the Gauss-Hermite beam model[20,21] is needed to provide nodal values of the incident field. This model works conveniently with our formulation since it provides point by point field values and is also time-harmonic.

Scattering from Voids

Voids are a common class of defect in structural materials. Computationally they are comparatively simple to handle. The BIE needs only to be computed for the host domain and the surface tractions are known to be zero. Consequently, the Equation set (2) simplifies and the U_{ij} kernels need not be calculated.

Comparison with MOOT

Figures 5a and 5b give results for an axisymmetric shape which is known as "Pinocchio" to the NDE research community. This shape is formed by two spheres and a connecting cylindrical section as depicted by Figure 2. The "back" is defined as the end opposite the small sphere or "nose". "Side" incidence refers to any direction perpendicular to the symmetry axis. The 56 element discretization is rather crude but gives good results for $k_L a$ up to 3.5. Figure 5b demonstrates the typical degradation of accuracy as frequency is increased. This decrease in accuracy is understood to be caused by the inability of the interpolating polynomials to adequately represent the spatial variations in the field as wavelength decreases. The remedy is to increase the number of elements in the model. Mesh requirements and accuracy will be dealt with in detail in a subsequent paper.

Previously[22], we presented similar backscatter results for the "side" and "back" of a related shape. That shape, known as "Mickey Mouse", is identical to "Pinocchio" except that the "nose" does not include the cylindrical section. In that paper, our initial disagreement with the MOOT solution for "Pinocchio" was hypothesized to be due to inadequate mesh in the nose/sphere region. Subsequent calculations have removed that disagreement. The problem was actually caused by inconsistent definitions of the length of the "nose" (cf. References 7 and 23). Our definition is now consistent with Reference 7. The radius of the large sphere is a, the small spherical cap has radius of $a/2$, and the cylindrical section has length $(3-\sqrt{3})a/2$. Also in Reference 22 are selected comparisons of oblate spheroidal void solutions with MOOT. All the voids are in a "generic" host material having properties as given in Table I.

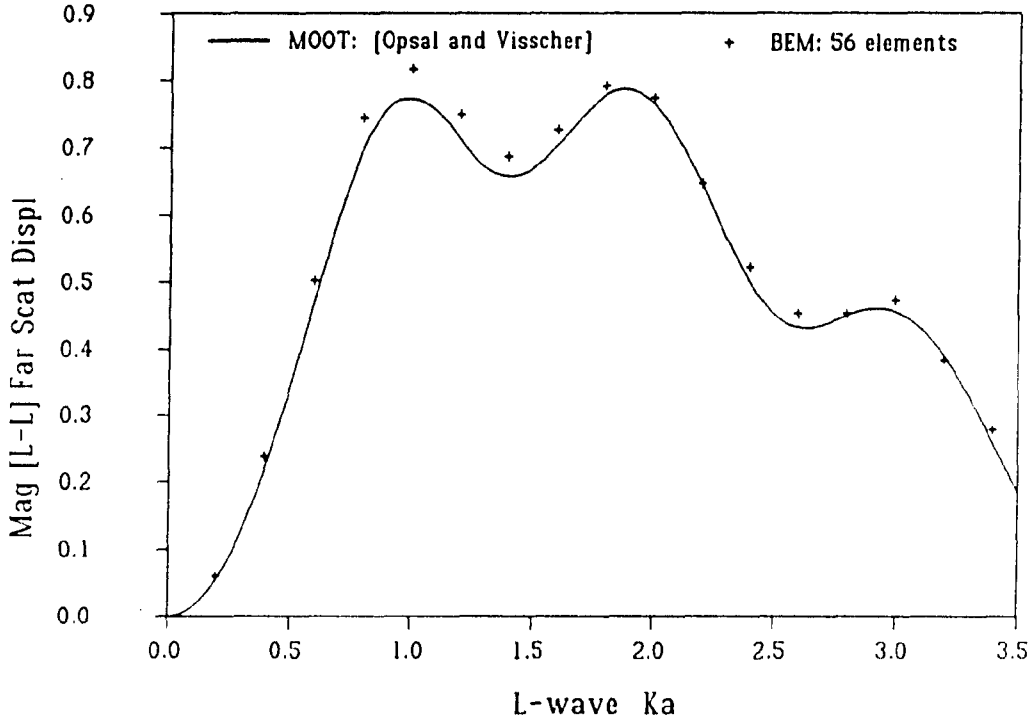

Figure 5a L-wave to L-wave backscatter from Pinocchio's side

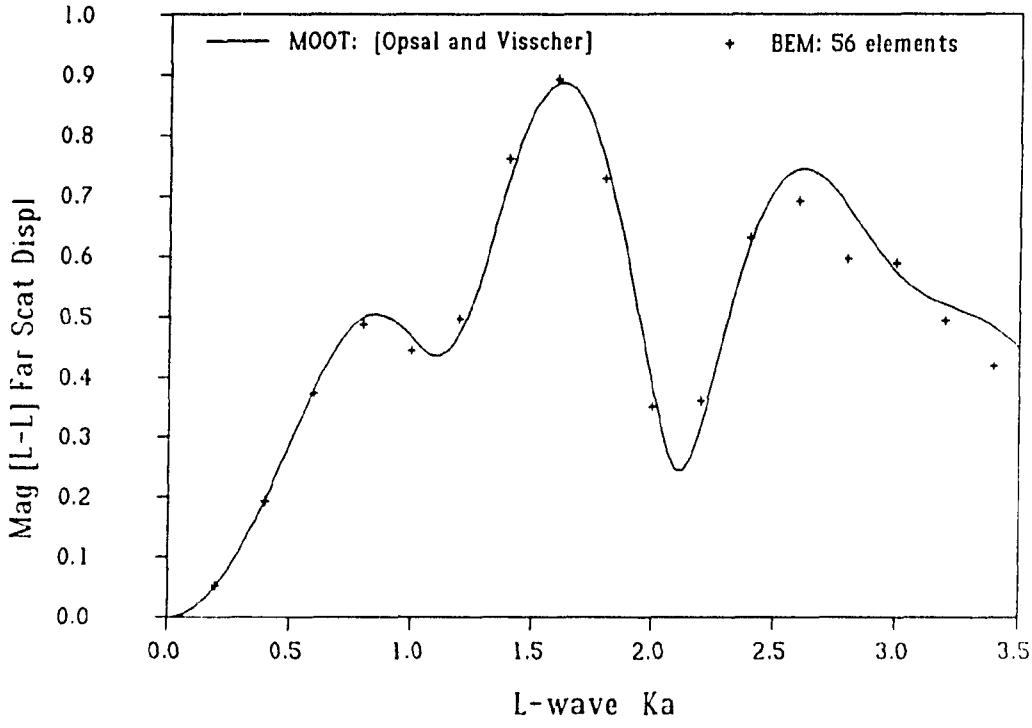

Figure 5b L-wave to L-wave backscatter from Pinocchio's back

Table I: Material Properties Used

	Longitudinal Wavespeed (cm/μs)	Transverse Wavespeed (cm/μs)	Density (g/cc)
Copper	0.460	0.230	8.90
Generic Material	1.000	0.500	1.00
IN100	0.631	0.329	7.85
Lucite	0.272	0.134	1.18
Titanium Alloy	0.634	0.303	4.42
Tungsten Carbide	0.666	0.398	13.82

Comparison with experiment

In the arena of truly 3D shapes (no axis of symmetry) and intermediate frequency, the basis of comparison is essentially limited to experiment. Since the conversion of experimental measurements to absolute unbounded medium scattering amplitudes has already been demonstrated[12], the comparison to experiment for volumetric defects, Figures 6 and 8, show best fit scaled results.

Truly 3D void specimens with known, controlled dimensions are rare. In Reference 22, results from an ellipsoidal model of one such specimen[24] were compared with the envelope of the scattered flaw signal as reported in Reference 25. Since then,

the actual shape of that flaw, including edges (see Fig. 3), has been modeled and the titanium alloy specimen was obtained for additional experiments. The incident L-wave was made normal to the flat side of the void so that a single model employing symmetry could be used. Scattering amplitudes are plotted in Figure 6 as a function of azimuthal angle where the polar direction is aligned with the incident wave propagation direction. Dimensionless frequency is based on the major semi-axis a with a value of 2500 μm. Agreement is excellent. The experimental results suggest that the fabricated void is not perfectly symmetrical from tip to tip.

Scattering from Inclusions

Solutions for inclusions require matrices that are twice as large since both displacement and traction are unknown on the flaw surface.

Comparison with T-Matrix

Figure 7 gives results for a 2:1 oblate spheroidal inclusion of tungsten carbide in a titanium alloy. The comparison is with an axisymmetric T-Matrix solution from Reference 8. These results are different from the previous examples in that they are the mode converted solution which is also always obtained. The agreement with the T-Matrix solution is quite good even though the very crude 12 element model shown in Figure 1 was used. In general, our time-harmonic formulation with its quadratic elements can handle volumetric shapes at fairly low frequencies with coarse meshes.

Comparison with experiment

A three-axis ellipsoid is an interesting non-axisymmetric shape to investigate. To make the comparison experiment simple, a spectrum of backscatter amplitudes was

calculated for an incident L-wave normal to the "flat" side of our specimen[26]. Since the system response is a function of frequency, deconvolution techniques were used to extract the experimental flaw scattering amplitude from the measured signal. The experimental results show the roll-off effect of limited bandwidth and also that the flaw is not exactly the shape desired. (Results from "Top" and "Bottom" sides vary slightly.) The BEM results predict the trend fairly well over the $k_L a$ range (1 to 8) shown in Figure 8. The BEM solution shows a slight jump at about 0.9 MHz due to the switch from a 40 to a 72 element model.

Scattering from Open "Cracks"

The most notorious structural defect is the crack. The geometric details of fatigue cracks on a microscopic scale can be quite varied. It is known that the surfaces of fatigue cracks are generally rough due to the crack growth process. Furthermore, the zone of plastic deformation just ahead of a growing crack tip applies residual stresses which tend to close the crack. In the absence of external loads, which usually is the case at the time of inspection, real cracks may have opposing faces in contact at their peaks (or asperities) with very tiny gaps in between. Characterizing this crack closure is a whole issue in itself.

Simulation models of cracks tend to fall into two categories - open cracks and closed cracks. Open cracks are really very thin, smooth voids in which the opposing crack faces do not come in contact. Closed cracks have contact over at least part of the area of their faces to simulate the effects noted above. In some cases, the degree of contact is taken to be independent of load. In others, the faces are assumed to remain in contact under compressive tractions but to open under any slight tensile loadings. In this section, we present results for an open crack model but do not claim that this model is the best predictor of real crack response. However, it is noted that crack specimens used

in the calibration of NDE techniques are often fabricated by electro-discharge machining (EDM) or other means which leave a true "open" crack such as we have modeled.

In this formulation of the BIE, our open crack model is actually a very thin void. The aspect ratio needed to obtain crack-like behavior is a function of incident and scattered angle and also frequency. The results in this section have been derived from models sufficiently flat for the range of parameters given unless otherwise noted. Determination of this aspect ratio is a matter of solution convergence as this ratio increases and of the near singular nature of the surface integration when opposing crack faces are in close proximity. These matters will be dealt with as part of a separate paper. For all of the crack simulations presented, the results are from a 140 element model similar to the example in Figure 4. In many cases the results did not differ significantly from those obtained with 72 or 40 element models but an effort was made to provide as accurate a solution as possible. Host material Poisson's ratio is 1/3.

Backscatter from circular cracks

The circular crack scattering problem has been studied by many authors. However, to our knowledge, backscatter amplitudes for T-T waves at intermediate frequency have never appeared in the literature. Figure 9 presents our solution at selected angles for $k_T a$ up to six. (a is the crack radius.) Our model was checked by comparing the accompanying mode converted result (T-L) with an available MOOT solution[27] for L-T via the principle of mode conversion reciprocity[28].

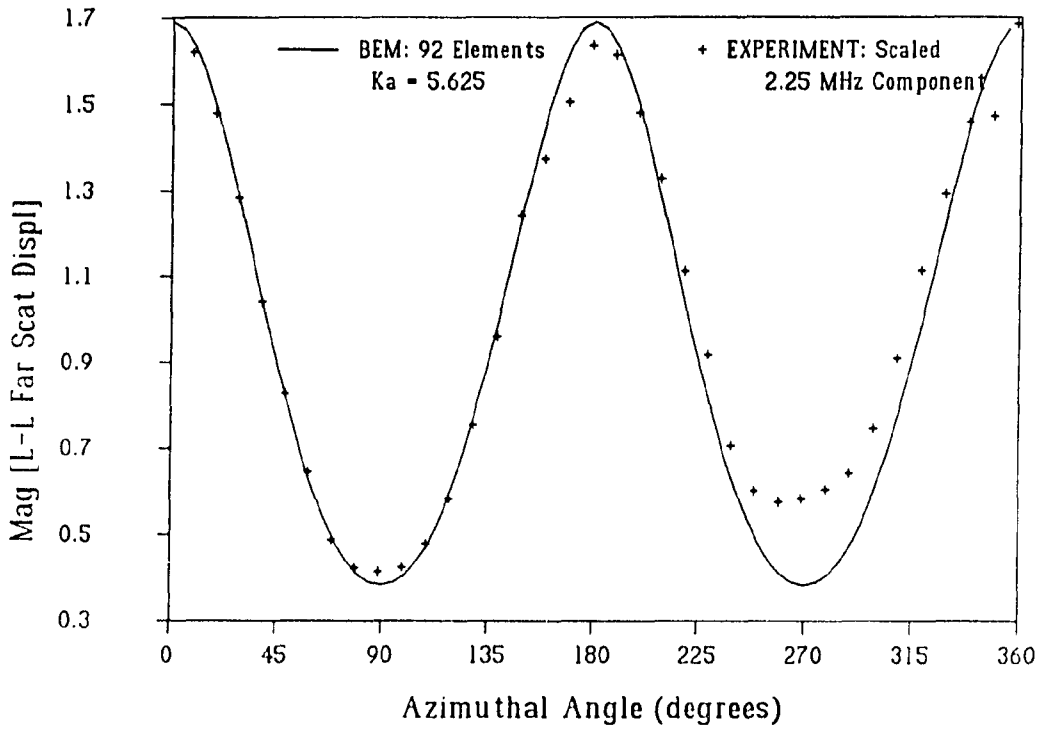

Figure 6 Comparison of BEM predictions and experiment for Rockwell elliptical (50:12:5) disc void for normal incidence L-waves at a scattered angle of 150°

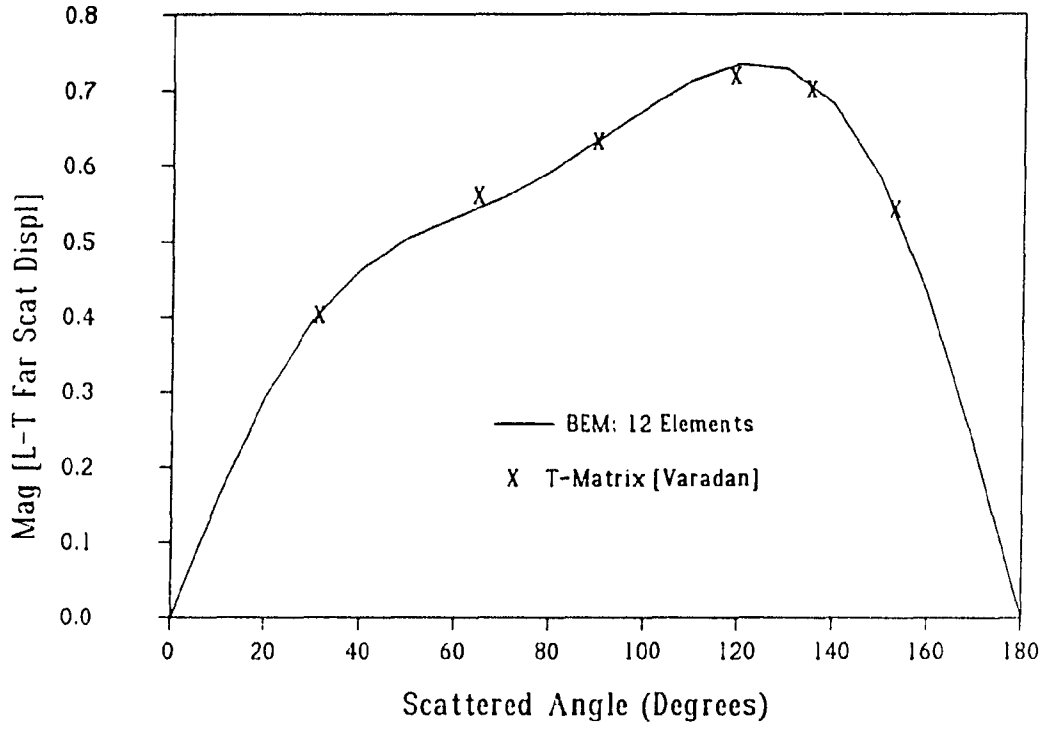

Figure 7 Mode converted scattering from oblate (2:2:1) spheroidal inclusion of tungsten carbide in titanium at $k_L a = 1$. Incident field is propagating parallel to the symmetry axis

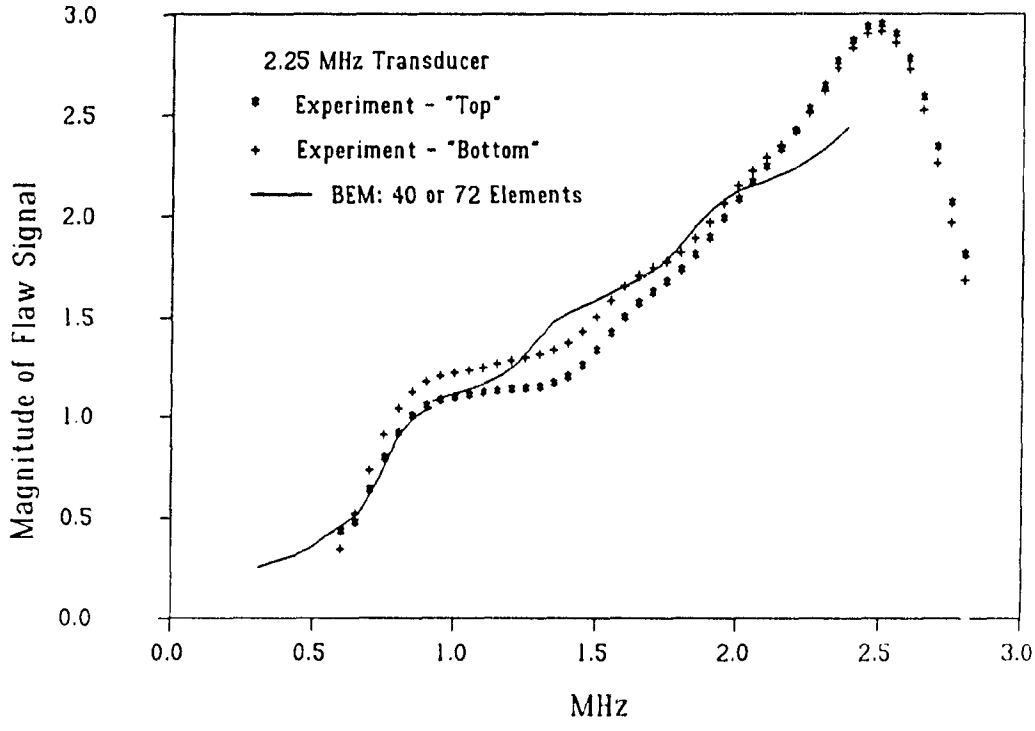

Figure 8 Backscatter from three-axis copper ellipsoid in Lucite[26]

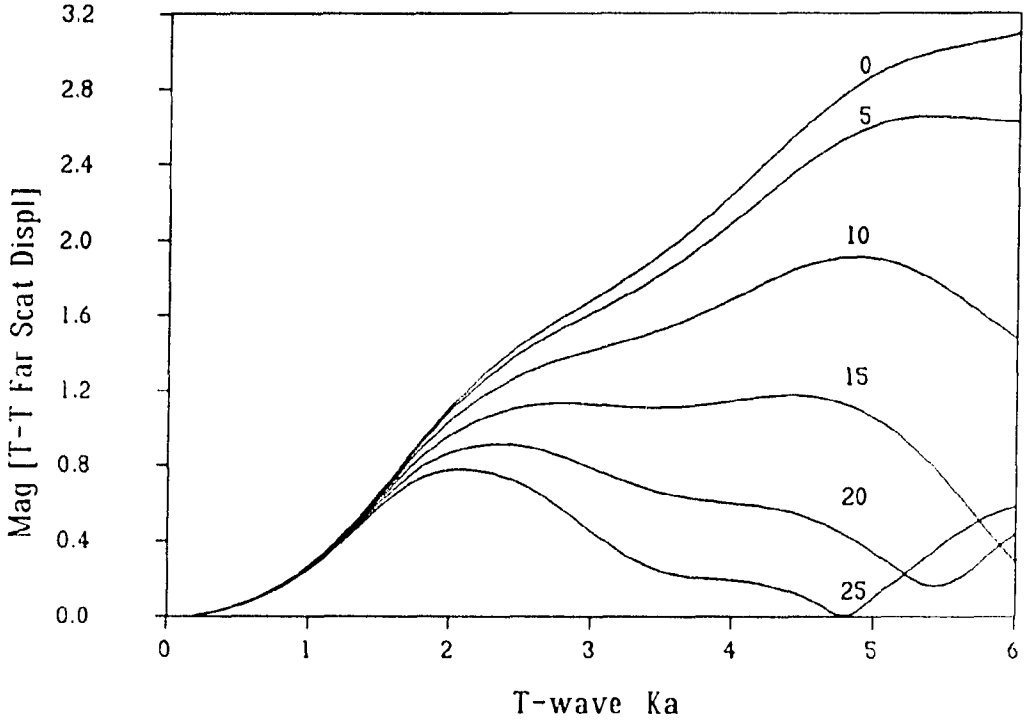

Figure 9a Backscatter from circular "crack" - incidence at 0,5,10,15,20, and 25 degrees relative to normal

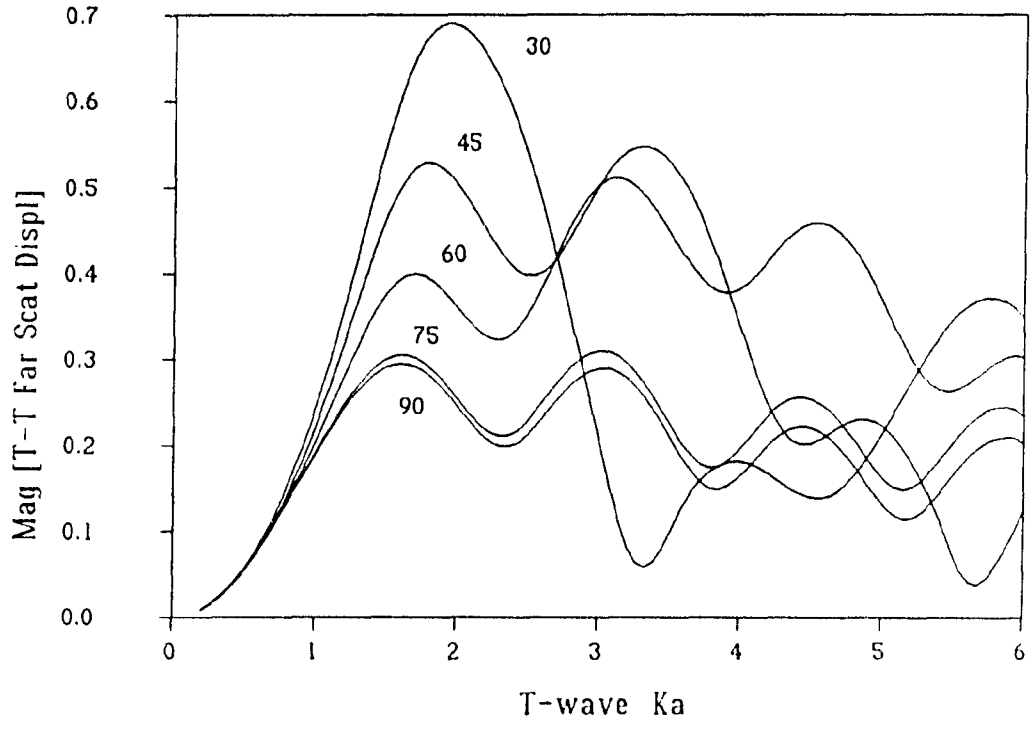

Figure 9b Backscatter from circular "crack" - incidence at 30,45,60,75, and 90 degrees relative to normal

Comparison with Kirchhoff approximation The Kirchhoff approximation is a very useful method for obtaining scattering solutions at high frequency. It is accurate for near-specular directions as noted in Reference 13. Although it is a high frequency theory, Kirchhoff does fairly well at intermediate frequencies for near normal incidence backscatter. To show this, we use the T-T BEM solution and compare it with a Kirchhoff solution[29] based on the theory of Adler and Achenbach[3]. Figure 10 shows that Kirchhoff produces the major trend of T-T backscatter versus frequency for incident angles of 0 and 15 degrees (as measured from normal incidence). At 30 degrees, the two solution methods show increasing discrepancy, but still have reasonable agreement.

At 45 degrees from normal, the two theories do not agree well at all, as expected and shown in Figure 11. To determine which is in error, they have been compared with an experiment of the same geometry. The experimental signal has been processed by the measurement model described in Reference 12 and so is an absolute, unscaled comparison with the BEM. The data[29] were taken from a 0.08 cm diameter "crack" in a nickel based superalloy, IN100, having an aspect ratio of approximately 10:1. Poisson's ratio for IN100 is about 94% of that of the generic material simulated so the comparison is valid. See Table I for material properties of IN100. The excellent agreement of the data with the predictions of the BEM model supports the accuracy of that approach.

Rayleigh wave influence One cause of the undulations of the actual solution about the Kirchhoff approximate solution for high frequency scattering from cracks is interference of Rayleigh waves traveling along the crack surface. Some manifestation of this is seen in Figure 10. These undulations persist into the intermediate frequency range for normal incidence as shown in Reference 22 with BEM and MOOT solutions for a 10:1 oblate spheroid. The ultrasonic echoes due to a pulsed excitation of these surface waves will arrive later in time and can be gated out experimentally[3]. Thus approximate theories, such as Kirchhoff and GTD which do not account for this surface

wave effect, can be compared directly with experiment. Time harmonic solutions such as our BEM include the effects of these Rayleigh waves. In principle, a scattering amplitude spectrum provided by the BEM could be transformed to the time domain, gated, and transformed back - thus removing the Rayleigh wave effects just as is done with the experimental data. However, parameter studies have shown us that there is some discrepancy in the phase of the scattering amplitudes from our oblate spheroid model as compared to the mathematical crack. This phase error varies with frequency and may distort the transformation process. A more straightforward check is possible.

Gautesen *et al.*[30] have provided a modified version of GTD that is valid for the normal incidence caustic and includes this surface ray effect. An expression (Equation 92 in Reference 30) for the scattering cross section of a circular crack as a function of frequency is given for normal incidence longitudinal waves in terms of wave speeds and Weiner-Hopf auxiliary function factor integrals. The scattering cross section can be related to the forward scattering amplitude by the elastodynamic version of the optical theorem[28]. Our conventions differ from that of Reference 28. For flaws with finite extent (3D), such a circular crack, our correlation is with the imaginary part rather than the real part. Figure 12 compares the BEM solution with the GTD based theory. The agreement is remarkable considering that GTD is a high frequency asymptotic result. In fact the two agree all the way down to the quasistatic regime where the scattering amplitude is almost entirely real. The period of the fluctuation is set by the Rayleigh wave $k_R a$. The periods of the two theories matches quite well even though Rayleigh waves are not "programmed" into the BEM solution but arise as a solution to the BIE. Our BEM "crack" model has finite thickness and so our comparison requires some interpretation.

The amplitude of the fluctuation in the BEM solution is less than the GTD theory for two reasons. First, the forward scattering amplitude of a mathematical crack is

purely imaginary while that of our BEM model also has a real component. Again this phase error makes our comparison sensitive to the aspect ratio of the model used. A (20:20:1) oblate spheroid model was used to create as near to a planar object as practical with this formulation. Second, even though the Rayleigh wave fluctuation decreases with frequency in the GTD theory, the effect decays more rapidly in the BEM result. This is also due to the volumetric nature of our model. As frequency increases, the rounded edge of the spheroid seems less like a singularity and so the Rayleigh waves are not excited as strongly.

Elliptical cracks

In this section we present selected results for a family of elliptical "cracks" ranging from circular to a 4:1 aspect ratio. All the cracks are modeled so that the major semi-axis has length of one unit. The thickness of the model ellipsoid ranges from 1/10th to 1/20th of a unit. (Note that the aspect ratios in the figure legends are normalized to integer ratios.) This sliding thickness scale was needed over the crack aspect ratio range studied, in order to avoid overly difficult numerical integration as noted at the beginning of this section on open cracks. For the results presented, this variation has little effect. The $k\alpha$ listed is for α being the major semi-axis length.

Comparison with Kirchhoff approximation Figure 13 gives results for specular scattering with 45 degree incidence along the major axis. For this specular scatter, the Kirchhoff approximation is expected to be valid in the high frequency limit[13], so the scattering amplitudes of each crack have been scaled according to its area. Over the intermediate $k_L\alpha$ range given, the curves have not coalesced into the single straight line proportional to frequency that the Kirchhoff approximation predicts. Although we saw Kirchhoff do quite well at intermediate frequency for normal incidence specular scatter in Figure 10, that robustness does not carry over to this situation.

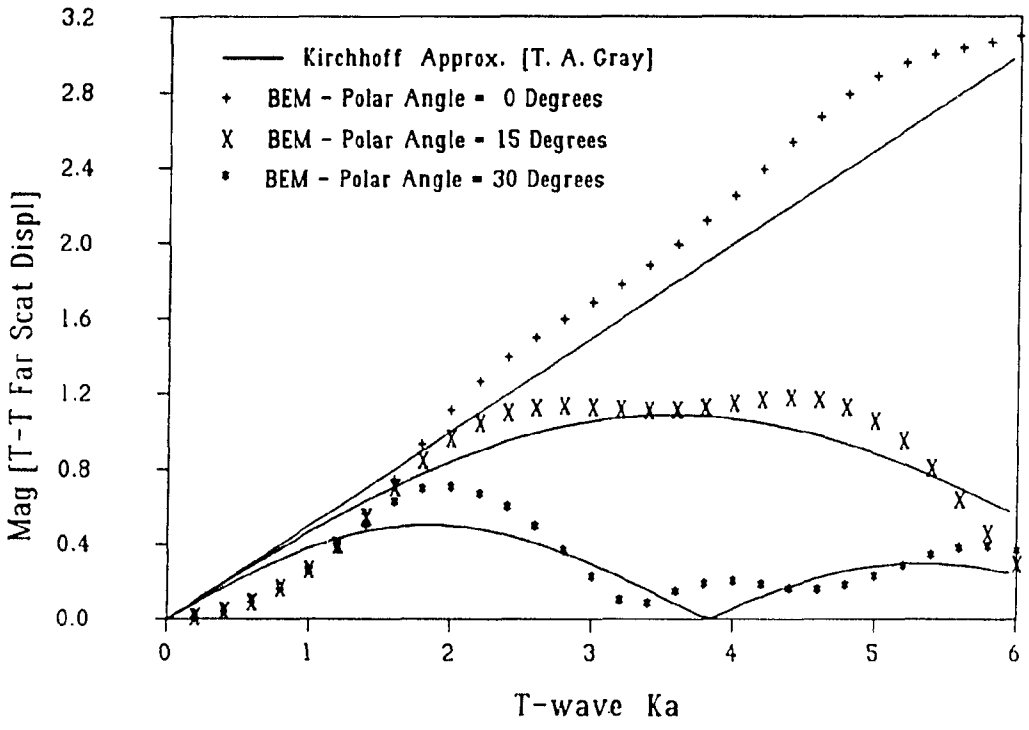

Figure 10 Backscatter from circular "crack" - Kirchhoff approximation versus BEM solution

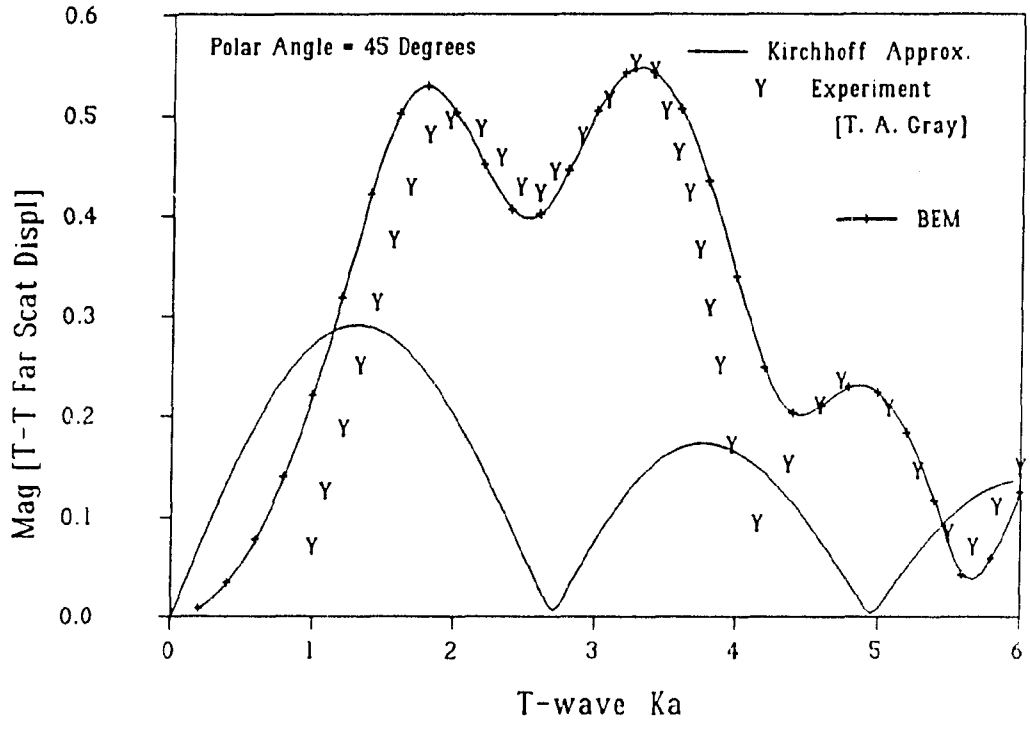

Figure 11 Backscatter from circular "crack" at 45 degree incidence - Kirchhoff approximation versus BEM solution versus experimental data

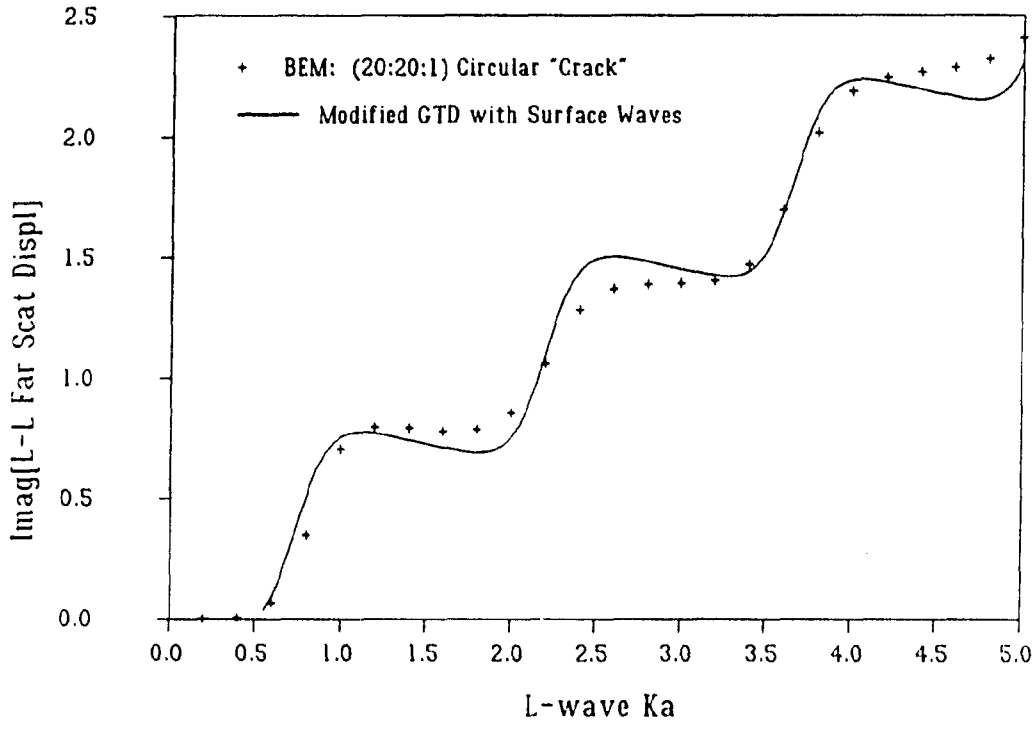

Figure 12 Imaginary part of forward scattering amplitude for circular "crack" at normal incidence - GTD with Rayleigh wave correction versus BEM solution

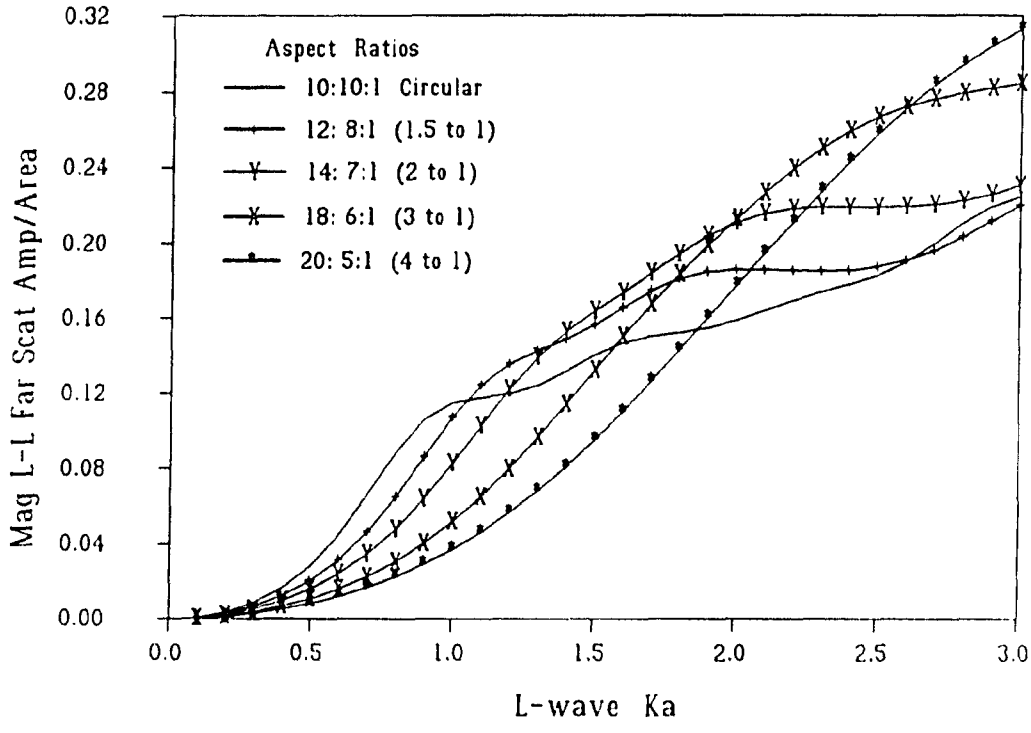

Figure 13 Specular scatter from elliptical "cracks" at 45 degree incidence - normalized according to Kirchhoff approximation

Figure 14 shows backscatter results for the same situation as in Figure 13. For this scattered direction, Kirchhoff would not be expected to be valid. The scattering amplitudes here have not been normalized to crack model area. Beside the difference in magnitude of the backscattered response, the $k_L a$ of the lowest resonant peak shifts to higher frequency as the crack becomes more elliptic. Bear in mind that the corresponding $k_L b$ of the minor semi-axis gets smaller as ellipticity increases. A similar migration of this peak with aspect ratio for elliptical cracks was reported by Budreck and Achenbach[31]. Their formulation was an alternative BIE specialized for planar cracks.

Comparison with GTD GTD can handle the 45 degree backscatter case of Figure 14 in the high frequency limit. We now explore the extension of GTD into intermediate frequency. Coffey and Chapman[13] provide a convenient form for determining the signal amplitude from diffraction coefficients and other geometrical and field parameters. For the special case of farfield backscatter for planar incident waves, the signal from the leading or trailing edge is proportional to:

$$Signal \propto F(\beta)\sqrt{\frac{\eta}{k|\cos(\beta)|}} \qquad (16)$$

where F is the diffraction coefficient, β is the angle between the ray and the crack plane, and η is the local radius of curvature of the crack edge. Temple[32] gives a formula for η for a non-skewed elliptical crack. The GTD predicted signal for this class of cracks turns out to be proportional to area, just as with the Kirchhoff approximation. Using diffraction coefficients also from Temple[33], the two edge signals are combined in a time-harmonic fashion by accounting for the phase shift due to the difference in propagation path length. The result, for any elliptical crack with area equal to π, is plotted in Figure 15.

Also shown on Figure 15 are the BEM solution results from Figure 14 for 1:1, 2:1, and 4:1 aspect ratios. These results are scaled according to the edge curvature (area) correction discussed above. GTD predicts that these scaled results should fall on a single curve, but clearly they do not. GTD does agree to a first approximation with the overall magnitude of the response except down in the quasistatic regime where extrapolation is inappropriate. The relative heights of the peaks in the BEM solutions are consistent with the results in Reference 31. So we believe our BEM results are correct. The circular crack solution agrees somewhat with GTD, although this agreement is probably fortuitous at $k_L a \sim 1$. We must note that as before the $k_L b$ values of the elliptical cracks are significantly influencing the result and since they are smaller than the nominal $k_L a$ values plotted, the high frequency assumption is violated further. Clearly, GTD does not extrapolate down into the intermediate frequency range for this situation.

Comparison with quasistatic approximation At the opposite end of the spectrum, the quasistatic approximation allows for simplified scattering solutions when the crack is small relative to the inspection wavelength. Teitel[2] has used such an approach to obtain solutions for elliptical cracks. Figure 16 contrasts the quasistatic approximation with the BEM solution over a $k_L a$ range from 0 to 1. For L-wave backscatter at normal incidence, the average error in the approximate solution is less than 5 percent at $k_L a$ equal to 0.1. However, the error grows steadily with increasing frequency, as expected, until it reaches almost 28 percent at $k_L a$ equal to one. For low frequencies where the quasistatic approximation is expected to be good, the two methods agree on the scattering amplitude as a function of crack aspect ratio, even though that amplitude varies by more than an order of magnitude.

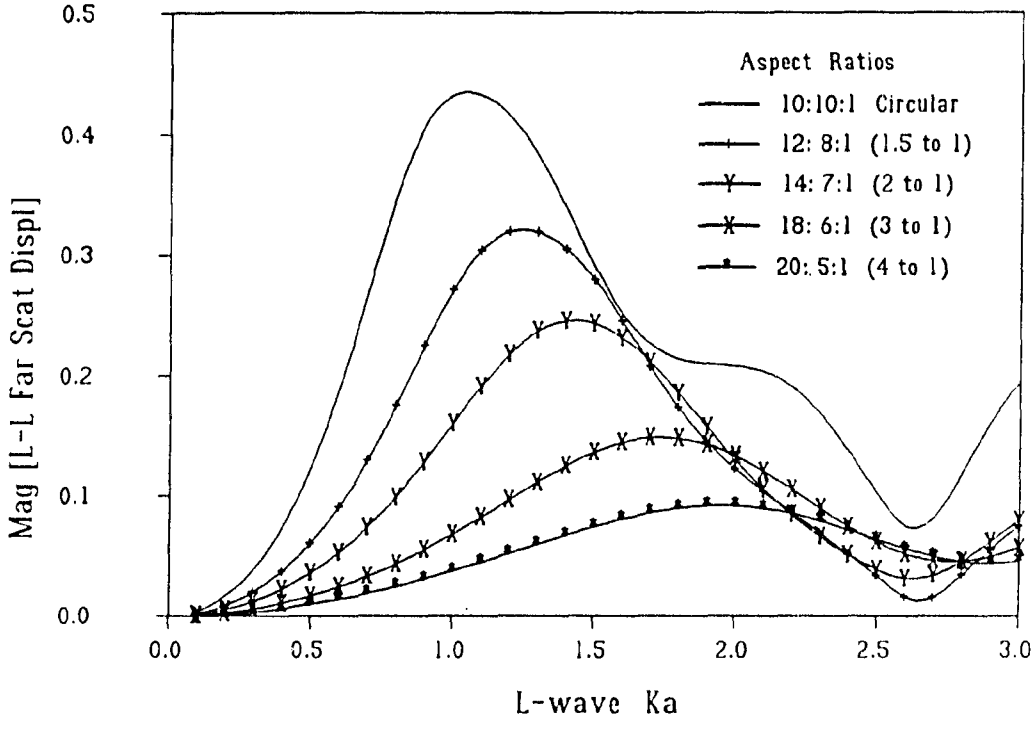

Figure 14 Backscatter from elliptical "cracks" at 45 degree incidence

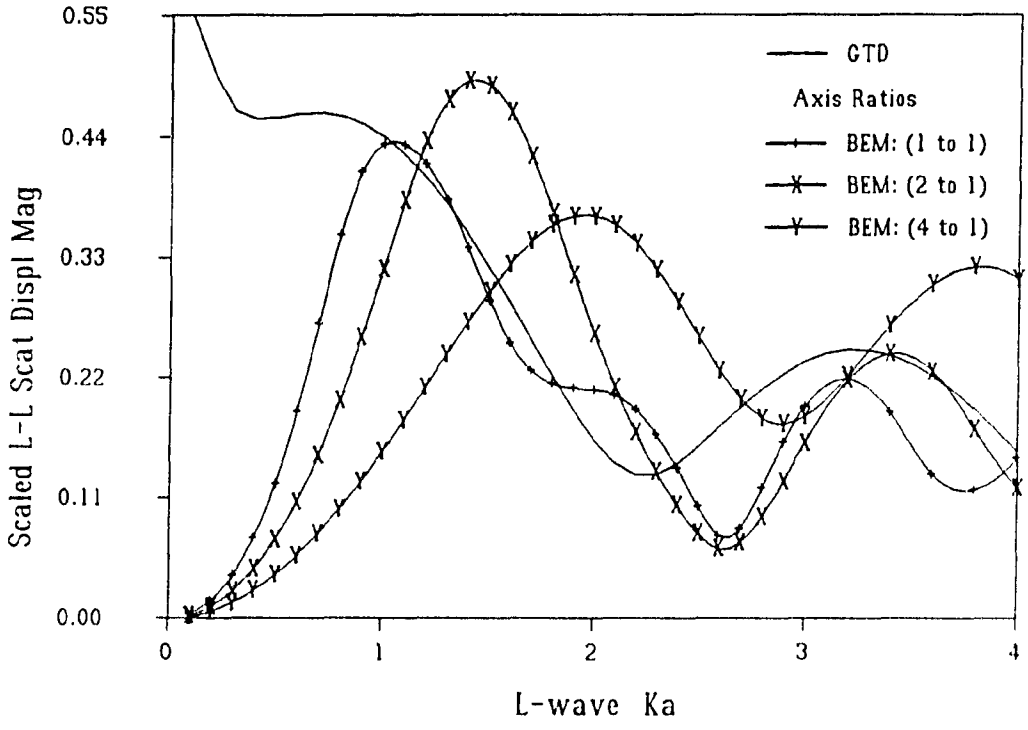

Figure 15 Backscatter from elliptical "cracks" at 45 degree incidence - comparison of GTD and normalized BEM solutions

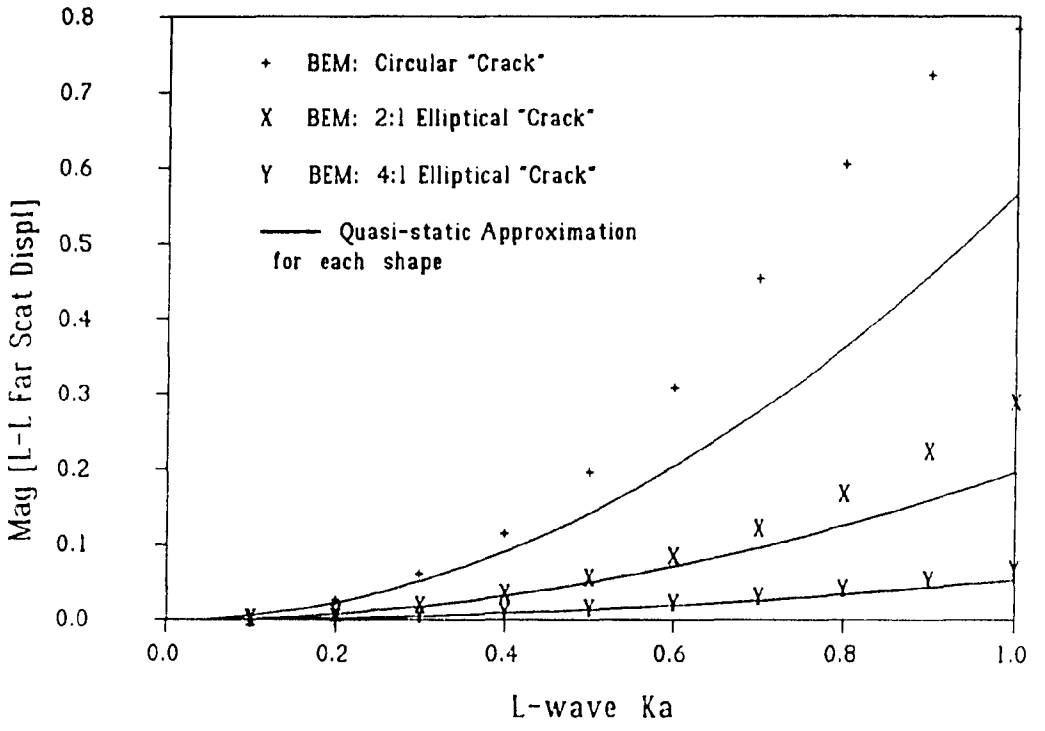

Figure 16 Backscatter from elliptical "cracks" at normal incidence - quasistatic approximation versus BEM solutions. Note: data points denoted by "+", "X", and "Y" are at the symbol's intersection point

Crack characterization

This section illustrates one scenario of how intermediate frequency scattering information could be used to do "inverse scattering". Given the *a priori* knowledge that a defect is an elliptical crack, it is reasonable to assume that the normal incidence direction could be determined through testing. Examination of our simulations reveals that characterization is then possible from the L-L backscatter spectrum. The transition out of the Rayleigh regime is manifested as a "knee" in the magnitude of these scattering amplitude spectrums. For our family of elliptical cracks, this "knee" can be placed at $ka' \sim 1$ if the characteristic dimension a' is defined appropriately (see Figure 17).

$$a' = .59\sqrt{area}\,(b/a)^{.08} \tag{17}$$

Figure 17 also shows that the signal generated per area increases as the crack becomes more elliptical for frequencies at least up to $k_L a = 3$. This trend can be fit by a simple empirical power law expression at $k_L a' = 1$.

$$|A_{L\text{-}L}(ka' = 1)| = .241\,(area)\left(\frac{a}{b}\right)^{.45} \tag{18}$$

By combining Equations (17) and (18), the aspect ratio can be determined from values of k_L and A at the "knee" of an experimentally derived scattering amplitude curve.

$$\frac{b}{a} = \frac{.547}{[k_L\sqrt{|A_{L\text{-}L}|}]^{3.28}} \tag{19}$$

Then Equation (18) can be solved for area and the elliptical crack is characterized.

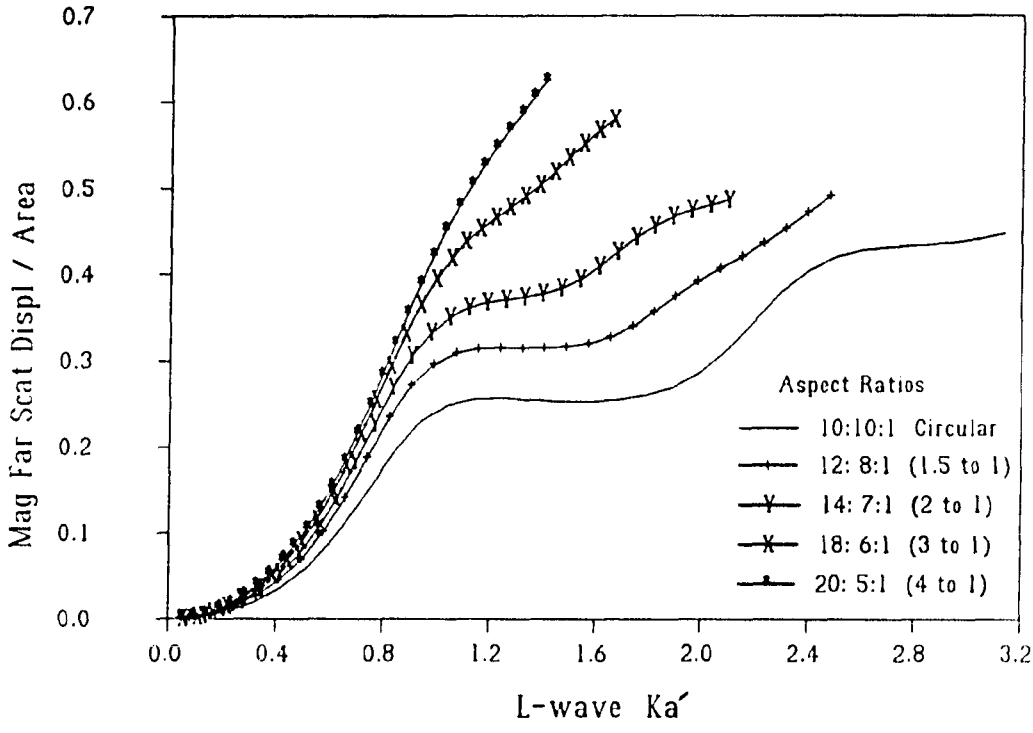

Figure 17 Normalized backscatter from elliptical "cracks" at normal incidence

Because a circular crack generates the least signal per unit area (for this inspection arrangement), the assumption that an unknown crack is circular rather than elliptical will result in a seemingly conservative overestimate of the crack's area. But since the actual important quantity is stress intensity factor rather than area, we investigate the relationship of stress intensity and signal strength for this family of cracks in the simple case of a normal uniaxial stress field[34]. Table II gives values of maximum K_I per unit stress for a given major semi-axis length a. The table also provides the ratio of actual stress intensity to that of an assumed circular crack which would generate the same strength backscattered signal at $k_L a' = 1$. This information shows that assuming a detected crack is circular, can result in an unconservative estimate of the stress intensity.

Table II: Stress Intensity Factors and Ratios for Elliptical Cracks

b/a	$\frac{\max K_I}{\sqrt{a}\ unit\ \tau}$	$\frac{\max K_I\ actual}{\max K_I\ assumed}$
1	1.128	1.00
2/3	1.095	1.09
1/2	1.035	1.11
1/3	0.919	1.10
1/4	0.827	1.07

Scattering of Nonplanar Fields

Finally, we give a simple example of the BEM's ability to handle nonplanar incident fields. There are three situations which come to mind when the quasi-plane wave assumption may not be valid. First, when the flaw size is large compared to the nominal size of the transducer's beam. This situation occurs in the heavy wall sections of pressure vessels. In this case, the flaw dimensionless frequency will typically exceed our current BEM capability. Second, nonplanar fields occur when there is an adjacent defect or material interface. Problems like this often must involve multiple scattering and are most efficiently handled by a hybrid technique[35]. Third, it may be invalid in the nearfield of an ultrasonic transducer when the field is not locally planar, even for moderately sized flaws. In our example of this phenomenon, we consider the field variations near the central axis of a circular, contact, L-wave transducer.

Along the central axis itself, the relative field strength can be determined for a transducer modeled as a uniform traction disk in a housing with impedance equal to that of the elastic medium[36].

$$I_a(z) = 2\left|\sin\left[k_L(\sqrt{z^2+B^2}-z)/2\right]\right| \tag{20}$$

B is transducer radius and z is the distance into the elastic material. Within the quasi-plane wave assumption, a plane wave of strength I_a is used to define all incident nodal displacements. Without this assumption, the incident field must be represented by a beam model. In the Gauss-Hermite beam model[21] used here, the Fresnel approximation is employed and so accurate results are only expected from the farfield in through the outer few on-axis nulls.

The example problem treats two spherical voids of different size centered on the transducer central axis and at various depths into the solid. Transducer kB equals 32. Figure 18 gives the magnitude of the flaw signal (as calculated via Equation 12) per unit plane wave scattering amplitude. Therefore, the fact that the scattering amplitude is different because the spheres have different radii has been accounted for. In the quasi-plane wave assumption, the two spheres are indistinguishable. But for the nonplanar field, the results are somewhat different. The small sphere follows the quasi-plane wave approximation more closely. The larger sphere deviates from that most noticeably at the peaks and null. This behavior is easily understood by looking at the off-axis field near the outer peak and null. See Reference 37. The off-axis field is not so extreme near these locations and so an "average" field over the larger sphere is also not as extreme as the on-axis value suggests. The nonzero signals for non-infinitesimal flaws near a null obviously has good implications for detectability. The signal at the inner peak is stronger than the approximation suggests - probably due to the gradient in the field from the front to the back of the sphere. In the transducer farfield, all three solutions converge as expected.

Conclusions

The boundary element method has a number of features which make it attractive as a means of calculating elastic wave scattering of 3D defects at intermediate frequency. Since the BIE only requires a 2D integration, this method is much more efficient than domain type methods for homogeneous, isotropic media. Our time-harmonic formulation with adjustable integration scheme and quadratic elements allows for relatively simple meshes. The BIE also treats the (seemingly) unbounded host medium rigorously and therefore does not require artificial boundaries at the end of the simulated domain. Our BIE formulation does suffer from the fictitious eigenfrequency difficulty with exterior domains, but this problem has been successfully remedied by an

approach known as BIFILM[17]. The work of Temple[14] and recent results of Lord in 3D give the additional option of anisotropic and/or inhomogeneous scatter and near field host materials. Bond reviews all major approaches for the elastic wave scattering problem in Reference 38.

Efficient formalisms for scattering amplitude and flaw signal calculation are provided and their interrelation shown. It is shown how parameter studies needed to support POD models, inversion schemes, and bounds for approximate theories could be done from a library of previously formed and decomposed matrices. Additionally, the similarity of BEM and finite element mesh definition allows us to interface with commercial computer-aided-engineering software for flaw shape definition and interpretation of solutions[22].

The method handles solitary voids and inclusions of arbitrary shape. Selected problems involving axisymmetric defects were solved so as to compare with MOOT and T-matrix calculations. Truly 3D shaped defect results were compared against experiment since no other numerical method results are available. In all cases, agreement between methods was good. In principle, MOOT and T-matrix could be implemented in 3D but the eigenfunction expansions would be much more complicated to deal with than in 2D.

Although our formulation is more efficient for volumetric defect calculations, the importance of the crack defect and the richness of approximate solutions for it prompted us to present numerous crack results. Our main objective was not to challenge these approximations in their realm of applicability but rather to show that extrapolation into intermediate frequencies requires great scrutiny. For informational purposes, we presented shear wave backscatter results for a penny-shaped crack. Then we showed how the Kirchhoff approximation breaks down as expected for backscatter at directions

away from normal incidence but that the BEM solution still agrees with experimental data. The postulated effect of Rayleigh waves on crack surfaces is clearly consistent with our model results. We have shown how sometimes high frequency approximations robustly extend into the intermediate frequency range but under other conditions they fail. We verified our solutions in the low frequency limit and determined the error in quasistatic approximations as a function of frequency for elliptical cracks. The information provided suggests that elliptical cracks can be characterized by intermediate frequency scattering and an example was given. An alternate BEM formulation for true zero thickness cracks that utilizes a hypersingular BIE is under development[39] and eventually will be able to generate similar information.

Finally, the quasi-plane wave assumption was contrasted to beam model results for elastic scattering in the nearfield of a circular transducer.

Acknowledgements

This work was sponsored by the Center for NDE at Iowa State University and was performed at the USDOE Ames Laboratory which is operated by Iowa State under Contract No. W-7405-ENG-82. One author (Rizzo) was partially supported by the Office of Naval Research under Contract No. N00014-86-K-0551. We acknowledge D. D. Bennink for a version of the Gauss-Hermite Beam Model code which computes stress states in an elastic solid and also the many developers of the core BEM code from the University of Kentucky.

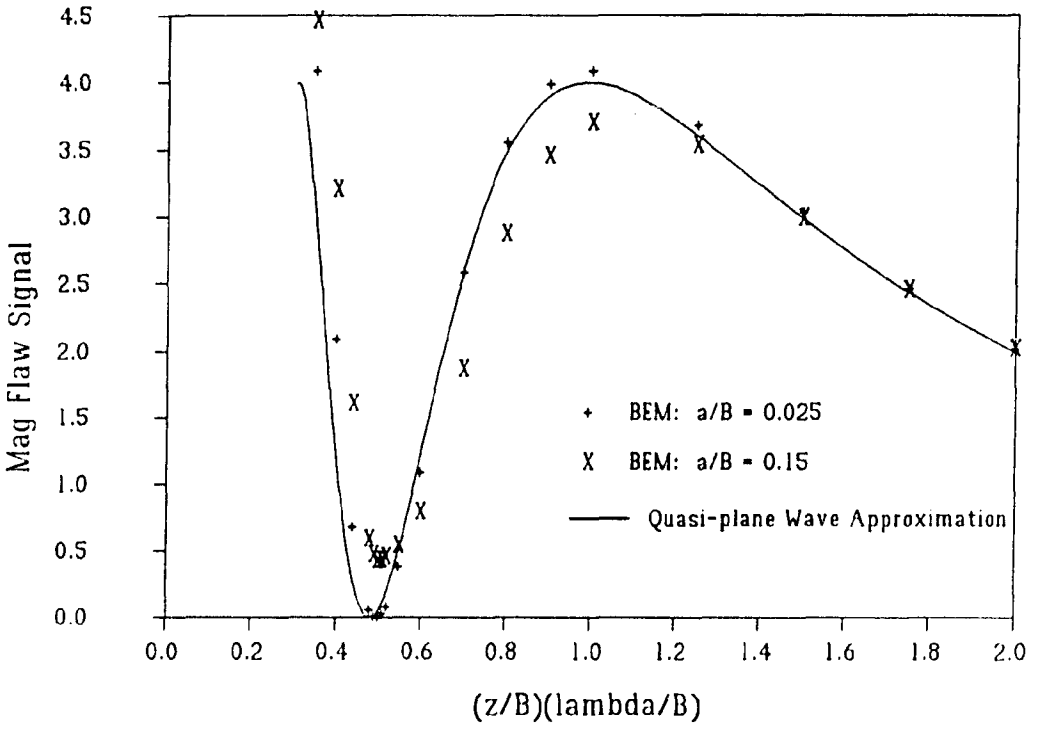

Figure 18 Quasi-plane wave approximation versus BEM solutions for on-axis nearfield of a circular transducer

Appendix

In this Appendix we derive compact expressions for farfield scattering amplitudes and show that they are directly related to flaw signals measured by transducers, if the fields produced by those transducers are planar at the flaw. The polarization of the incident field enters through the resulting surface displacements and tractions. In the equations that follow for scattering amplitudes, that polarization is indicated by the symbol "?". Other nomenclature was defined in the sections on the BEM and its adaptation to ultrasonics.

Without loss of generality, we take $\mathbf{p}_0$ to lie on the $-X_3$ axis with $|\mathbf{p}_0| \to \infty$. Noting that

$$\frac{\partial r}{\partial x_j} = \delta_{3j} \tag{A1}$$

the farfield kernels become:

$$\mathbf{U}^{\infty} = \frac{1}{4\pi\rho\omega^2 r}\begin{bmatrix} k_T^2 e^{ik_T r} & 0 & 0 \\ 0 & k_T^2 e^{ik_T r} & 0 \\ 0 & 0 & k_L^2 e^{ik_L r} \end{bmatrix} \tag{A2}$$

$$\mathbf{T}^{\infty} = \frac{i}{4\pi\rho\omega^2 r}\left\{ k_L^3 e^{ik_L r}\begin{bmatrix} 0 & 0 & \lambda n_1 \\ 0 & 0 & \lambda n_2 \\ 0 & 0 & (\lambda+2\mu)n_3 \end{bmatrix} + \mu k_T^3 e^{ik_T r}\begin{bmatrix} n_3 & 0 & 0 \\ 0 & n_3 & 0 \\ n_1 & n_2 & 0 \end{bmatrix}\right\} \tag{A3}$$

Then using (5), (6), and realizing $r \sim |p_3 - q_3|$:

$$A_{?-L} = u_3^S(-r)e^{ik_L p_3}/I_a = -ru_3^S e^{ik_L(q_3-r)}/I_a$$

$$= -\frac{1}{4\pi\rho\omega^2 I_a}\int_S \{t_3 - ik_L[\lambda(\mathbf{u}\cdot\hat{\mathbf{n}}) + 2\mu u_3 n_3]\}k_L^2 e^{ik_L q_3} dS(\mathbf{q}) \qquad (A4)$$

Likewise for scattered transverse waves with an arbitrary polarization direction parallel to X_2

$$A_{?-T} = u_2^S(-r)e^{ik_T p_3}/I_a = -ru_2^S e^{ik_T(q_3-r)}/I_a$$

$$= -\frac{1}{4\pi\rho\omega^2 I_a}\int_S \{t_2 - i\mu k_T(u_2 n_3 + u_3 n_2)\}k_T^2 e^{ik_T q_3} dS(\mathbf{q}) \qquad (A5)$$

Alternatively with a reciprocity approach, we begin with (12). By definition,

$$\vec{\tau}_a \cdot \hat{\mathbf{n}} = \mathbf{t} \qquad (A6)$$

For a receiver (acting as a transmitter) that produces L-waves of amplitude I_b at the flaw, the "b"-state displacement field is

$$\mathbf{u}_b = \begin{Bmatrix} 0 \\ 0 \\ I_b e^{i(k_L x_3 - \omega t)} \end{Bmatrix} \qquad (A7)$$

So at surface point $\mathbf{q}$

$$\vec{\tau}_b \cdot \hat{\mathbf{n}} = ik_L I_b e^{i(k_L q_3 - \omega t)} \begin{Bmatrix} \lambda n_1 \\ \lambda n_2 \\ (\lambda + 2\mu)n_3 \end{Bmatrix} \qquad (A8)$$

Velocity fields are merely $-i\omega$ times the corresponding displacement field. Then factoring out the $e^{-i\omega t}$ time dependence,

$$\delta\Gamma_F = \frac{\omega I_b}{4P}\int_S \{k_L[\lambda(\mathbf{u}_a\cdot\hat{\mathbf{n}})+2\mu u_{3a}n_3]+it_{3a}\}e^{ik_L q_3}dS(\mathbf{q}) \qquad (A9)$$

The T-wave analogs for Equations (A7 - A9) are:

$$\mathbf{u}_b = \begin{Bmatrix} 0 \\ I_b e^{i(k_T x_3-\omega t)} \\ 0 \end{Bmatrix} \qquad (A10)$$

$$\vec{\tau}_b\cdot\hat{\mathbf{n}} = i\mu k_T I_b e^{i(k_T q_3-\omega t)}\begin{Bmatrix} 0 \\ n_3 \\ n_2 \end{Bmatrix} \qquad (A11)$$

$$\delta\Gamma_F = \frac{\omega I_b}{4P}\int_S \{\mu k_T(u_{2a}n_3+u_{3a}n_2)+it_{2a}\}e^{ik_T q_3}dS(\mathbf{q}) \qquad (A12)$$

By comparing (A4) with (A9) and (A5) with (A12), it is clear that (14) is satisfied with $E_2 = 0$ - therefore, the surface of the flaw is an appropriate surface of integration.

References

1. J. E. Gubernatis, 'Long-wave approximations for the scattering of elastic waves from flaws with applications to ellipsoidal voids and inclusions', *J. Appl. Phys.* **50**(6), 4046-4058 (1979).

2. S. Teitel, 'Determination of crack characteristics from the quasistatic approximation for the scattering of elastic waves', *J. Appl. Phys.* **49**(12), 5763-5767 (1978).
3. L. Adler and J. D. Achenbach, 'Elastic wave diffraction by elliptical cracks: Theory and experiment', *J. Nondestr. Eval.* 1(2), 87-99 (1980).
4. J. D. Achenbach and A. K. Gautesen, 'Geometrical theory of diffraction for three-D elastodynamics', *J. Acoust. Soc. Am.* **61**(2), 413-421 (1977).
5. Jer-Shi Chen and L. W. Schmerr, Jr., 'The scattering response of voids -- A second order asymptotic theory', in *Review of Progress in QNDE*, edited by D. O. Thompson and D. E. Chimenti (Plenum Press, New York, 1988), Vol. 7A, pp. 139-145.
6. C. F. Ying and R. Truell, 'Scattering of a plane longitudinal wave by a spherical obstacle in an isotropically elastic solid', *J. Appl. Phys.* **27**(9), 1086-1097 (1956).
7. J. L. Opsal and W. M. Visscher, 'Theory of elastic wave scattering: Applications of the method of optimal truncation', *J. Appl. Phys.* **58**(3), 1102-1115 (1985).
8. V. K. Varadan and V. V. Varadan, 'Scattering matrix for elastic waves. III. Application to spheroids', *J. Acoust. Soc. Am.* **65**(4), 896-905 (1979).
9. J. H. Su, V. V. Varadan, and V. K. Varadan, 'Finite element eigenfunction method (FEEM) for elastic wave scattering by arbitrary three-dimensional axisymmetric scatterers', *J. Appl. Mech. Trans. ASME* **51**(3), 614-621 (1984).
10. L. J. Bond, N. Saffari, and M. Punjani, 'Modeling ultrasonic waves using finite difference methods', in *Review of Progress in QNDE*, edited by D. O. Thompson and D. E. Chimenti (Plenum Press, New York, 1987), Vol. 6A, pp. 135-144.
11. Z. You and W. Lord, 'Finite element study of elastic wave interaction with cracks', in *Review of Progress in QNDE*, edited by D. O. Thompson and D. E. Chimenti (Plenum Press, New York, 1989), Vol. 8A, pp. 109-116.
12. R. B. Thompson and T. A. Gray, 'A model relating ultrasonic scattering measurements through liquid-solid interfaces to unbounded medium scattering amplitudes', *J. Acoust. Soc. Am.* **74**(4), 1279-1290 (1983).
13. J. M. Coffey and R. K. Chapman, 'Application of elastic scattering theory for smooth flat cracks to the quantitative prediction of ultrasonic defect detection and sizing', *Nuclear Energy* **22**(5), 319-333 (1983).

14. J. A. G. Temple, 'Modelling the propagation and scattering of elastic waves in inhomogeneous anisotropic media', *J. Phys. D: Appl. Phys.* **21**, 859-874 (1988).
15. T. A. Gray and R. B. Thompson, 'Use of models to predict ultrasonic NDE reliability', in *Review of Progress in QNDE*, edited by D. O. Thompson and D. E. Chimenti (Plenum Press, New York, 1986), Vol. 5A, pp. 911-918.
16. F. J. Rizzo, D. J. Shippy, and M. Rezayat, 'A boundary integral equation method for radiation and scattering of elastic waves in three dimensions', *Int. J. Numer. Methods Eng.* **21**(1), 115-129 (1985).
17. M. Rezayat, F. J. Rizzo, and D. J. Shippy, 'On time-harmonic elastic-wave analysis by the boundary element method for moderate to high frequencies', *Comput. Methods Appl. Mech. Engrg.* **55**(3), 349-367 (1986).
18. B. A. Auld, 'General electromechanical reciprocity relations applied to the calculation of elastic wave scattering coefficients', *Wave Motion* **1**, 3-10 (1979).
19. D. D. Bennink, Iowa State University Center for NDE, suggested that this proof was possible.
20. R. B. Thompson, T. A. Gray, J. H. Rose, V. G. Kogan, and E. F. Lopes, 'The radiation of elliptical and bicylindrically focused piston transducers', *J. Acoust. Soc. Am.* **82**(5), 1818-1828 (1987).
21. B. P. Newberry and R. B. Thompson, 'A paraxial theory for the propagation of ultrasonic beams in anisotropic solids', *J. Acoust. Soc. Am.* **85**(6), 2290-2300 (1989).
22. P. J. Schafbuch, R. B. Thompson, F. J. Rizzo, and T. J. Rudolphi, 'Elastic wave scattering by arbitrarily shaped voids', in *Review of Progress in QNDE*, edited by D. O. Thompson and D. E. Chimenti (Plenum Press, New York, 1989), Vol. 8A, pp. 15-22.
23. B. R. Tittmann, E. Domany, J. L. Opsal, and K. E. Newman, 'Elastic wave scattering from irregular voids', *J. Appl. Phys.* **54**(11), 6079-6085 (1983), Fig. 7.
24. C. C. Bampton, 'Ultrasonic test samples', in *Review of Progress in QNDE*, edited by D. O. Thompson and D. E. Chimenti (Plenum Press, New York, 1982), Vol. 1, pp. 315-319.
25. B. R. Tittmann, 'Scattering of ultrasound by ellipsoidal cavities', in *Proceedings of the ARPA/AFML Review of Progress in QNDE*, AFML-TR-77-44, 173-179 (1977).
26. Sample "B", a (7:5:1) ellipsoid of copper in Lucite with a major semi-axis of 1.414 mm, was provided by D. K. Hsu from Iowa State University Center for NDE.

27. J. L. Opsal, Therma-Wave, Fremont, California, private communication, based on method of Reference 7.
28. V. Varatharajulu, 'Reciprocity relations and forward amplitude theorems for elastic waves', *J. Math. Physics* **18**(4), 537-543 (1977).
29. T. A. Gray, Iowa State University Center for NDE, private communication.
30. A. K. Gautesen, J. D. Achenbach, and H. McMaken, 'Surface-wave rays in elastodynamic diffraction by cracks', *J. Acoust. Soc. Am.* **63**(6), 1824-1831 (1978).
31. D. E. Budreck and J. D. Achenbach, 'Scattering from three-dimensional planar cracks by the boundary integral equation method', *J. Appl. Mech. Trans. ASME* **55**(2), 405-412 (1988).
32. J. A. G. Temple, 'Predicted ultrasonic responses for pulse-echo inspections', *Br. J. Nondestr. Test.* **28**(3), 145-154 (1986).
33. J. A. G. Temple, Theoretical Division of AREA Harwell, Oxfordshire, private communication with R. B. Thompson.
34. G. R. Irwin, 'Crack-extension force for a part-through crack in a plate', *J. Appl. Mech. Trans. ASME* **29**(4), 651-654 (1962).
35. G. T. Schuster, 'A hybrid BIE + Born series modeling scheme: Generalized Born series', *J. Acoust. Soc. Am.* **77**(3), 865-886 (1985).
36. G. S. Kino, 'The application of reciprocity theory to scattering of acoustic waves by flaws', *J. Appl. Phys.* **49**(6), 3190-3199 (1978).
37. G. S. Kino, *Acoustic Waves* (Prentice-Hall, Englewood Cliffs, New Jersey, 1987).
38. L. J. Bond, 'Numerical techniques and their use to study wave propagation and scattering - a review', in *Proceedings of the IUTAM Symposium on Elastic Wave Propagation and Ultrasonic Nondestructive Evaluation* (Elsevier, Amsterdam, 1990).
39. G. Krishnasamy, L. W. Schmerr, T. J. Rudolphi, and F. J. Rizzo, 'Hypersingular boundary integral equations: Some applications in acoustic and elastic wave scattering', *J. Appl. Mech. Trans. ASME* **57**(2), 404-414 (1990).

PART II.

EIGENFREQUENCIES OF AN ELASTIC SPHERE WITH FIXED BOUNDARY CONDITIONS

Introduction

One basic problem of elastodynamics which has an analytical solution is the free vibration of a homogeneous, isotropic elastic sphere. Lamb[1] first solved this problem and classic texts on elasticity such as Love[2] often cite or reproduce his solution. Eringen and Suhubi[3] provide tables of eigenfrequencies for this traction free boundary condition case. However, the equally fundamental case of fixed displacement boundary conditions has, to our knowledge, been largely ignored. Perhaps this is due to a lack of physical situations for which a true fixed boundary condition exists. The traction free boundary condition case was motivated by geophysical considerations. Research into boundary integral equation formulations of elastic wave scattering has produced a need to know the characteristic frequencies of the fixed displacement or Dirichlet problem.

Some work has been done on this problem in a quantum mechanical context. In his fundamental work on the theory of specific heats, Peter Debye[4] considered an elastic sphere with fixed boundary conditions and looked at asymptotic limits of the size and number of eigenfrequencies. To do this, he developed the general characteristic equations but left them unsolved. In this brief note, we provide solutions to these equations for selected cases.

Debye's Equations

Debye's approach parallels that of Lamb in that time harmonic motion is assumed, but he introduces both scalar and vector potential functions. In more modern nomenclature we then write the displacement field as

$$\mathbf{u} = \nabla\Phi + \nabla \times \vec{\Pi} \tag{1}$$

with $\nabla \cdot \vec{\Pi} = 0$ to isolate the irrotational and incompressible field components. The problem can then be broken down into a set of three Helmholtz equations for Φ, Π_1, and Π_2. Each of the potential functions can be written as an infinite sum where the angular dependence is expressed in terms of spherical harmonics. For example,

$$r\Pi_1 = \sum_{n=0}^{\infty} A_n \psi_n(k_T r) S_n(\theta, \phi) \tag{2}$$

where (r, θ, ϕ) are spherical coordinates and k_T is the wavenumber for a transverse (shear) wave. For each spherical harmonic, S_n, there is a corresponding function ψ_n which defines the radial (r) dependency. These radial functions turn out to be Riccati-Bessel functions and are related to the spherical Bessel function of the first kind, j_n, which in turn can be expressed in terms of the common Bessel function as

$$\psi_n(z) = z j_n(z) = \sqrt{\frac{\pi z}{2}} J_{n+\frac{1}{2}}(z). \tag{3}$$

Note that our definition of ψ_n is consistent with that of Debye but differs by a factor of z from that in References 1 and 2. The expansion coefficients, e.g., A_n, are determined

via the Dirichlet boundary conditions to within a multiplicative constant for the eigenvalue problem.

For the sake of brevity, the complete derivation will not be reproduced but merely the results stated. Just as with the traction free case there are two classes of motion possible. Class I motions are based on shear distortions where the displacement field remains completely solenoidal. The characteristic equation for this motion is expressed as a simple function of the dimensionless frequency $k_T a$ where a is the sphere radius.

$$\psi_n(k_T a) = 0 \tag{4}$$

Class II motion involves coupled longitudinal and transverse internal wave fields which taken together satisfy the boundary conditions. The characteristic equation is hence also a function of $k_L a$, the longitudinal wave dimensionless frequency, and has the form

$$n(n+1)\psi_n(k_T a)\psi_n(k_L a) = (k_T a)(k_L a)^2 \frac{d\psi_n(k_T a)}{d(k_T a)} \frac{d}{d(k_L a)}\left[\frac{\psi_n(k_L a)}{k_L a}\right]. \tag{5}$$

The longitudinal and transverse wavenumbers are related through the material's Lamé constants (λ, μ) or Poisson's ratio (ν).

$$\frac{k_T}{k_L} = \sqrt{\frac{\lambda + 2\mu}{\mu}} = \sqrt{\frac{2(1-\nu)}{(1-2\nu)}} \tag{6}$$

Characteristic Equations (4) and (5) have, in general, infinitely many roots (modes m) for each harmonic n.

Two similar classes of motion exist in a hollow sphere as discussed by Shah, Ramkrishnan, and Datta[5]. Our approaches and solution methods are akin, except for differences relating to boundary conditions.

Solution Method

Inspection of Equations (3) and (4) shows that the eigenfrequencies associated with Class I shear motions are simply related to the zeroes of spherical Bessel functions of order n. The zeroth spherical surface harmonic is a constant which precludes this kind of motion. Thus beginning with the first harmonic the eigenfrequencies are

$$\omega_{ln}^{(m)} = \frac{z_n^{(m)}}{a}\sqrt{\frac{\mu}{\rho}} \tag{7}$$

where $z_n^{(m)}$ is the mth zero of the nth spherical Bessel function and ρ denotes the density.

If harmonics or zeroes beyond available tabulated values are desired, the ψ_n functions can be built up from a recursion relationship,

$$\psi_{n+1}(z) = -z^{n+1}\frac{d}{dz}\left[\frac{\psi_n(z)}{z^{n+1}}\right] = \frac{2n+1}{z}\psi_n(z) - \psi_{n-1}(z) \tag{8}$$

realizing that $\psi_0(z) = \sin(z)$. These functions become cumbersome to generate explicitly for high harmonics even with symbolic manipulation programs. However, the functional form need not be generated. The functions' values can be generated point by point numerically, by the two-level recursion formula on the far right hand side of Equation (8). Roots of Equation (4) are then found numerically in either case.

Solutions for Class II motion can be obtained by a similar procedure. If the functional forms are not generated explicitly, the following formulas can supply values of the derivatives needed for the numerical solution of Equation (5).

$$\frac{d\psi_n(k_T a)}{d(k_T a)} = \psi_{n-1}(k_T a) - \frac{n}{k_T a}\psi_n(k_T a) \tag{9}$$

$$k_L a \frac{d}{d(k_L a)}\left[\frac{\psi_n(k_L a)}{k_L a}\right] = \psi_{n-1}(k_L a) - \frac{(n+1)}{k_L a}\psi_n(k_L a) \tag{10}$$

The zeroth harmonic for this motion class is a special case. Equation (5) for n equal to zero reduces to

$$k_L a = \tan(k_L a) \tag{11}$$

which is independent of the transverse wavenumber, k_T, since the motion is purely dilatational.

Results

Equation (7) showed that the eigenfrequencies of Class I motion are related to spherical Bessel function zeroes. Since these zeroes are tabulated in mathematics handbooks such as Abramowitz and Stegun[6], they will not be reproduced here. The eigenfrequencies of the radial ($n = 0$) modes of Class II motion are also related to spherical Bessel function zeroes. As can be inferred from Equations (3), (8), and (11),

$$\omega_{II0}^{(m)} = \frac{z_1^{(m)}}{a}\sqrt{\frac{\lambda + 2\mu}{\rho}}. \qquad (12)$$

In terms of $k_L a$, these are 4.49341, 7.72525, 10.90412, etc.

Table I gives values of $k_T a$ corresponding to Class II eigenfrequencies, $\omega_{IIn}^{(m)}$, for Poisson's ratios of 1/4 and 1/3 and $n > 0$. All the modes with $k_T a$ less than 20 are given. For a Poisson's ratio of 1/4, there are 52 Class II modes in this range. For ν equal to 1/3, there are only 47 modes. As Poisson's ratio increases, the material becomes less compressible, so an individual mode's frequency increases. The number of Class I modes is independent of Poisson's ratio and remains fixed at 38 for $k_T a < 20$. The eigenfrequencies of each harmonic and Class are interlaced, but there is an orderly increase in the eigenfrequency for the fundamental mode of each subsequent harmonic. The only exception is the Class II radial modes which have higher frequencies than their rotatory ($n = 1$) counterparts.

Verification

Our motivation for solving this problem also provides an independent means of checking the calculations. Integral equation representations of exterior domain elastodynamic problems are plagued by certain irregular frequencies at which the equation has infinitely many or no solutions. When these equations are solved numerically, this difficulty presents itself as an ill-conditioned matrix. Martin[7] has shown that these irregular frequencies are the eigenfrequencies of the associated interior problem with Dirichlet boundary conditions. We have checked the eigenfrequencies (up through harmonic five) reported here by comparing the condition number of a boundary

element method (BEM) generated matrix (see Reference 8) at the predicted frequency with the condition number of nearby frequency matrices. The results confirm these calculations.

Conclusion

These results are useful to BEM and other integral equation researchers who are attempting to understand and solve the irregular frequency problem in elastodynamics. In particular, precise knowledge of all these frequencies allows countermeasures such as the BIFILM algorithm[8] to be tested. These results can also serve as a check on numerical methods for elastic continuum modal analysis.

Acknowledgements

This work was sponsored by the Center for NDE at Iowa State University and was performed at the USDOE Ames Laboratory which is operated by Iowa State under Contract No. W-7405-ENG-82. One author (Rizzo) was partially supported by the Office of Naval Research under Contract No. N00014-86-K-0551.

References

1. H. Lamb, 'On the vibrations of an elastic sphere', *London Math. Soc. Proc.*, 13, 189-212 (1882).
2. A. E. H. Love, *A Treatise on the Mathematical Theory of Elasticity*, 4th Ed. (Dover, New York, 1927).
3. A. C. Eringen and E. S. Suhubi, *Elastodynamics*, Vol. II (Academic Press, New York, 1975).
4. P. Debye, 'Zur theorie der spezifischen wärmen', *Annalen der Physik*, Ser. 4, Bd. 39, 789-839 (1912).

5. A. H. Shah, C. V. Ramkrishnan, and S. K. Datta, 'Three-dimensional and shell-theory analysis of elastic waves in a hollow sphere', *J. Appl. Mech. Trans. ASME*, **36**(3), 431-444 (1969).
6. M. Abramowitz and I. A. Stegun, *Handbook of Mathematical Functions* (Dover, New York, 1965).
7. P. A. Martin, 'Identification of irregular frequencies in simple direct integral-equation methods for scattering by homogeneous inclusions', to appear, *Wave Motion* (1991).
8. M. Rezayat, D. J. Shippy, and F. J. Rizzo, 'On time-harmonic elastic-wave analysis by the boundary element method for moderate to high frequencies', *Comput. Methods Appl. Mech. Engrg.* **55**(3), 349-367 (1986).

Table I. Transverse Wave Dimensionless Eigenfrequencies of Class II Motion

Harmonic	$\nu = 1/4$		$\nu = 1/3$	
1	3.98978	6.20296	4.31104	6.28319
	9.25856	10.32782	9.30867	11.80491
	12.49756	15.57714	12.56637	15.64226
	16.00854	18.79676	18.35945	18.84956
2	5.77510	7.73594	6.14067	8.00848
	10.67013	12.59144	10.75399	13.76003
	13.99104	17.06532	14.70966	17.12557
	18.40041			
3	7.29284	9.32252	7.60292	9.81182
	12.06687	14.61599	12.22253	15.22962
	15.57109	18.50656	17.12725	18.63066
4	8.65331	10.92254	8.90405	11.54633
	13.46630	16.30743	13.74763	16.65140
	17.37159	19.93332	19.29100	
5	9.92375	12.49147	10.13181	13.14327
	14.88209	17.77994	15.34071	18.07228
	19.29420			
6	11.14131	14.00203	11.32014	14.60584
	16.32227	19.17997	16.97116	19.51348
7	12.32560	15.44445	12.48389	15.96990
	17.78588		18.58437	
8	13.48730	16.82213	13.63065	17.26947
	19.26246			
9	14.63266	18.14550	14.76475	18.52695
10	15.76561	19.42638	15.88893	19.75568
11	16.88873		17.00505	
12	18.00383		18.11444	
13	19.11222		19.21809	

PART III.

BOUNDARY ELEMENT METHOD SOLUTIONS FOR ELASTIC WAVE SCATTERING IN 3D

Summary

Time-harmonic elastic wave scattering problems encountered in ultrasonic nondestructive evaluation are solved by the boundary element method (BEM). Selected results for spherical and spheroidal shaped voids and inclusions are compared with analytical and other numerical solutions. Results for ellipsoids, which require a full three dimensional formulation, are presented. The modeling of cracklike defects with this formulation is discussed. Recent theoretical findings regarding the fictitious eigenfrequency difficulty are explored numerically.

Introduction

This work is motivated by the needs of ultrasonic nondestructive evaluation (NDE)[1]. Understanding how ultrasound interacts with a material anomaly is paramount in quantifying the inspection process. The basic problem that we address, therefore, is one of elastic wave scattering by some arbitrarily shaped defect. Except for the case of a flaw near a component surface, the defect(s) can usually be considered as isolated in an elastic full-space since inspections are done with pulsed excitation and responses are time gated. Even for situations with a simple defect such as a cavity or a homogeneous, isotropic inclusion, this problem requires a numerical solution except for special cases of simple geometry or in some low/high frequency limit.

This paper deals with the numerical considerations of using the BEM as a means for solving scattering problems in a homogeneous, isotropic elastic medium. The BEM makes quantifying both the near *and far* scattered field for an arbitrarily shaped scatterer feasible. Previously known formalisms and numerical algorithms are combined and optimized to create a tool for NDE research and application. However, the methods are general in the sense that other elastodynamic scattering problems can be addressed. Figure 1 depicts the general problem of which all the examples in this paper are special cases. A planar incident displacement field traveling in the spherical coordinate direction (θ^I, ϕ^I) impinges on an ellipsoidal inhomogeneity with half-axis lengths a, b, and c. A scattered displacement field is generated which can be characterized far from the scatterer as a spherically spreading wave that varies with the angles (θ^S, ϕ^S). It will be shown why the BEM is so well suited for these kinds of problems.

To understand how this capability augments the state-of-the-art in elastic wave scattering, we first mention other approaches for obtaining solutions. There are two basic strategies. The first strategy is to use an exact method which can be implemented for a limited set of scatterer shapes such as spherical, axisymmetric, or planar. For example, the spherical scatterer can be solved by an analytical separation of variables technique and was done most notably by Ying and Truell[2] and Pao and Mow[3]. Practical results for *axisymmetric* scattering problems have been dominated by eigenfunction expansion based numerical methods such as transition matrix (T-matrix) method [4-6] and by the method of optimal truncation (MOOT)[7,8]. The second strategy is to find an approximate solution which is valid under certain circumstances, such as high frequency. We mention only a few. If the properties of the scatterer can be considered as a perturbation of the host material properties, the weak scattering Born approximation from quantum mechanics can be applied successfully[9]. Ray methods are often successful at high frequency[10]. Low frequency approximations have been used for

elliptical cracks[11] and ellipsoidal volumetric defects[12]. Bond recently reviewed a variety of techniques from both strategies[13]. Clearly there existed a gap in the capabilities for arbitrarily shaped (3D) scatterers, especially at intermediate frequencies.

To properly select and optimize a numerical method to fill this gap, one must be cognizant of the intended uses. Current thinking in NDE gives three major uses for a general elastic wave scattering computation capability. Probability of detection modeling[14] can be done to ensure that a given inspection plan for a particular component will reliably indicate the presence of defects. A large number of potential defect locations, orientations, sizes, and types are considered and the distribution of their scattered signals are analyzed statistically. Secondly, inverse methods attempt to characterize and size an unknown defect after it has been detected. These methods often rely on a forward scattering capability[1]. The intermediate frequency range, which we address, is particularly rich in sizing information[1]. Finally, the limits of applicability of approximate methods such as those mentioned previously must be established in a quantitative sense. In Reference 15, we give some examples of this application using our BEM capability. All of these uses require being able do a large number of cases with a reasonable computer resource.

Formalisms and Algorithms

We begin by briefly reviewing the main features and advantages of our approach. The BEM deals rigorously with the infinite extent of the host medium and the associated Sommerfeld radiation condition, as does MOOT and T-matrix. In contrast, domain type numerical methods such as finite difference and finite element must truncate the discretization at some point[16], introduce some absorbing boundary[17], use infinite elements (i.e., consistent boundaries[18]), add exterior wave functions as in GLFEM[19], or introduce an artificial boundary for which the Dirichlet and Neumann boundary

conditions can be related as in the DtN method[20]. Secondly, BEM reduces the dimensionality of problems by one, thus making 3D dynamic analysis practical with current computers. These problems can be cast in the time domain[21] or in a time-harmonic (frequency) domain form. Solutions in the frequency domain are often the most convenient. If a time domain response is desired, it can be acquired from the Fourier or Laplace transformation of these frequency domain solutions[22]. This may seem indirect but a comparison of our approach with time domain based, finite element and finite difference methods applied to scattering indicates that the allowable distance between nodes is reduced with the frequency domain form. The mesh required to avoid excessive accumulation of dispersive and dissipative errors when time-stepping a hyperbolic PDE is much finer than that needed to make an "adequate" interpolation of the field at some instant in time (as with a time-harmonic approach)[23].

Boundary integral equation

When the linear differential operator governing elastic wave propagation is written in time-harmonic form, it has an elliptical nature and a generalized form of Green's reciprocal identity can be readily applied to it. By using the fundamental solution, the displacement field can be expressed in terms of a surface integral only (in 3D), if, as in our case, no body forces are involved. A boundary integral equation (BIE) results when the field point of the kernel functions is taken to this surface and the dimensionality of the problem is thus reduced. The Somigliana formula for the host medium, which we use, is derived by writing the BIE for the incident field in the domain of the scatterer as if it were made of the host material and again for the scattered field in the complementary domain[24]. This formula is

$$\mathbf{C}^T(\mathbf{p})\mathbf{u}(\mathbf{p},\omega) = \oint_S [\mathbf{U}^T(\mathbf{p},\mathbf{q},\omega)\mathbf{t}(\mathbf{q},\omega) - \mathbf{T}^T(\mathbf{p},\mathbf{q},\omega)\mathbf{u}(\mathbf{q},\omega)]dS + \mathbf{u}^I(\mathbf{p},\omega) \qquad (1)$$

where $\mathbf{p}$ is the field point which has been taken to the boundary and $\mathbf{q}$ is a generic point of the inhomogeneity boundary S. The displacement vector $\mathbf{u}$ and traction vector $\mathbf{t}$ are complex due to the time-harmonic formulation. We use an $e^{-i\omega t}$ implied time dependence. The U tensor represents the fundamental solution and T is related to its normal (to S) derivative through Hooke's law. The functional form of these tensors is given in Reference 25. They are singular when field point $\mathbf{p}$ equals $\mathbf{q}$ and thus the integral's value exists only in a Cauchy principal value (CPV) sense. The C tensor depends on the topology of S at $\mathbf{p}$, i.e., if $\mathbf{p}$ is on a side, edge, or corner[25]. Superscript I on $\mathbf{u}$ denotes the incident field, while no superscript implies the total field. The T superscript on the tensors indicates the transpose. Equation (1) is used to find the unknown total field quantities at the surface from specified boundary conditions and the incident field.

In general a boundary surface may contain regions of Dirichlet, Neumann, and Churchill (mixed) boundary conditions. But for scattering the entire boundary usually only has one type. For a void, tractions are all specified as zero and the displacements are unknown. Conversely, displacements are all zero for a "rigid" scatterer and the tractions are solved for. For an elastic inclusion, the BIE is written again for the total field in the inhomogeneity. This time there is no explicit incident field term as in Equation (1). The incident field's effect is passed through the boundary. When the displacements and tractions are matched up at the boundary, we have a pair of coupled BIEs which define the so-called transmission problem[26].

Fields

The incident field displacements must be specified for the BIE. For an incident plane transverse (T) wave which is linearly polarized[27], these displacements are given by

$$\mathbf{u}^I(\mathbf{p}) = I_\alpha e^{i\mathbf{k}\cdot\mathbf{p}}\hat{\mathbf{d}} \qquad (2a)$$

with the implied harmonic time dependence. $\mathbf{k}$ is the wave number vector and I_α is the amplitude. The admissible polarization unit vectors, $\hat{\mathbf{d}}$, must be perpendicular to $\mathbf{k}$ since T-wave displacements are orthogonal to the direction of propagation. See Figure 1b. A single polarization angle,

$$\alpha = \sin^{-1}\left(\hat{\mathbf{d}} \cdot \begin{Bmatrix} -\cos\theta^I \cos\phi^I \\ -\cos\theta^I \sin\phi^I \\ \sin\theta^I \end{Bmatrix} \right) \qquad (2b)$$

then uniquely defines the field. (The more general case of elliptical transverse motion can be constructed via superposition from two linearly polarized T-wave fields). The incident field propagation direction angles (θ^I, ϕ^I) are implied by $\mathbf{k}$. A similar expression for longitudinal (L) waves is given in Reference 15. Incident fields need not be planar[15] but will be for all the examples in this paper.

A special, non-BIE form of Equation (1) is needed to determine the scattered field from the boundary solution. Using superscript S to denote the scattered field,

$$\mathbf{u}^S(\mathbf{p}) = \mathbf{u}(\mathbf{p}) - \mathbf{u}^I(\mathbf{p}) = \int_S [\mathbf{U}^T(\mathbf{p},\mathbf{q})\mathbf{t}(\mathbf{q}) - \mathbf{T}^T(\mathbf{p},\mathbf{q})\mathbf{u}(\mathbf{q})]dS(\mathbf{q}) \quad (3)$$

This formula, known as the interior representation integral, is written for the host domain. The field point $\mathbf{p}$ now denotes any point of that open set (not on the boundary) and consequently $\mathbf{C}^T$ is the identity matrix.

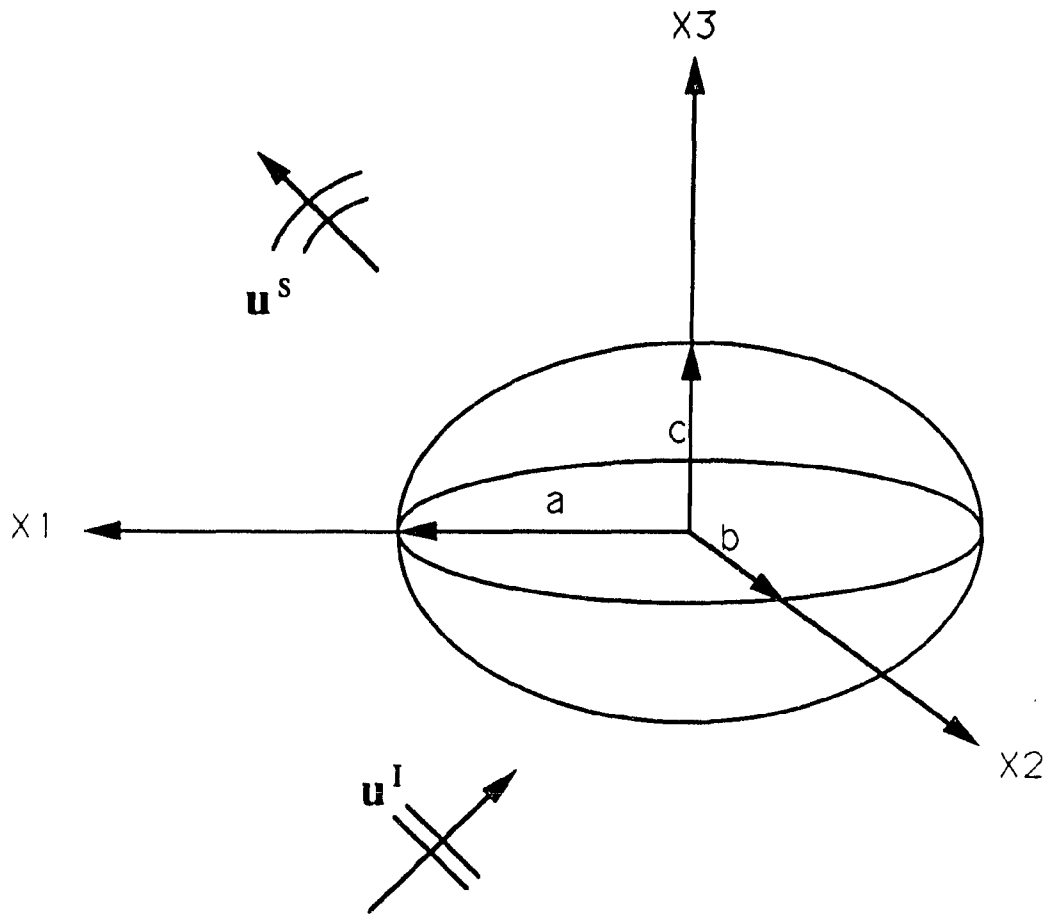

Figure 1a General scattering problem: Defect in fields

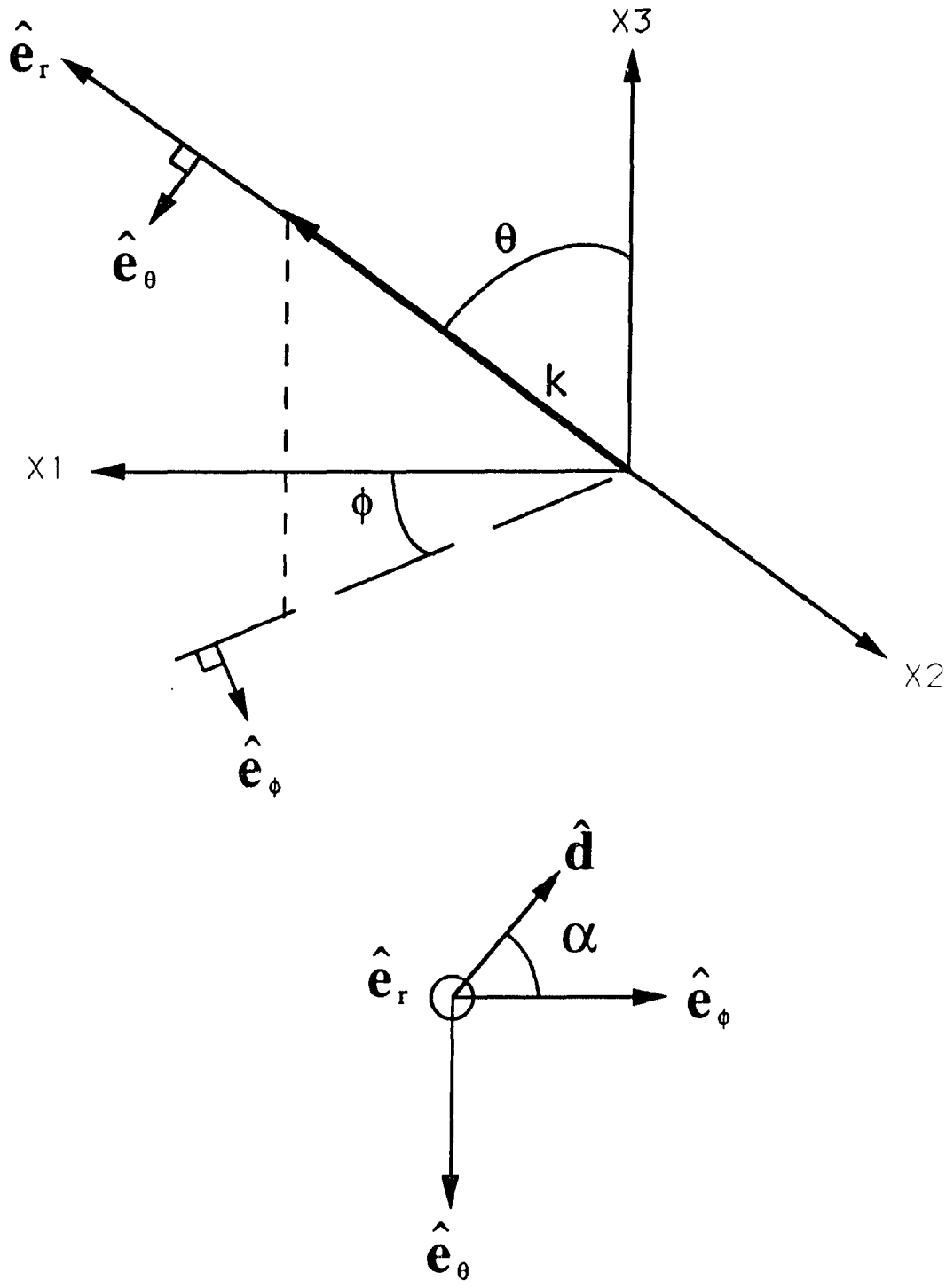

Figure 1b General scattering problem: Wave and polarization unit vector definitions

Since the transducers used to sense scattered waves in ultrasonic NDE are often in the farfield of the flaw, a convenient quantity known as the scattering amplitude, A, is often used to quantify the scattered field. A rigorous definition of A may be found in Reference 15 but heuristically it defines the magnitude and relative phase of the spherically spreading wave generated in the farfield of a scatterer due to an incident plane wave. A is a function of scatterer shape and properties, host properties, incident and scattered directions, and frequency. "A"s are defined for all combinations of incident and scattered wave types (L-L, L-T, T-L, and T-T) and polarizations. The scattered displacement vector computed by (3), with the distance r between p and q large, may be converted to scattering amplitudes as shown in Reference 15. Just as with the incident field, the most general (e.g., in directions not along a plane of symmetry) scattered T-wave field can be characterized by two, orthogonal, linearly polarized waves. These component motions are arbitrarily taken to be parallel with the unit vectors associated with the polar and azimuthal angles, $\hat{\mathbf{e}}_\theta$ and $\hat{\mathbf{e}}_\phi$. Often transverse motion is equivalently expressed as a combination of two circularly polarized waves with opposite chirality[27]. Additionally, Reference 15 shows that the asymptotic form of U and T for large r may be used in Equation (3) to make this process algebraically simpler and consequently twice as fast on the computer.

Numerical integration and matrix equations

The nonsingular portion of the BIE surface integrals and the interior representation integrals are computed by an identical numerical approach. The surface is discretized into isoparametric curvilinear quadratic elements. Both three and four sided elements are used. The number of Gauss quadrature points per element is adjusted as needed according to the severity of the integration. Severity is determined from element shape and position relative to the field point (elastostatic severity) and from the maximum variation in distance between the field point and the element nodes

divided by the shortest wavelength (elastodynamic severity). Details of these procedures are given in Reference 22. The CPV portion of the BIE is first regularized through the use of the elastostatic Kelvin tensor[25] and then dealt with numerically after a transformation to polar coordinates[22].

Since computational efficiency is of great importance, a feature of the code allows a symmetry plane to be defined for problems having such symmetry. Only one-half the scatterer surface needs to meshed, as is exemplified for a sphere in Figure 2. Integration is still carried out over the entire surface through the use of an image of the field point p . However, collocation needs only to be done at each node of the partial mesh as the image nodes must have "reflected" field values.

Collocating the discretized BIE(s) at each node results in a set of simultaneous linear algebraic equations. For a void, rigid, and elastic inclusion, respectively, the matrix equations have the form:

$$\{u\} = [H_{ext}]^{-1}\{u'\} \tag{4a}$$

$$\{t\} = [G_{ext}]^{-1}\{u'\} \tag{4b}$$

$$\begin{Bmatrix} u \\ t \end{Bmatrix} = \begin{bmatrix} H_{ext} & G_{ext} \\ H_{int} & G_{int} \end{bmatrix}^{-1} \begin{Bmatrix} u' \\ 0 \end{Bmatrix} \tag{4c}$$

The complex coefficients which comprise the matrices G and H are functions of frequency, material properties, and the inhomogeneity geometry. The subscripts refer to the BIEs for the internal or external domain, respectively[26]. The G matrix comes from integration of the fundamental solution kernel, whereas the H matrix is from the gradient

kernel and both are fully populated. For all the examples in this paper, these matrices are in single precision. When boundary conditions are not mixed, it is very advantageous to have special subroutines which only compute the necessary kernel components. The formal inverses are not computed as such but represent an LU decomposed matrix from which boundary solutions may be obtained for various incident fields via the forward elimination and backward substitution processes. Various flaw orientations can be cast equivalently as a single orientation with various incident field directions. Consequently, the form of the matrix equations is very convenient for the repetitive parameter studies needed by NDE.

Multiple scatterers

Up until this point we have presented our method as though the inhomogeneity from which the scattering occurs is defined mathematically by one connected domain. However the same governing BIE can be derived for multiple scatterers. In fact the scattering from multiple defects can be done by the methods described thus far, if the domain of the integral in Equations (1) and (3) is taken to be the surface of all the scatterers. In terms of computer implementation one must only modify the node and element definitions of the second (and so on) surfaces to lie in sequence and at the appropriate position.

The following discussion is an illustration for two scatterers but the concept extends to any number of scatterers. The matrix for two scatterers can be arranged into the matrices for each one individually and the matrices linking them.

$$\begin{bmatrix} \begin{bmatrix} H_{ext} & G_{ext} \\ H_{int} & G_{int} \end{bmatrix}_{11} & \begin{matrix} H_{12} & G_{12} \\ 0 & 0 \end{matrix} \\ \begin{matrix} H_{21} & G_{21} \\ 0 & 0 \end{matrix} & \begin{bmatrix} H_{ext} & G_{ext} \\ H_{int} & G_{int} \end{bmatrix}_{22} \end{bmatrix} \begin{Bmatrix} u_1 \\ t_1 \\ u_2 \\ t_2 \end{Bmatrix} = \begin{Bmatrix} u_1^I \\ 0 \\ u_2^I \\ 0 \end{Bmatrix} \tag{5}$$

where the $[\ ]_{ii}$ are the self-influence matrices created by applying (1) to each scatterer. Since the nodes of the first (second) scatterer are in the host domain of the second (first) scatterer, the displacements due to scattering from the other inhomogeneity can be computed from (3). The G_{ij} and H_{ij} are cross-influence matrices relating to tractions and displacements, respectively. This interpretation will be useful in understanding the fictitious eigenfrequency difficulty (FED) for multiple scatterers.

Single Medium Solutions

In this section we provide some illustrative examples which give insight into mesh requirements and accuracy. In all cases the host medium is equivalent to material A from Table I.

Modeling volumetric flaws

Of the two single medium types of problems, the cavity is the more important from an NDE viewpoint. The availability of an analytical solution[2] for scattering amplitudes for a spherical void makes it an excellent benchmark for numeric computation. Surface solutions for the cavity by this BEM formulation were previously compared to the analytical solution in References 22 and 25. In Figure 3a, the magnitude of farfield scattered L-wave generated due to an incident L-wave with $k_L a$ equal to 3.6 is shown as a function of scattered angle. In this case the BEM data are all generated by repeated use of the asymptotic form of Equation (3) on one boundary solution. While the error is

quite small, we see that it does vary with the scattered direction. Since the scattering amplitude is based on an integral of the surface solution[15], we expect some errors in the surface solution to cancel.

It is also important to determine the phase correctly so that transformations to the time domain can be executed accurately. Figure 3b shows the complex components of the L-L scattering amplitude as a function of frequency for a constant scattered angle of 0 degrees (forward scatter). For these moderate frequencies, the 40 element mesh did well in getting the real and imaginary components correct. In general, however, the accuracy is better when predicting magnitudes.

The rigid scatterer, as we have it defined, has no motion relative to a fixed reference frame. Physically this corresponds to an inelastic entity with infinite mass. Pao and Mow[3] correctly point out that a solution for a finite mass scatterer which moves with rigid body motion is more realistic. They also point out that the infinite mass rigid scatterer does not exhibit Rayleigh scattering behavior at low frequency. In fact, the total scattering cross section does not approach zero for an arbitrarily low frequency as it does for other scatterer types. (Total cross section, like scattering amplitude, is a useful measure of wave scattering phenomena. It relates the total energy scattered to the incident plane wave energy flux.)[28] Since we wish to investigate the validity of our formulation under unusual conditions, the comparison with the analytical solution[3] for rigid scatterers, shown in Figure 3c, was made. The BEM values for total cross section were obtained from the imaginary part of the forward scattering amplitude via the elastodynamic version of the optical theorem[28]. The BEM results matched the analytical solution - even down to $k_L a$ equal 0.01 where the unusual low frequency behavior occurs.

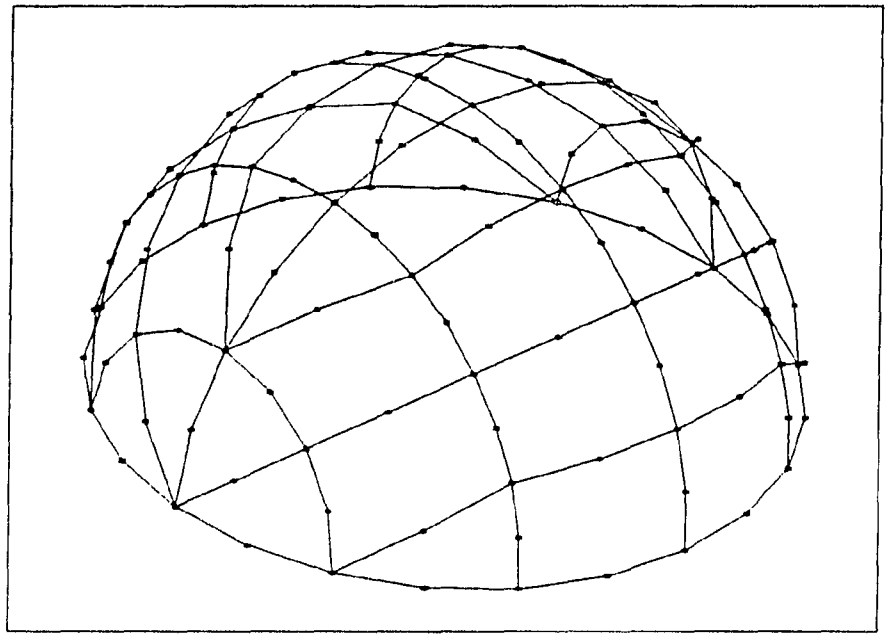

Figure 2 Sphere model - 40 elements

Table I: Material Properties Used

	Longitudinal Wavespeed ($cm/\mu s$)	Transverse Wavespeed ($cm/\mu s$)	Poisson's Ratio	Density (g/cc)
Material A	1.000	0.500	.333	1.00
Material B	0.750	0.433	.250	16.00
Lucite	0.272	0.134	.340	1.18
Solder	0.301	0.145	.349	8.41
Titanium Alloy	0.634	0.303	.352	4.42
Tungsten Carbide	0.666	0.398	.222	13.82

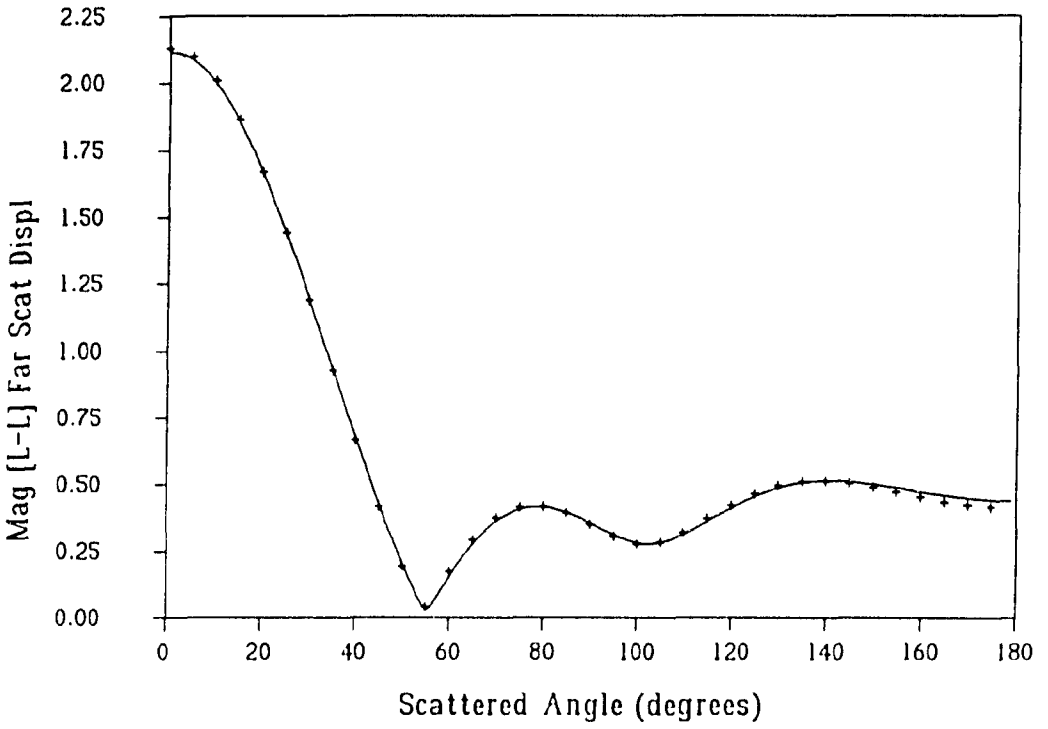

Figure 3a Comparison of BEM results (+) from a 40 element model with analytical solution (——) for spherical scatterers: Angular dependence of scattering from a void at $k_L a = 3.6$

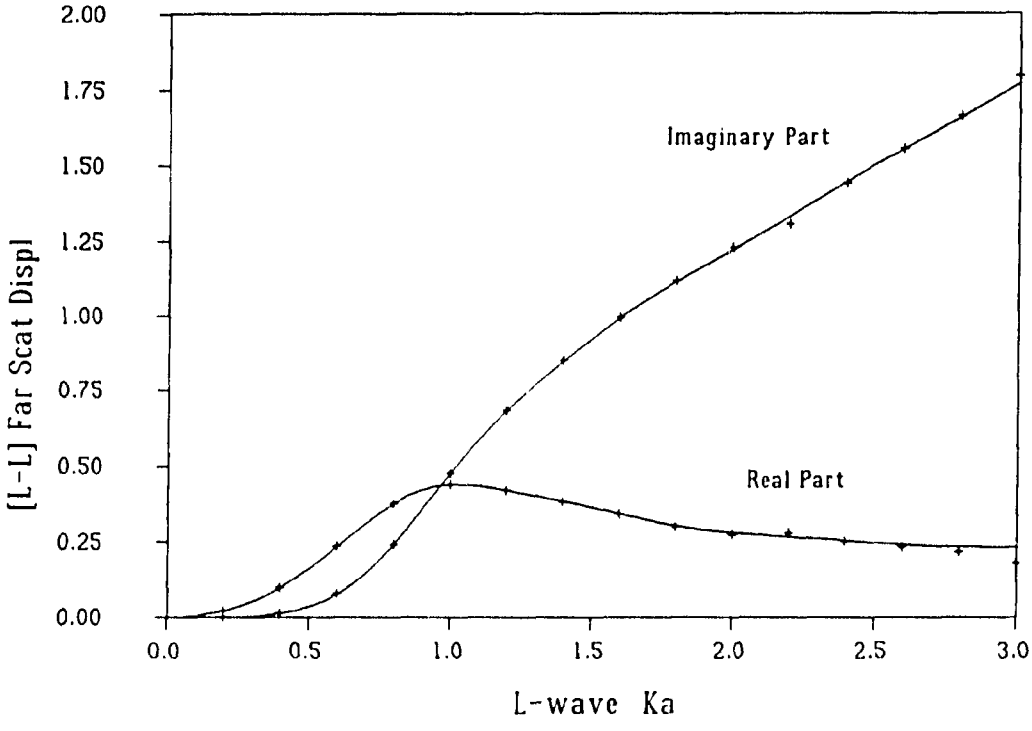

Figure 3b Comparison of BEM results (+) from a 40 element model with analytical solution (——) for spherical scatterers: Frequency dependence of forward scatter ($\theta^S = 0^I$, $\phi^S = \phi^I$) from a void

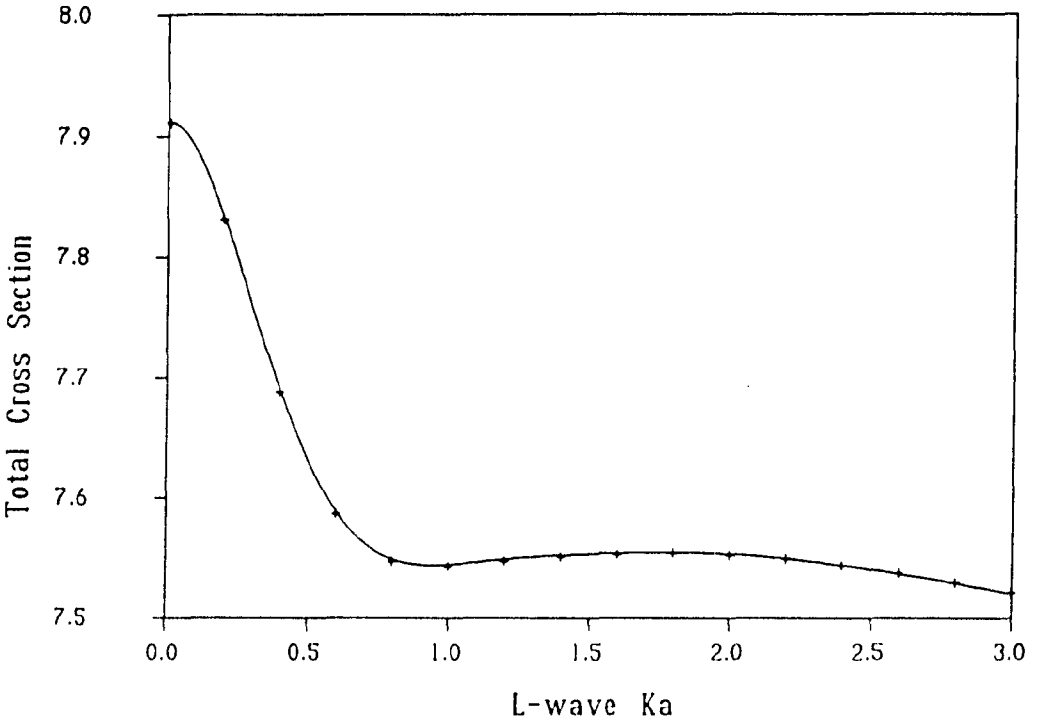

Figure 3c Comparison of BEM results (+) from a 40 element model with analytical solution (——) for spherical scatterers: Frequency dependence of total cross section from a rigid, infinite mass sphere

In Figure 4 we compare BEM and MOOT[8] results for magnitude of L-L backscatter from an oblate (2:2:1) spheroidal void. For this shape, backscatter is a function of both orientation and frequency. In general, finer meshes are required as frequency is increased since the surface solution which is being approximated by the elemental interpolation functions has a correspondingly shorter length scale. We have found a good rule of thumb for a nominal accuracy is at least one quadratic element per quarter wavelength when predicting L-L scattering amplitudes. "Nominal" accuracy means that the essential variations of A with respect to frequency, scattered angle, etc. are predicted correctly. In Figure 4a we see that the 40 element mesh results agree quite well with MOOT through $k_L a$ equal to 5. There are problems at $k_L a$ equal to 3.4 and 4.2 which are caused by the FED that will be discussed later. By comparing 4a and 4b, we see that accuracy for a given mesh can also be a function of orientation. As is often the case, accuracy degrades as incidence moves away from the blunt side of the spheroid. At $k_L a$ equals 3.5, the 40 element model has about four elements per wavelength. At higher $k_L a$, the rule of thumb indicates a loss of accuracy may occur. Figure 4b exemplifies the unsystematic errors which typically occur when a mesh is used beyond its capability. The 140 element model agrees with the MOOT result throughout the plotted frequency range because it still has from four to ten elements per wavelength at $k_L a$ equal five. These results are both consistent with the previously stated rule of thumb. Similar comparisons of this method and MOOT may be found in References 15 and 29 for other axisymmetric shapes.

Modeling cracks

Cracks are a very important class of structural defect. We have modeled an open crack in which the opposing faces of the crack do not contact each other. Our crack models are ellipsoidal voids with one semi-axis length much smaller than the other two. Often cracks are modeled as having zero thickness, especially by analytical methods[30],

but also by alternate BEM formulations[31,32]. We expect the hypersingular BIE formulation[32] to eventually replace our singular BIE approach for thin cracks. However, experimental crack samples are often fabricated with non-negligible thickness so our "cracklike" models may continue to be needed to resolve differences in experimental and simulated behavior.

The question is how thin must the void be to achieve "cracklike" behavior in the farfield. The answer turns out to be at least a function of frequency, orientation, and scattered direction. In Figure 5 the predicted magnitude and phase of A_{L-L} from a 140 element model is plotted for ellipsoids with a thickness c ranging from 0.25 to 0.05 when a and b are 1.0 and 0.5 respectively. The magnitude of normal incidence backscatter (Fig. 5a) is quite insensitive to the thickness for these moderate frequencies. However, the phase is sensitive to the thickness except for frequencies below $k_L a \sim 1$. Note that the phase difference increases monotonically with increasing thickness.

The majority of this variation in phase can be accounted for by considering the assumption used by the high frequency Kirchhoff approximation[1]. With Kirchhoff, the shadow side of the crack is assumed to remain motionless and the illuminated side is assumed to act locally like an infinite planar reflector. With our nonzero thickness void models, the position of that illuminated side changes with the thickness. The scattering amplitude, which is referenced to the flaw centroid, is thus phase shifted as the reflector position changes. Figure 5c shows the same BEM results as Figure 5b except with a compensating $2k_L\bar{x}_3$ phase shift. $\bar{x}_3$ is the average x_3 coordinate value of the illuminated half of the ellipsoid. This simple phase adjustment very nearly collapses all these values to a single constant for $k_L a > \sim 2$. Furthermore, the value of that constant is approximately $\pi/2$ (purely imaginary) which is precisely the phase predicted by the Kirchhoff approximation for a zero thickness crack. Comparison of Figures 5a and 5c shows that this phase adjustment causes the phases below $k_L a = 1$ to diverge with

respect to void thickness. At these long wavelengths, the Kirchhoff approximation is not appropriate and the unadjusted phase (Fig. 5b) is insensitive to aspect ratio. At frequencies above the Rayleigh scattering regime, both the magnitude and "shifted" phase of normal incidence backscattering amplitudes are also not controlled significantly by the sharpness of the "crack" tip.

Figure 6 is similar to 5a except it is for forward scatter with L-wave incidence at 45 degrees from normal. Comparison of Figs. 5a and 6 exemplifies that oblique incidence results are more sensitive to aspect ratios than the normal incidence case at a given frequency. Parameter studies like these can determine how thin a void must be made to adequately mimic a crack for a given frequency and for a particular set of incident and scattered directions.

There is a practical limitation to how thin a model can be made with this formulation. The elastostatic integration severity for collocation nodes directly across from a given crack face element goes up as the opposing faces come together. Special meshes, much finer than dictated by wavelength considerations, are used to minimize this problem. These models, such as the 140 element model used for Figures 5 and 6, still have their highest aspect ratio determined by the number of Gauss quadrature points available. A nominally square, 8-node quadrilateral element with 144 quadrature points can have the opposing crack face as close as one-half the length of an element side and still meet the integration requirements established in Reference 22.

For examples of what is achievable with this approach to modeling cracks, see Reference 15.

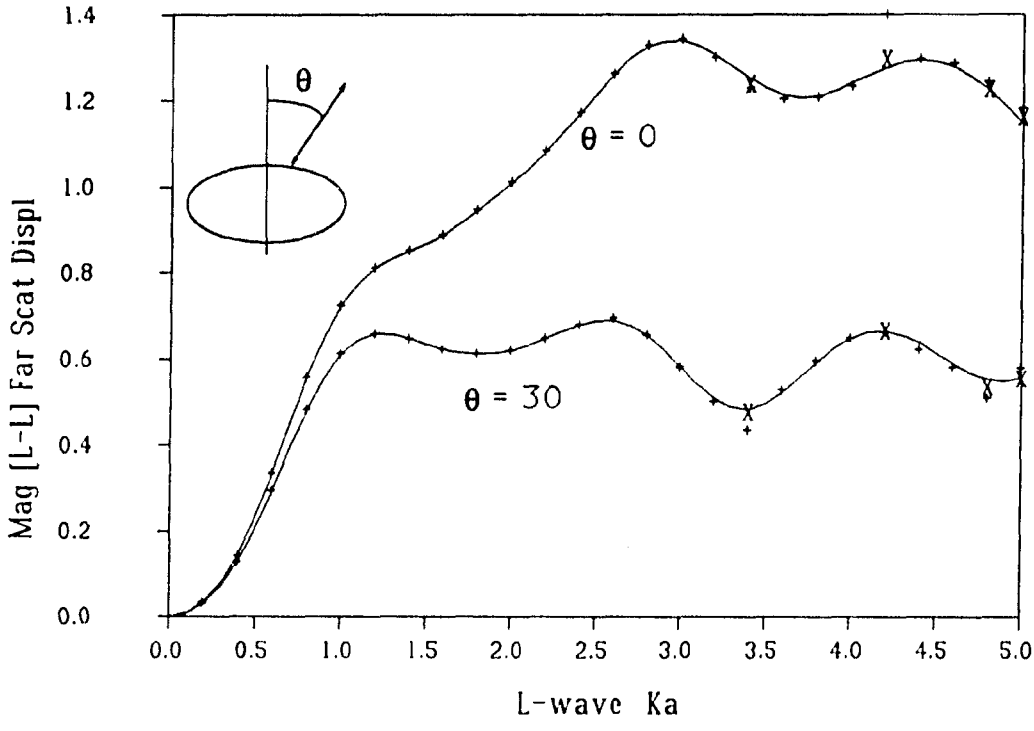

Figure 4a Comparison of BEM results (+ / X) from a (40 / 140) element model with the MOOT solution (—) for frequency dependence of backscatter from an oblate (2:2:1) spheroidal void: Polar angles, θ, of 0° and 30°

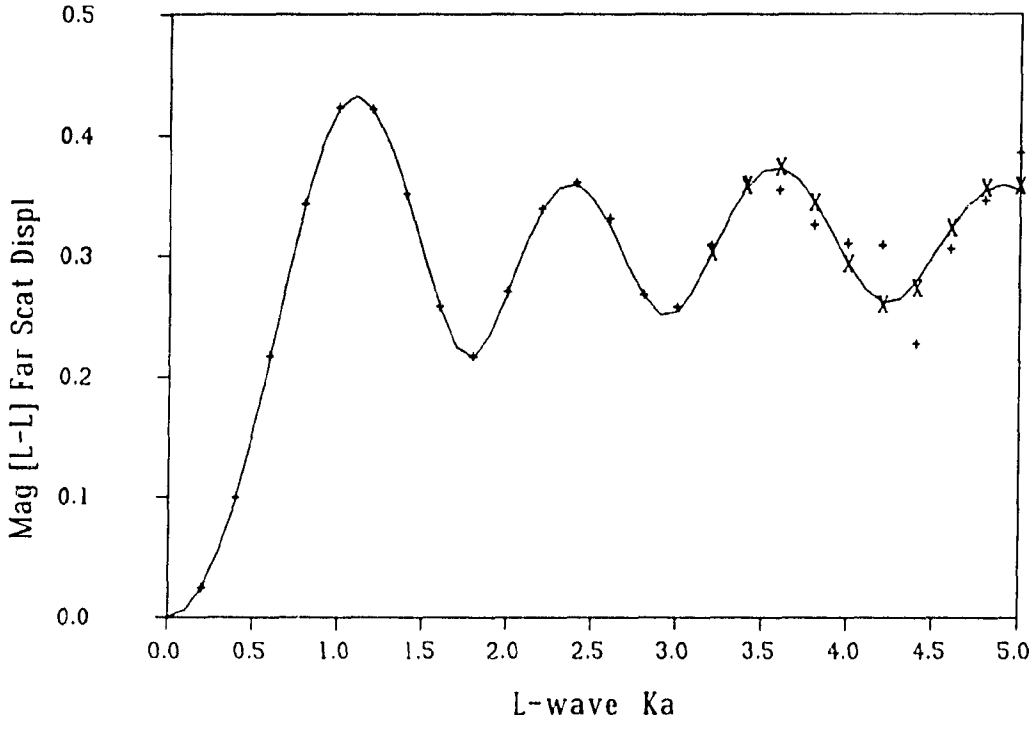

Figure 4b Comparison of BEM results (+ / X) from a (40 / 140) element model with the MOOT solution (—) for frequency dependence of backscatter from an oblate (2:2:1) spheroidal void: Polar angle, θ, of 60°

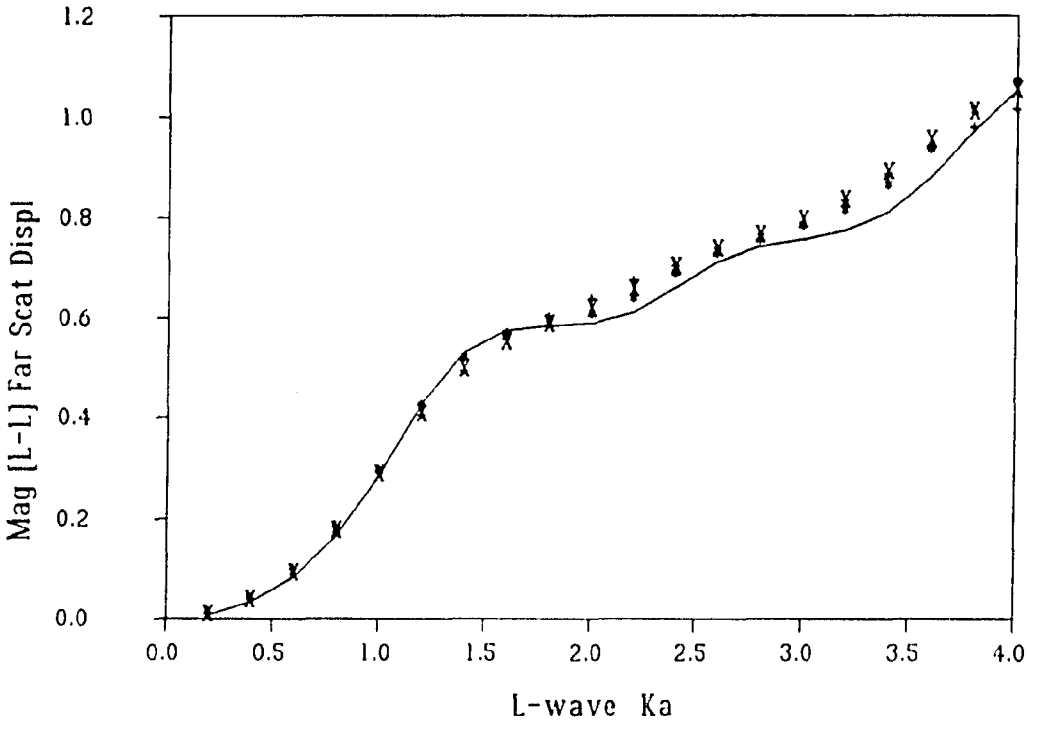

Figure 5a Backscatter from ellipsoidal voids for "normal" incidence along $+X_3$ - Aspect ratios: [+ (1:0.5:0.25)] [X (1:0.5:0.16667)] [* (1:0.5:0.1)] [— (1:0.5:0.05)] - Magnitude of A_{L-L}

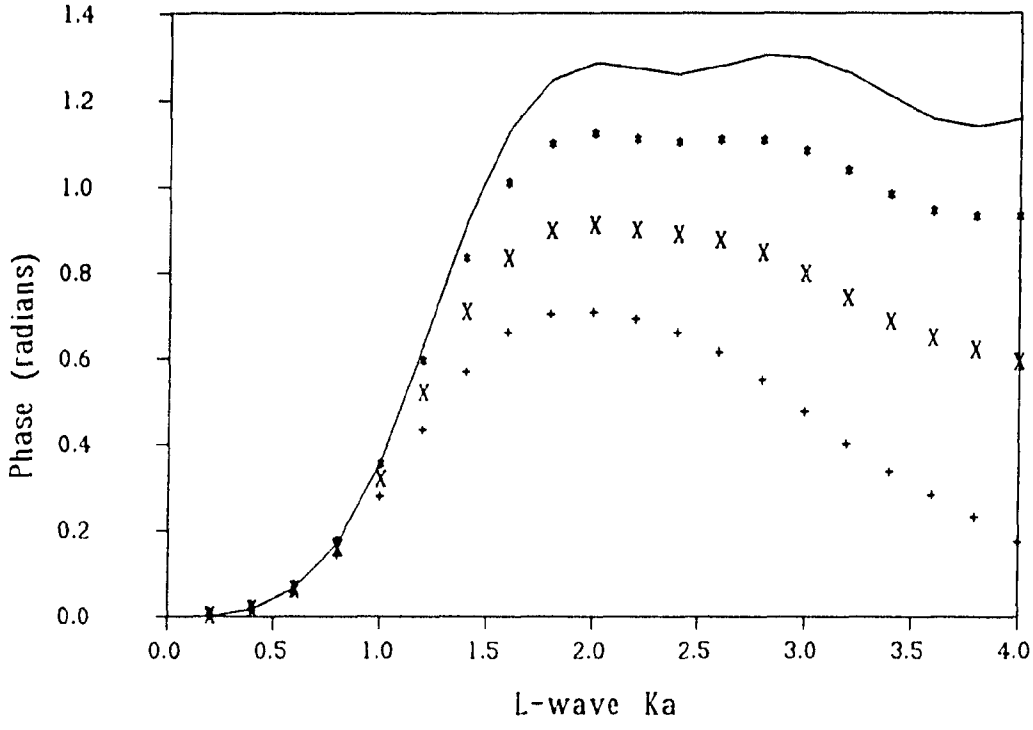

Figure 5b Backscatter from ellipsoidal voids for "normal" incidence along $+X_3$ - Aspect ratios: [+ (1:0.5:0.25)] [X (1:0.5:0.16667)] [* (1:0.5:0.1)] [—— (1:0.5:0.05)] - Phase of A_{L-L}

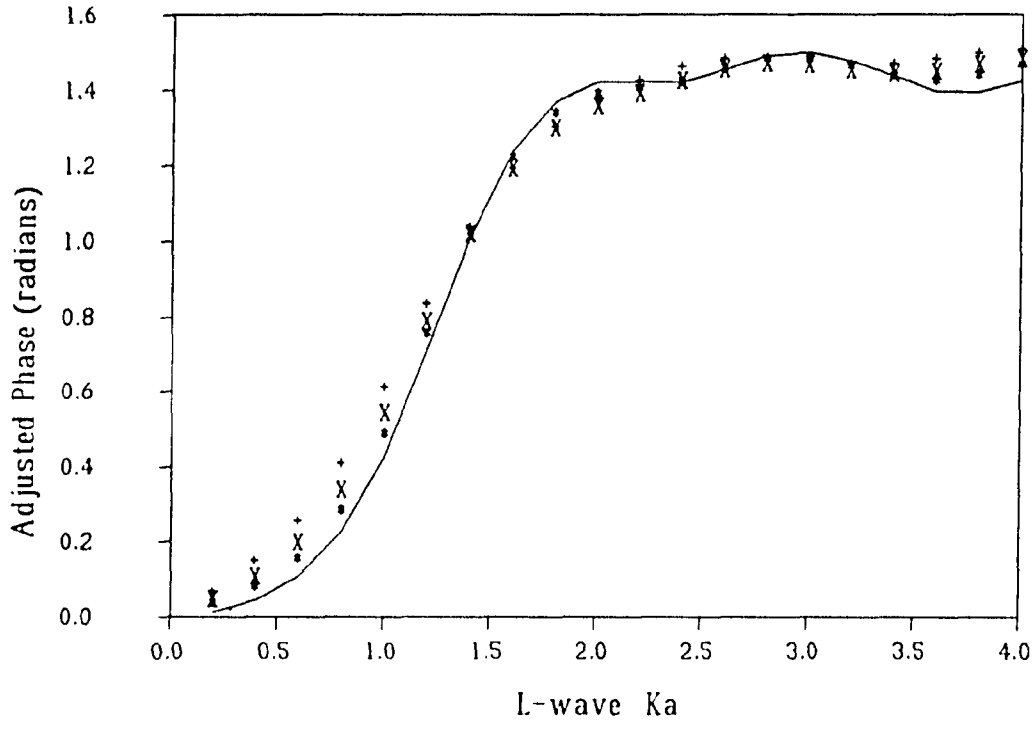

Figure 5c Backscatter from ellipsoidal voids for "normal" incidence along $+X_3$ - Aspect ratios: [+ (1:0.5:0.25)] [X (1:0.5:0.16667)] [* (1:0.5:0.1)] [— (1:0.5:0.05)] - Adjusted Phase of A_{L-L}

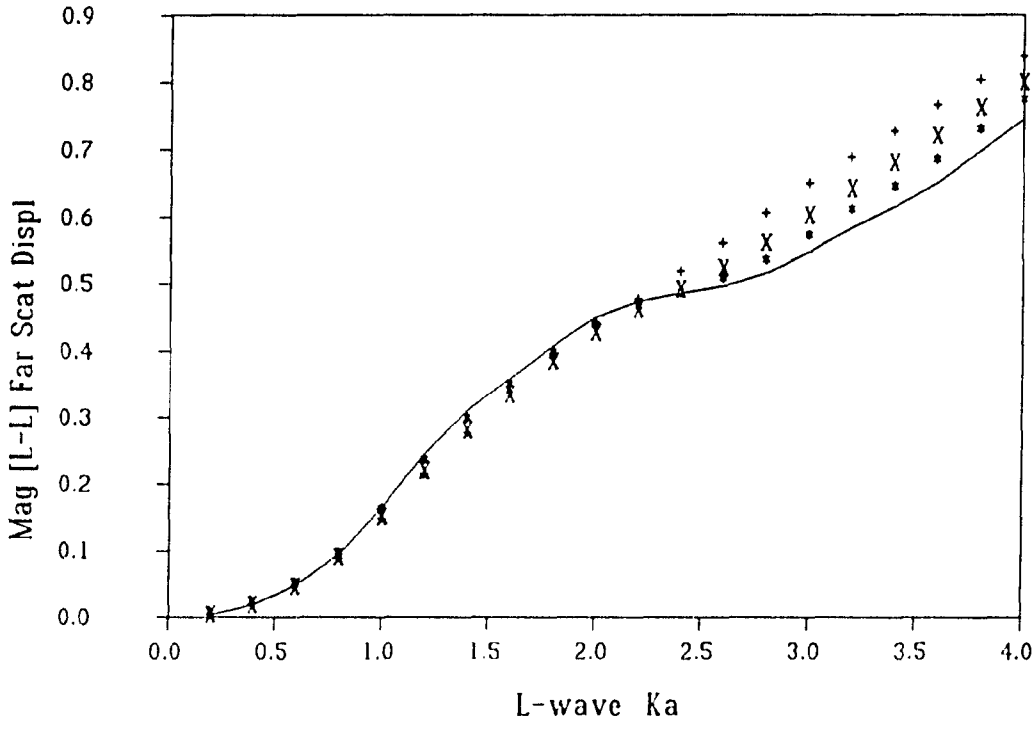

Figure 6 Similar to 5a but for forward scatter due incidence along the major axis and inclined 45° from "normal" ($\theta^I = 45°, \phi^I = 0°$)

Two Medium Solutions

Impurities in a material or desirable second phases will scatter an elastic wave field. If the interphase bond is good we have a situation previously described as the transmission problem. We now consider spheres of titanium alloy and solder in Lucite. See Table I for properties. The solder/Lucite combination is a experimental model system for relatively strong scatterers which have wavespeeds similar to the host material. The strong scattering is caused by the density change. The titanium in Lucite combination again represents a relatively strong scatterer but with wavespeeds much faster than those in the host material. The titanium/Lucite scattering amplitude spectrum shown in Figure 7a is reminiscent of void spectrums in that it is a smooth, slowly oscillating curve. On the other hand, the solder/Lucite combination, shown in Figure 7b, has a backscatter spectrum with considerable structure. The BEM is able to capture this structure with the same 40 element mesh. Initially, we expected that the surface solution was likewise more intricate and/or resolving this fine detail might require significantly better accuracy in the boundary solution. Apparently, this is not the case as the errors are roughly the same for both material combinations. The errors at $k_L a$ equal to 3.1 and 4.4 in Figure 7a are due, at least in part, to the FED which will be discussed in detail in the next section.

A comparison with the T-matrix method[5] is shown in Figure 8 for a prolate spheroid. The mode converted (L-T) scattering amplitudes are given for incidence along the polar axis of a tungsten carbide inclusion in a titanium alloy host. The results agree quite well except for the discrepancy at $k_L a$ equal to 3.6 which is also FED induced error. Other comparisons with T-matrix and experiment for inclusions are given in Reference 15.

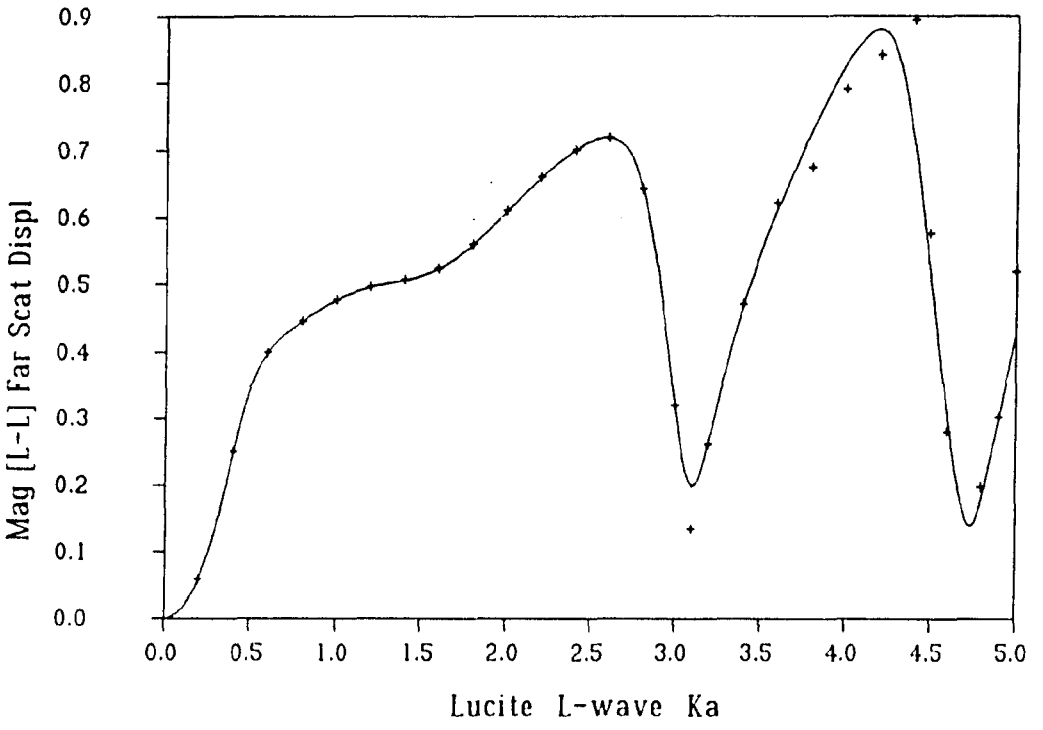

Figure 7a Comparison of BEM results (+) from a 40 element model with analytical solution (—) for frequency dependence of backscatter from a spherical inclusion: Titanium in Lucite

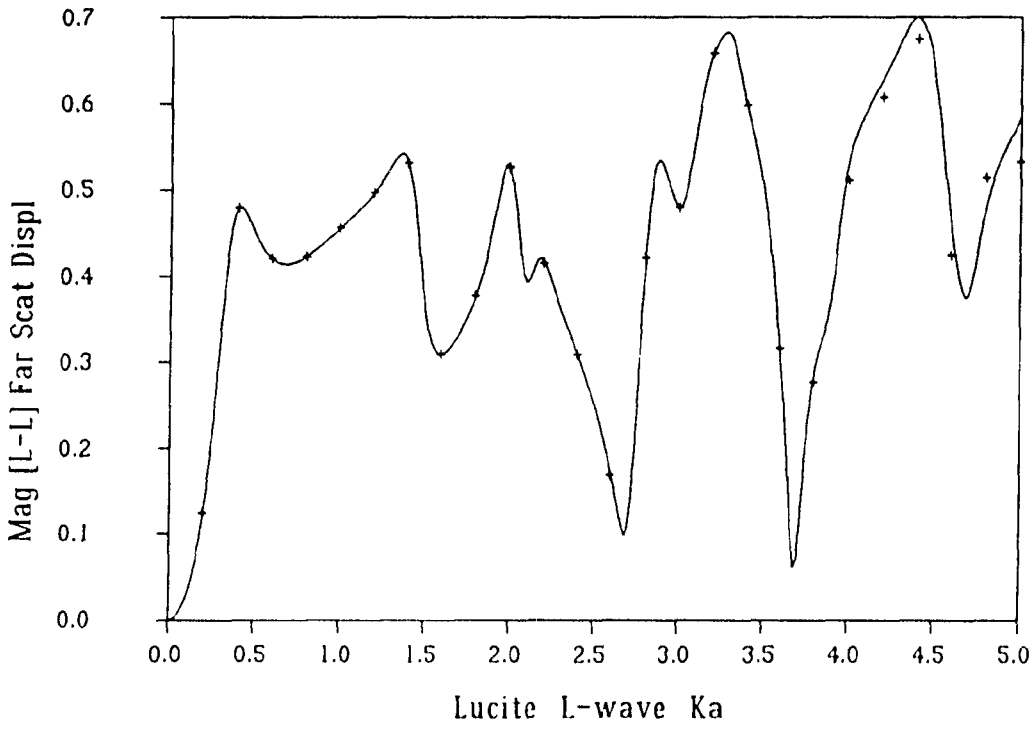

Figure 7b Comparison of BEM results (+) from a 40 element model with analytical solution (——) for frequency dependence of backscatter from a spherical inclusion: Solder in Lucite

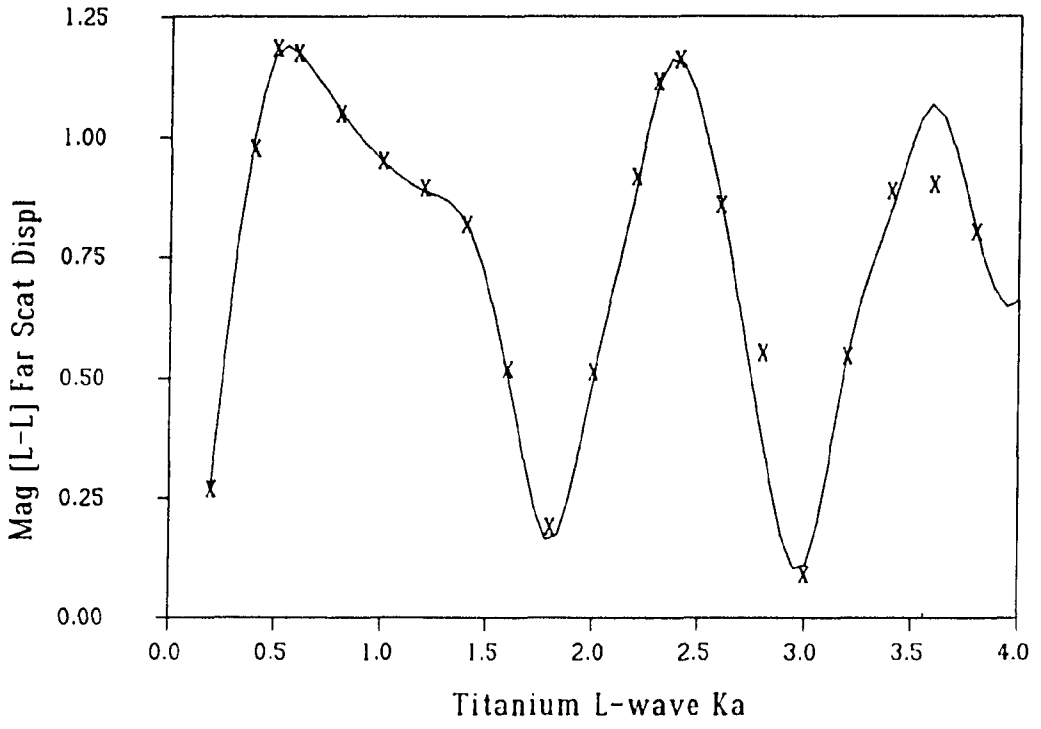

Figure 8 Comparison of BEM results (——) with T-matrix results (X): 90° scatter due to prolate (1:1:2) spheroidal inclusion of tungsten carbide in titanium with incidence along polar axis

In Figure 9 we give an example of an inclusion which requires a full 3D capability such as the one presented here. The scatterer is an ellipsoid with an axis length ratio of 3:2:1 where the longest dimension is a and the shortest is c. Material properties for the host and inclusion are given in Table I as material A and material B, respectively. Mode converted L-T scattering amplitudes are given for an incident field with $k_L a$ equal to three, propagating along the $+X_3$ axis. These graphs correspond to signal amplitudes which would be measured by a T-wave transducer in an NDE experiment, as a function of polar and azimuthal angles, when aligned with $\hat{\mathbf{e}}_\theta$ or $\hat{\mathbf{e}}_\phi$. Phase information can also be generated. The azimuthal motion component shown in Figure 9(a) is small compared to the $\hat{\mathbf{e}}_\theta$ oriented motion of 9(b) since the ellipsoid is not radically nonaxisymmetric. Nevertheless, the particle motion of the T-wave scattered field is elliptical, except along symmetry planes. To characterize the entire far scattered field of a 3D inhomogeneity for all angles of incidence would require a large dataset, as evidenced by this single incident field (and a symmetric one no less) result which is based on 740 different "A_{L-T}"s. This illustration substantiates our philosophy of storing decomposed matrices, from which needed computations can be done quickly, rather than large catalogs of scattering amplitudes.

Fictitious Eigenfrequency Difficulty

One fundamental problem with boundary integral equation formulations of external elastodynamic problems is the so-called "fictitious eigenfrequency difficulty". At certain frequencies, the solution to the BIE as we have it formulated becomes nonunique. The matrix which we generate becomes ill-conditioned at frequencies near these irregular frequencies. The physical significance of these frequencies has not been completely understood until recently. Martin[33] has proven mathematically that the only frequencies at which this ill-conditioning may occur are the eigenfrequencies of the

inhomogeneity's domain comprised of the host material with fixed boundary conditions (cf. Refs. 22, 26, and 34). The nature of the scatterer, whether a void, rigid, or elastic inclusion, does not influence these fictitious eigenfrequencies.

In order to numerically substantiate this theory and to more fully understand its implications for numerical computation, we have determined the condition number of matrices as a function of frequency for each of our problem classes. In Figure 10a the results for a spherical void in host material with Poisson's ratio of 1/4 are shown. Values of eigenfrequencies for an elastic sphere with Dirichlet[35] and Neumann[36] boundary conditions are marked. Clearly, the fixed boundary conditions are the troublesome species just as predicted. In Figure 10b, results for the BIE with zero displacements rather than zero tractions are shown. Still the interior sphere's eigenfrequencies for Dirichlet B.C.s create the problem.

The elevated condition number occurs over a very narrow range of frequencies. To define how narrow these peaks really are, condition numbers for frequencies just slightly above and below (on the order of $\pm 0.3\%$) the expected peak were computed and used in plotting Figures 10-12, the later to be discussed subsequently. It was anticipated that the fictitious eigenfrequencies of a *discretized* sphere might be altered from those of the analytical computation. With the 40 element model used for all these fictitious eigenfrequency computations, there is only one indication of this occurring. In Figures 10a, 10b, and 12 the condition number for the expected peak at $k_T \alpha$ of 7.29284 was less than the condition number computed at a $k_T \alpha$ of 7.27548. Any shifting that is occurring is still very slight at most.

As one would expect, the height and narrowness of these peaks is increased with a finer mesh. We have also found that a fine mesh may indicate an ill-conditioned state which a coarse mesh run at the same frequencies does not distinguish from the nominal

condition number level. This is not to say that a finer mesh produces erroneous results when a coarser mesh does not. To the contrary, using a mesh beyond the frequency at which it can adequately interpolate the field at the boundary produces significantly less accurate scattering amplitudes near a fictitious eigenfrequency than does using a finer mesh. For example, the 140 element results are much more accurate for the previously indicated FED points in Figure 4a. The condition number is only a measure of the potential loss of accuracy, but the largest errors occur when a matrix based on inadequate interpolation becomes ill-conditioned.

The actual peak values of condition number for a given mesh are not completely understood, but appear related to the ability of the mesh to spatially resolve the eigenmode. We have found that fictitious eigenfrequencies of higher harmonics[35] have lower peaks and/or require finer meshes to detect them. Higher harmonics have more intricate mode shapes at the surface and hence require a finer mesh to capture them properly. (Note that by "mode shape" for a fixed displacement problem, we mean the distribution of traction). Interestingly enough, the previously mentioned short peak (with the noticeable frequency shift in Figures 10a, 10b, and 12) is for a third harmonic, the highest harmonic which occurs in the given frequency band. For a given harmonic, all modes create similar levels of ill-conditioning since only the radial dependence of the field becomes more intricate with increasing mode number[36].

Figure 11 is an example of this analysis for a transmission problem. The host medium now has a Poisson's ratio of 1/3 and the inclusion's is 1/4. The longitudinal wavespeed of material B, the inclusion, was defined to be 3/4ths of that of material A in order to separate the different eigenfrequencies as much as possible. The density of the inclusion was set arbitrarily at 16 times that of the host so as to create a strong scatterer.

Again the results agree with Martin's theorem. When the host and inclusion materials were interchanged, the peak locations shown in Figures 10a and 10b reappeared but the "background" condition number values were much lower than in Figure 11.

Lastly, we looked at two spherical voids together - one with a equal to 1 and the other with a radius of 0.6. The smaller sphere's eigenfrequencies are shifted upward such that only the lowest two peaks remain in the displayed range. From the previous discussion on the makeup of a compound matrix for two scatterers, we expect the self-influence sub-matrices to exhibit the FED if taken individually. Initially it was not clear what effect the cross-influence portions of the complete matrix would have. From the results shown in Figure 12, it appears that the FED for multiple scatterers occurs at the union of the set of FEDs for all scatterers taken individually.

In general, we found ill-conditioning occurring whenever nonuniqueness of the BIE was indicated. In addition to the previously noted examples of the FED causing solution inaccuracies, we also show subtle evidence of its effect in Figure 3b at $k_L a$ equal to 2.2 and 3.0. There are remedies for this problem such as BIFILM[22,26] and combining Equation (1) with the hypersingular gradient equation[34]. Understanding the FED and its influence on subsequent numerical methods is crucial in overcoming the problem.

Concluding Remarks

The BEM has a number of significant advantages for elastic wave scattering calculations in 3D. First, it rigorously treats the infinite nature of the host medium while remaining algebraically manageable to program in 3D, unlike methods which are based on exterior wave functions. Second, the reduction in dimension of the problem makes general 3D problems tractable with current computers. Third, the form of the matrix equations allows simulations to be quickly executed from a library of previously formed

and decomposed matrices. Finally, the commonalty of element definitions between finite elements and boundary elements allows for the use of commercial CAE software in the creation and evaluation of meshes.

A variety of benchmark solutions were provided which demonstrate suitable accuracy with reasonable mesh requirements. For example, the entire BEM solution provided in Figure 3a requires 67 seconds on an Apollo DN10000 workstation. The 140 element "crack" models used for Figures 5 and 6 were the most time consuming at 22 to 28 minutes per frequency. If solutions for additional incident fields are needed, they can be obtained from an existing matrix in approximately 5 seconds each for these largest models and in a fraction of a second with a 40 element model.

Acknowledgement

This work was sponsored by the Center for NDE at Iowa State University and was performed at the Ames Laboratory which is operated by Iowa State for the USDOE. It was also partially supported by the Solid Mechanics Program of the Office of Naval Research with Dr. Y. Rajapakse as the program officer. We also acknowledge the many developers of the core BEM code from the University of Kentucky. Special thanks are due Paul Martin, of the University of Manchester, England, for valuable conversations on the fictitious eigenfrequency difficulty.

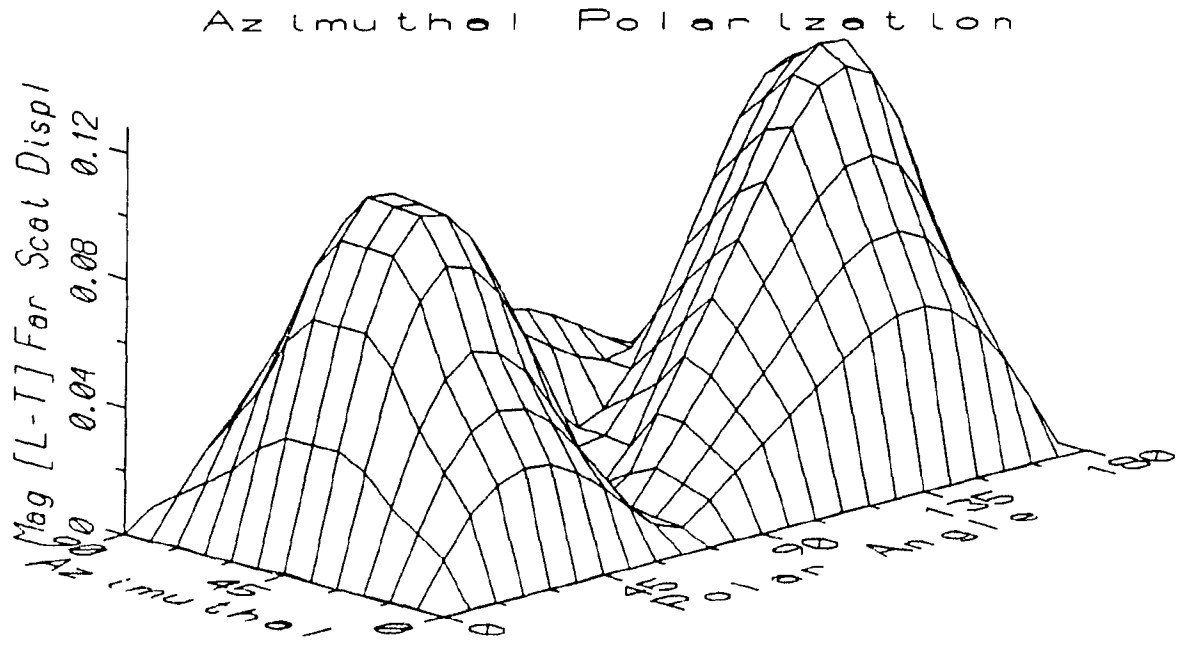

Figure 9a Mode converted scattering from ellipsoidal (3:2:1) inclusion of material B in material A at $k_L a = 3$. Incident field is propagating parallel to the $+X_3$ axis. Scattered field components polarized parallel to $\hat{e}_\phi$

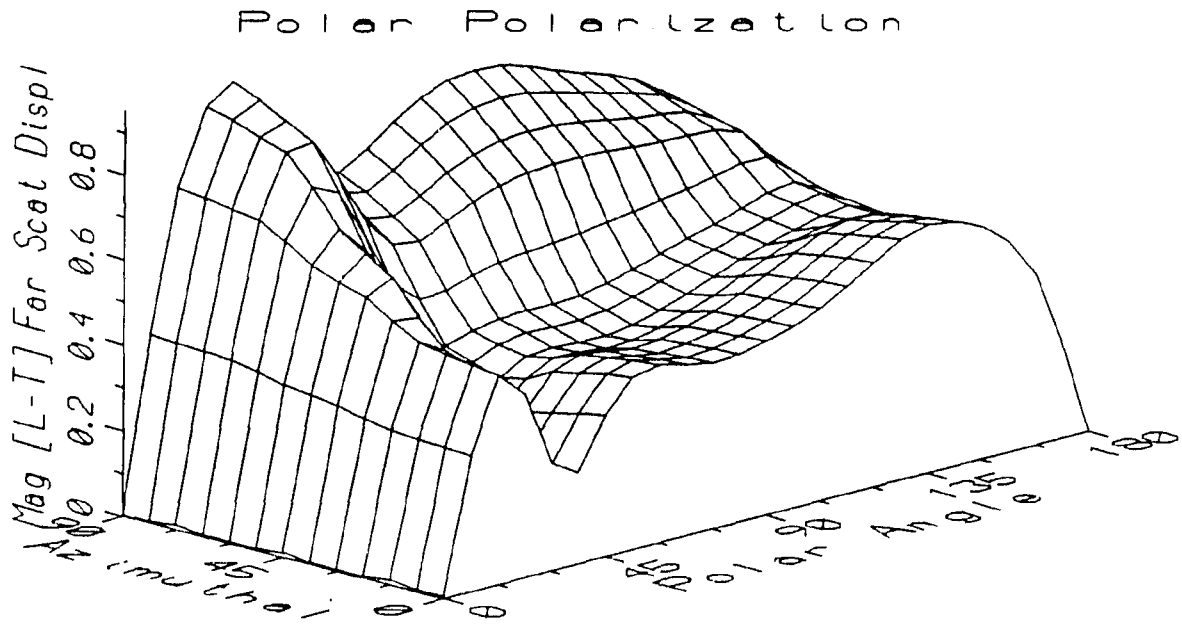

Figure 9b Mode converted scattering from ellipsoidal (3:2:1) inclusion of material B in material A at $k_L a = 3$. Incident field is propagating parallel to the $+X_3$ axis. Scattered field components polarized parallel to $\hat{e}_\theta$

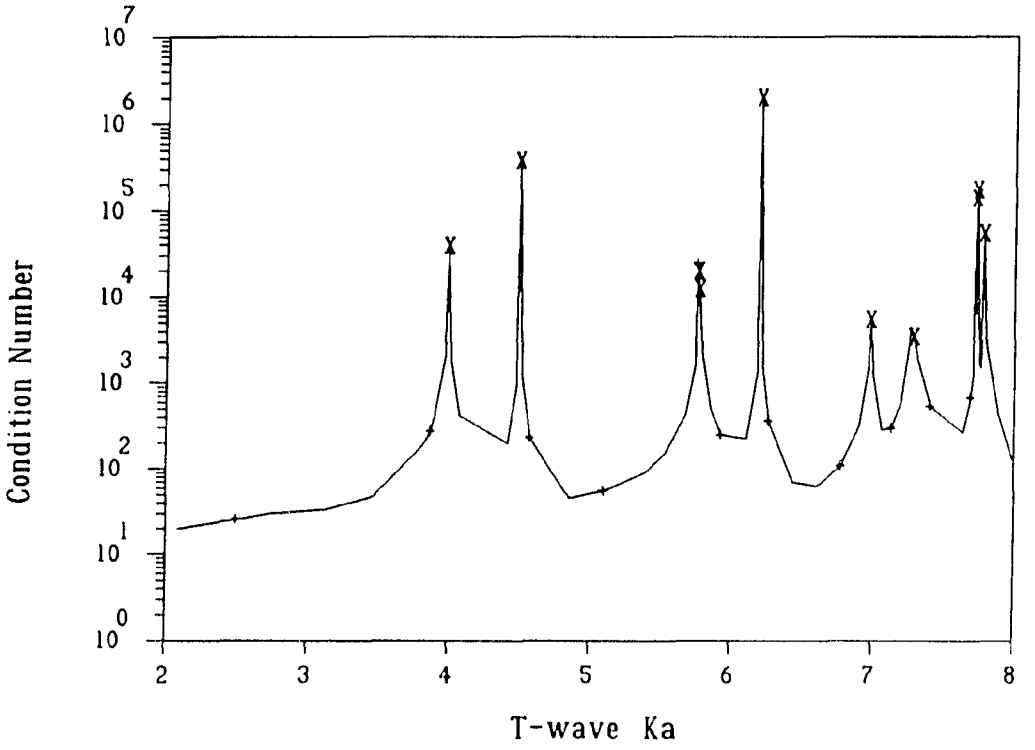

Figure 10a Relationship of matrix condition number and eigenfrequencies for elastic spheres: Void in material B

[+ eigenfrequency of host material with free B.C.]

[X eigenfrequency of host material with fixed B.C.]

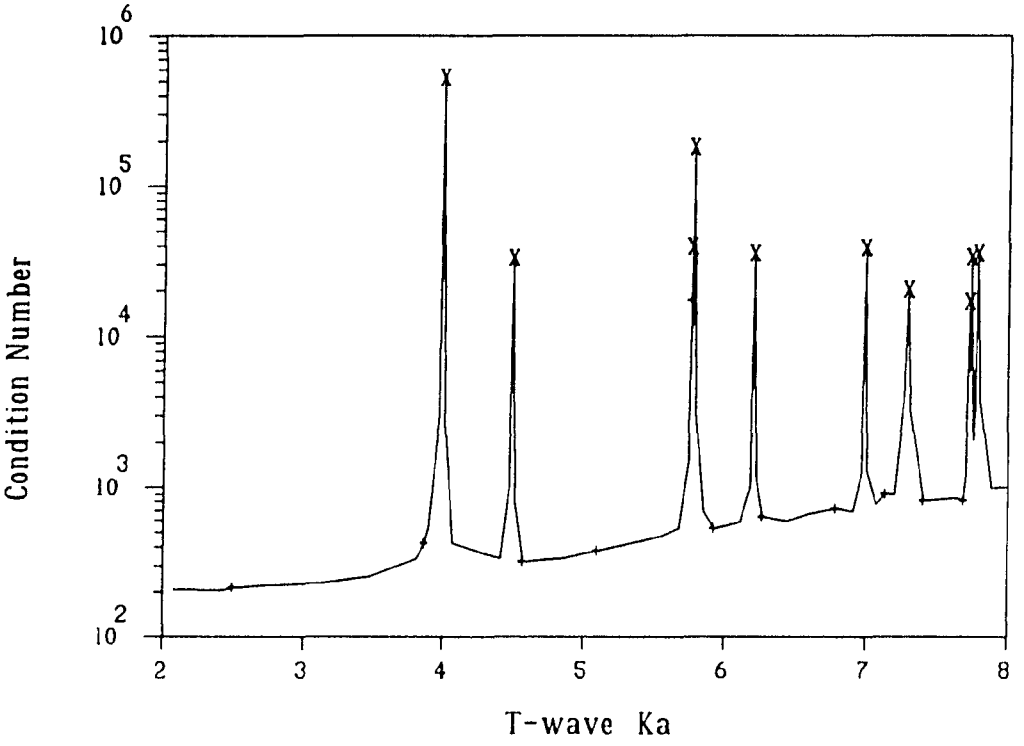

Figure 10b Relationship of matrix condition number and eigenfrequencies for elastic spheres: Rigid inclusion in material B

[+ eigenfrequency of host material with free B.C.]

[X eigenfrequency of host material with fixed B.C.]

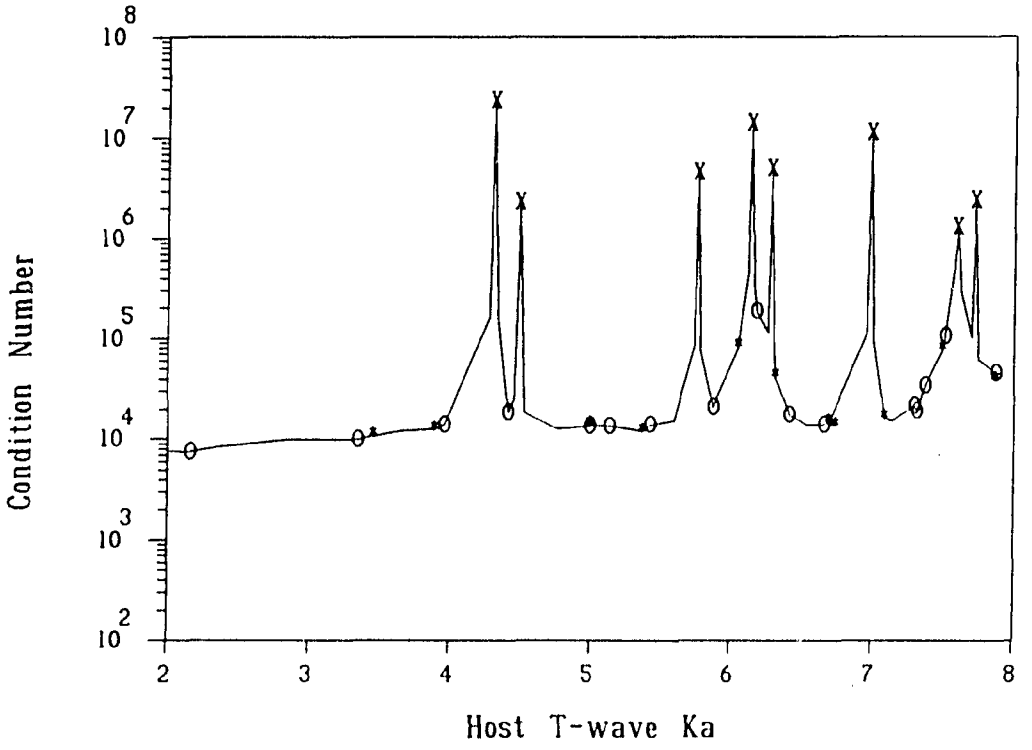

Figure 11 Relationship of matrix condition number for elastic inclusion of material B in material A and eigenfrequencies for elastic spheres -
[X eigenfrequency of host material with fixed B.C.]
[0 eigenfrequency of inclusion material with free B.C.]
[* eigenfrequency of inclusion material with fixed B.C.]

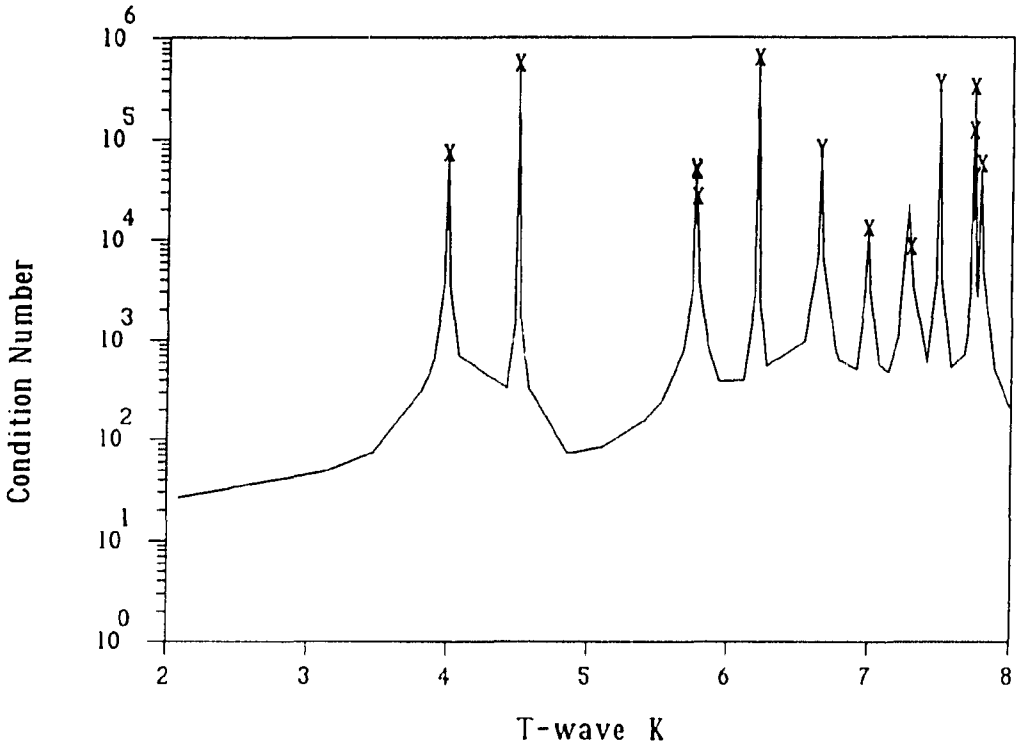

Figure 12 Relationship of matrix condition number for two spherical voids in material B and eigenfrequencies for elastic spheres -
[X eigenfrequency of host material with fixed B.C. and α = 1]
[Y eigenfrequency of host material with fixed B.C. and α = 0.6]

References

1. R. B. Thompson and H. N. G. Wadley, 'The use of elastic wave-material structure interaction theories in NDE modeling', *CRC Crit. Rev. Solid State* **16**(1), 37-89 (1989).
2. C. F. Ying and R. Truell, 'Scattering of a plane longitudinal wave by a spherical obstacle in an isotropically elastic solid', *J. Appl. Phys.* **27**(9), 1086-1097 (1956).
3. Y-H Pao and C. C. Mow, 'Scattering of plane compressional waves by a spherical obstacle', *J. Appl. Phys.* **34**(3), 493-499 (1963).
4. P. C. Waterman, 'Matrix theory of elastic wave scattering', *J. Acoust. Soc. Am.* **60**(3), 567-580 (1976).
5. V. K. Varadan and V. V. Varadan, 'Scattering matrix for elastic waves. III. Application to spheroids', *J. Acoust. Soc. Am.* **65**(4), 896-905 (1979).
6. A. Boström, 'Scattering by a smooth elastic obstacle', *J. Acoust. Soc. Am.* **67**(6), 1904-1913 (1980).
7. W. M. Visscher, 'A new way to calculate scattering of acoustic and elastic waves II. Application to elastic waves scattered from voids and fixed rigid obstacles', *J. Appl. Phys.* **51**(2), 835-845 (1980).
8. J. L. Opsal and W. M. Visscher, 'Theory of elastic wave scattering: Application of the method of optimal truncation', *J. Appl. Phys.* **58**(3), 1102-1115 (1985).
9. J. E. Gubernatis, E. Domany, J. A. Krumhansl, and M. Huberman, 'The Born approximation in the theory of the scattering of elastic waves by flaws', *J. Appl. Phys.* **48**(7), 2812-2819 (1977).
10. J. D. Achenbach, A. K. Gautesen, and H. McMaken, *Ray Methods for Waves in Elastic Solids with Applications to Scattering by Cracks* (Pitman, Boston, 1982).
11. J. E. Gubernatis and E. Domany, 'Rayleigh scattering of elastic waves from cracks', *J. Appl. Phys.* **50**(2), 818-824 (1979).
12. G. Dassios and K. Kiriaki, 'The ellipsoidal cavity in the presence of a low-frequency elastic wave', *Quart. Appl. Math.* **44**(4), 709-735 (1987).
13. L. J. Bond, 'Numerical techniques and their use to study wave propagation and scattering - a review', in *Proceedings of the IUTAM Symposium on Elastic Wave Propagation and Ultrasonic Nondestructive Evaluation* (Elsevier, Amsterdam, 1990).

14. J. N. Gray, T. A. Gray, N. Nakagawa, and R. B. Thompson, 'Models for predicting NDE reliability', *Metals Handbook* (ASM, Materials Park, Ohio, 1989), Vol. 17, 9th Ed.
15. P. J. Schafbuch, R. B. Thompson, and F. J. Rizzo, 'Application of the boundary element method to elastic wave scattering by irregular defects', to appear, *J. Nondestr. Eval.* **9**(2-3), (1990).
16. J. A. G. Temple, 'Modeling the propagation and scattering of elastic waves in inhomogeneous anisotropic media', *J. Phys. D: Appl. Phys.* **21**, 859-874 (1988).
17. R. Clayton and B. Engquist, 'Absorbing boundary conditions for acoustic and elastic wave equations', *Bull. Seism. Soc. Am.* **67**(6), 1529-1540 (1977).
18. E. Kausel and J. M. Roësset, 'Semianalytical hyperelement for layered strata', *J. Eng. Mech. Div. ASCE* **103**, 569-588 (1977).
19. D. B. Goetschel, S. B. Dong, and R. Muki, 'A global local finite element analysis of axisymmetric scattering of elastic waves', *J. Appl. Mech. Trans. ASME* **49**(4), 816-820 (1982).
20. D. Givoli and J. B. Keller, 'A finite element method for large domains', *Comput. Methods Appl. Mech. Engrg.* **76**(1), 41-66 (1989).
21. P. K. Banerjee, S. Ahmad, and G. D. Manolis, 'Transient elastodynamic analysis of three-dimensional problems by boundary element method', *Earthquake Eng. Struct. Dyn.* **14**(6), 933-949 (1986).
22. M. Rezayat, F. J. Rizzo, and D. J. Shippy, 'On time-harmonic elastic-wave analysis by the boundary element method for moderate to high frequencies', *Comput. Methods Appl. Mech. Engrg.* **55**(3), 349-367 (1986).
23. D. A. Anderson, J. C. Tannehill, and R. H. Pletcher, *Computational Fluid Mechanics and Heat Transfer* (Hemisphere, New York, 1984).
24. Y-H Pao and V. Varatharajulu, 'Huygens' principle, radiation conditions and integral formulae for the scattering of elastic waves", Dept. of Theoretical and Applied Mechanics, Cornell University (July 1975).
25. F. J. Rizzo, D. J. Shippy, and M. Rezayat, 'A boundary integral equation method for radiation and scattering of elastic waves in three dimensions', *Int. J. Numer. Methods Eng.* **21**(1), 115-129 (1985).

26. I. R. Gonsalves, D. J. Shippy, and F. J. Rizzo, 'The direct boundary integral equation method for the three-dimensional elastodynamic transmission problem', to appear, *Computers Math. Applic.*
27. J. M. Stone, *Radiation and Optics* (McGraw-Hill, New York, 1963), Ch. 2.
28. J. E. Gubernatis, E. Domany, and J. A. Krumhansl, 'Formal aspects of the theory of the scattering of ultrasound by flaws in elastic materials', *J. Appl. Phys.* **48**(7), 2804-2811 (1977).
29. P. J. Schafbuch, R. B. Thompson, F. J. Rizzo, and T. J. Rudolphi, 'Elastic wave scattering by arbitrarily shaped voids', in *Review of Progress in QNDE*, edited by D. O. Thompson and D. E. Chimenti (Plenum Press, New York, 1989), Vol. 8A, pp.15-22.
30. A. K. Mal, 'Interaction of elastic waves with a Griffith crack', *Int. J. Eng. Sci.* **8**(9), 763-776 (1970).
31. D. E. Budreck and J. D. Achenbach, 'Scattering from three-dimensional planar cracks by the boundary integral equation method', *J. Appl. Mech. Trans. ASME* **55**(2), 405-412 (1988).
32. G. Krishnasamy, L. W. Schmerr, T. J. Rudolphi, and F. J. Rizzo, 'Hypersingular boundary integral equations: Some applications in acoustic and elastic wave scattering', *J. Appl. Mech. Trans. ASME* **57**(2), 404-414 (1990).
33. P. A. Martin, 'Identification of irregular frequencies in simple direct integral-equation methods for scattering by homogeneous inclusions', to appear, *Wave Motion* (1991).
34. D. S. Jones, 'Boundary integrals in elastodynamics', *IMA J. Appl. Math.* **34**(1), 83-97 (1985).
35. P. J. Schafbuch, F. J. Rizzo, and R. B. Thompson, 'Eigenfrequencies of an elastic sphere with fixed boundary conditions', to appear, *J. Appl. Mech. Trans. ASME.*
36. A. C. Eringen and E. S. Suhubi, *Elastodynamics* (Academic Press, New York, 1975), Vol. II.

PART IV.

ELASTIC SCATTERER INTERACTION VIA GENERALIZED BORN SERIES AND FARFIELD APPROXIMATIONS

Abstract

Methods for solving elastic wave scattering problems in 3D with multiple inhomogeneities are discussed. The problem of homogeneous, isotropic elastic defects in an otherwise homogeneous, isotropic elastic full-space is formulated as a boundary integral equation. This equation is solved by discretizing the surface of each scatterer in a fashion known as the boundary element method. The resulting matrix equation may be solved in a fully implicit manner just as with single scatterer problems. A more efficient hybrid, implicit-iterative, method is interpreted as expanding a portion of the nonsingular integral operator in a Neumann series. A physical correspondence of the hybrid method to Nth order Born approximations of the scatterers' interaction is discussed. The relative advantage of this hybrid scheme depends on the number of iterations required. Except for closely situated voids, terms higher than the first few orders are not significant and thus the method can be quite advantageous. Still, convergence is not always achieved when the flaws are very close and the fully implicit method is then required. When the separation is larger (and in some instances even when it is not), an approximate method which ignores the evanescent portion of the near scattered field and further neglects the curvature of the spherically spreading scattered waves is quite appropriate. Results from the converged, implicit-iterative approach are compared with this farfield approximation of the interaction for many situations

involving spherical, spheroidal, and ellipsoidal voids - even in nonsymmetrical arrangements. The validity of this approximation, which can analytically express multiple reflections in terms of scattering amplitudes, is explored in the near field.

Introduction

The problem of scatterer interaction appears in acoustic, elastic, and electromagnetic contexts. Our focus here is on elastic wave scattering. Determining elastic wave scattering by a single, isolated inhomogeneity in an otherwise homogeneous, isotropic host medium is by itself a formidable problem. However, material inhomogeneities can and do occur in clusters. In the ultrasonic nondestructive evaluation (NDE) context, from which we derive our motivation, these clusters can be porosity in metal castings or disbonds in composite materials, etc. Our approach to this class of problems is based on deterministic knowledge of each individual scatterer. Much of the early work on this topic[1-3] has relied on the T-matrix method and addressed problems involving pairs of spheres and spheroids. More recently, results based on the boundary element method (BEM) have appeared for a periodic array of cracks[4], two cracks at various orientations[5], and a crack/cavity combination[6]. Another related class of problems deals with discrete random media which has many scatterers and only statistical knowledge of size, shape, orientation, etc., is available[7]. In this paper we present our results for two interacting voids based on methods which are formulated more generally in terms of two elastic scatterers. These methods are extendable to the "few" body problem and the results have implications for the many bodied (random media) problem.

This work is different from previously cited efforts in that it is based on a *three dimensional* BEM implementation of the governing time-harmonic form of the direct boundary integral equation (BIE). A 3D formulation can handle any arbitrarily shaped,

finite scatterer and thus provides the most generality. BIE formulations inherently treat the infinite nature of the host medium rigorously, just as the axisymmetric T-matrix methods do. The underlying 3D BEM for solitary scatterers was recently developed and used for ultrasonic NDE problems by the current authors[8,9].

Solving multiple scatterer problems is possible by a straightforward interpretation of the procedure for a single isolated scatterer. However, a much more efficient procedure is possible for many situations of importance to NDE. Schuster[10] presented a hybrid method for multiple acoustic scattering which deals with the interaction between the scatterers in an iterative fashion and each scatterer's self-interaction by a fully implicit approach. Schuster's method should not be confused with methods which attempt to solve for an individual scatterer's self-interaction iteratively. Iterative methods for solitary scatterers include those based on the standard Born approximation, which is known to fail with void inhomogeneities for most intermediate frequency situations[11]. Iterative methods for solving a single scatterer's BIE generated matrix equation[12] are also fundamentally different from Schuster's approach.

In this paper, Schuster's hybrid method is generalized to the elastic wave case. Theoretical insight is given into why iterative solutions can work easily for cross-interaction but have difficulty with self-interaction. This efficient hybrid means for solving multiple scattering problems is used to generate and investigate the accuracy of truncated Born series solutions for cross-interaction and to understand the physics of multiple scattering including interference and resonance. The limits of applicability of some very simple multiple scattering approximations are investigated and found to be good over a large parameter space.

Solitary Scattering Procedures

A numerical approach is required to determine scattering from solitary defects of arbitrary shape even when both the defect and host materials are homogeneous and isotropic. The details of the BIE formulation and its numerical implementation are reviewed here only to a sufficient level to allow understanding of the extension to multiple scattering. For more background, see References 13 through 15.

Boundary integral equation

When the linear differential operator governing elastic wave propagation is written in time-harmonic form, it has an elliptical nature and a generalized form of Green's reciprocal identity can be readily applied to it. If one of the identity's operands is chosen to be the fundamental solution (free-space Green's function), an integral equation can be derived when the field point, p, of that Green's function is taken to the boundary. When no body forces are present, the resulting boundary integral equation (BIE) involves a surface integral only (in 3D) - thus the dimensionality of the problem is reduced. By writing the BIE for the incident field in the domain of the scatterer as if it were made of the host material and again for the scattered field in the complementary domain, the Somigliana formula which we use is derived. This formula is

$$\mathbf{C}^T(\mathbf{p})\mathbf{u}(\mathbf{p},\omega) = \int_S [\mathbf{U}^T(\mathbf{p},\mathbf{q},\omega)\mathbf{t}(\mathbf{q},\omega) - \mathbf{T}^T(\mathbf{p},\mathbf{q},\omega)\mathbf{u}(\mathbf{q},\omega)]dS(\mathbf{q}) + \mathbf{u}^I(\mathbf{p},\omega) \qquad (1)$$

where q is a point of the inhomogeneity boundary S. The displacement vector u and traction vector t are complex due to the time-harmonic formulation. An $e^{-i\omega t}$ time dependence is implied. The U tensor represents the fundamental solution and T is related to its normal (to S) derivative through Hooke's law. The functional form of these

tensors in given in Reference 13. They are singular when the field point $\mathbf{p}$ is at $\mathbf{q}$ and the integral involving $\mathbf{T}^T$ exists only in the sense of the Cauchy principal value (CPV). The $\mathbf{C}$ tensor depends on the topology of S at p, i.e., if $\mathbf{p}$ is on a side, edge, or corner[13]. Superscript I on $\mathbf{u}$ denotes the incident field, while no superscript implies the total field. Equation (1) is used to find the unknown total field quantities at the surface from specified boundary conditions and the incident field.

In general, a boundary surface may contain regions of Dirichlet, Neumann, and Robin (mixed) boundary conditions. But for scattering the entire boundary usually only has one type. For a void, tractions are all specified as zero and the displacements are unknown. For an elastic inclusion, the BIE is written again for the total field in the inhomogeneity. This time there is no explicit incident field term as in Equation (1). The incident field's effect is passed through the boundary. When the displacements and tractions are matched up at the boundary, a pair of coupled BIEs which define the so-called transmission problem results[15].

Boundary element method

With the boundary element method the surface integrals in the BIE are computed by dividing S into sections (i.e., elements). Three and four sided elements with curved edges are used and each element is defined by either six or eight nodes, respectively. The location of the nodes is defined in three-space and the value of the field at those locations are the discrete values being solved for. Over each element, both the geometry (the curvature of the element face) and the field values are interpolated with quadratic shape functions in each direction. The integral over each element is approximated by Gauss quadrature in terms of the nodal field values. The number of Gauss quadrature points per element is adjusted as needed. Details of these procedures are given in Reference 14.

Collocating the discretized BIE(s) at each node results in a set of simultaneous linear algebraic equations. For a void and elastic inclusion, respectively, the matrix equations have the form:

$$\{\mathbf{u}\} = [\mathbf{H}_{ext}]^{-1}\{\mathbf{u}^I\} \tag{2a}$$

$$\begin{Bmatrix}\mathbf{u}\\ \mathbf{t}\end{Bmatrix} = \begin{bmatrix}\mathbf{H}_{ext} & \mathbf{G}_{ext}\\ \mathbf{H}_{int} & \mathbf{G}_{int}\end{bmatrix}^{-1}\begin{Bmatrix}\mathbf{u}^I\\ \mathbf{0}\end{Bmatrix}. \tag{2b}$$

The complex coefficients which comprise the matrices G and H are functions of frequency, material properties, and the inhomogeneity geometry. The subscripts refer to the BIEs for the internal or external domain, respectively. The G matrix comes from integration of the fundamental solution kernel, U^T, whereas the H matrix is from the gradient kernel, T^T, and both are fully populated. The formal inverses are not computed as such but represent a decomposed matrix from which boundary solutions may be obtained for various incident fields via the forward elimination and backward substitution processes[16].

Incident and scattered fields

The incident field displacements must be specified at the BEM nodes. For an incident plane longitudinal (L) wave, these displacements are given by

$$\mathbf{u}^I(\mathbf{p}) = I_a \frac{\mathbf{k}}{|\mathbf{k}|} e^{i\mathbf{k}\cdot\mathbf{p}} \tag{3}$$

with the implied harmonic time dependence. p is the coordinate vector of the node, k is

the wave number vector, and I_a is the amplitude. Incident fields can also be due to transverse (T) waves or can even be nonplanar[9] but all the examples in this paper are for planar L-waves.

A form of Equation (1) can be used to determine the scattered field from the BIE boundary solution. Using superscript S to denote the scattered field and employing the field decomposition rule,

$$\mathbf{u}^S(\mathbf{p}) = \mathbf{u}(\mathbf{p}) - \mathbf{u}^I(\mathbf{p}) = \int_S [\mathbf{U}^T(\mathbf{p},\mathbf{q})\mathbf{t}(\mathbf{q}) - \mathbf{T}^T(\mathbf{p},\mathbf{q})\mathbf{u}(\mathbf{q})]dS(\mathbf{q}). \quad (4)$$

This formula, known as the interior representation integral, is written for the exterior domain and the field point **p** now denotes any point in the host medium and not on the boundary.

One particularly convenient and commonly used measure of the scattered field is known as the scattering amplitude, A. By definition,

$$\lim_{r\to\infty} \frac{\mathbf{u}^S \cdot \hat{d}^S}{I_a} = \frac{A(\theta^I, \phi^I, \hat{d}^I, \theta^S, \phi^S, \hat{d}^S)}{r} e^{ik_m r} \quad (5)$$

where r is the distance from the apparent center of the spherically spreading wave. k_m is the wave number of the scattered wave mode being considered and $\hat{d}^S$ is its polarization (i.e., direction of particle motion). A is a function of scatterer shape and properties, host properties, and incident and scattered directions (θ, ϕ). Physically A defines the magnitude and relative phase of the spherically spreading wave generated in the farfield of a scatterer due to an incident plane wave. "A"s are defined for all combinations of incident and scattered wave types (L-L, L-T, T-L, and T-T).

Another convenient quantity which will be used extensively in this paper is the total scattering cross section, σ. It relates the total power in the scattered field (summed over all modes) to the power flux in the incident field. A conservation of energy argument then relates the total cross section to the power removed from the incident field (the forward scattering amplitude)[17]. Utilizing our nomenclature and conventions,

$$\sigma = \frac{4\pi a^2}{k_L a} \mathrm{Im}[A(\theta^I = \theta^S, \phi^I = \phi^S, \hat{d}^I = \hat{d}^S)]. \tag{6}$$

Multiple Scattering Procedures

Up until this point we have presented our method as though the inhomogeneity from which the scattering occurs is defined mathematically by one connected domain. However the same governing BIE can be derived for multiple scatterers. In fact, the scattering from multiple defects can be calculated by the methods described thus far, if the domain of the integral in Equations (1) and (4) is taken to be the surface of all the scatterers. In terms of computer implementation, only the node and element definitions of the second (and so on) surfaces must be modified to lie in sequence and at the appropriate position. The complete set of equations for all the scatterers is then solved via a single LU decomposition process. This approach is termed the fully implicit method.

Schuster[10] explains his hybrid approach in terms of operators and matrices and refers to it as a generalized Born series. We shall first explain his concept in terms of classical integral equation theory because we find additional meaning in this interpretation. Then the mathematical framework is given physical significance and finally the numerical implementation is explained in terms of the solitary scatterer

procedures.

Neumann series

We wish to express the generalized Born series concept for elastodynamics as a vector BIE. By manipulating a standard model integral equation, formulas are derived which can be generalized to the desired 3D, vector form. The standard Fredholm integral equation of the second kind has the form:

$$y(x) = f(x) + \lambda \int_{\xi 1}^{\xi 2} K(x,\xi) y(\xi) d\xi \qquad (7)$$

where y is the independent variable, K is a two point kernel function, and x represents the domain coordinate(s). Under certain circumstances regarding the characteristic number λ, Equation (7) may be solved iteratively[18]. By defining $K_1 = K$, the nth iterated kernel is given by the recurrence relation,

$$K_n(x,\xi) = \int_{\eta 1}^{\eta 2} K(x,\eta) K_{n-1}(\eta,\xi) d\eta. \qquad (8a)$$

Further, the integral operator, $\mathcal{K}$ is defined by

$$\mathcal{K}[g(x)] = \int_{\xi 1}^{\xi 2} K(x,\xi) g(\xi) d\xi \qquad (8b)$$

which can be applied repeatedly to yield

$$\mathcal{K}^n[g(x)] = \int_{\xi 1}^{\xi 2} K_n(x,\xi) g(\xi) d\xi. \qquad (8c)$$

The solution to (7) is then expressible as an infinite sum of successive applications of the integral operator upon the load function f,

$$y(x) = f(x) + \lambda \mathcal{K}[y(x)] = f(x) + \sum_{n=1}^{\infty} \lambda^n \mathcal{K}^n[f(x)]. \qquad (9)$$

Equation (9) is known as the Neumann series solution to the integral equation. For scattering problems the Neumann series is also known as the Born series, since the Nth Born approximation is the Nth partial sum of this series.

Applying this approach to Equation (1) requires making several conceptual steps. Integral equation texts[18-20] often present the domain as an interval and x as only a scalar, but this is only a conceptual simplification and not a necessary restriction. A vector integral equation over a domain such as (1) can be cast equivalently as a scalar integral equation[19] and thus utilize theory developed for scalar equations. The domain may be a finite number of bounded subdomains with no common points, so multiple scatterers are permissible. The imposition of boundary conditions on (1) leaves one independent vector unknown over the domain (or over each subdomain). For voids and elastic inclusions, the form of (1) then appears to be that of (7) except that the kernel functions are singular.

In order to ensure convergence of the Neumann series, some restrictions must be put on the kernel. Various alternative sufficient conditions for uniform convergence are that K must be bounded[18], Riemann integrable[19], or square integrable[20].

In any case, the singular nature of the kernels in our BIE is a problem. The domain of the CPV integral can be divided into two parts - one part containing the field point (where the kernels become singular) and the other part, the remainder of the domain. In the integral operator notation from the model integral equation,

$$\mathcal{K}[g(x)] = \hat{\mathcal{K}}[g(x)] + \underline{\mathcal{K}}[g(x)] \tag{10a}$$

where $\hat{\mathcal{K}}$ denotes the singular integration region. A Neumann series can then be written appropriately for the nonsingular portion, $\underline{\mathcal{K}}$. The integral equation is

$$y = f + \lambda\hat{\mathcal{K}}[y] + \lambda\underline{\mathcal{K}}[y]. \tag{10b}$$

Assume that the solution, y, is known so that the function

$$F = f + \lambda\hat{\mathcal{K}}[y] \tag{11a}$$

is fixed for a given f. Using Equation (9), the Neumann series solution is

$$y = F + \lambda\underline{\mathcal{K}}[y] = F + \sum_{j=1}^{\infty} \lambda^j \underline{\mathcal{K}}^j[F] \tag{11b}$$

which is permissible since $\underline{\mathcal{K}}$ is an integral operator with a bounded kernel. Unlike Equation (9), this series form does not remove the unknown function $y(x)$ as an (implied) argument of the iterated kernel. Equation (11b) in not yet in a form useful for computation.

The practical use of Equation (9) requires the value of y to be estimated by a truncated Nth partial sum of the series. Therefore, consider an Nth partial sum, y_N, of the above series as an estimate of the true solution, y.

$$y_N = F_N + \sum_{j=1}^{N} \lambda^j \underline{\mathcal{K}}^j [F_N] \tag{12a}$$

where F_N is also based on that estimate of y, namely

$$F_N = f + \lambda \hat{\mathcal{K}}[y_N]. \tag{12b}$$

Likewise for the (N-1)th partial sum:

$$y_{N-1} = F_{N-1} + \sum_{j=1}^{N-1} \lambda^j \underline{\mathcal{K}}^j [F_{N-1}] = \sum_{j=0}^{N-1} \lambda^j \underline{\mathcal{K}}^j [F_{N-1}] \tag{13a}$$

by conveniently defining any $\underline{\mathcal{K}}^0$ as the identity operator and

$$F_{N-1} = f + \lambda \hat{\mathcal{K}}[y_{N-1}]. \tag{13b}$$

An operator can be factored out of Equation (12a) so that

$$y_N = F_N + \lambda \underline{\mathcal{K}} \left[\sum_{j=0}^{N-1} \lambda^j \underline{\mathcal{K}}^j [f + \lambda \hat{\mathcal{K}}[y_{N-1} + \Delta y_N]] \right] \tag{14a}$$

where the backward difference, Δy_N, is defined by

$$\Delta y_N = y_N - y_{N-1}. \tag{14b}$$

Finally using Equations (12b), (13a,b), and (14a),

$$y_N = f + \lambda \hat{\mathcal{K}}[y_N] + \lambda \underline{\mathcal{K}}[y_{N-1}] + \lambda \hat{\mathcal{K}}\left[\sum_{j=1}^{N} \lambda^j \underline{\mathcal{K}}^j[\Delta y_N]\right]. \tag{15a}$$

For the uniformly convergent Neumann series $\Delta y_N \to 0$ for large N, so when N is large

$$y_N \sim f + \lambda \hat{\mathcal{K}}[y_N] + \lambda \underline{\mathcal{K}}[y_{N-1}]. \tag{15b}$$

In the next section, the use of Equations (9) and (15b) as solution schemes for the governing BIE (Eqn. 1) is discussed. The formalism expressed by (15b) removes some of the implicit nature of a multiple scattering calculation as compared to a direct application of Equation (1).

Generalized Born series approximation

The Born approximation originated in the context of quantum mechanical scattering theory, but it has been used extensively and successfully in both acoustic and elastic wave scattering. Often, the term *Born approximation* carries the connotation - first Born approximation. From Equation (9), we see the first term in the Neumann series merely replaces the unknown function y under the integral with the inhomogeneous term f. Physically, the total field on the scatterer surface is being estimated by the incident field. This implies that the scattered field must be comparatively weak. Some useful solitary scatterer problems can be solved rather easily by this approximation since it replaces solving the integral equation with performing a

spatial Fourier transform[11]. As might be expected, this approximation works best for weak scatterers (impedance similar to host impedance) - even in some cases for intermediate and high frequency. It will always break down above some frequency, depending on the defect.

For strong solitary scatterers one might expect that including additional terms of the Neumann series would provide a satisfactory approximate solution. However, Reference 21 shows that this series does not always converge. For situations that do converge, adding more terms improves accuracy but the $k_L a$ range which converges is still limited for voids. Kleinman *et al.* have shown recently that the parameter space over which the Neumann (Born) series will converge can be expanded by over-relaxing the equation[22].

As might be deduced from the $\frac{1}{r}$ decay in the strength of the scattered field, the interaction of multiple inhomogeneities is only important if the scatterers are fairly close[2,3]. An approximation for the *interaction* between multiple scatterers which is somewhat analogous to the first Born approximation is to assume that the scatterers do not affect one another. The scattering amplitude or total cross section is merely the complex sum of those values for each solitary scatterer as adjusted by the proper phase according to relative position. This approximation was used in References 2, 3, and 23 and we will refer to it as the first order multiple scattering approximation. Neglecting the interaction is similar to a first order Born approximation because it assumes the incident field at a given scatterer location is much stronger than the field due to scattering from the other inhomogeneities.

For the higher order Neumann series approximations of the interaction, the governing BIE (Eqn. 1) is written in split domain form as was the model integral equation (Eqn. 10b). The complete domain S is separated into two parts - the individual

scatterer in which the collocation point resides, S_p, and the remaining scatterer(s), Ω_p. By comparing the integral over Ω_p with Equation (4), it is evident that the resulting formalism is equivalent to a BIE for the solitary scatterer S_p with a net incident field equal to the global incident field plus the field scattered by the other inhomogeneities. Since the scattered field from the other inhomogeneities is not known until Equation (16) has been solved for them, the previous partial sum ($\mathbf{u}_{N-1}$, $\mathbf{t}_{N-1}$) is used as a basis for an estimate (cf. Eqn. 15b),

$$\mathbf{C}^T\mathbf{u}_N = \oint_{S_p} [\mathbf{U}^T\mathbf{t}_N - \mathbf{T}^T\mathbf{u}_N]dS + \int_{\Omega_p} [\mathbf{U}^T\mathbf{t}_{N-1} - \mathbf{T}^T\mathbf{u}_{N-1}]d\Omega + \mathbf{u}^I. \qquad (16)$$

There is a clear physical interpretation to the boundary solution partial sums. For N equal to one, the scattered field is due to each scatterer acting individually - hence the waves have only been scattered by one object. For N equal two, the once scattered solution is used to determine the net incident field on S_p so the result includes the influence of both once and twice scattered waves. For N equal to three, thrice scattered waves are also included and this argument extends on to higher order N. However, the solution for a single scatterer contains the influence of all *internal* reverberations for the given net incident field. Note that this interpretation is inconsistent in the time domain for small N if the scatterers are close together, because the time for all significant internal effects may then be on the order of the inter-flaw wave transit time.

There are other reasons for dividing the domain in this fashion. Separating out a small zone around the collocation point would, in principle, eliminate the singular nature of the integral operator. However, the influence of the kernels on nearby integration areas is quite strong and the error introduced by omitting the iterated integral of Δy_N for small N in Equation (15b) may cause divergence. In many cases the scatterers are separated by a distance much greater than the characteristic dimension of a single

inhomogeneity. In these instances, such errors are minimized by splitting the domain into each scatterer. Additional advantages will become evident as we examine the matrix equations corresponding to Equation (16) in the next section.

While the Born approximation and the generalized Born series approximation share some underlying mathematics, they are quite different physically.

Hybrid implicit-iterative method

The two scatterer problem is illustrated, but the approach is easy to extend conceptually to additional scatterers. The compound matrix formed by dealing with both scatterers simultaneously can be segregated into the matrices for each one individually and the matrices linking them, as suggested by Equation (16). Using subscripts 1 or 2 to identify the two scatterers,

$$\begin{bmatrix} \begin{bmatrix} H_{ext} & G_{ext} \\ H_{int} & G_{int} \end{bmatrix}_{11} & \begin{matrix} H_{12} & G_{12} \\ 0 & 0 \end{matrix} \\ \begin{matrix} H_{21} & G_{21} \\ 0 & 0 \end{matrix} & \begin{bmatrix} H_{ext} & G_{ext} \\ H_{int} & G_{int} \end{bmatrix}_{22} \end{bmatrix} \begin{Bmatrix} u_1 \\ t_1 \\ u_2 \\ t_2 \end{Bmatrix} = \begin{Bmatrix} u_1^I \\ 0 \\ u_2^I \\ 0 \end{Bmatrix} \qquad (17)$$

where the $[\,]_{ij}$ are the self-influence matrices created by applying Equation (1) to each scatterer. Since the nodes of the first (second) scatterer are in the host domain of the second (first) scatterer, the displacements due to scattering from the other inhomogeneity can be computed from Equation (4). The G_{ij} and H_{ij} are cross-influence matrices relating to tractions and displacements, respectively. Up to 1/4 (for two inclusions) of the entire matrix actually consists of zero coefficients since any equations written for the internal fields of each scatterer are unaffected by the other scatterer. The

matrix equation (17) can be divided into two matrix equations, each of one-half the dimension, that couple through the right hand side (RHS). Since the resulting RHS is a function of the solution, an iterative solution is suggested:

$$\begin{bmatrix} H_{ext} & G_{ext} \\ H_{int} & G_{int} \end{bmatrix}_{ii} \begin{Bmatrix} u_i^{(N+1)} \\ t_i^{(N+1)} \end{Bmatrix} = \begin{Bmatrix} u_i^I - [H_{ij}]\{u_j^{(N)}\} - [G_{ij}]\{t_j^{(N)}\} \\ 0 \end{Bmatrix} \quad (i,j) = (1,2),(2,1). \qquad (18)$$

The first Born approximation for the interaction neglects any coupling so the cross-scattering is assumed zero for the first iteration. The form of Equation (18) is a direct interpretation of the BIE (Eqn. 16).

Of particular interest is the potential for significant computational savings on parameter studies needed by NDE research and application. Sets of linear algebraic equations, such as those represented by Equations (2a), (2b), and (17), are often solved by a factoring process known as LU decomposition[16]. The advantage of this method over standard Gauss elimination occurs when the solution of multiple RHSs is required. Once the decomposition process has been completed, the solution for each case is arrived at by computationally modest, forward and backward substitution processes. Just as a previously decomposed matrix for a single scatterer can be used with different incident fields[8], the *relative* orientations and combinations of any two scatterers can use previously formed and decomposed self-interaction matrices. The cross-interaction matrices must be formed for each relative orientation/position but can be reused with various incident fields. Since the matrices have only been rearranged, the matrix formation process only benefits from using pre-existing matrices but the decomposition process reaps benefits even for a single relative position. To illustrate this, consider two void meshes with the same number of nodes. Decomposing a complex nonsymmetric matrix requires approximately $144n^3$ floating point operations where n is the number of nodes[16]. Therefore, decomposing the compound matrix requires four times as many

operations ($144[2n]^3$) as the two individual self-interaction matrices do together ($2\times144n^3$). On the other hand, the hybrid method solution for each incident field requires an iterative set of forward and backward substitutions, and matrix-vector multiplications. Each iterative step requires approximately $288n^2$ floating point operations[16], which is the same as that required to solve the decomposed compound (2n by 2n) matrix completely. Clearly, the actual advantage of the hybrid method depends on the numbers of equations, iterations, and fields. But for a realistic 40 element model with 117 nodes, the decomposition phase for a single self-interaction matrix theoretically requires 234 times more operations than the solution phase and thus the CPU time for a few iterations is easily overwhelmed by the decomposition savings.

Generalized Born Series Approximation Results

The formalisms and procedures discussed in the preceding sections are now used to quantify the scattering from two cavities. Figure 1 is a 2D representation of the general 3D problem of two dissimilar shapes with a planar incident field propagating in an arbitrary direction. The combined scattered field can be computed for any direction. The first concern is whether the hybrid approach and the fully implicit approach produce similar results. A conservative convergence criterion was used, namely, that the maximum change in any nodal field value between successive iterations must be less than 0.001% of the incident field magnitude, I_a. In principle the two methods should agree, and in fact they do produce essentially identical results. A graphical demonstration of this agreement is omitted because it is rather uneventful, and not because it is insignificant. Unless otherwise stated, the BEM results in this paper are from the hybrid approach.

Truncated series

In this section the validity of a truncated, generalized Born series approximation is explored. In Figure 2, our converged BEM results are compared with similar T-matrix results of Boström[24] and with an approximate analytical solution. The problem is a specific case of the general two scatterer problem shown in Figure 1. The scatterers are identical unit radius spherical voids in an elastic material with a Poisson's ratio of 0.3. The separation of the sphere centers is three units and the dimensionless frequency, $k_L a$, equals one where a is the sphere radius. The magnitude of the backscatter ($\theta^S = 180° + \theta^I$) amplitude is given for incident angles ranging from 0° to 90°. The agreement between the BEM and the T-matrix results is exceptional, somewhat verifying our procedures.

The analytical approximation utilizes the first order approximation of multiple scattering. Since the cavities are spheres, a separation of variables solution[25] is used for the solitary scatterer computation - hence the approximate solution is entirely analytical. In this case, the effect of interaction appears as a perturbation of the first order approximation. The major variation, as a function of incident angle, is caused by the separation induced interference of the otherwise identical backscatter from the two spheres. The approximate solution accounts for this effect and thus captures the dominant variation.

Figure 3 shows the results for a two sphere problem similar to that depicted in Figure 2. The host material properties were changed to that of a titanium alloy with Poisson's ratio equal to 0.3188 in order to reproduce a previous calculation by Domany *et al.*[3] The incident field propagation direction is along the line which passes through both sphere centers, i.e., the coaxial direction. The magnitude of the scattering amplitude is shown as a function of scattered angle. Again the first order approximation

exhibits the dominant trends which are due to both interference and to scattering amplitude variation for each individual scatterer. In Reference 3, the solution to this problem was estimated by a second order multiple scattering approach. As these approximations are physically interpreted, second order means the *interaction* is approximated with the scattered field generated by the inhomogeneities acting individually. Judging from the success of the first order approximation in representing the dominate effects of the scattered field shown in Figure 2, it seems reasonable that the interaction might be approximated this way, at least for this separation and frequency. The second order BEM results given in Figure 3 are obtained by stopping the hybrid scheme after two iterations and they do nearly match our converged BEM results. The meticulous reader will note that the difference between the non-interacting and the second order solution is exactly opposite that of Reference 3, but that discrepancy has been resolved[26]. The magnitude of the perturbation due to interaction is the same and subsequent investigation has shown that the contribution of higher order terms is indeed negligible.

In Figures 4 through 6, the effect of scatterer shape and dimensionless frequency on the interaction between two voids is considered. In each case, the total scattering cross section is plotted as a function of separation distance. The cross section was selected because it is a standard measure of scattering and more importantly because it relates to the *forward* scattering amplitude, as previously mentioned. Forward ($\theta^s = \theta^i$) scattering is unique with multiple inhomogeneities because the non-interacting component is independent of relative position. The incident plus scattered propagation path length remains constant, thus the interference which occurred in the previous examples is not present. Higher order interaction effects can, therefore, be isolated from the sometimes dominant first order effect.

The results for two spherical voids at $k_L a$ equal $\pi/2$ are shown in Figure 4 for coaxial incidence. Separation between sphere centers ranges from 2.5 to 10 radial units, a. Poisson's ratio of the host material for this and all remaining examples is equal to 1/3. The solution based on a second order truncated series, like in Reference 2, looses accuracy as separation decreases. The third order generalized Born series approximation results are in much better agreement with the converged solution.

Figure 5 depicts a situation similar to that of Figure 4 except the spherical voids are replaced by oblate spheroidal voids. With a 10:1 aspect ratio, these voids display "cracklike" behavior when considered as isolated scatterers[8]. It is not clear whether these finite thickness "crack" models have near field behavior similar to zero thickness crack models, so the interaction of these two oblate spheroids may not be indicative of two cracks. The oblate spheroids are oriented parallel to each other with the small semi-axes oriented coaxial. The incident field propagation direction is also along this axis. The characteristic dimension a is the major semi-axis length. The same truncated series approximations are compared to the converged solution over the separation range of one to six a units. In both cases the second order approximation captures the major fluctuations in the converged solution except at small separations. Since the oblate spheroids can be brought closer together without overlapping (i.e., $d < 2a$), significant deviation between the third order approximation and the converged solution can be observed for this case. The most interesting behavior at this close range is that these lower order partial sums do not converge monotonically.

Frequency as well as shape plays a role in the accuracy of a given order Born approximation. Figure 6 shows results for the same oblate spheroids as Figure 5 but at twice the frequency, $k_L a$ equal π. Since the wavelength is smaller, there is more structure in the scattering cross section plot over a given separation range. Higher order

generalized Born series approximation solutions are needed to attain similar agreement with the converged solution. Still in general, the number of iterations needed to obtain an accurate solution is quite small for these closely positioned strong scatterers.

Resonance and convergence

Convergence of the hybrid method is an important issue. While the domain splitting eliminates the kernel singularity, the Neumann series may converge slowly or not at all in practice. Failure to converge can be traced to at least three sources: neglecting the contribution of the $\underline{\mathcal{K}}'[\Delta y_N]$, errors in the numerical solution to the solitary scatterer subproblems, and eigenvalues of the integral operator itself[18]. The physical significance of successive terms of the Neumann series as additional reflections suggests that convergence rate is dependent on the interaction strength. This idea is consistent with the strong versus weak scatterer convergence results of Kitahara and Nakagawa[27]. The iterations required to converge increased as separation distance decreased for the problems depicted in Figures 4 through 6, which is also consistent with this idea. Along with the impedance change and separation distance effects, the geometric arrangement determines the level of interaction.

If a resonance is set up by trapping waves between two scatterers, one might expect higher order generalized Born series approximation terms to be significant since multiple reflections are involved. To illustrate the concept of trapping energy between two scatterers, we consider the problem of two parallel oblate spheroidal voids whose centroids are separated by one major semi-axis length. A high frequency optical analogy to this arrangement would be two parallel mirrors. Energy density between the voids is characterized by the magnitude of the total displacement field, $|\mathbf{u}|$, at the midpoint of the common axis. This quantity is shown as a function of frequency in Figure 7. (This multi-frequency BEM data was generated by the fully implicit method as a matter of

convenience). The fundamental resonance is quite evident at $k_L a \sim \pi/4$. This peak is quite sharp considering that much of the incident energy is scattered off to infinity and not directed toward the other scatterer. Vibration can be thought of as a standing wave created by two propagating waves moving in opposite directions such as between two reflectors. Further use of the interior representation integral (Eqn. 4) allows a display of the fundamental mode shape from the BEM solution. Figure 8 shows the magnitude of the motion parallel to the common symmetry axis of these two voids at a frequency near the fundamental resonance. The phase of these points is similarly constant, thus we infer that the material between the voids is vibrating in an axial direction. Figure 8 also shows the radial distribution of this axial motion. The motion is reminiscent of the fundamental mode of a clamped circular plate as might be anticipated from the geometry.

Table I presents the convergence properties of the hybrid method for this problem. The number of iterations required rises dramatically as the voids are brought close together. Frequency affects the number of iterations but not in a way that is consistent with the resonance concept. At a separation of one, the hybrid method diverged at $k_L a$ equal to $5\pi/16$ but yet it converged at $\pi/4$ which is very near the fundamental frequency. This table along with Figures 5 and 6 illustrate how strict our convergence criteria is. At the upper end of the separation distance scales in those figures, there is very little difference between the converged solution and the low order truncated solutions. Yet, many additional iterations were required to meet the criteria. Even with these extra iterations, the hybrid scheme does provide substantial computational saving over the fully implicit method. At $k_L a$ equal to $\pi/2$, which has poorer than average convergence, a study of 191 relative positions took 148 CPU minutes on an Apollo DN10000 engineering workstation using the iterative method. Estimating from a single position run, the same study would have taken 820 minutes with the fully implicit method.

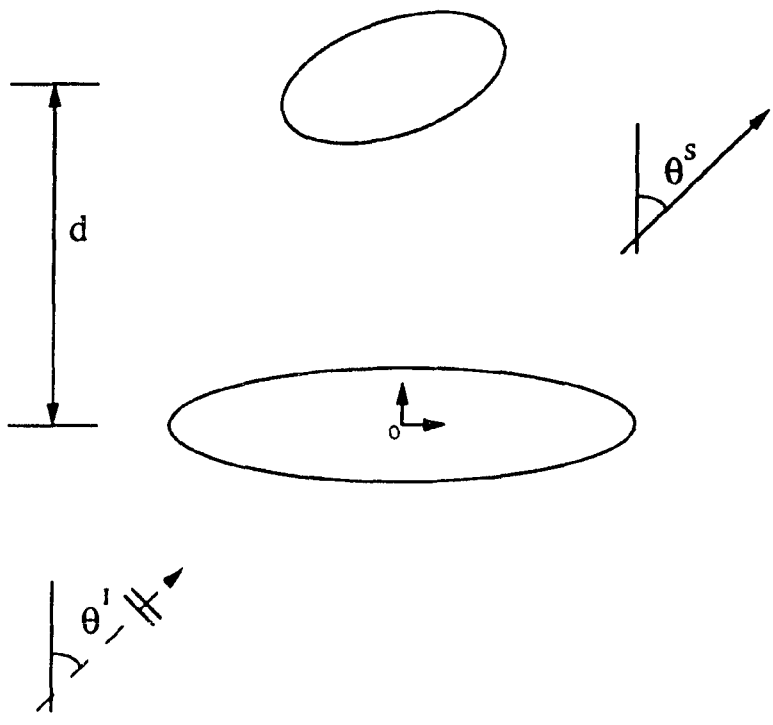

Figure 1 General problem of two, possibly dissimilar scatterers with an arbitrarily incident plane wave. The scatterer centroids are separated by distance, d, and the scattered field may be quantified in any direction

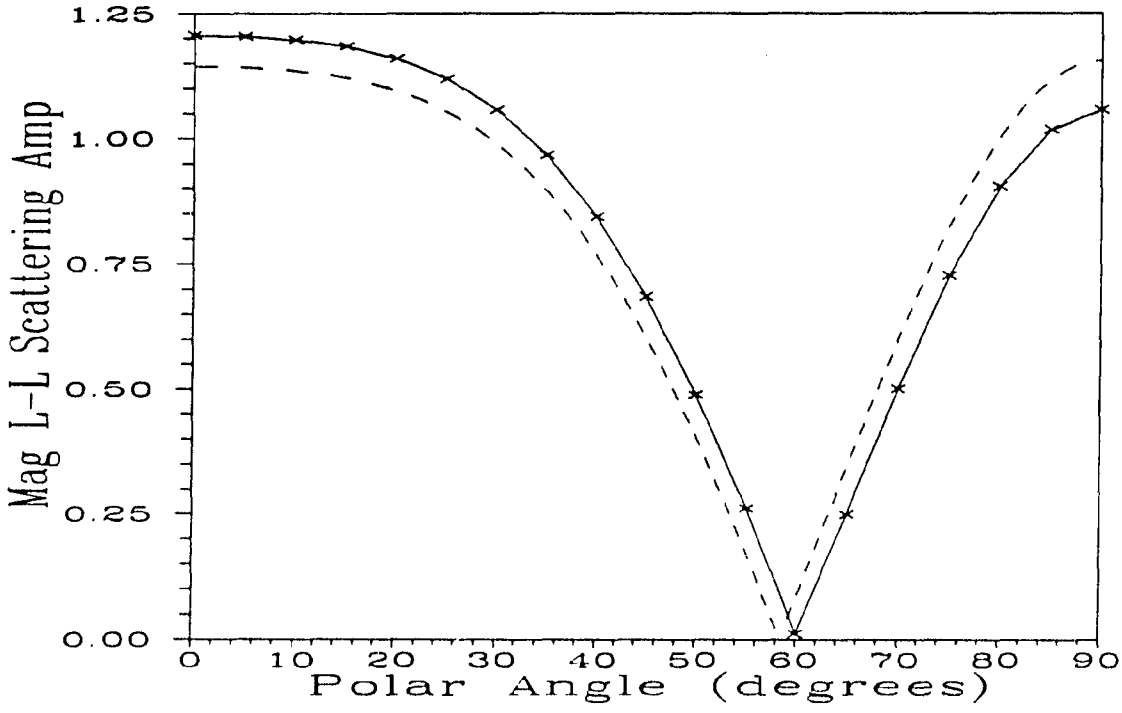

Figure 2 Backscatter from two spherical voids at $k_L a = 1$; $d = 3a$: Comparison of multiple scattering BEM (——) and T-matrix (X) results along with an analytical approximation which neglects interaction (- -)

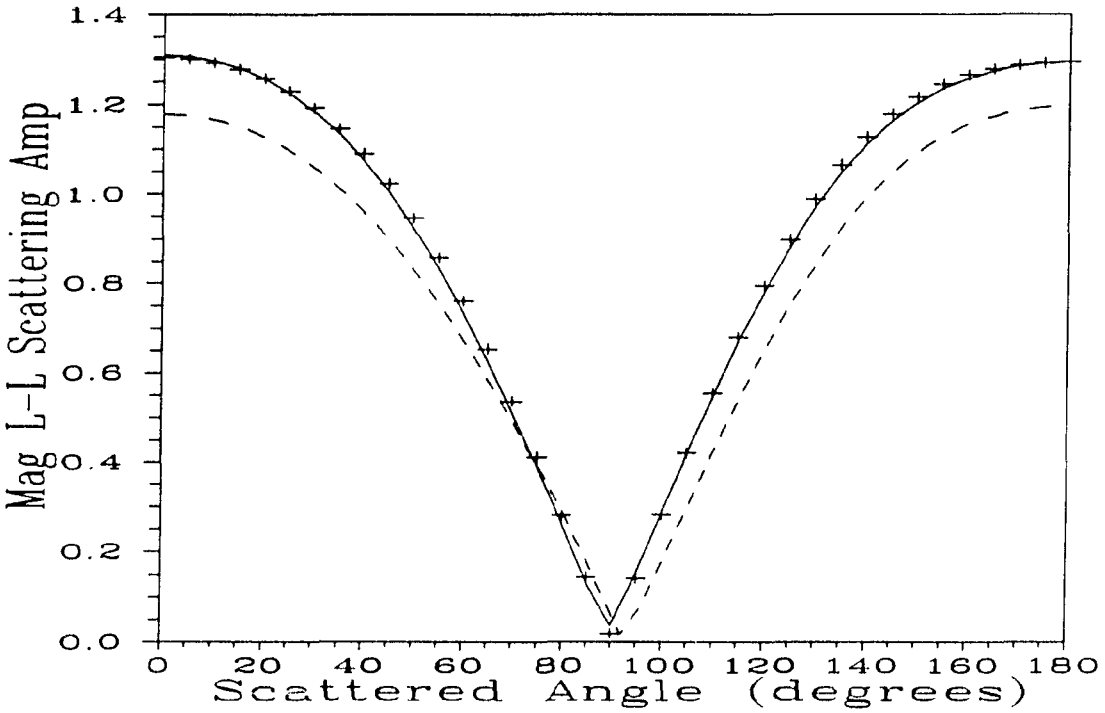

Figure 3 Scattering from two spherical voids in titanium at $k_L a = 1$; $d = 3a$ for coaxial incidence: Comparison of BEM generated second order (——) and converged (+) Born series approximations with a first order analytical approximation which neglects interaction (- -)

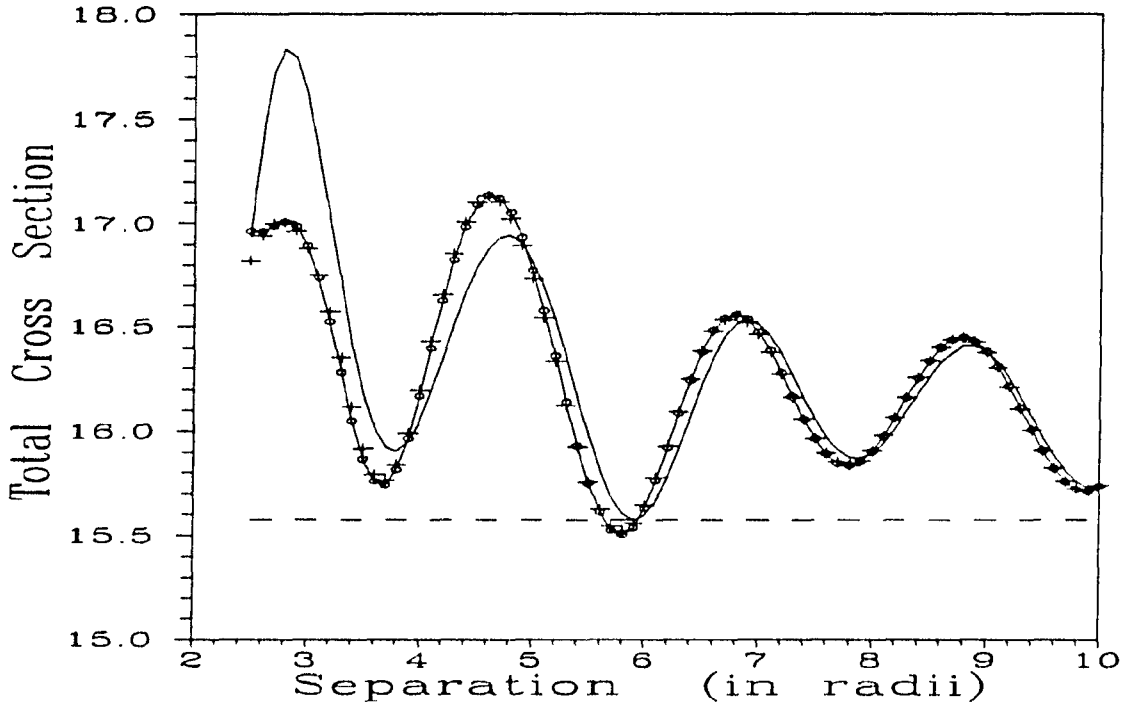

Figure 4 Total scattering cross section of two spherical voids at $k_1 a = \pi/2$ for coaxial incidence as a function of separation distance d: Comparison of first (- -), second (——), third (-⊖-), and converged (+) Born series approximations for the scatterer interaction

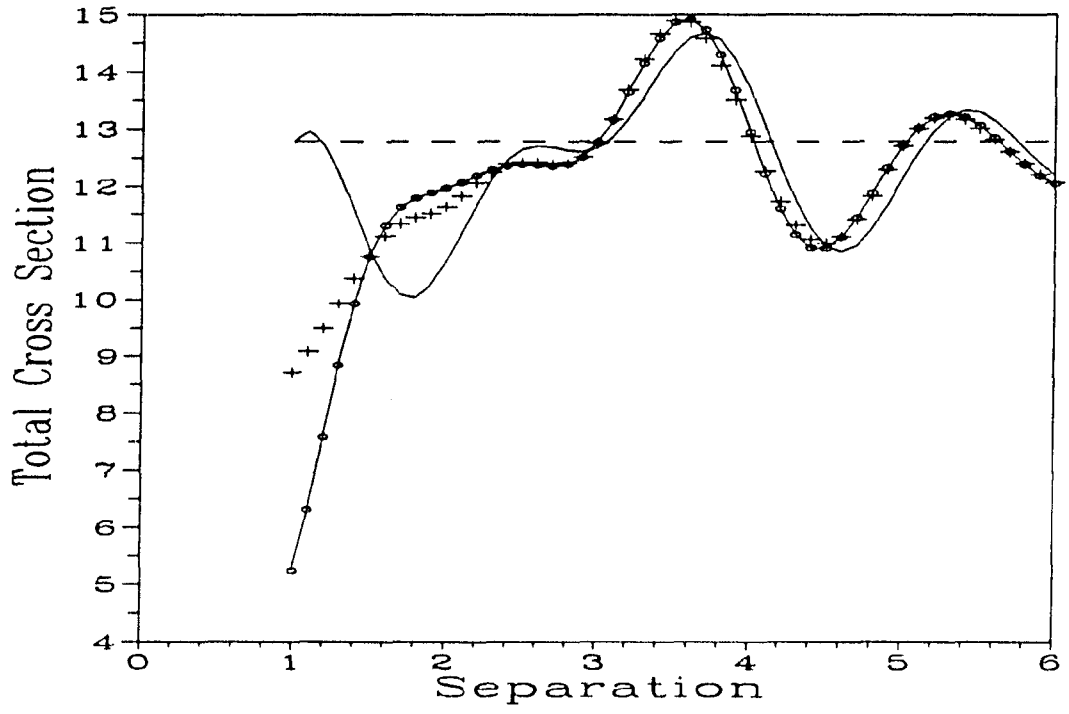

Figure 5 Total scattering cross section of two oblate (10:10:1) spheroidal voids at $k_L a = \pi/2$ for coaxial incidence as a function of separation distance d: Comparison of first (- -), second (——), third (-⊖-), and converged (+) Born series approximations for the scatterer interaction

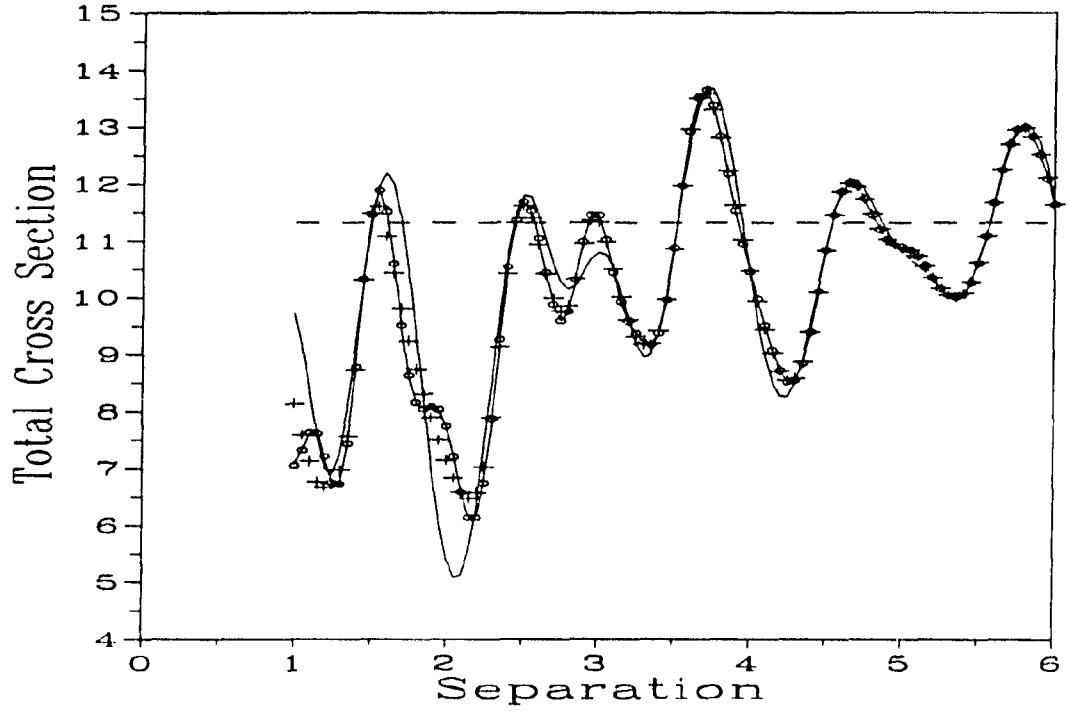

Figure 6 Total scattering cross section of two oblate (10:10:1) spheroidal voids at $k_L a = \pi$ for coaxial incidence as a function of separation distance d: Comparison of first (- -), third (——), fifth (-o-), and converged (+) Born series approximations for the scatterer interaction

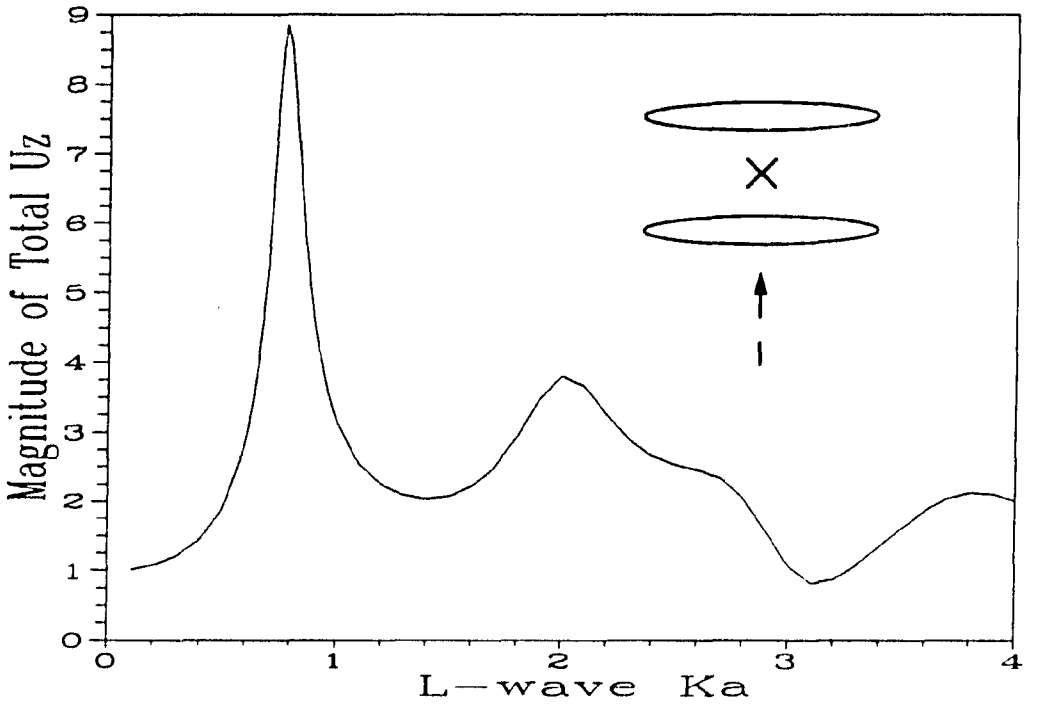

Figure 7 Magnitude of displacement at midpoint between two parallel oblate (10:10:1) spheroidal voids as a function of frequency. Separation distance is equal to one major semi-axis length and the exciting field is a planar longitudinal wave with coaxial incidence

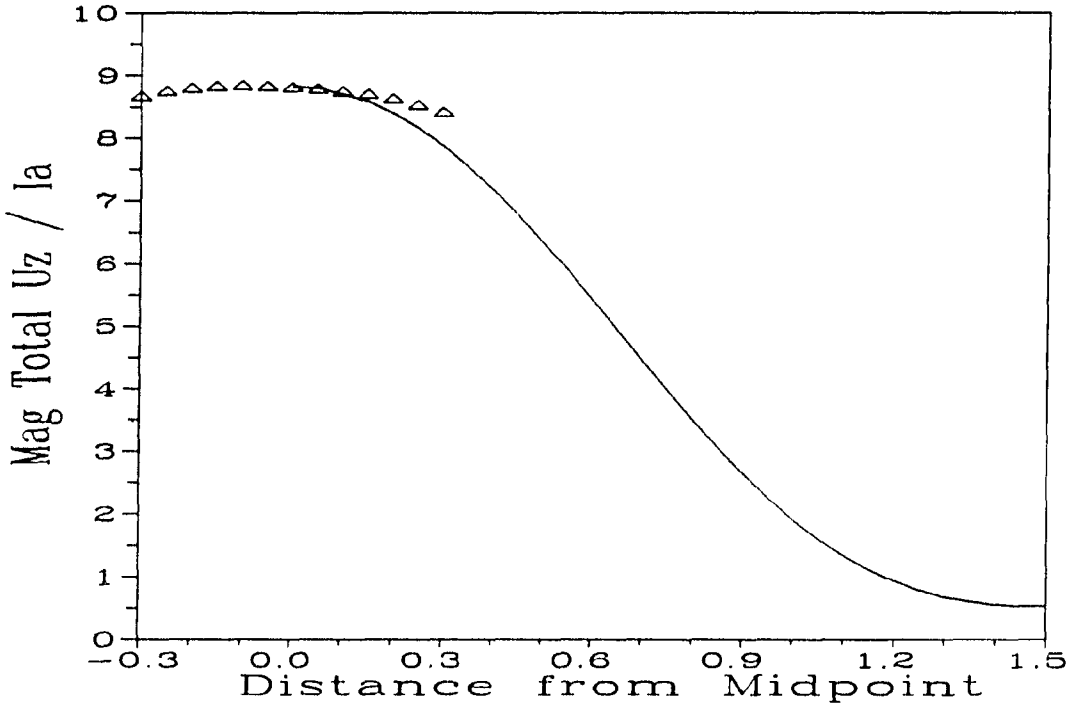

Figure 8 Distribution of total displacement magnitude along axial (Δ) and radial (——) directions from the midpoint of Figure 7 at $k_L a = \pi/4$. Distance is measured in radial units, a

Table I Iterations for the hybrid method to converge with two parallel, oblate (10:10:1) spheroidal voids at various frequencies. Separation, d, between centroids is in terms of major semi-axis length, a

d/a =	1.0	1.2	1.5	2.0	4.0	8.0
$k_L a$						
$\pi/8$	10	8	7	6	4	4
$\pi/4$	54	48	20	13	6	5
$5\pi/16$	∞	96	29	15	5	5
$3\pi/8$	254	48	23	12	5	5
$7\pi/16$	70	30	20	10	6	4
$\pi/2$	71	28	15	8	7	5
$5\pi/8$	30	18	12	8	8	5
$3\pi/4$	25	16	11	11	7	6
$7\pi/8$	22	15	10	13	8	6
π	29	18	14	14	8	6
$9\pi/8$	28	19	19	17	10	6
$5\pi/4$	28	25	26	20	10	7

Treating scatterer interaction with a generalized Born series approximation allows for efficient calculations that are often quite accurate even when only a few terms in the series are used. Next, we evaluate an even simpler approximation which is surprisingly robust.

Farfield Approximation

The farfield approximation for the interacting portion of the scattering process is a very simple approximation from both the conceptual and the implementation standpoints. From the generalized Born series approximation results, we have learned that the true solution can be thought of as a perturbation of the non-interacting approximation. The interaction can be strictly interpreted as sum of twice, thrice, etc., scattered waves. Further, we saw that the twice scattered waves comprise almost all of the interaction except when the defects are close together. In this section, we take this notion of countable wave-scatterer interactions and apply a simple estimate.

With the farfield approximation, the scattered field generated by a single scatterer is assumed to be characterized by the scattering amplitude everywhere. In other words, the nonradiating evanescent near field is ignored. This assumption improves as the distance between scatterers increases. Secondly, our farfield approximation ignores the curvature of the spherically spreading scattered wavefront and characterizes the interacting field as a single plane wave over the entire subsequent scatterer. This secondary assumption also improves as the distance between scatterer increases. This approximation is appealing because the entire interaction portion of the multiple scattering problem is reduced to an analytical calculation. Furthermore, it is expressed in terms of scattering amplitudes which can be computed by methods for solitary scatterers.

In the following subsections, this approximation is worked out for specific cases involving two scatterers.

Identical symmetric scatterers

Consider the case of two identical scatterers with at least three orthogonal symmetry planes, and further assume the spatial offset between the two scatterer centroids is along a symmetry plane intersection line. This arrangement was selected because it is sufficiently general to include spheres, spheroids, and ellipsoids which are commonly studied and yet it has enough symmetry to keep the illustrative calculation simple. The farfield approximation is not dependent on any symmetry assumption. The general problem is illustrated in Figures 1 and 9 in which the ϕ dependence, if any, is not shown. The incident field propagation direction may likewise be arbitrary. We consider two particular incident fields, one propagating parallel to the common axis (coaxial) and the other one propagating perpendicular (lateral) to it. Secondary and tertiary interactions for the lateral incidence situation are depicted in Figure 9. The coaxial incidence case is similar except that there are formally no transverse waves traveling between the two scatterers due to the additional symmetry.

The first order farfield approximation is identical with the first Born approximation of the interaction (i.e., no interaction). A formula for the combined scattering amplitude, B, with coaxial ($\theta^I = 0$) incidence is:

$$B^{(1)}_{L\text{-}L}(0,\theta^S) = A_{L\text{-}L}(0,\theta^S)\left[1 + e^{ik_L d(1-\cos\theta^S)}\right]. \qquad (19a)$$

This equation generates the non-interacting approximation shown in Figure 3 and in conjunction with Equation (6), also those in Figures 4 through 6. The complex

exponential expresses the relative phase shift due to the difference in propagation path length. For example, when θ^S equals 180° the backscattered signal from the second scatterer is $2k_L d$ radians out phase relative the signal backscattered from the first scatterer. In the forward direction ($\theta^S = 0$) the separation distance has no effect, as previously stated. The corresponding formula for lateral incidence is:

$$B^{(1)}_{L\text{-}L}(90,\theta^S) = A_{L\text{-}L}(90,\theta^S)\left[1 + e^{-ik_L d\cos\theta^S}\right]. \qquad (19b)$$

The second order farfield approximation includes the first order term plus the interaction shown schematically in Figure 9a. The interaction is shown as split into scattered fields emanating from the upper and lower inhomogeneities, to enhance understanding. Both processes occur simultaneously, but have different functional forms. For lateral incidence, the relationship is:

$$\begin{aligned} B^{(2)}_{L\text{-}L}(90,\theta^S) = B^{(1)}_{L\text{-}L}(90,\theta^S) + A_{L\text{-}L}(90,0)e^{ik_L d}[A_{L\text{-}L}(180,\theta^S) \\ + A_{L\text{-}L}(0,\theta^S)e^{-ik_L d\cos\theta^S}]/d + A_{L\text{-}T}(90,0)e^{ik_T d} \\ \left[A_{T\text{-}L}(180,\theta^S) + A_{T\text{-}L}(0,\theta^S)e^{-ik_T d\cos\theta^S}\right]/d. \qquad (20a) \end{aligned}$$

The T-L scattering amplitudes in this expression can be calculated from the methods of Reference 25 by applying the principle of mode conversion reciprocity[17]. For coaxial incidence the expression is somewhat simpler:

$$\begin{aligned} B^{(2)}_{L\text{-}L}(0,\theta^S) = B^{(1)}_{L\text{-}L}(0,\theta^S) + A_{L\text{-}L}(0,0)A_{L\text{-}L}(0,\theta^S)e^{ik_L d(1-\cos\theta^S)}/d \\ + A_{L\text{-}L}(0,180)A_{L\text{-}L}(180,\theta^S)e^{2ik_L d}/d. \qquad (20b) \end{aligned}$$

The third order approximation adds the effects from waves which scatter from the inhomogeneities three times before spreading into the farfield. The two possible paths of these waves for lateral incidence are shown in Figure 9b. For each increment in order, the path includes an additional traverse between the two scatterers (cf. Figs. 9a and 9b). The third order terms are similar to the first order except that the waves are first scattered to the other inhomogeneity and then back again. Fourth order terms are like the second order except for the same additional "over and back" scattering. This reasoning continues for fifth, sixth, etc., orders and the sum takes the form of a power series of a complex variable. Consequently, an infinite order farfield approximation can be written down in closed form by utilizing the common formula, $(1-z)^{-1} = \sum_{n=0}^{\infty} z^n$. For coaxial incidence it is:

$$
\begin{aligned}
B_{L-L}^{(\infty)}(0,\theta^S) = B_{L-L}^{(1)}(0,\theta^S) + \left[d e^{-ik_L d} - (A_{L-L}(0,180))^2 e^{ik_L d}/d \right]^{-1} \{ & A_{L-L}(0,0) \\
& \left[A_{L-L}(0,\theta^S) e^{-ik_L d\cos\theta^S} + e^{ik_L d} A_{L-L}(0,180) A_{L-L}(180,\theta^S)/d \right] \\
& + A_{L-L}(0,180) e^{ik_L d} [A_{L-L}(180,\theta^S) \\
& + e^{ik_L d(1-\cos\theta^S)} A_{L-L}(180,0) A_{L-L}(0,\theta^S)/d] \} \qquad (21)
\end{aligned}
$$

providing that $|A_{L-L}(0,180)| < d$.

Comparisons of the total scattering cross section are made between the farfield approximation and the converged generalized Born series solution. We will begin with the two spherical void problem under coaxial incidence. Figure 10 compares the converged solution from the hybrid method with the first, second, and infinite order farfield approximations. The second order farfield approximation captures the

oscillations of the solution but overestimates the deviation from the non-interacting approximation for separations less than two wavelengths (8 radii). The infinite order approximation differs significantly from the second order only for separations less than one wavelength. In that regime the farfield assumptions are suspect and including more terms offers no improvement.

Most of the structure in the BEM solution can be interpreted physically by inspecting the terms in Equation (20b) which approximates the dominate effects. The oscillations are due to the complex exponential in the last term and represent the interference of a doubly backscattered wave with the singly scattered waves. The spatial period is set by the longitudinal wavelength. The strength of the approximated fluctuation decays as $1/d$ since the farfield assumption implies the inter-flaw scattered field likewise decays. The oscillations are offset from the non-interacting approximation by the second term of (20b) which represents a doubly forward scattered wave and consequently also has the $1/d$ decay.

Figure 11 is for the same situation as Figure 10 except that the incidence is normal to the common axis. The second order farfield approximation very nearly matches the true solution all the way down to when the voids are almost touching. The fluctuations with respect to separation have the appearance of a superposition of a fundamental frequency and its first harmonic, both with an underlying $1/d$ decay. Recalling that the ratio of k_T to k_L is two and examining Equation (20a) reveals that this behavior is exactly what would be physically expected.

The oscillatory nature of the total cross section versus separation comes from terms of the form: e^{ikd}. Figure 12 shows a comparison versus frequency at a fixed separation of seven radii. The farfield approximations are provided by Equations (19a) and (20b). The dominant effect is due to the change in scattering amplitude with

frequency and thus the non-interacting approximation is quite good. The second order approximation captures the subtle fluctuations (e^{ikd} terms) up through a $k_L a$ of about two. The accuracy of the farfield approximation is frequency as well as separation dependent.

Although the farfield approximation formulas in this section are for identical scatterers, it is straightforward to construct relationships for unmatched flaws from these examples. Likewise, three or more scatterers could be treated but the interaction "bookkeeping" becomes difficult beyond second order.

Equivalent near field scattering amplitudes

A critical element to the success of the farfield approximation is the accuracy of the farfield scattering amplitude in predicting the near field. The actual near scattered field can be quantified by a distance dependent "equivalent scattering amplitude" which is given by an expression similar to Equation (5) but without the limit. The sphere is a convenient object to make these comparisons on, due to the availability of an analytical solution from which to gain insight. Reference 25 provides an expression for the radial displacement due to a θ' equal to 0° incident L-wave:

$$u_r^s(r,\theta^s) = \frac{1}{r}\sum_{n=0}^{\infty}\left[k_L r A_n \frac{dh_n(k_L r)}{d(k_L r)} - n(n+1)B_n h_n(k_T r)\right]P_n(\cos\theta^s) \qquad (22)$$

where A_n and B_n are coefficients dependent on frequency and material properties. The P_n and h_n are Legendre polynomials and spherical Hankel functions, respectively. These Hankel functions can be expressed as a power series in $1/z$ times e^{iz}/z where z is the function argument[28]. Considering the next order terms beyond the farfield asymptotic, an approximation to the equivalent scattering amplitude has the form:

$$A_{eq} \sim A_{L-L} + \sum_{n=0}^{\infty} \left[\tilde{A}_n / r + \tilde{B}_n e^{i(k_T - k_L)r} / r \right]. \qquad (23)$$

The tilde on $\tilde{A}_n$ and $\tilde{B}_n$ indicates an absorption of the Hankel function power series coefficients into the scattered field coefficients. The error in using the farfield value in the near field drops off as $1/r$ and has a spatial oscillation whose wavelength is determined by the difference in the wave numbers.

Figure 13 compares the complex components of an analytically generated equivalent scattering amplitude with the farfield asymptotic values. Backscattering amplitude is considered because its value is used repeatedly in higher order interaction terms. The decaying and oscillating behavior of the leading error terms is just as predicted by Equation (23). The magnitude of the deviation varies with frequency and scattered angle and would in general need to be studied for each case. But for this situation, the deviation of the equivalent scattering amplitude from the farfield value and the error in the farfield approximation shown in Figure 10 are consistent. Both approximations have significant problems at separations less than 3.5 radii at this frequency.

The accuracy of the equivalent scattering amplitudes in the near field of an oblate spheroid has also been studied by using the BEM[29]. Again, the breakdown of the farfield approximation is consistent with the difference between the equivalent scattering amplitude and its asymptotic. Figure 14 shows a comparison of the first and second farfield approximations for the total cross section with the hybrid solution for two oblate spheroids as a function of separation. The frequency is the same as the dual sphere problem of Figure 10 and the breakdown of the second order approximation occurs at roughly the same separation. The true cross section deviates from this second order approximation (Eqn. 20b) most noticeably near every fourth crossing of the first order

approximation line. Inter-scatterer shear waves whose propagation phase delay is $(k_T - k_L)d$ (see $\bar{B}_n$ term of Eqn. 23) rather than $2k_L d$ (see last term of Eqn. 20b) would exhibit this subharmonic behavior. The generation of diffracted T-waves by crack tips is a well known phenomenon[30] and Reference 9 has demonstrated the "cracklike" behavior of a 10:10:1 oblate spheroid. T-waves generated around the edge of a circular crack by a normally incident L-wave would cancel in the forward and backward directions due to symmetry. However, when the two spheroids are closely spaced, some inter-flaw propagation paths are slightly off-axis which would permit T-wave based interactions.

Anti-symmetric configuration

In all of the multiple scattering examples given thus far, the individual scatterers have had rotational symmetry. It is helpful to deal with simple shapes while building up an intuitive understanding of multiple scattering. But our underlying numerical capability can handle arbitrarily shaped scatterers in non-symmetrical arrangements and in this final example that ability is put to use. As was suggested by the behavior in Figure 14, the near scattered field can have some displacement components which cancel in the farfield due to symmetry. A problem was devised which intentionally thwarted symmetry to see if the robustness of the farfield approximation in the previous examples was fortuitously due to symmetry. A pair of ellipsoidal voids with semi-axes in the ratio 10:5:1 is considered. (These shapes still have three orthogonal symmetry planes). They are arranged with their major axes coplanar but orthogonal.

The incident field propagation vector is chosen to bisect the angle between the major axes so that the scatterers are anti-symmetric relative to the incident field. The non-interacting total backscatter is independent of separation distance with this arrangement and the expression is:

$$B^{(1)}_{L\text{-}L}(0,180) = 2A_{L\text{-}L}(45,225). \tag{24}$$

The individual scattering amplitude, A, has polar angles referenced to each ellipsoid's minor axis.

Further, the "cracklike" nature of these ellipsoids suggests that at sufficiently high frequencies their specular scattering will be quite strong[30]. (Specular implies the reflected angle with respect to the "crack" normal is equal to the similarly referenced incident angle). For this arrangement of high aspect ratio ellipsoids, the second order farfield approximation for backscatter includes a twice reflected, specular component. Figure 15 illustrates this process for incidence on the left hand scatterer and an identical process occurs simultaneously beginning on the right. Utilizing mode conversion reciprocity relations, the total backscattering amplitude is then:

$$B^{(2)}_{L\text{-}L}(0,180) = B^{(1)}_{L\text{-}L}(0,180) + 2\left\{e^{ik_L d}[A_{L\text{-}L}(45,135)]^2 - e^{ik_T d}\left[A_{L\text{-}T}(45,135)\frac{k_L}{k_T}\right]^2\right\}/d. \tag{25}$$

A schematic of the propagation path of third order contributions is also shown in Figure 15. Mode conversion occurs at each reflection due to the asymmetrical incidence. The inter-flaw paths can be L:L, L:T, T:L, and T:T waves, but through mode conversion reciprocity and symmetry the expression reduces to:

$$\begin{aligned} B^{(3)}_{L\text{-}L}(0,180) = B^{(2)}_{L\text{-}L}(0,180) + 2\{ & A_{L\text{-}L}(45,225)\left[e^{ik_L d}A_{L\text{-}L}(45,135)/d\right]^2 \\ & + 2A_{L\text{-}L}(45,135)e^{i(k_L+k_T)d}A_{L\text{-}T}(45,135)A_{L\text{-}T}(45,225)[k_L/(dk_T)]^2 \\ & - A_{T\text{-}T}(45,225)\left[e^{ik_T d}A_{L\text{-}T}(45,135)k_L/(dk_T)\right]^2\}. \end{aligned} \tag{26}$$

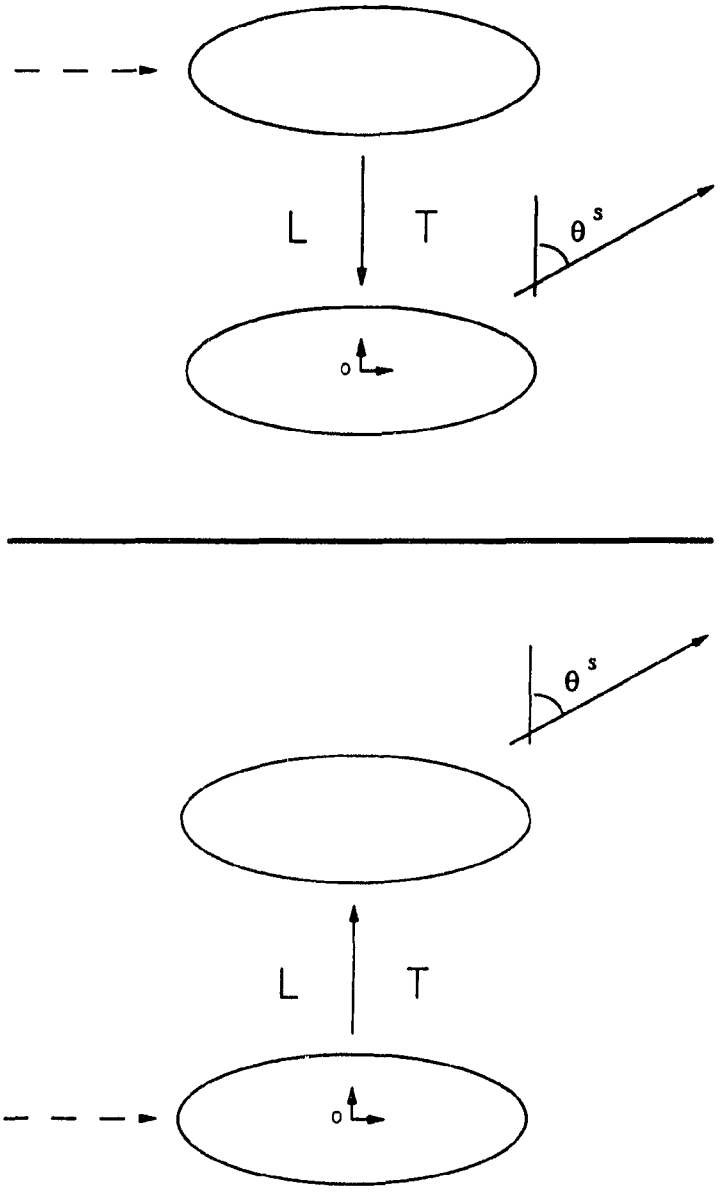

Figure 9a Propagation path of second order effects from two scatterers with a laterally incident plane wave

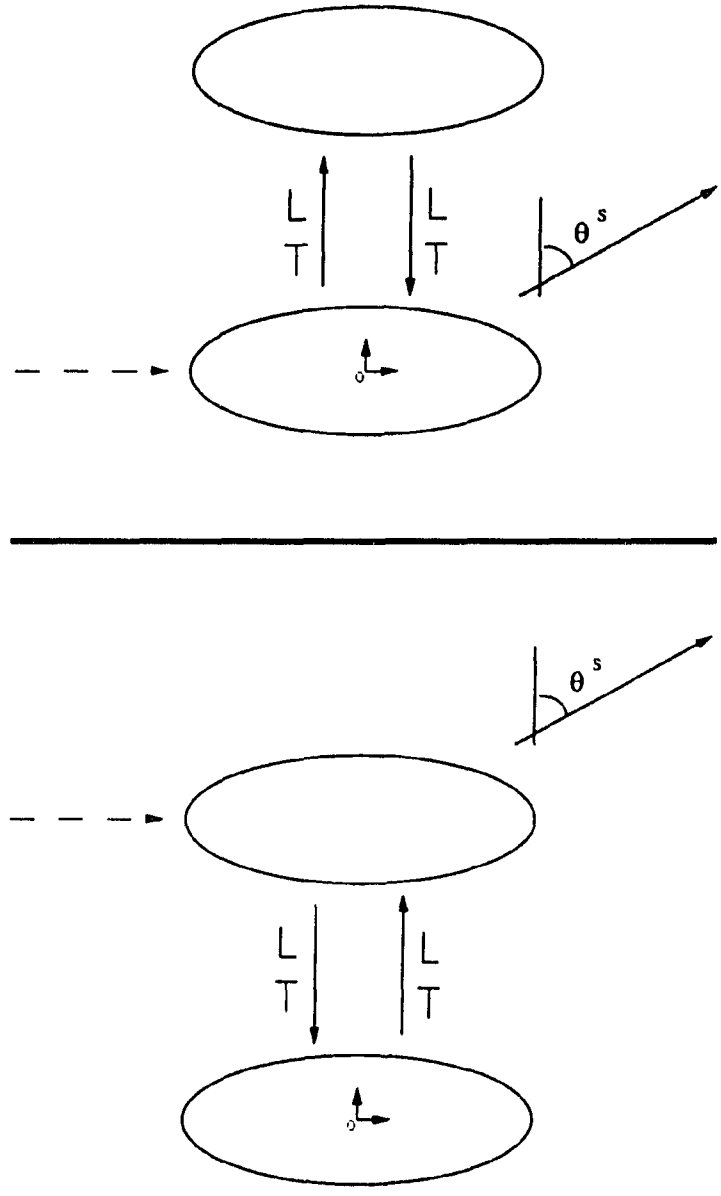

Figure 9b Propagation path of third order effects from two scatterers with a laterally incident plane wave

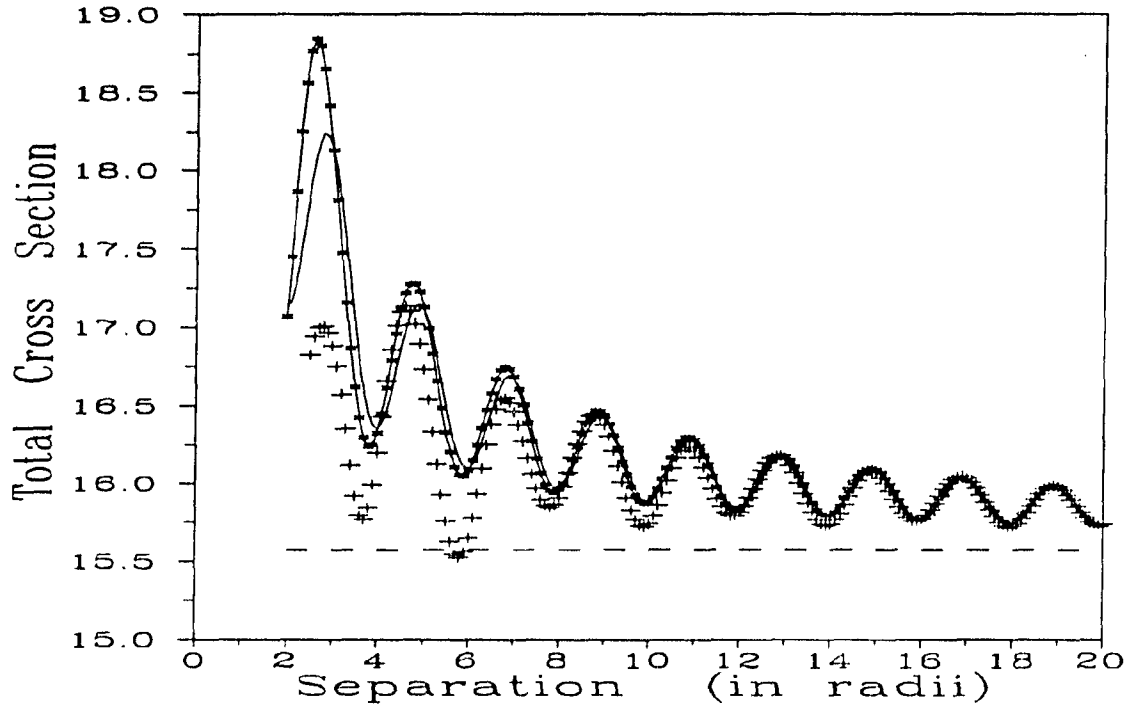

Figure 10 Total scattering cross section of two spherical voids at $k_L a = \pi / 2$ for coaxial incidence as a function of separation distance d: Comparison of first (- -), second (——), and infinite order ($\rightarrow\!\!\!\!\leftarrow$) farfield approximations with the converged BEM solution (+)

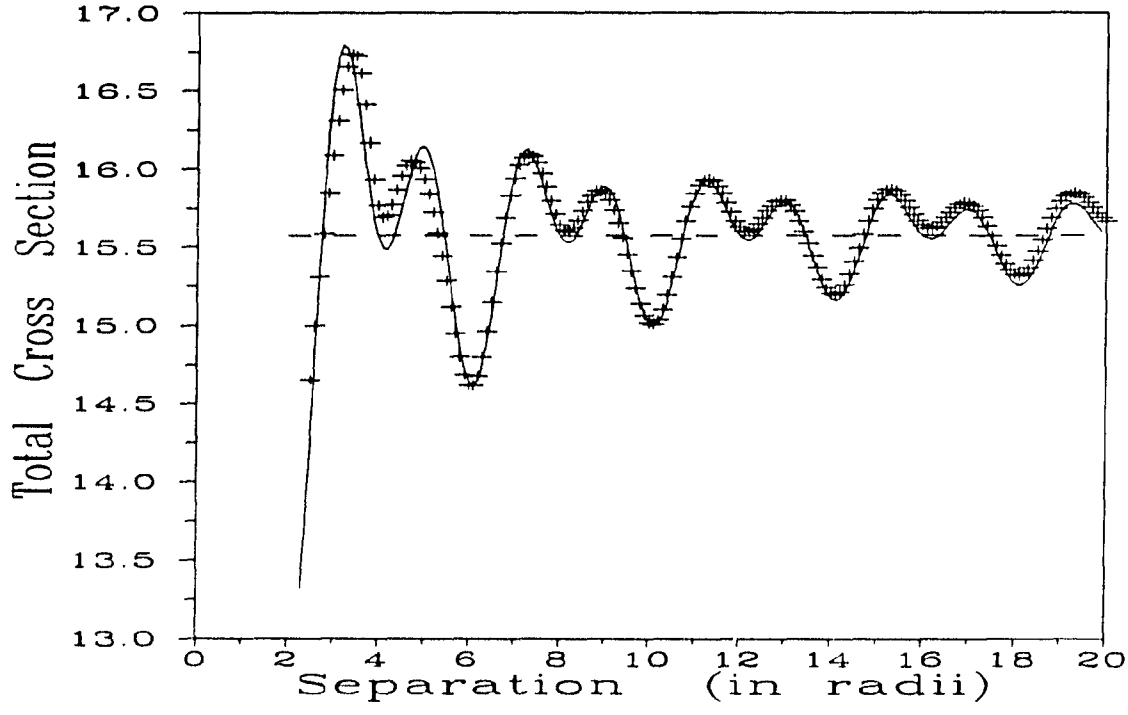

Figure 11 Total scattering cross section of two spherical voids at $k_L a = \pi/2$ for lateral incidence as a function of separation distance d: Comparison of first (- -) and second order (——) farfield approximations with the converged BEM solution (+)

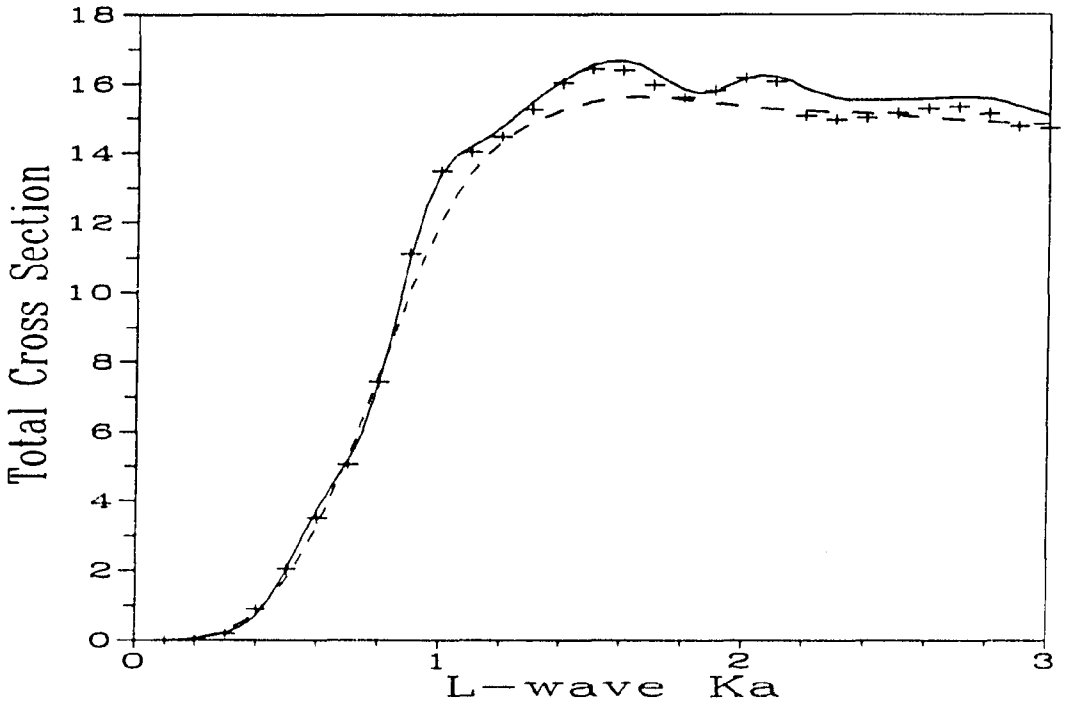

Figure 12 Total scattering cross section of two spherical voids at $d = 7a$ for coaxial incidence as a function of frequency: Comparison of first (- -) and second order (——) farfield approximations with the converged BEM solution (+)

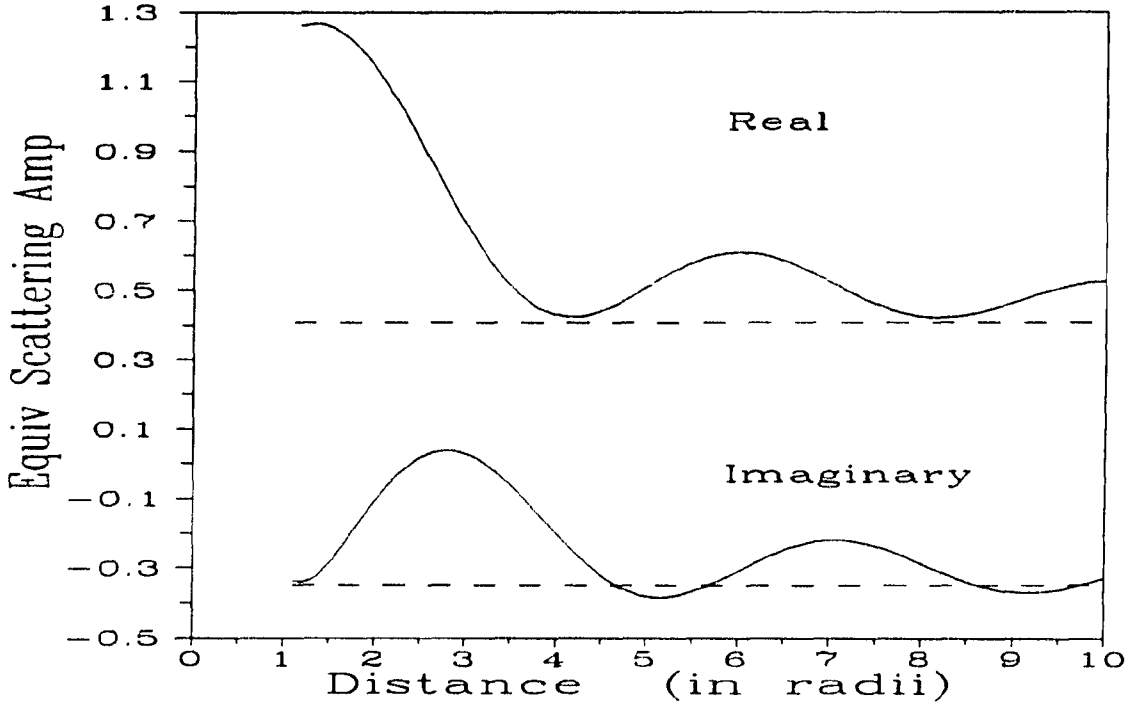

Figure 13 Equivalent backscattering amplitude of a single spherical void at $k_L a = \pi/2$ as a function of radial distance: Comparison of exact analytical solution components (——) with the farfield approximation (- -)

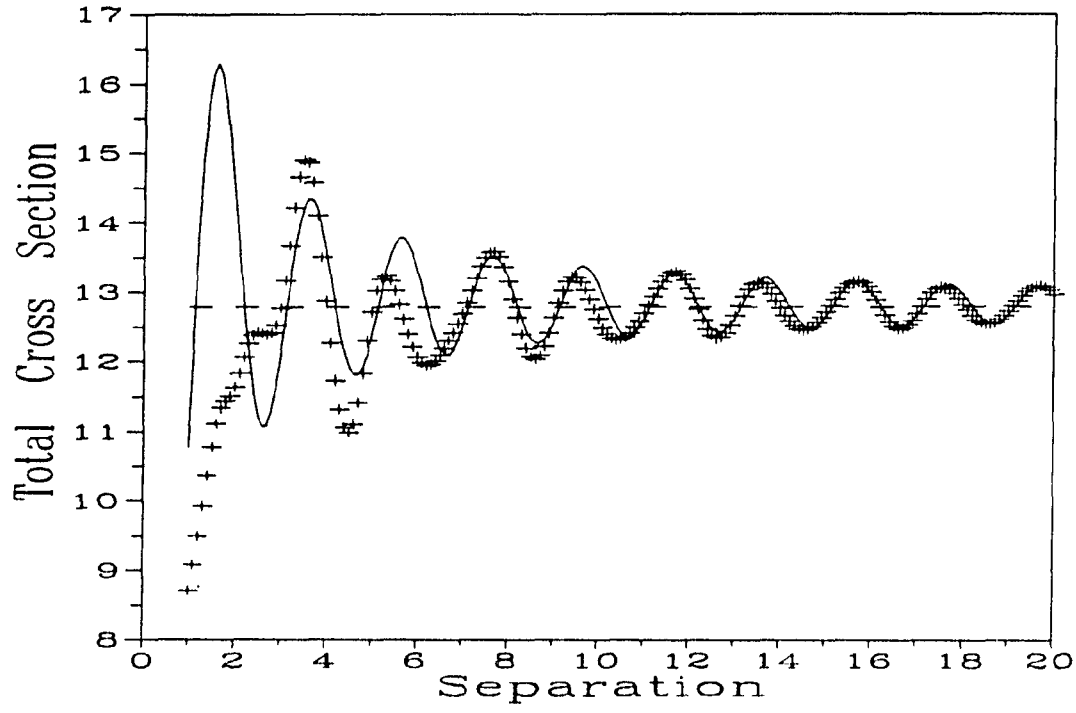

Figure 14 Total scattering cross section of two parallel oblate (10:10:1) spheroidal voids at $k_L a = \pi/2$ for coaxial incidence as a function of separation distance d: Comparison of first (- -) and second order (——) farfield approximations with the converged BEM solution (+)

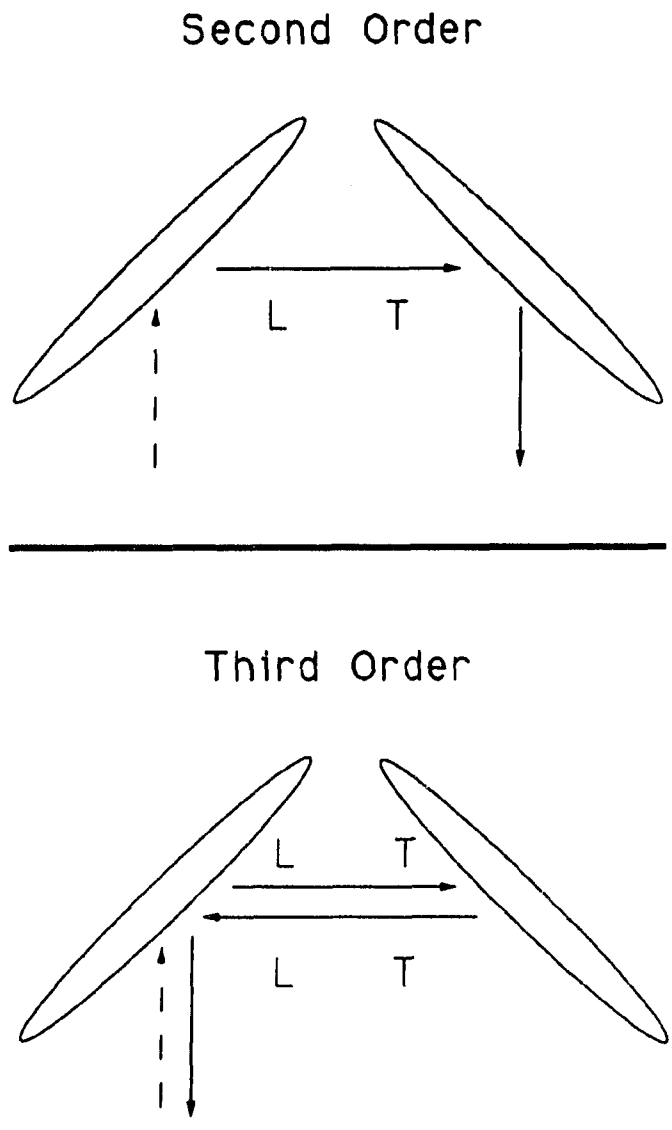

Figure 15 Propagation path of second and third order effects from two anti-symmetric ellipsoids in a specular scattering situation

Figure 16 compares the first, second, and third order farfield approximations with the converged, hybrid method solution. The second order farfield approximation does remarkably well at predicting the variation with respect to separation distance. The interference pattern is due to phase delays of the inter-flaw L and T-waves and thus exhibits the first/second harmonic pattern as in Figure 11. The phase delays are based on the distance between centroids although some ray paths are clearly shorter or longer. The effect of the third order terms is very slight even at small separations as might be expected since they contains a comparatively weak non-specular scattering amplitude. With this anti-symmetric arrangement, as with the previous examples, it seems some of the error introduced by the farfield approximation is self canceling.

Concluding Remarks

The simplest reasonable approximation of scatterer interaction is to simply ignore the interaction completely but to sum the individual scattered fields with the appropriate position dependent phase corrections. This non-interaction assumption is reasonably accurate for intermediate frequency scattering, if strong scatterers such as voids are separated by several wavelengths or more. For better accuracy and/or for smaller separations, the farfield approximation seems to work quite well. It has the advantage of reducing the interaction phenomena to an analytical calculation. Although for some configurations it is feasible to consider infinite multiple reflections with this approach, the contribution of reflections beyond the first few are small at low and intermediate frequency - except when the scatterers are separated by distances on the order of their dimensions. The farfield approximation cannot be expected to be reliable at such close distances. At intermediate separation distances the second order farfield approximation is appropriate and quite accurate - at least for the situations examined.

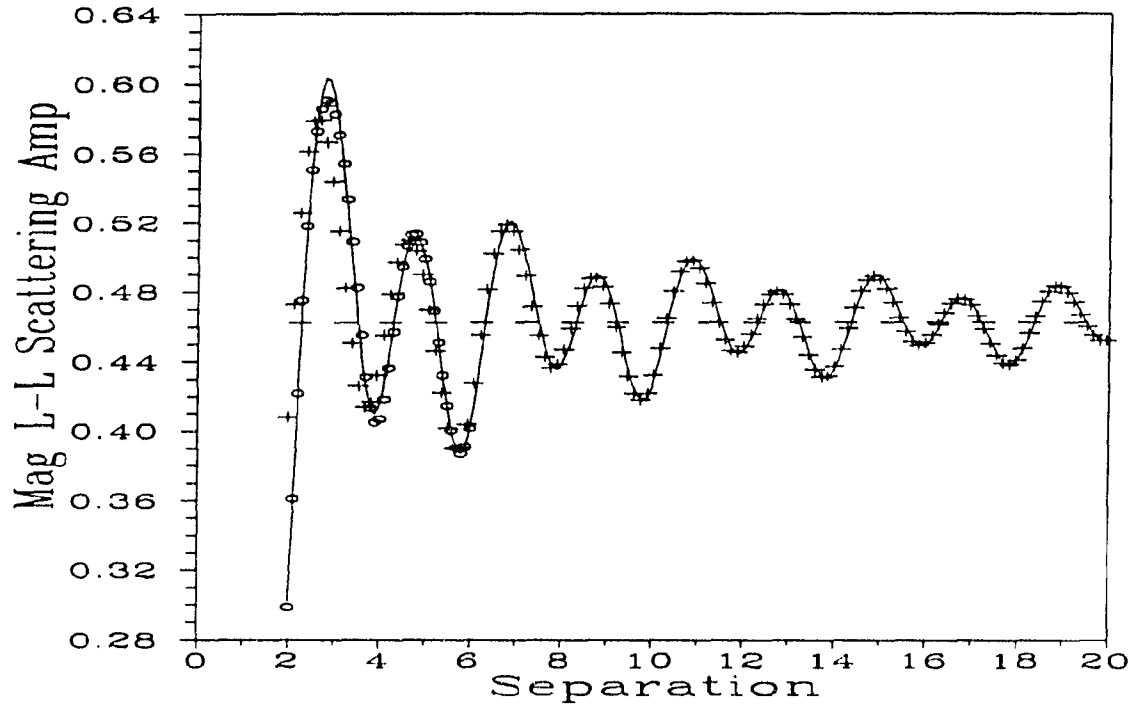

Figure 16 Magnitude of backscattering amplitude for two ellipsoidal (10:5:1) voids at $k_L a = \pi/2$ oriented as in Figure 15: Comparison of first (- -), second (——), and third order (o) farfield approximations with the converged BEM solution (+) as a function of separation distance, d

For inhomogeneities which are within each others' near scattered fields, the BEM based, hybrid implicit-iterative method provides an efficient means of computing combined scattering amplitudes for arbitrary shapes and configurations. This method is especially efficient if the decomposed BEM matrices for the individual scatterers already exist in a library as advocated in Reference 8. The convergence of this scheme is not always guaranteed, as we have seen, but the fully implicit method is always available in case of difficulty. For elastic inclusions, the advantages are greater than with voids since the number of simultaneous equations is doubled, half of the cross-influence matrix is identically zero, and the reduction in impedance mismatch enhances the convergence rate[27]. Often the number of iterations required to accurately predict farfield quantities is fairly modest. Admittedly, there is a temporal inconsistency in treating the individual scatterers implicitly, thus capturing all internal reverberations, and truncating the interaction series when the scatterers are close. Increasing the number of series terms included (i.e., number of iterations), as with a conservative convergence criteria, reduces the inconsistency.

All of our examples for the generalized Born series approximation have been two scatterer problems. Hinrichsen[31] has implemented Schuster's algorithm for acoustic problems involving two through six inhomogeneities. Achenbach and Kitahara[32] have utilized a 3D BEM (with constant field interpolation over each element) on a problem involving an array of spherical voids. But the most enticing extension is to half-space problems. Boström and Kristensson[33] and Domany and Entin-Wohlman[34] previously recognized interaction decoupling as a means to solve scattering by a sub-surface defect. Half-space problems can be solved via the BEM using half-space kernels or by using a full-space kernel and then also discretizing the section of the half-space boundary near the flaw[35]. When solved by a fully implicit method, the full-space kernel/discretized boundary approach proved not to be computationally competitive with the use of half-space kernels but affords the option of a curved boundary[35]. In the context of

NDE, crucial defects are often located below a sharply curved component surface. We surmise that near sub-surface flaw scattering problems can be handled quite efficiently by the discretized boundary approach once the flaw matrix is only iteratively coupled to the truncated boundary matrix.

Acknowledgement

This work was sponsored by the Center for NDE at Iowa State University. It was also partially supported by the Solid Mechanics Program of the Office of Naval Research with Dr. Y. Rajapakse as the program officer.

References

1. A. Boström, 'Multiple scattering of elastic waves by bounded obstacles', *J. Acoust. Soc. Am.* **67**(2), 399-413 (1980).
2. V. V. Varadan and V. K. Varadan, 'Configurations with finite numbers of scatterers - A self-consistent T-matrix approach', *J. Acoust. Soc. Am.* **70**(1), 213-217 (1981).
3. E. Domany, O. Entin-Wohlman, and L. Mizrachi, 'Multiple scattering formalism: Application to scattering by two spheres', *J. Appl. Phys.* **56**(1), 132-136 (1984).
4. Y. C. Angel and J. D. Achenbach, 'Reflection and transmission of elastic waves by a periodic array of cracks', *J. Appl. Mech. Trans. ASME*, **52**(1), 33-41 (1985).
5. Ch. Zhang and J. D. Achenbach, 'Scattering by multiple crack configurations', *J. Appl. Mech. Trans. ASME*, **55**(1), 104-110 (1988).
6. Ch. Zhang and J. D. Achenbach, 'Effect of an adjacent cavity on the interaction of elastic waves with a crack', *Int. J. Eng. Sci.* **27**(6), 711-722 (1989).
7. V. K. Varadan, Y. Ma, and V. V. Varadan, 'A multiple scattering theory for elastic wave propagation in discrete random media', *J. Acoust. Soc. Am.* **77**(2), 375-385 (1985).

8. P. J. Schafbuch, 'Application of the boundary element method to elastic wave scattering problems in ultrasonic nondestructive evaluation', Ph.D. Dissertation, Iowa State University, Ames, IA (1991), Part III.
9. P. J. Schafbuch, R. B. Thompson, and F. J. Rizzo, 'Application of the boundary element method to elastic wave scattering by irregular defects', to appear *J. Nondestr. Eval.* **9**(2-3), (1990).
10. G. T. Schuster, 'A hybrid BIE + Born series modeling scheme: Generalized Born series', *J. Acoust. Soc. Am.* **77**(3), 865-886 (1985).
11. J. E. Gubernatis, E. Domany, J. A. Krumhansl, and M. Huberman, 'The Born approximation in the theory of the scattering of elastic waves by flaws', *J. Appl. Phys.* **48**(7), 2812-2819 (1977).
12. S. Amini, C. Ke, and P. J. Harris, 'Iterative solution of boundary element equations for the exterior Helmholtz problem', *J. Vibr. Acoust. Trans. ASME*, **112**(2), 257-262 (1990).
13. F. J. Rizzo, D. J. Shippy, and M. Rezayat, 'A boundary integral equation method for radiation and scattering of elastic waves in three dimensions', *Int. J. Numer. Methods Eng.* **21**(1), 115-129 (1985).
14. M. Rezayat, F. J. Rizzo, and D. J. Shippy, 'On time-harmonic elastic-wave analysis by the boundary element method for moderate to high frequencies', *Comput. Methods Appl. Mech. Engrg.* **55**(3), 349-367 (1986).
15. I. R. Gonsalves, D. J. Shippy, and F. J. Rizzo, 'The direct boundary integral equation method for the three-dimensional elastodynamic transmission problem', to appear *Computers Math. Applic.*
16. J. H. Ferziger, *Numerical Methods for Engineering Application* (Wiley, New York, 1981).
17. V. Varatharajulu, 'Reciprocity relations and forward amplitude theorems for elastic waves', *J. Math. Physics* **18**(4), 537-543 (1977).
18. F. B. Hildebrand, *Methods of Applied Mathematics* (Prentice-Hall, Englewood Cliffs, 1965), 2nd ed., Chap. 3.
19. W. Pogorzelski, *Integral Equations and their Applications* (Pergamon, Oxford, 1966), Vol. I.
20. R. P. Kanwal, *Linear Integral Equations* (Academic Press, New York, 1971), Chap. 3.

21. J. E. Gubernatis and G. A. Baker, Jr., 'Elastic wave scattering calculations, the Born series and the matrix variational Padé approximant method', in *Review of Progress in QNDE*, edited by D. O. Thompson and D. E. Chimenti (Plenum, New York, 1982), Vol. 1, pp. 111-118.
22. R. E. Kleinman, *et al.*, 'An over-relaxation method for the iterative solution of integral equations in scattering problems', *Wave Motion* **12**(2), 161-170 (1990).
23. A. F. Seybert, B. Soenarko, F. J. Rizzo, and D. J. Shippy, 'A special integral equation formulation for acoustic radiation and scattering for axisymmetric bodies and boundary conditions', *J. Acoust. Soc. Am.* **80**(4), 1241-1247 (1986).
24. Private communication with A. Boström based on the method of Reference 1.
25. Y-H Pao and C. C. Mow, 'Scattering of plane compressional waves by a spherical obstacle', *J. Appl. Phys.* **34**(3), 493-499 (1963).
26. Private communication with the principal author of Reference 3 indicates that a sign error in equation (2.15) of that paper has apparently reversed the interaction effects in that investigation.
27. M. Kitahara and K. Nakagawa, 'Born series approach applied to three dimensional elastodynamic inclusion analysis by BIE methods', in *Proc. Fourth Japan. Nat. Symp. on Bound. Elem. Meth.*, Japan. Soc. Comp. Meth. Engr., Tokyo, 1987.
28. G. Arfken, *Mathematical Methods for Physicists* (Academic Press, Orlando, 1985), 3rd ed., Chap. 11.
29. P. J. Schafbuch, 'Application of the boundary element method to elastic wave scattering problems in ultrasonic nondestructive evaluation', Ph.D. Dissertation, Iowa State University, Ames, IA (1991), Apx. A.
30. R. B. Thompson and H. N. G. Wadley, 'The use of elastic wave-material structure interaction theories in NDE modeling', *CRC Crit. Rev. Solid State* **16**(1), 37-89 (1989).
31. E. Hinrichsen, 'Scattering of acoustic waves from multiple objects by a combined Born series and boundary element method', M.S. Thesis, Iowa State University, Ames, IA (1989).
32. J. D. Achenbach and M. Kitahara, 'Reflection and transmission of an obliquely incident wave by an array of spherical cavities', *J. Acoust. Soc. Am.* **80**(4), 1209-1214 (1986).

33. A. Boström and G. Kristensson, 'Elastic wave scattering by a three-dimensional inhomogeneity in an elastic half space', *Wave Motion* **2**(4), 335-353 (1980).
34. E. Domany and O. Entin-Wohlman, 'Application of multiple scattering theory to subsurface defects', *J. Appl. Phys.* **56**(1), 137-142 (1984).
35. I. R. Gonsalves, D. J. Shippy, and F. J. Rizzo, 'Direct boundary integral equations for elastodynamics in 3-D half spaces', *Comp. Mech.* **6**(3) 279-292 (1990).

GENERAL COMMENTS

The purpose in this effort is to improve the state-of-the-art in the numerical simulation of elastic wave scattering as it applies to nondestructive evaluation (NDE). Both solitary and multiple scatterers in an otherwise homogeneous, isotropic host medium are considered. The basic goal is to provide a scattering prediction capability for arbitrarily shaped homogeneous, isotropic defects which is devoid of any approximations other than those of linear elasticity. A second goal is to adapt and enhance a rudimentary boundary element method (BEM) for these purposes. A follow-up goal is to evaluate the resulting methods in order to identify strengths or weaknesses. Finally, this simulation capability is applied to an investigation of the limitations of various approximate scattering models.

The topics addressed in Parts I through IV of this dissertation evolved in the course of achieving these goals. The subjects were separated into topical papers targeted to specific scientific audiences. Part I explains how a general formulation was adapted and optimized for NDE calculations. Further the capability was demonstrated by detailed comparisons with experimental data, approximate theories, and other first principles models. The value to the NDE community was stressed. Part II presented the solution of a fundamental mechanics problem which was required to investigate the fictitious eigenfrequency difficulty (FED). Part III emphasizes the numerical aspects behind the method, including modeling considerations and numerical experiments substantiating FED theory. Part IV tells of an extension of this capability to the solution of multiple scattering problems through the implementation of Schuster's method[31] for elastic waves and used the extended capability to investigate alternative approximate methods.

Rather than reiterate the conclusions of each of the "parts" of this dissertation, this section presents some general statements and recommendations for future research.

In this author's opinion the methodologies described in this dissertation have proven themselves as viable means of simulating low and intermediate frequency elastic wave scattering from arbitrarily shaped defects. The results from such simulations have been shown to be quite accurate when certain modeling guidelines are followed. The value of such a first principles solution has been demonstrated in the evaluation of various approximations for both solitary and interacting scatterers. The boundary integral equation method has a theoretical elegance in the treatment of the infinite extent of the host medium and in the regularization of a boundary integral equation (BIE). The time-harmonic form fits very nicely with other ultrasonic simulations such as the Gauss-Hermite beam model. The quadratic elements, variable order integration scheme, specialized boundary condition subroutines, hybrid iterative/implicit solution scheme, and asymptotic forms of the Green's function all led to significant computational efficiencies. The BEM has a similarity to finite element methods, allowing the use of commercially available software for building and refining models.

While this work has advanced the BEM to the point of being a useful tool for NDE modeling, there are a few topics of further research which deserve mention. The needs of NDE will likely dictate how and when these will be pursued, but from this vantage point there are four areas which clearly show promise.

The major hurdle to broader and more reliable application of the methods described is the FED. As mentioned in Parts I and III, one remedy for this problem is to supplement the system of linear equations and make their solution unique with a Lagrange multiplier based scheme known as BIFILM[32]. Implementing this change into the program would be straightforward. Many of the results presented were for frequencies below the fundamental fictitious eigenfrequency and thus were not affected. In the frequency range where lower mode FEDs do occur, they sometimes have been manually avoided in the generation of scattering amplitude curves. At shorter

wavelengths the density of resonant states becomes so high it is not possible to effectively avoid one FED without encountering another. Thus, some treatment is needed. A more elegant and foolproof approach than BIFILM combines the standard BIE with its gradient equation to ensure unique solutions[33]. Implementing this approach for the elastodynamic case would entail considerable effort. The gradient equation is hypersingular rather than just a Cauchy principal value and requires a more sophisticated interpretation[25].

Improvements for higher frequency calculations would also be useful. Eliminating the FED problem will go far in helping the present quadratic element formulation handle higher frequencies. Finer meshes can then spatially resolve the finer displacement field structure which occurs with higher frequency. Still, the matrix coefficients will likely need to be carried in double precision for models involving significantly more elements, since round-off errors accumulate during each arithmetic operation in the matrix forming and solving processes. For significantly higher frequencies, p-refinement[34] and spectral elements[35] are intriguing as a means to keep matrix size reasonable.

One evolutionary extension of this capability is the treatment of anisotropic and/or inhomogeneous flaws. This capability could then treat anisotropic single grain inclusions or intermittently bonded inclusions, both of which are suspected to occur in practice. Recall that the current approach assumes homogeneous, isotropic inclusions that are perfectly bonded to a homogeneous, isotropic host medium. The elastodynamic behavior of the inclusion is modeled by a BIE. Except for a few special cases where a functional form might be attainable, anisotropic Green's functions are expressed as an integral[7] rather than in closed form and calculating matrix coefficients would be much

more difficult. Treating spatially varying material properties would be unwieldy. Continuing to pursue a pure BEM based approach for this more general class of inclusion seems ill-advised at this point.

The finite element method (FEM) is inherently better suited to deal with anisotropy and inhomogeneous domains. Temple[36] has demonstrated such a code for elastic wave scattering. However, as was pointed out in Part III, the FEM cannot deal directly with the infinite extent of the host medium. Consequently, the best way to deal with anisotropic host material is not clear. But using the BEM for a homogeneous, isotropic host medium and the FEM on an anisotropic, inhomogeneous inclusion in a combined method would exploit the best advantages of both methods. In this case the FEM generated algebraic equations for the inclusion simply replace those currently generated by the BEM for the internal domain. (See Equation (4c) in Part III). Other NDE researchers have already used such a BEM/FEM approach in electromagnetics[37].

Nonideal inclusion-to-host bonds which include zones of no contact (zero traction) and zones of zero relative displacement could be handled with BEM alone, at least for isotropic inclusions. If the interface is compliant, spring elements might also be included to model this behavior, as Kitahara *et al.* did[38], with an otherwise pure BEM approach. It seems, however, that modeling the inclusion with finite elements would allow using more sophisticated interface models when needed. The particular combination of BEM and FEM, with their similar element based interpolation approach, also has a theoretical advantage relating to interface displacements. If the interpolation functions at the surface of the volumetric finite elements match the interpolation functions of the mating boundary elements the coupling between the two material domains would be "conforming"[24]. If an eigenfunction expansion based method like T-matrix were used

for the exterior medium, there would be unintentional non-conformity in the displacements along the boundary due to the switching of basis functions. Non-conforming element schemes raise questions of convergence.

The final topic recommended for further research addresses near surface flaws. The premise of the capability described in Parts I and III is that the defect exists in an elastic full-space. Full-space results are applicable to measurements of defects in components with finite dimensions if the signal from a pulsed excitation is time-gated such that the echoes from component surfaces are eliminated. However, if the defect is located very near one of these surfaces, it may not be possible to isolate the flaw signal. Furthermore, the scattered field may not merely be the superposition of the flaw and surface (acting alone) scattered fields. They may interact as the two flaws did in the investigation of Part IV, work planned as a step toward the near surface flaw problem. The key piece of work, by Gonsalves *et al.*[39], modeled the effects of a nearby free surface with a truncated BEM mesh. (An alternative approach, using a half-space Green's function, was also investigated by Gonsalves, but that approach restricts the surface to be planar). It is suspected that by applying a hybrid scheme similar to the one in Part IV, the computational requirements of the truncated surface mesh approach will be substantially lessened. Goswami *et al.*[40] have investigated such a truncated BEM mesh on a fluid / solid interface. Since components are often immersed in a fluid during ultrasonic inspection, an integrated fluid / elastic solid / near surface flaw model may be needed in some instances. For isotropic materials, the complete model could be entirely BEM based. While such a model would be quite involved, the importance of near surface flaws as a defect class may warrant developing such a treatment.

Although the regular use of this elastic wave scattering simulation capability in everyday engineering practice has yet to be realized, the use of it in an NDE research environment will likely be ongoing. Initially, this BEM approach was expected to require

finer meshes than those actually used to achieve a given accuracy. Additionally, the treatment of cracklike defects was not expected to be feasible. It is recommended that the previously mentioned strategies for capability enhancement be pursued as solutions for arbitrary shapes in those problem classes become needed.

ACKNOWLEDGEMENT

I want to thank Professors Bruce Thompson and Frank Rizzo for their efforts in this work. Both have been as valuable as role models for professional conduct and scientific acumen as they have been as teachers of esoteric physical and mathematical concepts. I also want to thank my other Program of Study Committee members, Profs. James Bernard, Otto Buck, and William Lord, for serving in that capacity and especially Tom Rudolphi who was almost a third major professor in the early days of this effort. Members of the Center for NDE who have frequently and freely offered up their knowledge of scattering, computers, etc. include Tim Gray, Jim Rose, Steve Neal, Dave Bennink, Joe Stapleton, and Steve Nugent.

The ISU Center for NDE has facilitated this study via an IPRT fellowship, for which I am most grateful. Fisher Controls has contributed significantly through its academic leave of absence program due to Gary Icenogle's unwavering patronage. However, the largest debt is owed to my family who sacrificed time with their father, husband, and son in order for me to achieve this goal.

GENERAL REFERENCES

1. W. G. Moffatt, G. W. Pearsall, and J. Wulff, *The Structure and Properties of Materials: I. Structure* (Wiley, New York, 1964).
2. D. E. Bray and R. K. Stanley, *Nondestructive Evaluation: A Tool for Design, Manufacturing, and Service* (McGraw-Hill, New York, 1989).
3. S. T. Rolfe and J. M. Barson, *Fracture and Fatigue Control in Structures: Application of Fracture Mechanics* (Prentice-Hall, Englewood Cliffs, N.J., 1977).
4. R. B. Thompson and H. N. G. Wadley, 'The use of elastic wave-material structure interaction theories in NDE modeling', *CRC Crit. Rev. Solid State* **16**(1), 37-89 (1989).
5. J. Fagenbaum, 'Nondestructive evaluation', *Mech. Eng.* **104**(5), 28-40 (1982).
6. R. B. Thompson and D. O. Thompson, 'Ultrasonics in nondestructive evaluation', *Proc. IEEE* **73**(12), 1716-1755 (1985).
7. Y.-H. Pao, 'Elastic waves in solids', *J. Appl. Mech. Trans. ASME* **50**(4b), 1152-1164 (1983).
8. A. C. Eringen and E. S. Suhubi, *Elastodynamics* (Academic Press, New York, 1975), Vol. II.
9. R. B. Thompson, 'Quantitative nondestructive evaluation methods', *J. Appl. Mech. Trans. ASME* **50**(4b), 1191-1201 (1983).
10. F. J. Rizzo, D. J. Shippy, and M. Rezayat, 'A boundary integral equation method for radiation and scattering of elastic waves in three dimensions', *Int. J. Numer. Methods Eng.* **21**(1), 115-129 (1985).
11. I. S. Sokolnikoff, *Mathematical Theory of Elasticity* (McGraw-Hill, New York, 1956).
12. P. M. Morse and H. Feshbach, *Methods of Theoretical Physics* (McGraw-Hill, New York, 1953).
13. J. D. Achenbach, *Wave Propagation in Elastic Solids* (North-Holland, Amsterdam, 1973).
14. B. A. Auld, *Acoustic Fields and Waves in Solids* (Wiley, New York, 1973).
15. K. F. Graff, *Wave Motion in Elastic Solids* (Ohio State University Press, Columbus, 1975).
16. P. M. Morse and K. U. Ingard, *Theoretical Acoustics* (McGraw-Hill, New York, 1968).
17. A. D. Pierce, *Acoustics* (McGraw-Hill, New York, 1981).

18. L. M. Milne-Thompson, *Theoretical Hydrodynamics*, 4th ed. (Macmillan, New York, 1962).
19. M. Born and E. Wolf, *Principles of Optics*, 6th ed. (Pergamon Press, Oxford, 1980).
20. J. D. Jackson, *Classical Electrodynamics* (Wiley, New York, 1962).
21. W. V. Houston and G. C. Phillips, *Principles of Quantum Mechanics* (North-Holland, Amsterdam, 1973).
22. W. Kaplan, *Advanced Calculus*, 3rd ed. (Addison-Wesley, Reading, Mass., 1984).
23. D. A. Anderson, J. C. Tannehill, and R. H. Pletcher, *Computational Fluid Mechanics and Heat Transfer* (Hemisphere, Cambridge, 1984), Part 1.
24. O. C. Zienkiewicz, *The Finite Element Method*, 3rd ed. (McGraw-Hill, London, 1977).
25. P. A. Martin, F. J. Rizzo, and I. R. Gonsalves, 'On hypersingular boundary integral equations for certain problems in mechanics', *Mech. Res. Commun.* **16**(2), 65-71 (1989).
26. C. A. Brebbia, *The Boundary Element Method for Engineers* (Pentech, London, 1978).
27. M. N. Sayhi, Y. Ousset, and G. Verchery, 'Solution of radiation problems by collocation of integral formulations in terms of single and double layer potentials', *J. Sound Vib.* **74**(2), 187-204 (1981).
28. F. B. Hildebrand, *Methods of Applied Mathematics*, 2nd ed. (Prentice-Hall, Englewood Cliffs, 1965), Chap. 3.
29. P. J. Schafbuch, R. B. Thompson, F. J. Rizzo, and T. J. Rudolphi, 'Elastic wave scattering by arbitrarily shaped voids', in *Review of Progress in QNDE*, edited by D. O. Thompson and D. E. Chimenti (Plenum Press, New York, 1989), Vol. 8A, pp.15-22.
30. P. J. Schafbuch, R. B. Thompson, F. J. Rizzo, and T. J. Rudolphi, 'Elastic wave scattering by arbitrarily shaped flaws', in *Review of Progress in QNDE*, edited by D. O. Thompson and D. E. Chimenti (Plenum Press, New York, 1990), Vol. 9A, pp.45-52.
31. G. T. Schuster, 'A hybrid BIE + Born series modeling scheme: Generalized Born series', *J. Acoust. Soc. Am.* **77**(3), 865-886 (1985).
32. M. Rezayat, F. J. Rizzo, and D. J. Shippy, 'On time-harmonic elastic-wave analysis by the boundary element method for moderate to high frequencies', *Comput. Methods Appl. Mech. Engrg.* **55**(3), 349-367 (1986).

33. D. S. Jones, 'Boundary integrals in elastodynamics', *IMA J. Appl. Math.* **34**(1), 83-97 (1985).
34. S. S. Rao, *The Finite Element Method in Engineering*, 2nd ed. (Pergamon, Oxford, 1989), p. 125.
35. Y. Maday and A. T. Patera, 'Spectral element methods for the Navier-Stokes equations', in *State-of-the-art Surveys in Computational Mechanics* (ASME, New York, 1987).
36. J. A. G. Temple, 'Modeling the propagation and scattering of elastic waves in inhomogeneous anisotropic media', *J. Phys. D: Appl. Phys.* **21**, 859-874 (1988).
37. S. Nath, Y. K. Shin, T. J. Rudolphi, and W. Lord, 'Boundary integral and finite element simulation of electromagnetic NDE phenomena', in *Review of Progress in QNDE*, edited by D. O. Thompson and D. E. Chimenti (Plenum Press, New York, 1990), Vol. 9A, pp.303-310.
38. M. Kitahara, K. Nakagawa, and J. D. Achenbach, 'Scattering characteristics of partially debonded compliant inclusion-matrix interphase', in *Review of Progress in QNDE*, edited by D. O. Thompson and D. E. Chimenti (Plenum Press, New York, 1990), Vol. 9A, pp.69-76.
39. I. R. Gonsalves, D. J. Shippy, and F. J. Rizzo, 'Direct boundary integral equations for elastodynamics in 3-D half spaces', *Comp. Mech.* **6**(3) 279-292 (1990).
40. P. P. Goswami, T. J. Rudolphi, R. R. Roberts, and F. J. Rizzo, 'Ultrasonic transmission through a curved interface by boundary element method', to appear *Review of Progress in QNDE*, edited by D. O. Thompson and D. E. Chimenti (Plenum Press, New York, 1991), Vol. 10A.
41. J. L. Opsal, Therma-Wave, Fremont, CA, private communication, based on method of J. L. Opsal and W. M. Visscher, 'Theory of elastic wave scattering: Applications of the method of optimal truncation', *J. Appl. Phys.* **58**(3), 1102-1115 (1985).
42. J. E. Gubernatis, E. Domany, and J. A. Krumhansl, 'Formal aspects of the theory of the scattering of ultrasound by flaws in elastic materials', *J. Appl. Phys.* **48**(7), 2804-2811 (1977).
43. Equivalent scattering amplitudes were defined in Part IV.
44. ANSYS is a registered trademark of Swanson Analysis Systems, Inc., Houston, PA.
45. G. J. DeSalvo and R. W. Gorman, *ANSYS Engineering Analysis System User's Manual*, Vols. I and II, Rev. 4.3 (Swanson Analysis Systems, Houston, PA., 1987).

46. I-DEAS is a registered trademark of Structural Dynamics Research Corporation, Milford, OH.
47. *I-DEAS Users Guide*, Vols. I and II, Level 4 (SDRC, Milford, Ohio, 1988).
48. *I-DEAS Geomod Solid Modeling and Design Users Guide*, Level 4 (SDRC, Milford, Ohio, 1988).
49. *I-DEAS Supertab Pre/Post Processing Engineering Analysis Users Guide*, Level 4 (SDRC, Milford, Ohio, 1988).
50. B. P. Newberry and R. B. Thompson, *J. Acoust. Soc. Am.* **85**(6), 2290-2300 (1989).
51. H. Goldstein, *Classical Mechanics*, 2nd ed. (Addison-Wesley, Reading, MA., 1980), Fig. 4.7.
52. D. D. Bennick, 'Modeling of ultrasonic scattering experiments with applications to system and transducer characterization', Ph.D. Dissertation, Iowa State University, Ames, IA (1990).

APPENDIX A. OTHER RESULTS

This appendix contains a few additional results which need to be recorded for future reference. These results pertain to the modeling of cracklike voids in a host medium with a wave speed ratio of two. In Part I the verification of 10:1 oblate spheroid BEM models against a comparable MOOT calculation[41] was mentioned. Figures A1 and A2 are examples of such comparisons for $k_L a$ up to three. Figure A1 is a direct comparison of an L-T scattering amplitude with MOOT. Figure A2 is an indirect verification of a BEM generated T-L scattering amplitudes. Except for approximations, scattering solutions for shear wave incident fields are rare and we wished to verify our T-wave incident field code. The principle of mode conversion reciprocity[42] is used to convert the BEM generated T-L scattering amplitudes to corresponding L-T values. For both the L-T and T-L scattering, the agreement is quite good.

One concern with constructing high aspect ratio shapes, such as our open crack models, is the resulting high integration severity[32]. The results depicted in Figure A3 are similar to those in Figure A1, but for substantially thicker 4:1 oblate spheroid models. In both cases, the 40 and 140 element models have some node/element combinations with high severity levels. But the "average" severity level is greater with higher aspect ratio and fewer elements, as would be expected. There is no indication in Figures A1 or A3 that accuracy is proportionally degraded by these influences. It appears the integration severity criteria is sufficiently conservative and that high Gauss point density is not a problem.

In all the Figures A1 through A3, a component of the complex scattering amplitude is plotted rather than the magnitude, thus providing a more sensitive measure of accuracy. The agreement is similar for comparisons of the imaginary part.

Such comparisons for circular cracklike shapes give us confidence to generate data for cracklike ellipsoidal voids. Direct validation of the scattering predictions for these truly three dimensional shapes by independent means is not possible, since no other exact results are available. Comparisons were made with various approximate solutions, such as those in Part I, but any approximation induces unknown errors. When the BEM result and the approximate solution do not agree, it is not certain which is in error. However, in many cases when these errors of approximation are expected to be small, the agreement is quite good. Additionally, internal comparisons were made by repeating the same calculations with 40, 72 and 140 element models. When the solution does not change appreciably with a finer mesh, it is believed that the converged result has been obtained. Figures A1 and A3 demonstrate such a convergence.

Figures A4 through A13 pertain to a family of elliptical "cracks" and are based on results from 140 element models. The scattering amplitudes for selected incident and scattered directions are intended as a reference for future hypersingular BEM work or as data for inverse scattering schemes. Normal incidence indicates the incident field is propagating parallel to the minor semi-axis of the ellipsoid. $\theta°$ incidence means the incident field is propagating $\theta°$ from normal and in the plane containing the major and minor semi-axes. In the crack modeling sections of Parts I and III, some of the influences of finite thickness "crack" models such as these are discussed. For the frequency range given, the aspect ratios used are sufficiently thin for the given results to be fairly insensitive to the actual aspect ratio.

Finally, the near field generated by normal incidence of an L-wave on a 10:1 oblate spheroid is presented in Figure A14. The near displacement field is expressed as an equivalent scattering amplitude[43] and is compared with the farfield value as a function of distance. This information supports claims made in Part IV.

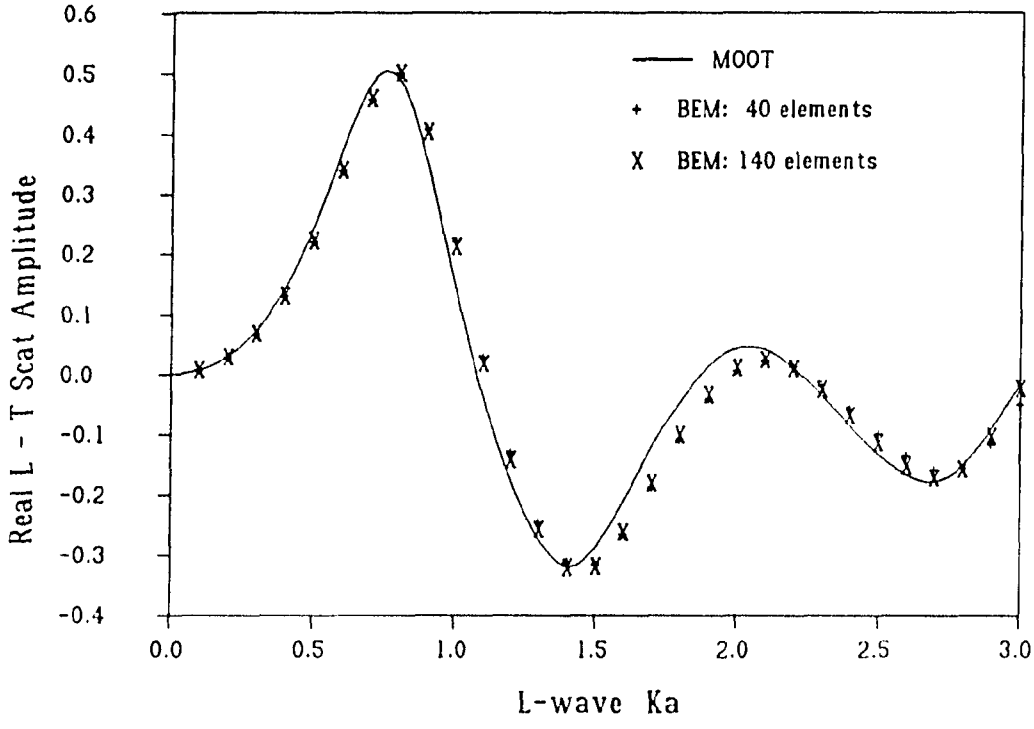

Figure A1 Comparison of MOOT and BEM for a 10:1 oblate spheroidal void - 30° incidence backscatter

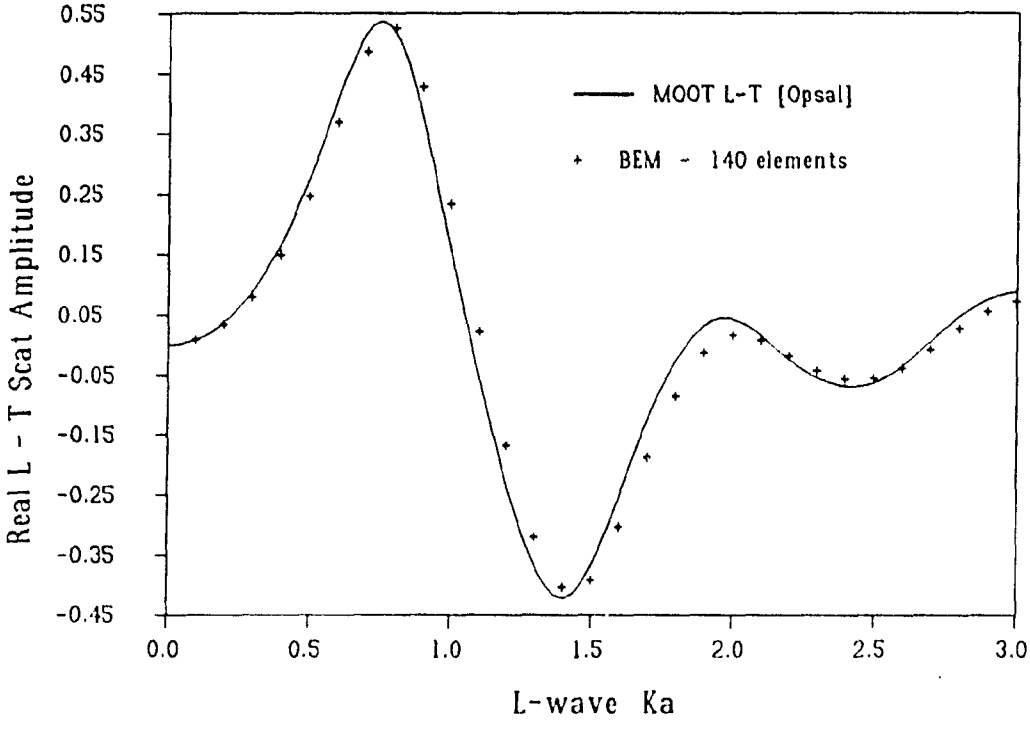

Figure A2 Comparison of MOOT and BEM for a 10:1 oblate spheroidal void - 45° incidence backscatter. BEM calculations are for T-L scattering and converted to L-T by reciprocity arguments

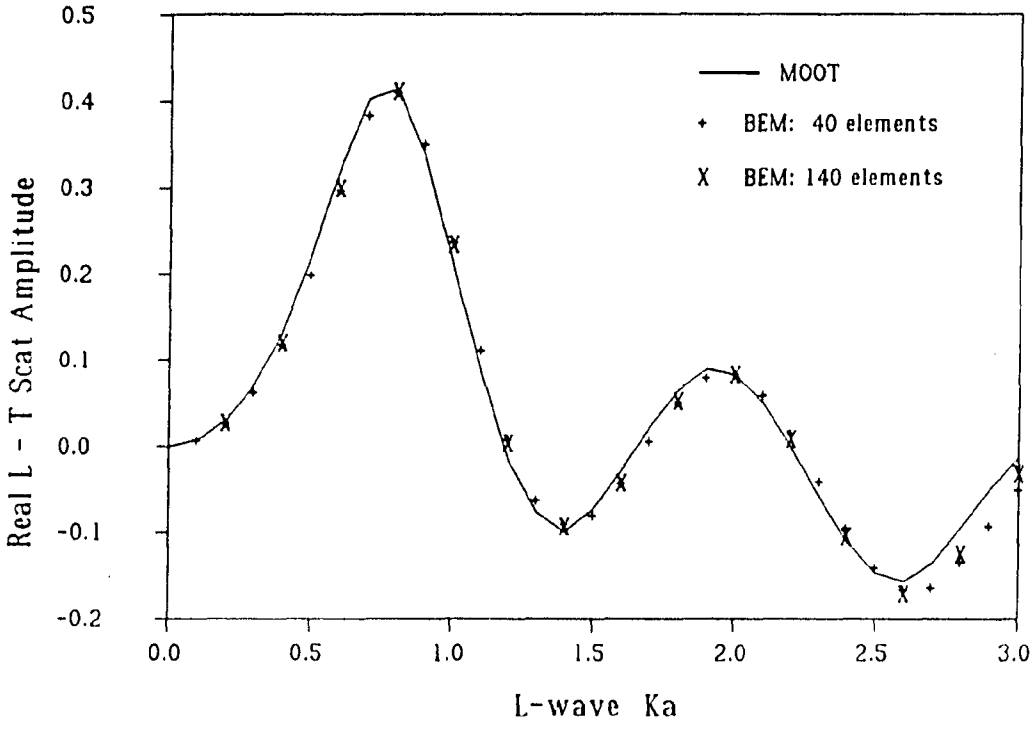

Figure A3 Comparison of MOOT and BEM for a 4:1 oblate spheroidal void - 30° incidence backscatter

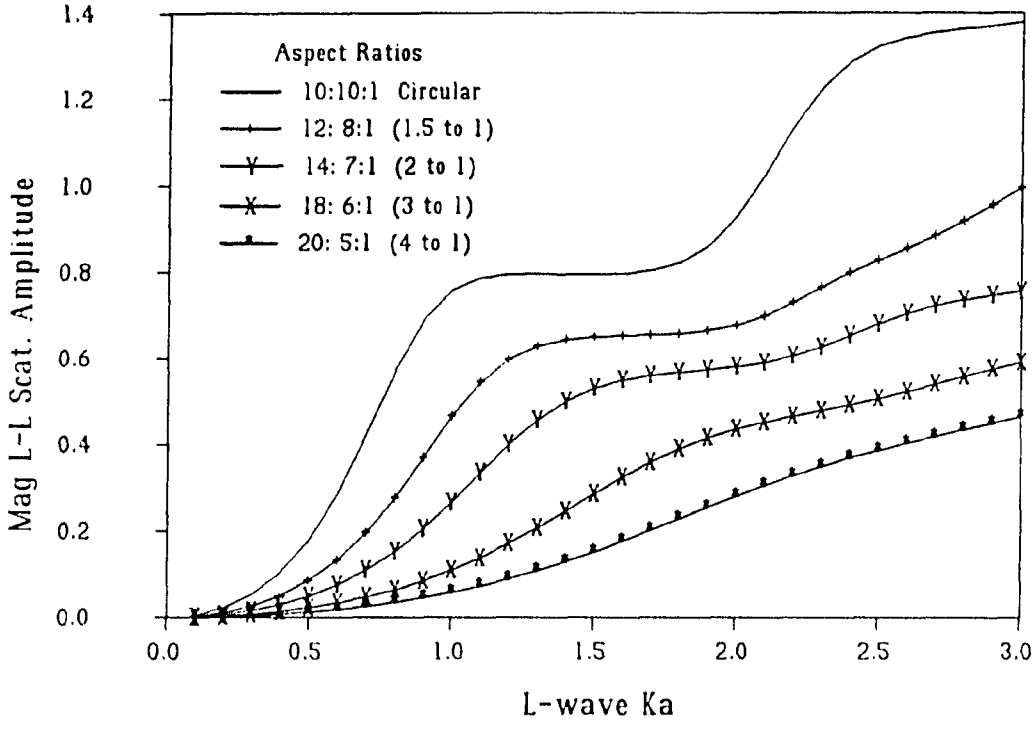

Figure A4 Magnitude of scattering amplitudes predicted by BEM models for a family of elliptical cracks - normal incidence forward scatter

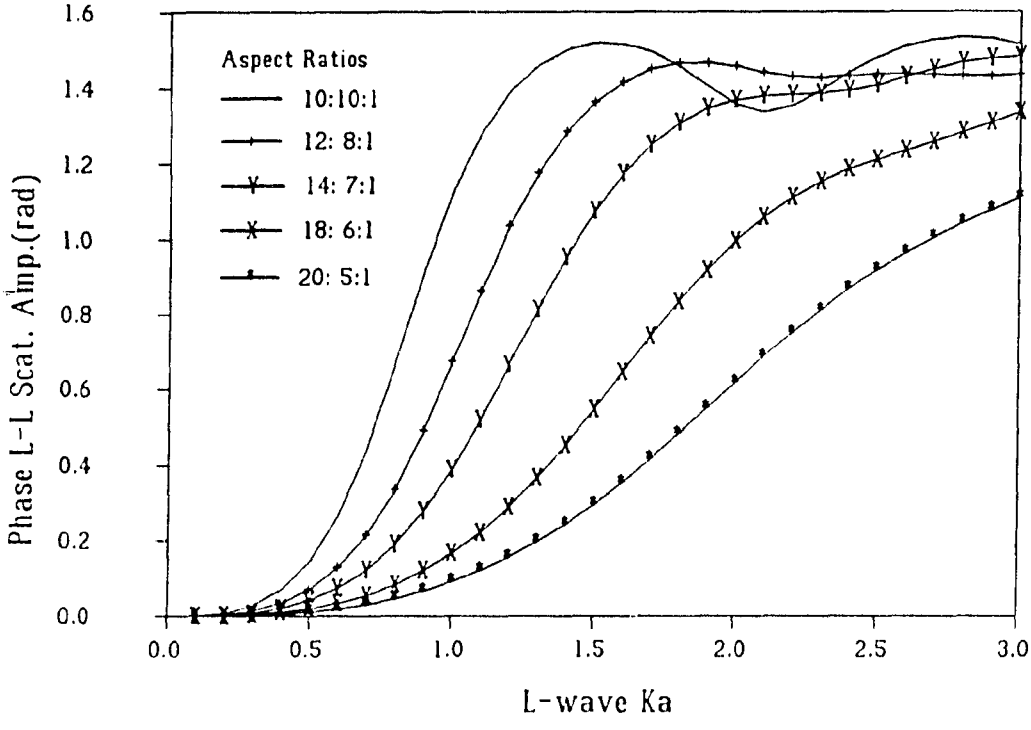

Figure A5 Phase of scattering amplitudes predicted by BEM models for a family of elliptical cracks - normal incidence forward scatter

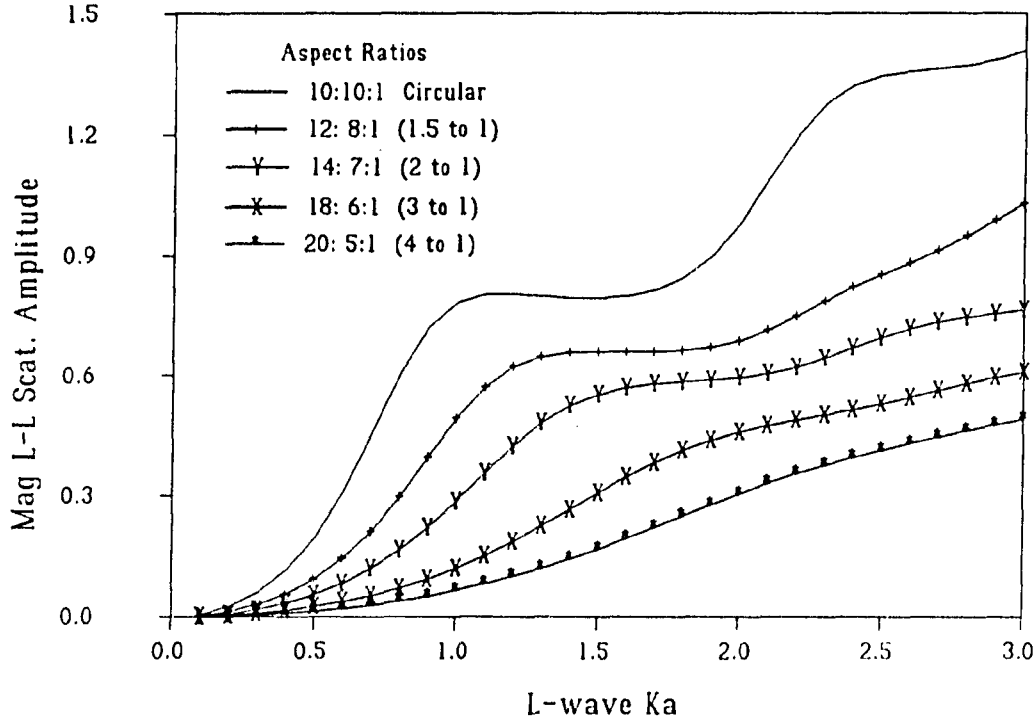

Figure A6 Magnitude of scattering amplitudes predicted by BEM models for a family of elliptical cracks - normal incidence backscatter

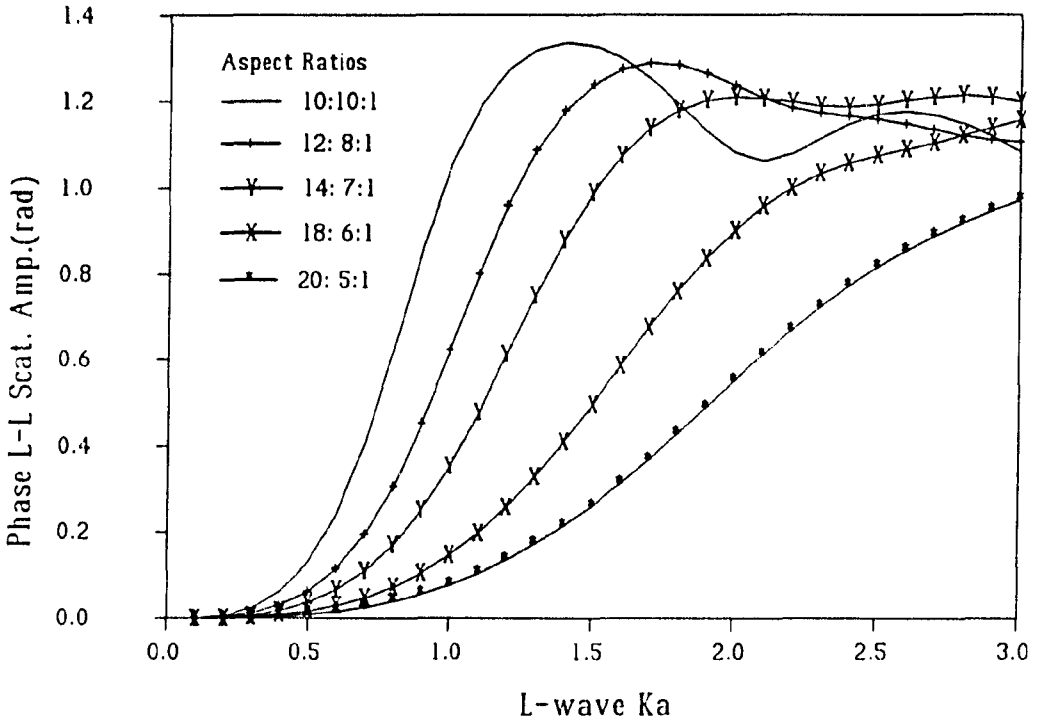

Figure A7 Phase of scattering amplitudes predicted by BEM models for a family of elliptical cracks - normal incidence backscatter

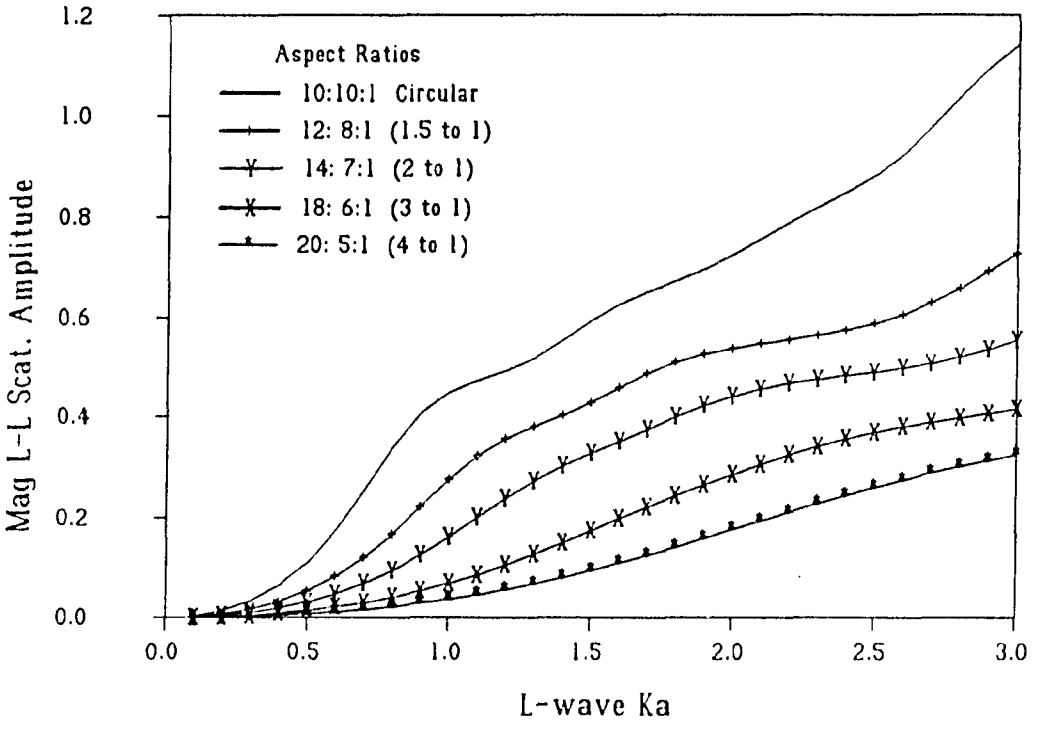

Figure A8 Magnitude of scattering amplitudes predicted by BEM models for a family of elliptical cracks - 45° incidence forward scatter

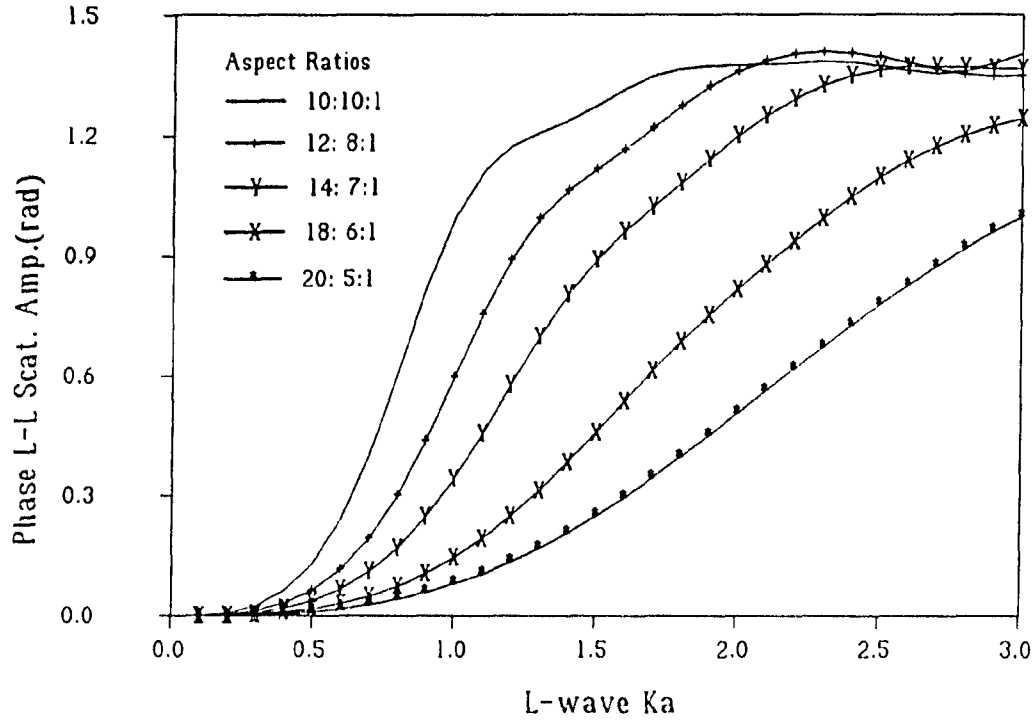

Figure A9 Phase of scattering amplitudes predicted by BEM models for a family of elliptical cracks - 45° incidence forward scatter

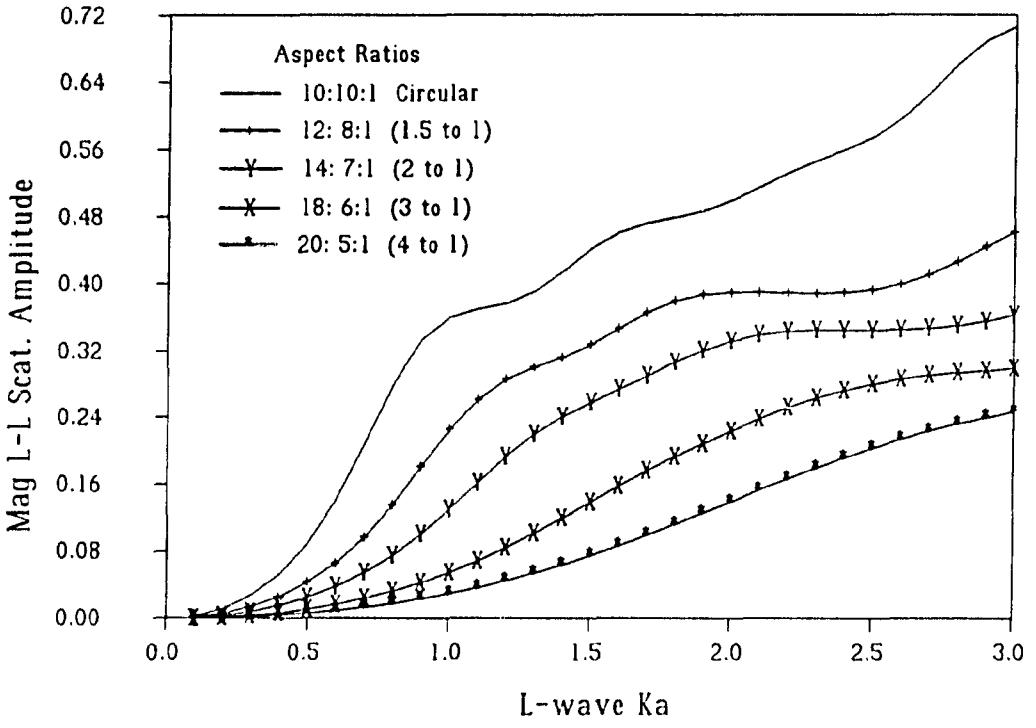

Figure A10 Magnitude of scattering amplitudes predicted by BEM models for a family of elliptical cracks - 45° incidence specular scatter

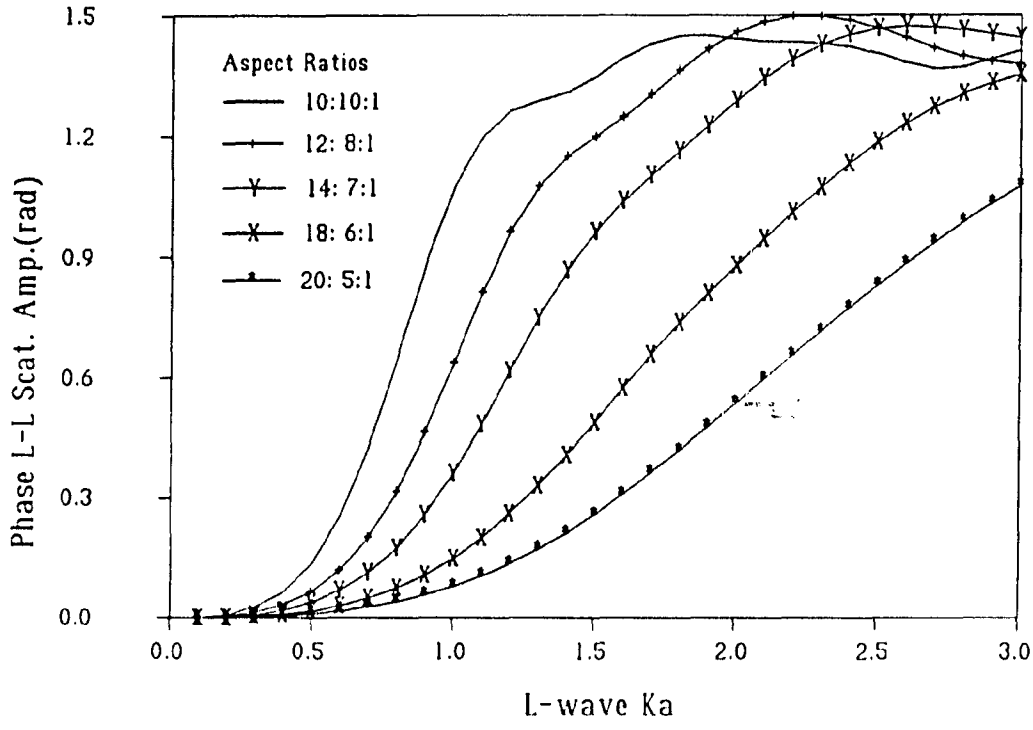

Figure A11 Phase of scattering amplitudes predicted by BEM models for a family of elliptical cracks - 45°incidence specular scatter

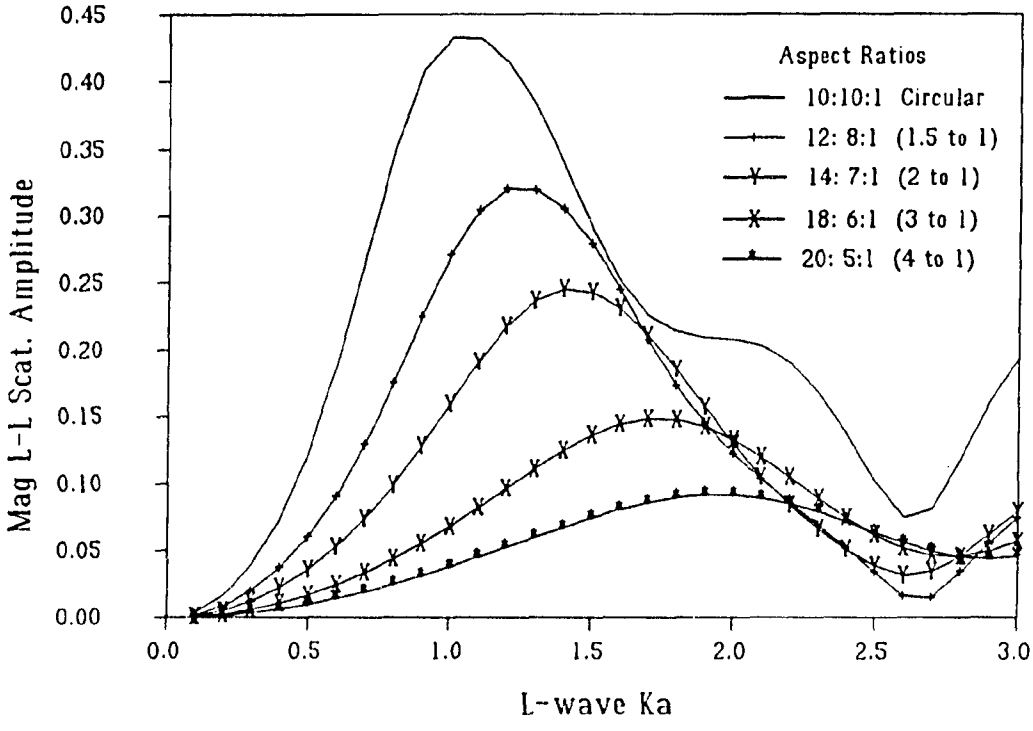

Figure A12 Magnitude of scattering amplitudes predicted by BEM models for a family of elliptical cracks - 45°incidence backscatter

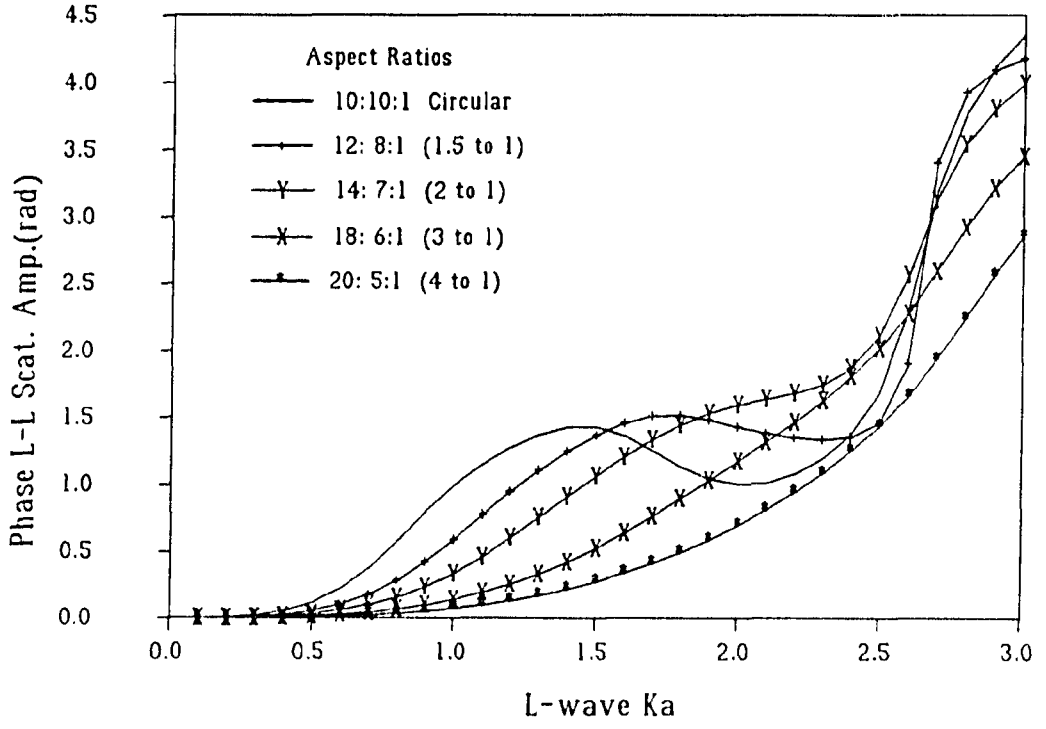

Figure A13 Phase of scattering amplitudes predicted by BEM models for a family of elliptical cracks - 45°incidence backscatter

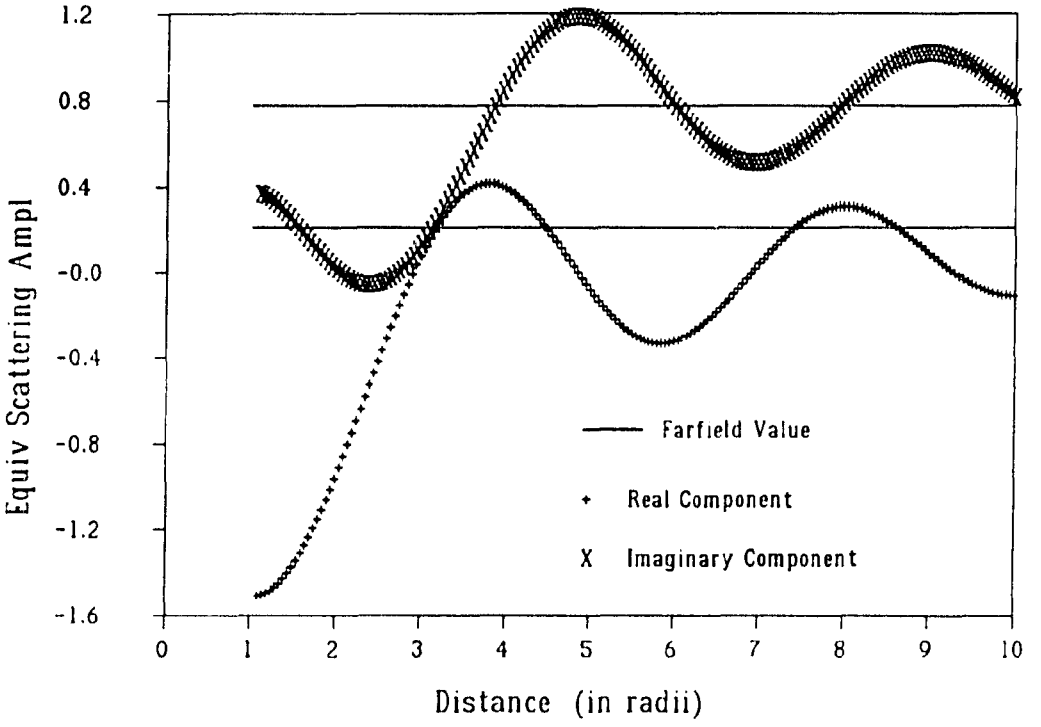

Figure A14 Equivalent backscattering amplitude [L-L] of a 10:1 oblate spheroidal void at $k_L a = \pi/2$ and normal incidence as a function of distance from the centroid along the symmetry axis: Comparison of BEM generated near field components with the farfield approximation

APPENDIX B. SOFTWARE USER'S GUIDE

Introduction

A major portion of the effort in achieving the results of this dissertation was expended in developing the computer code itself. This appendix serves as a brief overview the software, its file structure, and interface to commercial computer aided engineering (CAE) software and special utility programs. Two major programs were developed - one for Solitary Elastic Wave Scatterers (SEWS) and one for Two Interacting Elastic wave Scatterers (TIES). Both use many of the same subroutines and together can generate all of the BEM results presented. By reading this appendix, a person with sufficient background in elastic wave scattering, boundary or finite element analysis, and computer systems should be able to use the program.

Mesh Generation

Defining the node locations and element connectivity can be done manually for models containing only a few elements. For larger models of specific shapes such as spheres, special programs can be written without unreasonable effort to automate the otherwise tedious mesh generation process. But for arbitrary shapes, for which these codes were written, developing an automated mesh generation code would be a major undertaking. Boundary element meshes are defined very similarly to certain kinds of finite element meshes. Finite element codes are used routinely in industry and very sophisticated mesh generation software has been developed by commercial firms. Our approach has been to utilize this commercial software, which is available at ISU and many other universities, and then convert the resulting files into BEM useable format.

Two rather simple FORTRAN77 translator programs were written. The first uses ASCII encoded node and element files from the ANSYS[44] finite element program. Specifically, these files are created by the GWRITE module of the PREP7 mesh pre-processor of ANSYS. They are generated by issuing the interactive commands: NWRITE and EWRITE, respectively. Unless otherwise specified by the PREP7 commands NFILE or EFILE, the node locations are written to the file associated with FORTRAN unit number 15 and the element connectivity definitions to the file associated with unit 14. Associated file names will vary depending on the installation. This translator program is called MESHATB (ATB denotes ANSYS To Boundary).

A complete description of the PREP7 pre-processor is given in Reference 45. No attempt will be made at paraphrasing those large documents here. Instead, only the information needed by an experienced PREP7 user to create translatable meshes is being provided. To generate elements which are translatable to boundary element form, the element type command (ET) must have the JSTIF field set to 93. This command establishes 8-node isoparametric 3D shell finite elements as the type to be generated. These elements are curved side quadrilaterals with midside nodes. A three sided option is available by collapsing one side to a single point. Care must exercised to ensure that the proper side is made degenerate so the translator creates a properly defined three-sided boundary element. Compare Section 4.93 of Reference 45 with the boundary element connectivity definitions in Figure B1. All of these discussions pertain to ANSYS Revision 4.0 through 4.4A. Earlier or later versions may not support or have differing formats for these features.

The second translator works with "universal" ASCII files created by the I-DEAS[46] program. It is called MESHUTB (Universal To Boundary). I-DEAS is a variable collection of engineering analysis modules. The Geomod module is a solid modeler which is useful in defining the flaw shape in 3D space. For example, the "Pinocchio"

shape discussed in Part I was created by Boolean combinations of two spheres and a circular cylinder. ANSYS's PREP7 has an analogous but less sophisticated solids modeling capability. The mesh is built on the resulting surface by subdividing it with curves into areas. From the I-DEAS solid modeling perspective, the term "mesh" does not mean nodes and elements but rather a pattern of spatial gradation upon which the nodes and subsequently elements are defined. Each area had nodes and elements defined on it. Subdividing the solid surface into areas, meshing, and creating nodes and elements is done by a module historically called Supertab. Instructions for using Geomod and Supertab are in References 47 through 49. The following information will allow a user familiar with I-DEAS to create a boundary element mesh.

Within the I-DEAS menu structure, Supertab falls under the Pre/Post processing section of the Engineering Analysis module. Pre/Post has a "Task" menu with an entry called "Geometry Definition" for specifying the surface geometry. Another task, "Mesh Generation", has a submenu item, "Mesh Area", underneath which "Create" should be selected. At this point, thin shell parabolic quadrilateral or triangular elements can be specified. Only these elements will translate properly as boundary elements. Selections relative to material properties and thickness are not used, so default values may be taken. The direction of the implied unit normal for each element is determined by the order of mesh area definition. Care must be taken so that all normals point away from the host material domain. A convenient way to check this graphically is to apply a "face" pressure with the Task - "Analysis Cases", submenu "Structural Loads". (Positive pressure arrows point in the direction of the normal.) Connectivity of individual elements can be reversed from within the "Mesh Generation" task at the "Elements" menu.

Once a set of nodes and elements has been created by Supertab, it is written to universal file format. Again under the task called "Mesh Generation", there is a menu

selection "Universal_File" with a submenu. The "Entity Read/Write" switch called "FE-Only" should be turned on. This selection results in the least amount of extraneous information written from the complete geometry database. Another submenu choice, "Write" then creates the universal file. Typically this file will have the extension, ".unv". Dataset 15 contains the node information and dataset 71 contains the elements. MESHUTB automatically extracts these datasets from the others in the ".unv" file.

Both translators create node (".nod") and element (".ele") files which are directly useable by the SEWS program. The format of these files is given in the next section. Some additional FORTRAN utility programs are available to manipulate these files. DISTORT scales an existing node file in all of the global Cartesian directions. This program was used extensively to create spheroidal and ellipsoidal meshes from a basic spherical mesh. I-DEAS and earlier versions of ANSYS do not support ellipsoidal coordinate systems, so DISTORT was necessary to create these shapes and makes altering an aspect ratio very easy. A reverse direction translator was also written. MESHBTU (Boundary To Universal) converts ".nod" and ".ele" files back to universal files so that the results of DISTORT or other manipulations can be viewed graphically. Another program called TURN will rotate a set of nodes 90 degrees.

SEWS Program Architecture

SEWS is a fairly general program with a number of internal options. In the following subsection, these options are outlined. In the second subsection, the details of I/O files are given. An overview of the relationships among various files, SEWS, the CAE software, and the utility programs is given in Figure B2. Knowledge of the internal arrangement of SEWS is not required to use it. As with all research codes, it will likely be further enhanced and merged with other numerical models. In the last subsection a brief discussion of the internal organization is provided.

Capabilities

SEWS is normally executed in a batch process since it contains no input prompting. It has six basic job types. The COMPLETE_JOB is the standard mode and completes all the steps in a normal scattering problem. The FORM/DECOMPOSE/SAVE/GO type is functionally the same as COMPLETE_JOB but also saves the decomposed matrix for future use. This matrix can be read back in and used with a different incident field, integral type, etc. by specifying the RESTART job type. Rather than solve a specific problem, the FORM/DECOMPOSE/SAVE/STOP mode just creates a decomposed matrix. This mode is useful in providing self-interaction matrices for the TIES program. For executing large models on small computers, the job types FORM_ONLY and DECOMPOSE_ONLY can be used in succession to achieve the same result as FORM/DECOMPOSE/SAVE/STOP. This splits the job into two parts and possibly prevents problems with batch queue time limits, etc.

Models for three flaw types are included: the traction free cavity or VOID; a homogeneous, isotropic INCLUSION; and a RIGID infinite mass inclusion. Material properties are specified in terms of elastic constant, Poisson's ratio, and density. In the time-harmonic formulation, the matrix is also a function of frequency. Each frequency constitutes an individual problem, just as each new material property does. But since calculating scattering spectra is a common task, the COMPLETE_JOB type will solve the same problem for a list of frequencies. None of the other job types have this multiple frequency capability because they work with a single stored matrix. (Storing families of matrices is not always practical in disk space limited systems.)

If a symmetry plane exists in the geometry of the problem, only one half of the flaw surface needs to be modeled. Care must taken so the incident field also shares the same symmetry plane. Incident fields can be planar or generated by the Gauss-Hermite

(GHERMITE) beam model[50]. Unit amplitude, planar incident waves may be primary (longitudinal) or secondary (transverse) as designated by P-WAVE and S-WAVE, respectively. The propagation direction is determined by two spherical coordinate angles. Shear wave polarization is set by another angle, as described in Part III. The phase is relative to the coordinate system origin. Normally the defect centroid is placed at the origin.

The BEM solution fully describes the field at the flaw surface. The nodal values of displacement and traction may be written to the output file and/or universal files. Often the boundary solution is integrated over the defect surface to provide some specific information. The types of integrals are denoted by AULD, DISPLACE, FARFIELD, and INTERIOR. AULD is a numerical implementation of the electromechanical reciprocity integral of B. Auld. The value of this integral is proportional to the signal received in an analogous test situation. Both pulse-echo and pitch-catch experiments can be simulated. This integrated quantity is most useful in conjunction with nonplanar incident fields. The Cartesian vector components of the scattered displacement field at any point in the host is computed with the DISPLACE integral type via the interior representation integral. Scattering amplitudes are efficiently generated by the FARFIELD type which uses the farfield asymptotic values of the fundamental solution kernels. Equivalent scattering amplitudes[43] are provided by the INTERIOR type through the full kernels in the interior representation integral. Equivalent scattering amplitudes may be calculated at any distance from the scatterer (in the host medium) and differ significantly from the farfield scattering amplitudes only in the near field. The theory behind these calculations is presented in Part I. Both direct and mode converted scattering amplitudes are provided.

Parametric studies are often a task for this program. Results from the integral calculations can be sent to sorted datasets along with the corresponding frequency and

location (direction). The dataset to which a particular integral quantity is routed can be set individually. These datasets which contain only numerical data are very convenient as input for graphing programs, etc.

As discussed in Part IV, SEWS can compute the simultaneous scattering from multiple defects. The inhomogeneities must, however, be of the same type and have identical material properties. This restriction is not a limitation of the method and could be relaxed by modifying the code.

File structure

An attempt has been made to structure the input in modular form. This aids in performing parameter studies and in identifying particular results from a brief series of meaningful filenames. I/O file types are identified by their three letter file extensions. All SEWS executions are defined by a single input file known as the problem identification file (".pif"). This file contains single line records including: a title, a jobtype identifier, a series of filenames which supply the specific input data, and an output file group name. The sequence of filenames depends on the particular jobtype. See Figure B3 for details.

The geometry of the simulated flaw is input as a boundary element mesh through ".nod" and ".ele" files from the mesh translator programs. See Figures B4 and B5. It is convenient to scale the nodes so that the characteristic dimension of the defect is equal to one "unit". The computed scattering amplitudes will then be in terms of these "units" of length. Any symmetry plane used is inherently defined when the mesh is constructed.

A parameter (".par") file provides the necessary host material properties and those of the defect, if any. The ".par" file specifically defines the flaw type: VOID, RIGID, or

INCLusion. It also identifies the symmetry plane, if any, and lists the circular frequencies at which the problem should be run. Figure B6 gives the format of this file. The required material properties are Young's modulus, Poisson's ratio, and density. Any consistent set of units is permissible. Some users might be more accustomed to using wavespeeds. Young's modulus, E, and Poisson's ratio, ν, can be calculated from wavespeed data using the following relations:

$$\nu = \frac{2c_T^2 - c_L^2}{2(c_T^2 - c_L^2)}, \tag{B1}$$

$$E = (1+\nu)(1-2\nu)\rho c_L^2/(1-\nu). \tag{B2}$$

By examining Equation (B1), it is evident that wavespeed ratio uniquely determines Poisson's ratio. Similarly with scattering amplitudes for voids, the only relevant material property is wavespeed ratio. Consequently, the material properties can be scaled so that the longitudinal wavespeed in the host material equals one. Then the dimensionless frequency, $k_L a$, is conveniently equal to the input circular frequency. The same strategy can be applied to inclusions, if the inclusion density and wavespeeds are likewise appropriately scaled relative to the host's values. Noting this material property similitude reduces the number of parameter combinations to be studied.

With the exception of a saved matrix (".mat") file, all output files are given the file group name. They are identified by their file extensions. The specific files created depend on the jobtype and the entries in the control (".ctl") file. An output listing (".out") echos the ".pif" file and provides summaries of important execution information. Input data is echoed to the output listing as specified by the ".ctl" file. This file also determines if the complete boundary solution is written to universal datasets of

displacement (".dsp"), traction (".trc"), and/or the output listing. Additional information concerning the ".dsp" and ".trc" files is in the upcoming section on graphical post-processing. Up to ten datasets can be created that contain the sorted, integral quantities. They are designated ".ds0" through ".ds9" and their format is given in Figure B7. All control file options are listed in Figure B8.

Monitoring the output listing is a key ingredient in obtaining reliable simulation results. In addition to verifying the desired input files and data, the user should check integration severity levels. See Part III, Reference 32, and "SEVERITY" in the next section. Detailed severity level information can sometimes point out errors in the node and element definitions, e.g., coincident nodes. The matrix condition number is estimated during decomposition and a large value may indicate the presence of a fictitious eigenfrequency. See Part III. The actual value under normal circumstances is dependent on material properties, model size and shape, but usually increases slightly with frequency. A representative value for a 40 element inclusion model might be 10,000.

Incident fields are specified by the ".fld" file. Multiple fields can be run in a single job by listing them sequentially in the file. Each field on the list has an associated set of locations or directions for which the indicated INTEGRAL is performed. For all except the AULD INTEGRAL, the number of items in this set may range from zero to the value of the IMAX parameter in SEWS. Each item may have a sorting index ranging from one to ten. The ".fld" file is re-opened on each pass of a multiple frequency COMPLETE_JOB, thus the same set of fields is used again at each new frequency. The specification of planar fields is simple and is given in Figure B9.

The GHERMITE beam model is somewhat more complicated to use. The model treats a bicylindrically focused elliptical transducer submerged in a fluid. See Figure B10

for parameters which characterize the transducer. PISTONA and PISTONB are the ellipse's semi-axis lengths along the x_0 and y_0 axes, respectively. FOCALX and FOCALY are the transducer's focal lengths relative to these same axes. The distribution of motion at the transducer face can be adjusted through the parameters, Ns and Nf.

$$normal \quad velocity = [1 - (radial \quad fraction)^{Nf}]^{Ns} \qquad (B3)$$

The radial fraction is the distance from the center of the ellipse to the point in question divided by the distance to the edge of the ellipse in the same direction. At locations outside the ellipse, the probe surface velocity is zero.

The number of terms in the Hermite expansion, NT, can be adjusted. Between 30 and 50 is recommended and the maximum is set by a parameter in the GHFIELD subroutine at compile time. These coefficients are determined by trapezoidal rule integration. The number of intervals is equal to the value of GHFLAG. Thirty intervals is suggested. The matrix of coefficients for a given source can be reused by specifying EXISTING rather than NEWCOEFS. The filename for this matrix is normally identified by a ".ghc" extension.

The ultrasonic beam propagates to a bicylindrically curved fluid/solid interface where it refracts and then propagates further to the flaw location. The wavespeed in the fluid is C0 and the density is D0. The distance the central ray propagates in the fluid is Z0 and the angle that ray makes with respect to the outward normal at the interface is THT0. Setting MODE equal to zero generates the L-wave field in the solid. (The code has not been verified for the shear wave field). RXI and RYI are the radii of curvature of the interface in the plane containing the beam central ray and the x_0 and y_0 axes,

respectively. See Figure B11. If the radius is positive, the interface is concave on the fluid side and negative denotes the reverse. Entering zero as the radii will trigger special code for a planar interface.

The remaining input parameters locate and orient the flaw coordinate system relative to the beam central ray in the solid. Z1 is the distance to the defect coordinate origin along that central ray. Y1 is the offset of that origin from the central ray parallel to the y_0 axis. X1 is the remaining coordinate. See Figure B12. PHI, THT, and PSI are the Euler angles[51] of the beam axes relative to the flaw axes.

The details of this Gauss-Hermite model have been supplied by the code author, D. D. Bennick. See also Reference 52. The merger of this beam model with this BEM code has only been tested for normal incidence to the fluid/solid interface.

Internal organization

SEWS and its subroutines are written in FORTRAN and conform with the ANSI X3.9-1978 specification for easiest portability. There are a few exceptions to this compliance. The adopted GHFIELD subroutine uses the VMS extension DO-ENDDO. The other exception is the use of an inline comment delimiter (!). These constructs are commonly supported in other environments. Additionally, the OPEN statement for the ".pif" file uses special Aegis or VMS syntax and the TIMER subroutine uses system calls.

SEWS is based on three programs developed at the University of Kentucky: SE3D, ISE3D, and SS3D. Some of the subroutine structure and variable names remain the same. In fact, some subroutines have not been changed: FAIR, GAUS, PEQ, and SHAPE.

The main calling program serves to allocate variable space, handle file assignments, and control program flow. The size of matrices and vectors is controlled by a set of five integer parameters. These parameters can be adjusted prior to compile time to accommodate the maximum expected problem size. Program flow is controlled by the type of job, flaw, and integral calculated, and the number of frequencies, incident fields, and scattered directions. Almost no computation is performed at this main level. A brief synopsis of each supporting subroutine, in roughly the calling order, follows.

Since the CPU time needed to execute these calculations is not trivial, considerable effort has gone in to improving algorithms and coding. A quantitative measure of the computational load is provided by timing the execution of various program segments. The TIMER subroutine is machine specific because it makes operating system function calls. Two version are available: one for DEC VAX/VMS and the other for HP/Apollo DomainOS. The DEC version provides CPU times. The Apollo version measures wall clock elapsed time. In a workstation environment, this is not a problem unless significant other processes are sharing the same CPU.

RWMATRIX reads or writes matrix files. These files are sequential, binary files for fast access and lower storage space. A file header is included which gives the parameter, node, and element files upon which the matrix is based. An option to only read the header is provided. RWMATRIX also reads and writes the interaction matrix for TIES. See the section on TIES program architecture.

The parameter, node, and element files are read by MODEL. Nodes need not be numbered sequentially, since MODEL creates an internal node index for numbering the resulting equations. Output from BOUNDSOL is according to the external node numbers, thus the internal resequencing is transparent to the user.

GAUS calculates coordinates and integration weights for Gauss-Legendre quadrature of four-sided elements. FAIR has a similar function for three-sided elements. SHAPE computes the values of the shape functions and their derivatives at the Gauss points for non-singular quadrature of both element classes.

SEVERITY takes care of sorting the severity numbers for more efficient looping in the coefficient routines. A severity number is determined for each collocation point/element combination and ranges up to a value of eight. It sets the number of integration points to be used. SEVERITY also prints a table of severity numbers if requested. If more Gauss points are needed than available, a warning message is printed and the maximum number available is used. The actual computation of the severity numbers is handled by NMDS. This version of NMDS combines the separate versions from SE3D and SS3D.

There are two coefficient matrix generating subroutines for single medium problems. COEFRIGID is a specialized form of CTE3 from SE3D for the case of prescribed zero displacements over the entire flaw. The T tensor components are not calculated. For zero traction boundary conditions, the subroutine COEFVOID is called. In this case the U tensor is not calculated. While the rigid flaw is not a very realistic flaw model, the VOID model is used extensively for porosity and open cracks. For that reason the COEFVOID subroutine is optimized further. Multidimensional arrays are addressed as vectors with a base address and an offset. Intermediate result variables are introduced so as much invariant code could be moved outside of loops as is feasible. Unfortunately, these steps make the code very difficult to read.

COEFINCL calculates the coefficient matrix for INCLUSION problems. COEFINCL is derived from the CTE3 subroutine of SS3D and the only changes have been to standardize parameter passing with the other coefficient routines. All of the

matrix generating subroutines call PEQ, which is analogous to SHAPE but is for singular integration. PEQ utilizes some rather large arrays for the shape functions: SHAPQ, SHAPT, etc. The space for these arrays could be local to the COEFxxxx level. However, stack size limitations on the Apollo SR10.X operating system required permanent allocation via the FORTRAN "save" statement.

Equation solution is done by subroutines from the public domain LINPACK library. SEWS calls CGECO to perform the complex LU decomposition and CGESL to do the forward elimination / back substitution solution. They in turn call LINPACK routines: CAXPY, CDOTC, CGEFA, CSSCAL, CSCAL, ICAMAX, and SCASUM. CGECO also provides an estimate of the condition number of the matrix which is needed to detect fictitious eigenfrequencies. The matrix coefficients are in single precision. Problems with larger numbers of equations may require using double precision.

PFIELD provides the complex values of a unit amplitude time harmonic incident planar wave field. It calculates the stress tensor at each node point in addition to the displacements. The stresses are only needed by the reciprocity integral but take very little extra time to evaluate so are always provided. GHFIELD is the controlling subroutine for the Gauss-Hermite beam model. It calls subroutines: INITGH, COEFSM, SOLIDS, XMITGH. These in turn call TRANCO and the functions HERM and VNGHM. From the input beam modeling parameters, this collection of subroutines calculates the incident field displacement vector and stress tensor at each boundary element node.

The BOUNDSOL subroutine is responsible for printing out the nodal values of displacement and traction. If requested it writes the boundary solution to universal files for graphical post-processing.

ISEV is similar to SEVERITY but is used when the field points are not on the boundary. INMDS is analogous to NMDS but is also for "integrated quantity" calculations. FARFIELD generates the farfield scattering amplitudes from the complete boundary solution. For proper calculation of the severity numbers the distance from the flaw should be much larger than the flaw dimensions. The scattering amplitude is independent of the actual value used.

The subroutine INTERIOR calculates a quantity proportional to the scattered displacement field at selected locations in the host domain. EQUIVSA takes the result from INTERIOR and writes equivalent scattering amplitudes to the sorted datasets. The location of the equivalent scattering amplitudes is in terms of spherical coordinates. It also writes the magnitude of these complex quantities to the output listing. Similarly DSPLCMNT writes these magnitudes to the ".out" file, but writes the Cartesian vector components of the scattered displacement to the datasets along with Cartesian location coordinates.

AULD calculates the value of the value of $\delta\Gamma_F$ from the measurement model as discussed in Part I. To be consistent with unit amplitude plane waves, the electrical power, P, is assumed to be one. This reciprocity integral does not use the integration severity system since the integrand is a product of two quantities which are quadratically interpolated. In Part I it was shown that for plane wave incidence, $\delta\Gamma_F$ is strictly proportional to the scattering amplitude. Therefore, the integration approach in this subroutine is an alternative to that in FARFIELD for calculating scattering amplitudes.

Graphical Post-Processing

The main purpose in establishing the link to I-DEAS is to create a graphical display capability for the field solution at the boundary. For our intents and purposes,

the pre-processing capability of the ANSYS program is sufficient. However, sending information from SEWS back through I-DEAS's universal file structure to be post-processed was deemed easier to accomplish than with ANSYS. Neither program was intended to display complex (i.e., real and imaginary) displacement fields. However, some types of the finite elements defined in I-DEAS can carry bending stresses and hence have rotation as well as translation degrees of freedom at each node. These element types hence provide the six (in 3D) scalar variables needed at each node. The ".ctl" file gives options for displaying the three Cartesian components of the displacement field as either a magnitude and phase or a real and imaginary pair. A similar option exists for the traction field. I-DEAS is "tricked" into displaying magnitude/phase or real/imaginary as displacement/rotation. The ".dsp" and ".trc" files written by the BOUNDSOL subroutine conform to I-DEAS dataset 55 format. Multiple boundary solutions from a single job are all written to the same files.

Within I-DEAS, the Pre/Post section of the Engineering Analysis module has a task called "Post-Process". There is a menu selection "Universal_File" with a submenu, just as in "Mesh Generation". This time the "Entity Read/Write" switch should be set to "ALL" before the dataset(s) 55 are read in. The node and element definition information may come from a ".unv" file, but normally the two complete model files (".mf1" and ".mf2") created during mesh generation are kept for post-processing purposes. If multiple solutions are in the same file, the menu choice "Analysis Data Set" is used to make the desired set "Current". Before contour plots can be made, the elements of interest must be put in a "Group". Finally, the "Data Component" must be selected. Temporal magnitudes or real components are mapped to the translational degrees of freedom while phase or imaginary components are mapped to the rotational degrees of freedom. The spatial component mappings are as expected: $u_1 \rightarrow UX$, etc. The ability of I-DEAS to calculate the magnitude of normal "displacement" is especially interesting in this boundary element context.

The benefits of this graphical post-processing capability are espoused in Reference 30 and in Part III.

TIES Program Architecture

The TIES program utilizes much of the file structure, many of the subroutines, and most of the nomenclature from the SEWS program. TIES has fewer options than SEWS and is at a state of development similar to one of the early versions of SEWS. It would be straightforward to bring TIES up to the current level of SEWS.

Capabilities

The purpose of TIES is to efficiently calculate combined scattering amplitudes for two interacting scatterers. There are only two JOBTYPEs, namely, ITERATE_TO_CONVERGENCE and NTH_ORDER_ONLY. The first type is the basic iterative solution to multiple scattering problems as discussed in Part IV. The second type was used to investigate truncated Born series solutions of scatterer interaction also from Part IV. As implemented, only the VOID type of defect is available. Since TIES deals with stored self-interaction matrices, multiple frequencies in a single job are not supported. Instead, multiple relative positions can be done sequentially. The INTEGRAL type INTERIOR is the only post solution option. All the incident field options are, however, available.

The two flaws must be defined in the same host material and at the same frequency. One defect is selected as the PRIMARY flaw and the other is denoted as SECONDARY. The origin of the PRIMARY flaw coordinate system is considered the global coordinate system origin. The incident and scattered fields are referenced to this position. The relative location of the SECONDARY flaw origin with respect to the

PRIMARY is given in terms of three Cartesian translation components. The secondary flaw could also be rotated relative to its defined orientation, but this capability has not been included. This program handles self-interaction matrix files for models with a symmetry plane but the two models must have a common symmetry plane.

It is possible to use TIES, as written, with problems of three or more scatterers. This requires separating the scatterers into two groups and using SEWS to create a fully implicit, combined matrix for each group. TIES then would solve the system, including interaction between the groups.

File structure

The file structure of TIES is very similar to that of SEWS. All of the required input files have the same format as with SEWS. The only exception to this is with the ".pif" file. Its format is similar to the analogous SEWS file but in addition contains a list of relative flaw locations. See Figure B13 for details. The ".fld", ".ctl", and ".mat" are identical but options must be limited to those supported. The ".nod", ".ele", and ".par" files used to make the self-interaction matrices must be available to the TIES program at runtime, even though they are not listed in the ".pif". Figure B14 gives an overview of the file to program relationships.

The output files are very similar to SEWS - only the important differences are highlighted here. In order to use the graphical post-processing capability, a given node number cannot be repeated in the two models. If ".dsp" or ".trc" are not to be used, it is permissible to reuse node numbers or even use the same matrix for both the primary and secondary defects. Alternately, the program could have been constructed so pairs of ".dsp" (or ".trc") files were written, but the two surface solutions could not be displayed simultaneously by I-DEAS. Since all TIES jobs are for a single frequency, the separation

distance is substituted for the k_L value in the sorted datasets. Separation is defined as the magnitude of the distance between the origins of the PRIMARY and SECONDARY inhomogeneities.

Internal organization

TIES is written with an organizational philosophy and a compliance to FORTRAN similar to SEWS. In addition to parameters which control the allowable problem size, the main program contains a compiled-in convergence criterion. Many of TIES's subroutines are identical to those used by SEWS: BOUNDSOL, FAIR, GAUS, GHFIELD, INMDS, INTERIOR, ISEV, MODEL, PFIELD, RWMATRIX, SHAPE, TIMER, and some of the LINPACK routines. See the section on SEWS internal organization for a discussion of their functions. Three subroutines are slightly modified versions of SEWS subroutines: EQUIVSAZ, INMDST, and ISEVT. Three others are substantially new.

CROSTALK calculates the cross-interaction matrices by applying the interior representation integral methods to all the nodes of the other scatterer. ISEVT and INMDST are used to determine the severity numbers for numerical integrations in CROSTALK. They correspond to ISEV and INMDS, respectively. They were modified so that results match identically with implicitly generated multiple scattering results from SEWS. INMDST is made consistent with NMDS, whereas INMDS differs slightly. In INMDS, some severity numbers may be boosted to a minimum of four with models utilizing symmetry. The corresponding coefficients in a compound matrix are not based on a boosted number of Gauss points since NMDS is used.

SOLVERIC solves Equation 18 from Part IV iteratively. It contains a compiled-in parameter which establishes the maximum number of iterations. The "IC" stands for

in-core which means that the code is written so both self-interaction matrices and both cross-interaction matrices are all in memory simultaneously. (A virtual memory machine may "page" portions of these matrices to disk, but this cannot be controlled from the program. Usually an engineering workstation or supercomputer will have sufficient random access memory (RAM) that paging is avoided.) Originally this program was written to store all four matrices on disk and have RWMATRIX read them in individually as needed during the iterative process. Disk access is so slow relative to RAM access that the computational savings of the hybrid method are wiped out by the repeated I/O waiting. SOLVERIC always uses the most recent nodal field values in the next step, thus speeding convergence. SOLVERN is functionally similar to SOLVERIC but stops after a pre-designated number of iterations. Since it is intended to compute Nth order generalized Born series approximations, the adjustment to the net incident field due to Mth order cross scatter is not applied until the (M+1)th computation cycle, rather than immediately as with SOLVERIC.

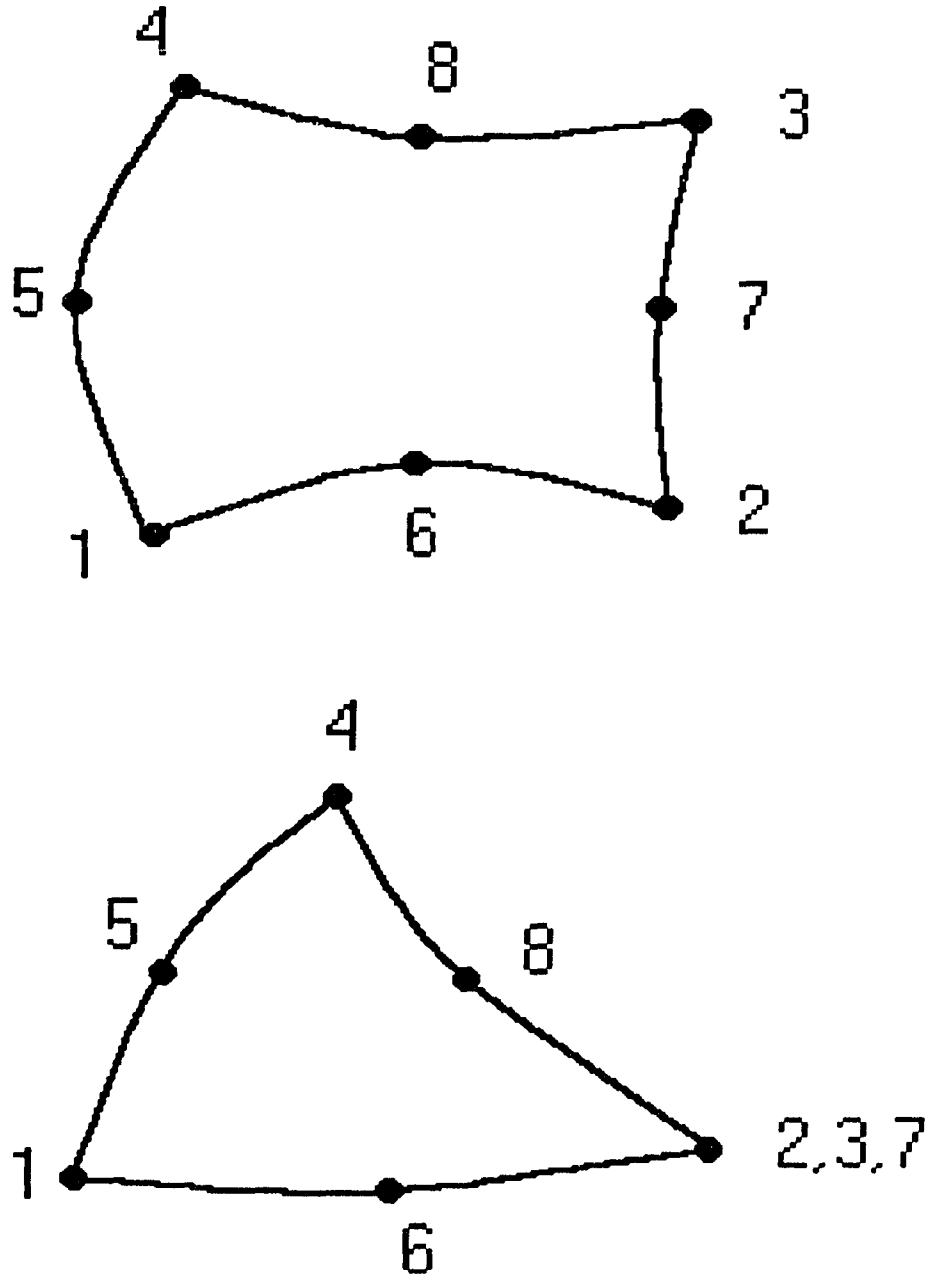

Figure B1 Boundary element connectivity definitions - local node numbering as shown implies a normal directed out of the page

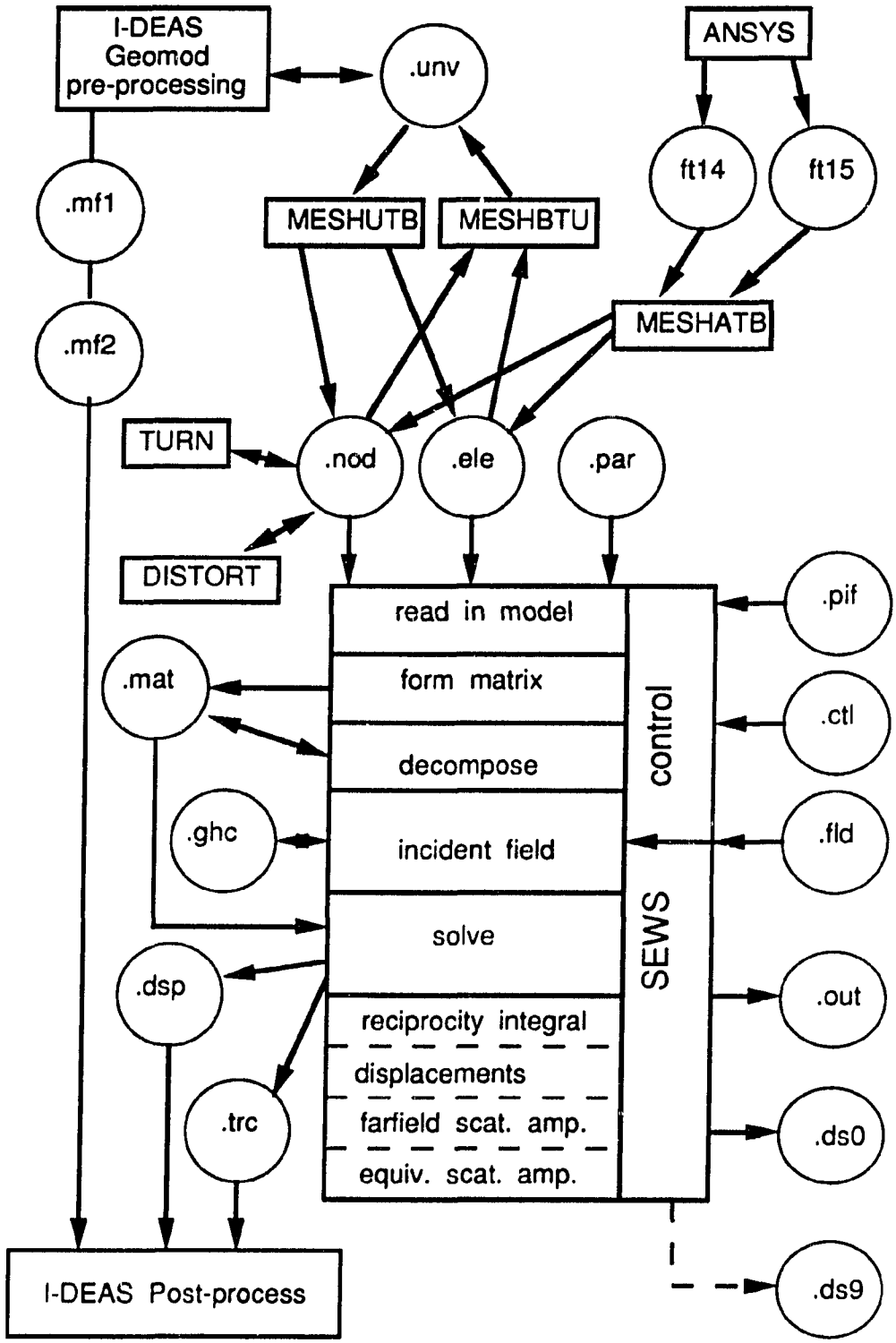

Figure B2 PROGRAM/file relationships for solitary elastic wave scatterer calculations

```
FORMAT:

title
COMPLETE_JOB
parameter filename
node filename
element filename
field filename
control filename
filegroup

     ---  or  ---

title
FORM/DECOMPOSE/SAVE/STOP
parameter filename
node filename
element filename
matrix filename
control filename
filegroup

     ---  or  ---

title
FORM/DECOMPOSE/SAVE/GO
parameter filename
node filename
element filename
matrix filename
field filename
control filename
filegroup

     ---  or  ---

title
RESTART
matrix filename
field filename
control filename
filegroup
```

Figure B3 Generic problem identification file (".pif") format for SEWS

```
FORMAT (continued):

title
FORM_ONLY
parameter filename
node filename
element filename
matrix filename
control filename
filegroup

     ---  or  ---

title
DECOMPOSE_ONLY
matrix filename
control filename
filegroup


NOTE:

     "Title" is a string of up to 80 characters.
     The JOBTYPE is a string of 25 characters and is left justified.
     All filenames are strings of up to 40 characters.
     "Filegroup" is a string of up to 36 characters that is used with
     various extensions to label output files:
          "filegroup".out   standard output
          "filegroup".ds0   sorted dataset #1
          "filegroup".dsp   boundary displacements  -  universal file
          "filegroup".trc   boundary tractions  -  universal file


EXAMPLE:

Example 1 can be run from all the generic file format examples
COMPLETE_JOB
canonicalvoid.par
sphere4.nod
sphere4.ele
crack.fld
brief.ctl
example1
```

Figure B3 (continued)

```
FORMAT:


number of nodes
global node number   X coordinate   Y coordinate   Z coordinate
global node number   X coordinate   Y coordinate   Z coordinate
.
.
.
global node number   X coordinate   Y coordinate   Z coordinate



NOTE:  all fields are free format, coordinates are single precision



EXAMPLE:

         13
          1  0.0000000E+00  0.0000000E+00   1.000000
          2  0.7071068      0.0000000E+00  0.7071068
          3   1.000000      0.0000000E+00  0.0000000E+00
          4  0.7071068      0.0000000E+00 -0.7071068
          5  0.0000000E+00  0.0000000E+00  -1.000000
          6 -0.7071068      0.0000000E+00 -0.7071068
          7  -1.000000      0.0000000E+00  0.0000000E+00
          8 -0.7071068      0.0000000E+00  0.7071068
          9  0.0000000E+00 -0.7071100      0.7071100
         10  0.7071068     -0.7071068      0.0000000E+00
         11  0.0000000E+00 -0.7071100     -0.7071100
         12 -0.7071100     -0.7071100      0.0000000E+00
         13  0.0000000E+00  -1.000000      0.0000000E+00
```

Figure B4 Generic node file (".nod") format

```
FORMAT:


number of elements
element number    global node 1      global node 2    ...    global node 8
element number    global node 1      global node 2    ...    global node 8
element number    global node 1      global node 2    ...    global node 8
.
.
.
element number    global node 1      global node 2    ...    global node 8



NOTE:     all fields are free format integers



EXAMPLE:

   4
   1      1      3      3     13      9      2      3     10
   2     13      3      3      5     11     10      3      4
   3      5      7      7     13     11      6      7     12
   4     13      7      7      1      9     12      7      8
```

Figure B5 Generic element file (".ele") format

```
FORMAT:


INCLUSION
host:       elastic constant       Poisson's ratio    density
inclusion:  elastic constant       Poisson's ratio    density
symmetry plane index        number of frequencies
frequency1
frequency2
.
.
.
frequencyN

    --- or ---

VOID
host:       elastic constant       Poisson's ratio    density
symmetry plane index        number of frequencies
frequency1
frequency2
.
.
.
frequencyN

    --- or ---

RIGID
host:       elastic constant       Poisson's ratio    density
symmetry plane index        number of frequencies
frequency1
frequency2
.
.
.
frequencyN
```

Figure B6 Generic parameter file (".par") format

NOTE:

All fields are free format except flawtype which must be left justified.

Symmetry plane index = 0 if symmetry plane feature is not used otherwise index = 1, 2, or 3 for x, y, or z planes, respectively.

Multiple frequencies are only allowed for COMPLETE_JOB jobtype.

EXAMPLE:

```
VOID
0.666666667    0.3333333    1.0
2    2
0.1
0.3
```

Figure B6 (continued)

OUTPUT RECORD FORMAT:

if INTEGRAL equals AULD:

ω θ ϕ $Re(\delta\Gamma_f)$ $Im(\delta\Gamma_f)$ $|\delta\Gamma_f|$

if INTEGRAL equals FARFIELD:

ω θ ϕ $Re(A_{?,-L})$ $Im(A_{?,-L})$ $|A_{?,-L}|$ $Re(A^{\theta}_{?,-T})$ $Im(A^{\theta}_{?,-T})$ $|A^{\theta}_{?,-T}|$ $Re(A^{\phi}_{?,-T})$ $Im(A^{\phi}_{?,-T})$ $|A^{\phi}_{?,-T}|$

if INTEGRAL equals DISPLACE:

K_L p_1 p_2 p_3 $Re(u^S_1)$ $Im(u^S_1)$ $Re(u^S_2)$ $Im(u^S_2)$ $Re(u^S_3)$ $Im(u^S_3)$

if INTEGRAL equals INTERIOR:

K_L ρ θ ϕ $Re(A_{?,-L})$ $Im(A_{?,-L})$ $|A_{?,-L}|$ $Re(A^{\theta}_{?,-T})$ $Im(A^{\theta}_{?,-T})$ $|A^{\theta}_{?,-T}|$ $Re(A^{\phi}_{?,-T})$ $Im(A^{\phi}_{?,-T})$ $|A^{\phi}_{?,-T}|$

NOTE:

"?" may have the value "L" or "T" depending on the incident field.

"L" denotes longitudinal which is synonymous with P-WAVE.

"T" denotes transverse which is synonymous with S-WAVE.

"Θ" denotes component polarized parallel to e_θ (see Part III).

"Φ" denotes component polarized parallel to e_ϕ (see Part III).

Figure B7 Sorted dataset file (".ds0" - ".ds9") format

```
FORMAT:

print_flags:    node       element       severity       displacement
dataset_flags: displacement   traction      scattering_amplitudes
intergral_type: (     AULD), (DISPLACE), (FARFIELD), or (INTERIOR)


NOTE:

print_flag encoding:
     (1=print    0=no_print)
displacement and traction flag encoding:
     (2=magnitude/phase  1=real/imaginery   0=no_write)
scattering_amplitudes encoding:
     (#=number of datasets to sort to)  (10 or less)

All flags are free format but integral_type character strings must be in
columns 1 through 8.

Filename extensions may be keyed to integral_type:
     (.ald) corresponds to AULD which implements the reciprocity integral.

     (.dis) corresponds to DISPLACE which uses the interior representation
     integral to calculate Cartesian displacements.

     (.far) corresponds to FARFIELD which uses the farfield asymptotic
     kernels in the representation integral to compute scattering
     amplitudes.

     (.int) corresponds to INTERIOR which calculates equivalent scattering
     amplitudes at any interior point, near or far away.


EXAMPLE:

1    1    0    0
1    0    5
FARFIELD
```

Figure B8 Generic control file (".ctl") format

```
FORMAT:


number of fields NF
  subtitle for first field
  type of incident field (  PLANAR) or (GHERMITE)
    if planar field:
      type of wave (  P-WAVE) or (  S-WAVE)
        if P-WAVE: polar and azimuthal angles
        if S-WAVE: polar, azimuthal, and polarization angles
    if Gauss-Hermite field:
      (EXISTING) or (NEWCOEFS) gauss_hermite_coefficient_filename
      transducer parameters: NT,Ns,Nf,PISTONA,PISTONB,FOCALX,FOCALY
      fluid/interface parameters: C0,D0,Z0,THT0,MODE,RXI,RYI
      flaw location parameters: X1(1),X1(2),X1(3),PHI,THT,PSI
  if INTEGRAL is (    AULD):
    number of receiving transducer locations NR
      receiver's field type (  PLANAR) or (GHERMITE), dataset_sorting_index
                                                      (optional)
        if planar field:
          type of wave (  P-WAVE) or (  S-WAVE)
            if P-WAVE: polar and azimuthal angles
            if S-WAVE: polar, azimuthal, and polarization angles
        if Gauss-Hermite field:
          (EXISTING) or (NEWCOEFS) gauss_hermite_coefficient_filename
          transducer parameters: NT,Ns,Nf,PISTONA,PISTONB,FOCALX,FOCALY
          fluid/interface parameters: C0,D0,Z0,THT0,MODE,RXI,RYI
          flaw location parameters: X1(1),X1(2),X1(3),PHI,THT,PSI
      [repeat above entries for 2nd, 3rd, ... NRth receiver]
  if INTEGRAL is (DISPLACE):
    number of scattered directions NI
      XI1, XI2, XI3, dataset_sorting_index (optional)
      XI1, XI2, XI3, dataset_sorting_index (optional)
      ...
      XI1, XI2, XI3, dataset_sorting_index (optional)
  if INTEGRAL is (FARFIELD) or (INTERIOR):
    number of scattered directions NI
      rho, theta, phi, dataset_sorting_index (optional)
      rho, theta, phi, dataset_sorting_index (optional)
      ...
      rho, theta, phi, dataset_sorting_index (optional)

  [repeat above entries starting with "subtitle" for 2nd, ... NFth field]
```

Figure B9 Generic field file (".fld") format

```
NOTE:

     All fields are free format except for field_type and wave_type
     character strings which must occupy columns 1 through 8.

     "Rho" is arbitrary (but must be >> flaw size) for FARFIELD.

     Filename extensions may be keyed to appropriate integral_type:
     (.ald) (.dis) (.far) (.int) as with control files.



EXAMPLE with INTEGRAL equal to (FARFIELD):


  2      number of fields
POLAR ANGLE = 0 DEGREES (+Z DIRECTION)
  PLANAR
  P-WAVE
  0    0              Euler angles of beam propagation
  2
  10000     0     0   1   rho,theta,phi coordinates of detector
  10000   180     0   2   last column is the dataset_sorting_index
POLAR ANGLE = 45 DEGREES ; AZIMUTHAL ANGLE = 0 DEGREES
  PLANAR
  P-WAVE
  45    0
  3
  10000    45     0   3
  10000   135     0   4
  10000   135   180   5
```

Figure B9 (continued)

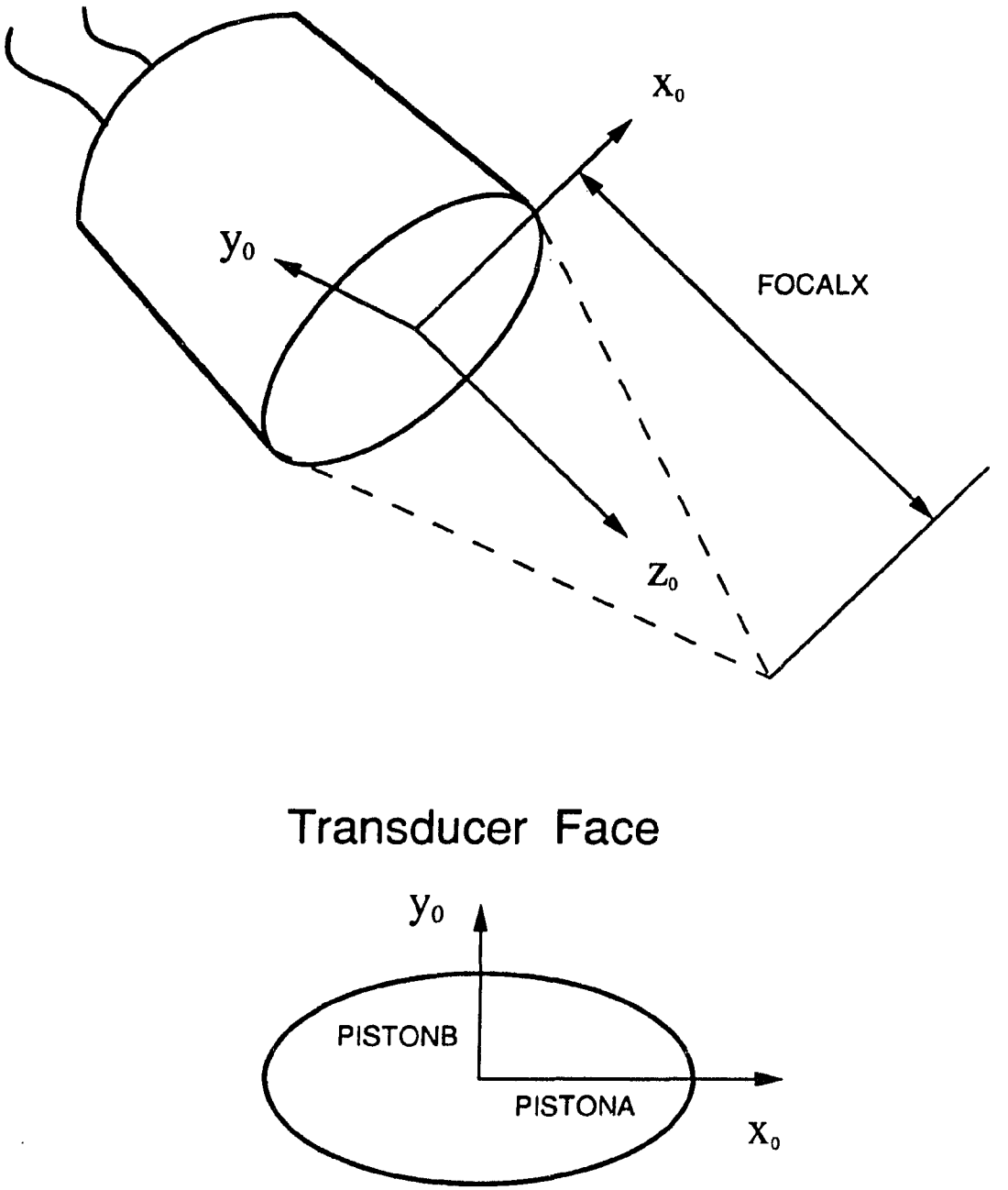

Figure B10 Focused elliptical ultrasonic transducer

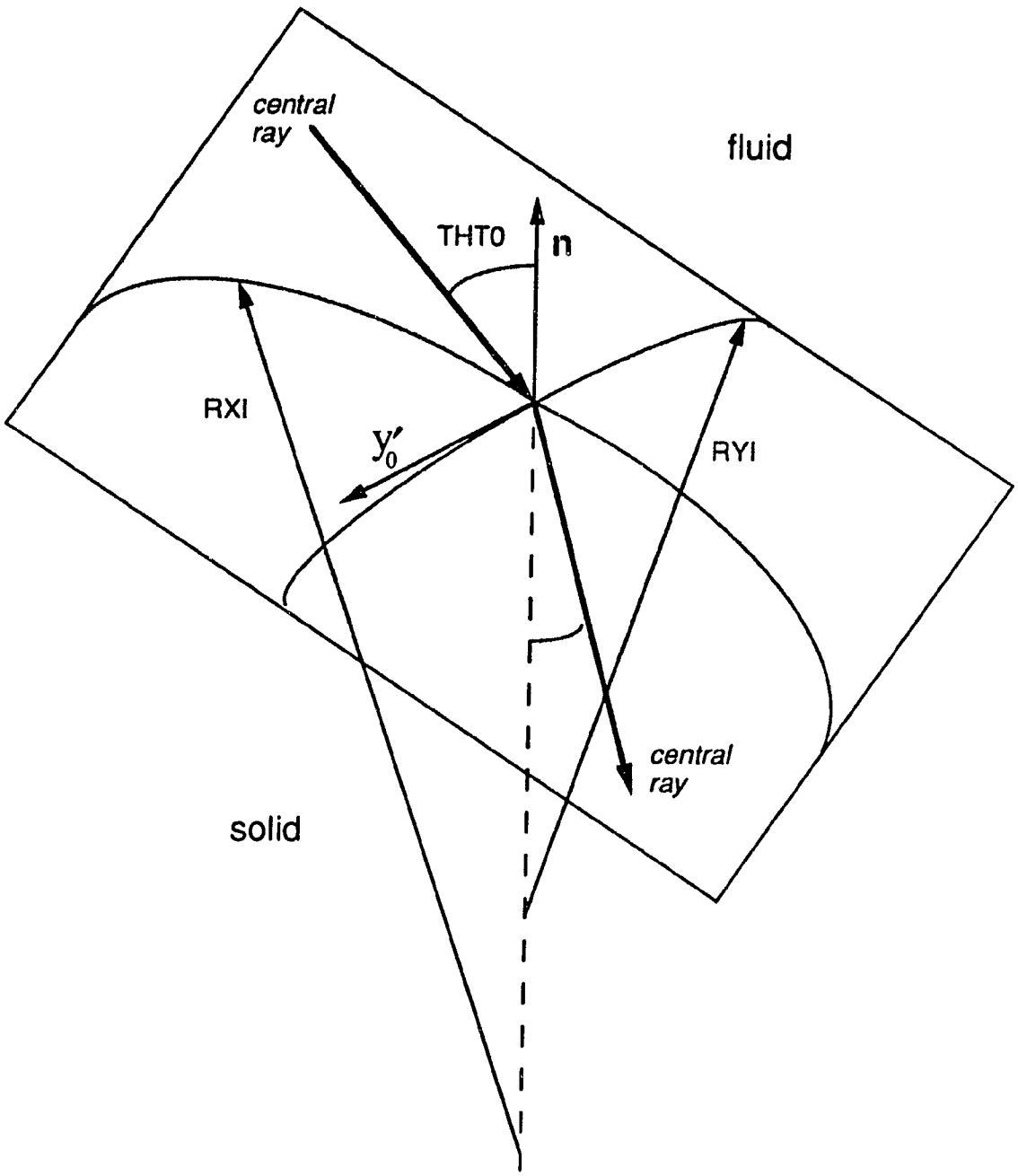

Figure B11 Bicylindrically curved fluid/solid interface - y'_0 is parallel to y_0 of Figure B10

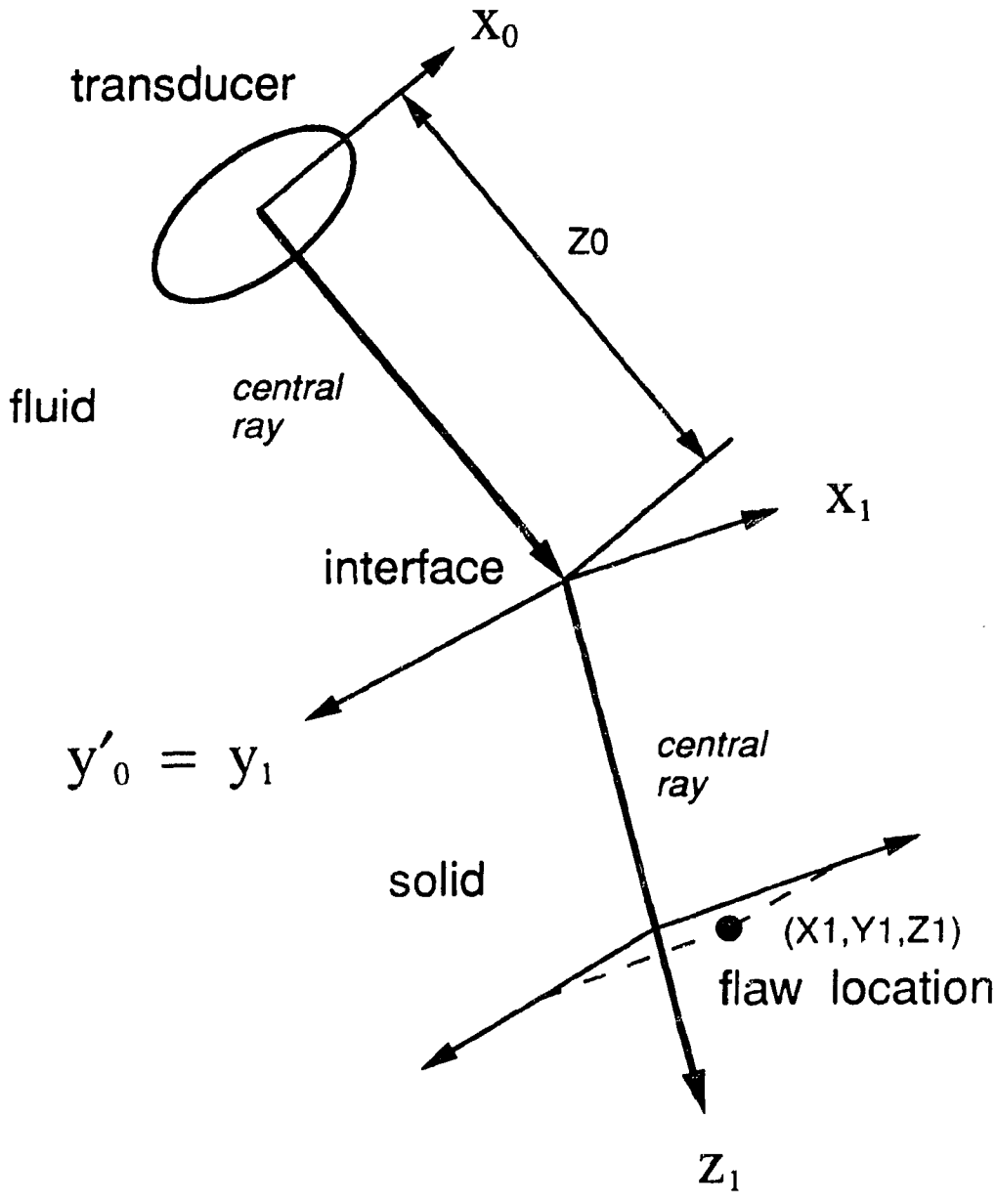

Figure B12 Flaw origin location relative to transducer, interface, and beam path

```
FORMAT:


title
ITERATE_TO_CONVERGENCE
PRIMARY matrix filename
SECONDARY matrix filename
field filename
control filename
filegroup
number of relative positions
Xrelative    Yrelative    Zrelative
.
.
.
Xrelative    Yrelative    Zrelative


     ---  or  ---


title
NTH_ORDER_ONLY
PRIMARY matrix filename
SECONDARY matrix filename
field filename
control filename
filegroup
number of relative positions
Xrelative    Yrelative    Zrelative
.
.
.
Xrelative    Yrelative    Zrelative
```

Figure B13 Generic problem identification file (".pif") format for TIES

NOTE:

"Title" is a string of up to 80 characters.

The JOBTYPE is a string of 25 characters and is left justified.

All filenames are strings of up to 40 characters.

"Filegroup" is a string of up to 36 characters that is used with various extensions to label output files:

"filegroup".out	standard output
"filegroup".ds0	sorted dataset #1
"filegroup".dsp	boundary displacements - universal file
"filegroup".trc	boundary tractions - universal file

EXAMPLE:

```
Forward and backscatter from 2 spheroids at Ka=1
ITERATE_TO_CONVERGENCE
o2s40cv1.mat
o4s40cv1.mat
forback.int
brief.int
spheroids
3
0.0   0.0   1.0
0.0   0.0   2.0
0.0   0.0   5.0
```

Figure B13 (continued)

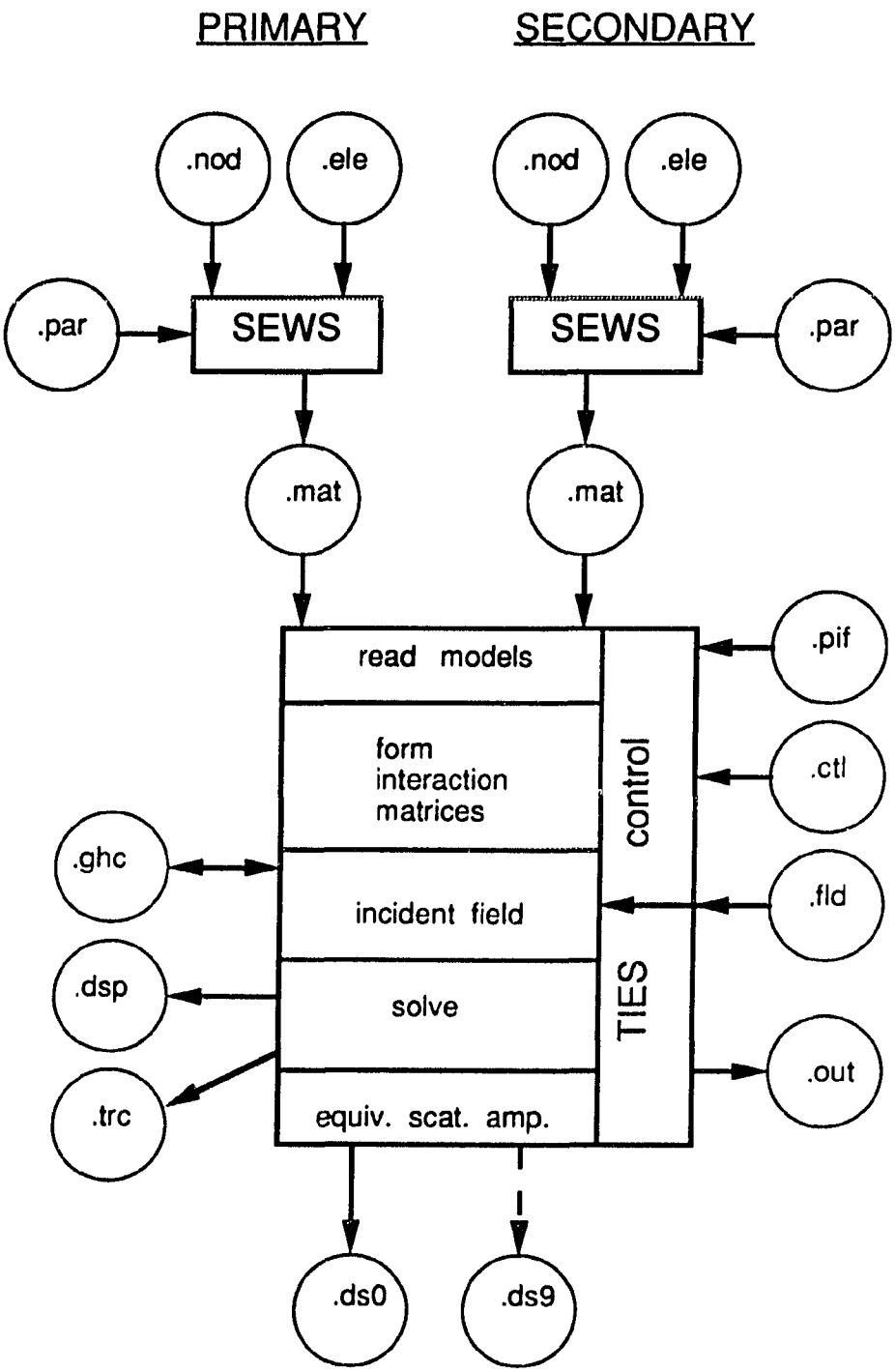

Figure B14 PROGRAM/file relationships for two interacting elastic scatterer calculations